Orthogonaal ontwerp van de elektronische structuur in nanoporeuze roosters

Orthogonal Electronic Structure Engineering in Nanoporous Frameworks

Arthur De Vos

Promotoren: prof. dr. ir. V. Van Speybroeck, dr. ir. K. Lejaeghere
Proefschrift ingediend tot het behalen van de graad van
Doctor in de ingenieurswetenschappen: toegepaste natuurkunde

UNIVERSITEIT
GENT

Vakgroep Toegepaste Fysica
Voorzitter: prof. dr. ir. C. Leys
Faculteit Ingenieurswetenschappen en Architectuur
Academiejaar 2020 - 2021

ISBN 978-94-6355-401-5
NUR 928
Wettelijk depot: D/2020/10.500/78

Members of the Examination Committee

Chair

Prof. dr. ir. Gert De Cooman (Ghent University)

Examination Board

Prof. dr. Pascal Van Der Voort (Ghent University)
Prof. dr. Stefaan Cottenier (Ghent University)
Ass. prof. dr. ir. Monique A. van der Veen (TU Delft)
Prof. dr. Johan Hofkens (KU Leuven)

Supervisors

Prof. dr. ir. Veronique Van Speybroeck (Ghent University)
Dr. ir. Kurt Lejaeghere (OCAS)

This research has been conducted at the Center for Molecular Modeling Research Group (CMM), in collaboration with:

- The Center for Ordered Materials, Organometallics and Catalysis Research Group (COMOC), Department of Inorganic and Physical Chemistry, Faculty of Sciences, Ghent University
- The Synthesis, Bioresources and Bioorganic Chemistry Research Group (SynBioC), Department of Green Chemistry and Technology, Faculty of Bioscience Engineering, Ghent University
- The LumiLab Research Group, Department of Solid State Sciences, Faculty of Sciences, Ghent University

Voorwoord

There is nothing impossible to him who will try.
Alexander the Great (336 – 323 BC)

Ik startte mijn doctoraat als voortzetting van mijn thesis, uitgevoerd aan het CMM onder leiding van Karen en Philippe. Niet lang na de start van dit doctoraat kon ik mijn thesiswerk verzilveren in een eerste artikel. Goed begonnen is half gewonnen, maar dit werk zou niet tot stand gekomen zijn zonder jullie hulp. Verder kon ik ook steeds rekenen op mijn begeleiders Kurt, Danny en Jonas die mee vorm gaven aan dit eerste artikel.

Jammer genoeg verliet Karen het CMM en veranderden mijn doctoraatsonderwerp en mijn promotor. Veronique nam me sindsdien onder haar vleugels en gaf me de kans om verder aan wetenschappelijk onderzoek te doen. Ik ben haar dan ook dankbaar voor al haar begeleiding tot de dag van vandaag. Gelukkig bleven er ook steeds enkele vaste mensen binnen mijn entourage. Op Kurt kon ik altijd rekenen, zowel op wetenschappelijk als op taalkundig en communicatief gebied. Ik durf dan ook te zeggen dat hij me geholpen heeft om op beide vlakken grote sprongen vooruit te nemen. De gecorrigeerde teksten, overgoten met opmerkingen, zal ik nooit vergeten. Op het einde van mijn doctoraat werd Kurt ook promotor, waarmee zijn begeleiding in de verf werd gezet. Ik wil hem nu dan ook nog eens bijzonder bedanken voor alle hulp en dagdagelijkse begeleiding die hij me gegeven heeft tijdens de voorbije jaren.

Verder kan ik in dit voorwoord mijn collega's van het CMM niet vergeten te vermelden, meer bepaald mijn bureaugenoten Sven, Jelle en Steven. Het was een genot om in zo'n divers lokaal te zitten, waar ik me soms wel wat de vreemde eend voelde. Jelle, jij bent een echte vriend geworden. Dat was al deels tijdens onze studies zo, maar is enkel gegroeid. De ontelbare vragen die jij, maar ook Sven en Steven hebben beantwoord, hebben me heel wat tijd bespaard. Je daagde me niet enkel uit op wetenschappelijk vlak, maar ook

op sportief en avontuurlijk vlak. Onze reis en het samen mountainbiken na de conferentie in Nieuw-Zeeland zal ik nooit vergeten.

Net zoals mijn promotor en doctoraatsonderwerp, veranderden ook mijn bureaugenoten gedurende mijn doctoraat. Zo kwam ik tijdens mijn laatste jaar terecht in het bureau van Klaas. Samen met ons tweeën op ons bureau, ik heb ervan genoten. Jij leerde me niet alleen mijn programeerskills, maar ook mijn klimtechniek verbeteren en samen met Michiel (aka de nanorangers) maakten jullie het een plezier om naar het CMM te komen. Gedurende mijn doctoraat zijn jullie beiden vrienden geworden. Met Klaas ging ik rondtrekken, zwaarbeladen en klaar voor het avontuur en met Michiel ging ik poolen, terwijl er ondertussen wel enige glazen werden verzet. Kortom, het was me een plezier zowel binnen als buiten het CMM.

Verder wil ik ook graag de mensen die mij dierbaar zijn bedanken: mijn familie, mijn vrienden en mijn vriendin. Lisa, bedankt voor al je steun en het nalezen van mijn thesis. Voortaan staat er, als alles goed gaat, een doctor naast je. Bedankt ook aan mijn ouders en mijn zus. Al jullie steun gedurende mijn studies en mijn doctoraat betekent ontzettend veel voor me.

A. De Vos
Ghent, 13 september 2020

Contents

Samenvatting

Om te kunnen blijven voorzien aan energie- en voedselbehoeften van de steeds groeiende wereldbevolking is een efficiëntere en milieuvriendelijkere winning van energie, materialen en chemicaliën nodig. Chemische transformaties door middel van katalyse is zeker één van de belangrijkste wegen in de zoektocht naar duurzame processen. Vooral heterogene fotokatalyse is een aantrekkelijke manier om chemische transformaties te activeren omdat de energie rechtstreeks uit zonlicht gehaald wordt dat overvloedig en vrij beschikbaar is. Bovendien maakt de heterogeniteit van de katalysator het mogelijk om de producten van de katalysator te scheiden zonder dat er een milieuonvriendelijke cyclus nodig is. Het ontwerp van heterogene fotokatalytische systemen die efficiënt gebruik maken van zonlicht en selectief chemische verbindingen activeren is dus een sleutelelement in de overgang naar schone chemische omzettingen. Een veelbelovend voorbeeld hiervan is het genereren van waterstofgas uit water. Ondanks de vele voordelen van heterogene fotokatalytische systemen hebben ze hun doorbraak in de industrie nog niet gevonden. De grote moeilijkheid ligt in het ontwerpen van een materiaal dat zeer actief, efficiënt en robuust is en een groot deel van de zonne-energie gebruikt.

Metaal-organische roosters (metal-organic frameworks of MOFs) en covalente organische roosters (covalent-organic frameworks of COFs) zijn recente klassen van nanoporeuze materialen die op een modulaire manier worden opgebouwd uit bouwstenen. MOFs zijn hybride materialen die bestaan uit anorganische en organische bouwstenen, terwijl COFs uitsluitend gemaakt zijn van organische bouwstenen. Beide materialen hebben zich ontwikkeld tot aantrekkelijke poreuze materialen voor heterogene fotokatalyse. Hun poreuze aard en de bijbehorende enorme oppervlakte zijn gewenste eigenschappen om als een heterogene katalysator te functioneren. Bovendien zijn beide materialen veelbelovend voor fotokatalytische toepassingen dankzij hun modulaire karakter waardoor een groot aantal aan mogelijke materialen met de gewenste optische functie kan worden geëxploreerd. Dit bouwsteenconcept biedt een enorme kans voor moleculair ontwerp, omdat bouwstenen

met verschillende eigenschappen op vele manieren gecombineerd kunnen worden. Maar juist het grote aantal mogelijke materialen vormt een grote uitdaging: hoe vind je materialen met de juiste (elektronische) eigenschappen?

De beschikbaarheid van enorme rekenkracht kan vandaag het ontwerpen van materialen met het juiste functionele gedrag vergemakkelijken door het gebruik van ab initio computationele modellering waarbij wordt gestart van een atomistische beschrijving. Dergelijke modellering biedt een grote toegevoegde waarde voor het begrijpen van experimentele waarnemingen en helpt bij het ontwerpen van betere materialen voor specifieke toepassingen. In dit doctoraat hebben we gebruik gemaakt van dergelijke computermodellering om de fotokatalytische eigenschappen van MOFs en COFs beter te begrijpen. De fotocatalytische activiteit van een materiaal kan verklaard worden vanuit zijn elektronische structuur die beschrijft hoe elektronen de elektronische toestanden binnen een materiaal bezetten. De elektronische structuur bepaalt onder meer hoe een materiaal interageert met licht en met de reagentia, door middel van reductie- of oxidatieprocessen, tijdens het fotokatalytische proces. Binnen dit doctoraat zijn daarom computertechnieken gebruikt om de elektronische structuur van modulaire materialen uit de MOF- en COF-familie te bepalen. De computationele werklast van elektronische structuurberekeningen op de betreffende materialen en het grote aantal mogelijke materialen voor MOFs en COFs maakt een uitgebreide screening echter onhaalbaar, zelfs met de huidige computationele middelen.

Het doel van dit doctoraat is dan ook de ontwikkeling van een strategie om de elektronische structuur van MOFs en COFs rationeel te ontwerpen op een meer effectieve en efficiënte manier. Hiervoor introduceren we het orthogonaal onwerp van de electronische structuur (orthogonal electronic structure engineering of OESE) in poreuze roosters, waarbij de elektronische structuur van modulaire materialen kan worden geconstrueerd door een superpositie te nemen van onafhankelijke (orthogonale) bijdragen van hun bouwstenen. Dit principe maakt het mogelijk om de elektronische structuur van het materiaal af te leiden uit de bouwstenen, en zou de weg kunnen vrijmaken voor brede screening en ontwerpcriteria voor specifieke toepassingen, terwijl er veel minder rekenkracht nodig is.

De geldigheid van het OESE-principe werd onderzocht voor twee modulaire poreuze materialen (UiO-66 en CTF), een modulair moleculair complex (Ru(II)L_3) en een gecombineerd systeem (Ru(II)L_3-CTF) waarbij een fotokatalytisch actieve constructie wordt gemaakt op basis van een CTF en een actief Ru-complex. We zijn gestart met UiO-66(Zr), een MOF die bestaat uit octaëdraal gecoördineerde Zr-atomen, die $Zr_6O_4(OH)_4$ nodes vormen, verbonden via benzeen dicarboxylaat linkers. UiO-66 is een zeer stabiele

MOF die de integratie van verschillende linkers en metalen mogelijk maakt en bovendien in toenemende mate wordt beschouwd als potentieel fotokatalytisch materiaal. Uit dit doctoraat bleek dat de elektronische structuur van UiO-66(Zr) inderdaad te vinden is door superpositie van de elektronische bijdragen van zijn constituenten. Quasideeltjesenergieën geassocieerd met metaalnodes en organische linkers konden duidelijk worden onderscheiden, en de elektronische structuur kon gezien worden als een combinatie van de onafhankelijke bouwstenen. Het geval van UiO-66 is dus een duidelijk bewijs van het concept van het OESE-principe.

De fotokatalytische activiteit van UiO-66(Zr) wordt bepaald door twee processen, de energie die nodig is om een elektron van de linker te exciteren (ΔE_{abs}) en de efficiëntie van de overdracht van dit geëxciteerde elektron naar de metaalnode, d.w.z. de ligand-naar-metaal ladingstransfer (ligand-to-metal charge transfer of LMCT). Deze twee processen zijn te onderscheiden in de elektronische structuur door twee energieverschillen, ΔE_{abs} en ΔE_{LMCT}, d.w.z. respectievelijk de energie die nodig is voor een excitatie en de daarop volgende LMCT van het geëxciteerde elektron. Om een efficiënte elektronenoverdracht naar de Zr-node en dus een hoge activiteit te verkrijgen, moet ΔE_{LMCT} in de buurt van nul of zelfs negatief zijn. Dit is niet het geval voor UiO-66(Zr) wat de activiteit beperkt. Bovendien is ΔE_{abs} van UiO-66(Zr) te groot en daarom niet geschikt voor het gebruik van zonlicht. Het ongefunctionaliseerde, defectvrije UiO-66(Zr) is dus niet de heilige graal in de fotokatalyse. Dankzij het modulaire karakter kan het echter gefunctionaliseerd worden om betere fotokatalytische eigenschappen na te streven, zoals ook uit experimenten is gebleken.

In overeenstemming met het OESE-principe kunnen beide problemen afzonderlijk worden aangepakt. ΔE_{abs} kan efficiënt gereduceerd worden door het incorporeren van amino gefunctionaliseerde linkers (elektronendonerende groepen), terwijl de efficiëntie van de LMCT verhoogd kan worden door het incorporeren van verschillende metalen in de node, waardoor de ΔE_{LMCT} effectief gereduceerd wordt. Dit laatste werd onderzocht door de incorporatie van isovalente atomen (Zr, Hf, Ti), waarbij werd geconcludeerd dat alleen Ti de LMCT verbetert in overeenstemming met experimentele resultaten. Verder hebben we het onderzoek uitgebreid naar de incorporatie van lanthaniden, bekend om hun interessante licht- en katalytische eigenschappen. Voor deze Ln-gedopeerde materialen bleek dat cerium incorporatie in de node een lege 4f-band introduceerde binnen de oorspronkelijke UiO-66 band gap wat aanleiding zou kunnen geven tot een efficiënte LMCT. Op basis van de ongevoeligheid van het lanthanidegedrag aan de chemische omgeving werden vergelijkbare ladingsovergangen afgeleid voor Yb en Eu, wat suggereert dat deze lanthaniden ook gebruikt kunnen worden om de fotokatalytische

activiteit te verhogen.

Het is bekend dat defecten alomtegenwoordig zijn in materialen en ze een aanzienlijk effect hebben op het functioneel gedrag van nanomaterialen. Dit geldt met name voor MOFs. Het is bekend dat UiO-66(Zr) defecten door ontbrekende linkers bevat die door het synthetisch proces kunnen worden ingebouwd met behoud van zijn stabiliteit. Deze defecten zorgen voor onverzadigde metalen die interessant zijn voor de katalyse. We hebben daarom de effecten van defecten op de elektronische structuur van UiO-66(Zr) bestudeerd en deze in verband gebracht met zijn fotokatalytische activiteit. Eerst werd een duidelijke notatie ingevoerd om deze structuren met ontbrekende linkers te classificeren. Deze classificatie geeft de gewijzigde nodeconfiguraties binnen de defectstructuur aan veroorzaakt door ontbrekende linkers. Vervolgens hebben we aangetoond dat het gedrag van de onbezette Zr d-orbitalen, die de efficiëntie van de LMCT regelen, voor een groot deel kan worden afgeleid uit de nodeconfiguraties die in de defectstructuur aanwezig zijn. Hoe meer linkers per node worden verwijderd, hoe meer deze orbitalen verlagen in energie en hoe meer het elektron gelokaliseerd wordt in de buurt van de plaats van de ontbrekende linkers. De waargenomen verlaging van de energie van de gelokaliseerde Zr d-orbitalen op de plaats van het defect vermindert effectief $\Delta \mathrm{E}_{LMCT}$ en verbetert de ladingsoverdracht naar de node en dus de fotokatalytische activiteit. Aan de andere kant blijven de linkertoestanden vrijwel constant voor alle defectstructuren, waardoor de absorptie-eigenschappen (ΔE_{abs}) behouden blijven. Het effect van ontbrekende linkers bevestigde dus het OESE-principe, waarbij de elektronische structuur kan worden afgeleid uit de bouwstenen.

Om de bredere toepasbaarheid van het OESE-principe te testen hebben we ook de elektronische structuur van COFs onderzocht. COFs zijn een zeer recente klasse van poreuze materialen die uitsluitend bestaan uit organische bouwstenen. Hun eigenschappen worden teweeggebracht door hun sterke, volledig covalente aard die zowel een hoge stabiliteit als een elektronische koppeling veroorzaakt. Dit laatste vormt een grote uitdaging voor het OESE-principe en is daarom een ideaal geval om de bredere toepasbaarheid ervan te testen. Daarnaast worden COFs onderzocht voor fotokatalyse, zoals bijvoorbeeld voor de splitsing van water. Hoewel ze geen anorganisch katalytisch centrum hebben, wat hun activiteit lijkt te beperken in vergelijking met MOFs, kan hun activiteit worden verhoogd door de incorporatie van fotokatalytische complexen. We hebben daarom covalente triazineroosters (covalent triazine frameworks of CTFs) bestudeerd en onderzocht hoe hun bouwstenen de elektronische structuur beïnvloeden. Verder werden de CTFs gefunctionaliseerd met Ru-polypyridylcomplexen, bekende homogene fotokatalysators, om een heterogene fotokatalysators met goed gedefinieerde

actieve sites te construeren. De heterogene constructie is een ideaal vertrekpunt om het OESE-principe verder te testen. Hiervoor werd de elektronische structuur van geïsoleerde fotoactieve Ru-polypyridylcomplexen, CTFs en de uiteindelijk verkregen heterogene constructies onderzocht.

CTFs zijn een veelbelovende klasse van COFs, omdat ze thermisch en chemisch stabiel zijn. CTFs zijn 2D poreuze roosters die gemaakt worden door trimerizatie van aromatische nitrillen. Bijzonder interessant zijn CTFs waarbij stikstofhoudende heterocyclische linkers in de structuur zijn opgenomen, aangezien deze stikstoflocaties kunnen fungeren als ankerpunten voor verschillende moleculaire complexen en, nog belangrijker, het Ru-polypyridylcomplex dat hier wordt onderzocht. De Ru-polypyridylcomplexen, Ru(II)L_3, bestaan uit een Ru(II)-kation omringd door drie heteroaromatische azines (L_3) - met bipyridine als meest bestudeerde ligand - en zijn interessante fotoactieve katalysatoren. De bidentale liganden, die deel uitmaken van de polypyridylklasse, maken ze bijzonder aantrekkelijk omdat ze gemakkelijk in de CTF geïntroduceerd kunnen worden. De fotoactiviteit van deze complexen wordt veroorzaakt door hun langlevende metaal-naar-ligand ladingstransfer (metal-to-ligand charge transfer of MLCT) die wordt geïnduceerd door lichtabsorptie. Deze MLCT en de daaruit voortvloeiende beschikbaarheid van het aangeslagen elektron op de liganden is de oorsprong van de goede prestaties als fotokatalysator voor verscheidene oxidatie- of reductiereacties.

Binnen dit doctoraat hebben we de elektronische structuur van zowel de ongefunctionaliseerde CTFs als de Ru(II)L_3-complexen onderzocht en vastgesteld dat ook voor deze systemen de elektronische structuur voor een groot deel kan worden afgeleid uit de afzonderlijke bouwblokken. Dit geeft aan dat het OESE-principe tot op zekere hoogte van toepassing is op CTFs (COFs) en Ru-polypyridylcomplexen (moleculaire complexen). Om inzicht te krijgen in het CTF-verankerde Ru-polypyridylcomplex (Ru(II)L_3@CTF), hebben we een breed scala aan verschillende CTFs en Ru(II)L_3-complexen op basis van polypyridylen beschouwd en aangetoond dat het energetisch gunstig is om Ru complexen op CTFs te verankeren. Een essentiële voorwaarde voor een efficiënte heterogene fotokatalysator is echter dat de fotoredoxeigenschappen van het Ru-polypyridylcomplex bij verankering in de CTF niet veranderen. We bevestigden dat de elektronische structuur van zowel het Ru(II)L_3 complex als de CTF grotendeels onveranderd blijft bij het combineren van de twee systemen en dat de redoxpotentiaal van het fotokatalytisch complex grotendeels dezelfde blijft. Dit is opnieuw een bevestiging van het OESE-principe, maar nu voor de combinatie van een COF en een moleculair complex.

De Ru(II)L_3@CTF is een interessant vertrekpunt voor het ontwerp van modulaire heterogene fotokatalytische systemen, omdat het laat zien dat het

systeem in bredere zin kan worden afgesteld door het rooster zelf, maar ook door variaties aan te brengen in het fotokatalytische complex. Het kan interessant zijn voor toekomstige studies om de toepasbaarheid van het OESE-concept op een breder scala van systemen te onderzoeken. Voor Ru(II)L_3@CTF werd afgeleid dat band gaps, ladingsoverdrachten en redoxpotentialen allemaal kunnen worden aangepast door het stikstofgehalte van de verschillende bouwblokken van de katalysator te wijzigen. Een hoger stikstofgehalte verlaagt typisch de energie van onbezette polypyridylniveaus en bezette Ru t_{2g} niveaus, terwijl bezette linker- of ligandtoestanden slechts weinig veranderen. Dit gedrag maakt het mogelijk om de lichtgeïnduceerde ladingsoverdracht te richten naar het rooster (roostergerichte-MLCT) of de porie (poriegerichte-MLCT) door het verhogen van respectievelijk de stikstofinhoud van de CTF of losse Ru-liganden. De veelzijdigheid van CTF-verankerde Ru(II)L_3-complexen geeft ze daarom de mogelijkheid om een hoge fotoredoxactiviteit te geven aan een breed scala aan doelwitreacties en katalytische opstellingen. De verkregen inzichten kunnen derhalve de elektronische opbouw van modulaire systemen, die bestaan uit een heterogene drager die zelf modulair is maar verder kan worden gefunctionaliseerd met fotoactieve modulaire complexen, aanzienlijk vooruithelpen.

Samengevat hebben we binnen dit doctoraat het concept van het ortogonaal ontwerp van elektronische structuren bedacht. Daarin wordt gesteld dat de elektronische structuur van modulaire materialen kan worden afgeleid uit de ontkoppelde bijdragen van hun componenten. Een belangrijk bewijs voor het OESE-principe werd gevonden in UiO-66, CTFs en moleculaire Ru-polypyridyl complexen. Ook de verankering van Ru-polypyridylcomplexen op CTFs toonde aan dat het principe geldig is wanneer het complex en de scaffold als bouwstenen worden beschouwd. Het levert een potentiële heterogene fotokatalysator op met een grote veelzijdigheid. Het OESE-principe biedt verder een rationele ontwerpstrategie om de bouwstenen van deze modulaire materialen af te stemmen op fotokatalytische toepassingen.

Summary

Sustaining the growing global population requires a more efficient and environmentally friendly harvesting of energy, materials and chemicals. Chemical transformation by means of catalysis is certainly one of the main pathways in search of improved sustainability. In particular heterogeneous photocatalysis offers an attractive route to activate chemical transformations, as its energy is directly harvested from sunlight abundantly present and freely available. Furthermore, the heterogeneity of the catalyst allows to separate the products from the catalyst without the need of an environmentally unfriendly cycle. The design of heterogeneous photocatalytic systems which efficiently harness sunlight and selectively activate chemical species is thus a cornerstone in the transition to clean chemical conversions, for example to generate hydrogen gas through water splitting. Despite the main advantages of heterogeneous photocatalysis such systems have not found their breakthrough in industry. The great difficulty lies in designing a material that is highly active, efficient, robust and uses a large part of the solar spectrum.

Metal-organic frameworks (MOFs) and covalent organic frameworks (COFs) are recent classes of nanoporous materials that are made in a modular way from building blocks. MOFs are hybrid materials made up of inorganic and organic constituents, whereas COFs are solely made from organic building blocks. Both materials have emerged as attractive nanoporous materials for heterogeneous photocatalysis. Their porous nature and consequently large surface area are desired properties to function as a heterogeneous catalyst. Furthermore, these materials are promising to explore for photocatalytic applications thanks to their modular nature, which allows to explore a large number of possible materials with the desired optical function. This building block concept offers an enormous opportunity for molecular design, as building blocks with distinct properties can be combined in multiple ways. However, exactly the high number of hypothetical materials poses a major challenge: how to find materials with the proper (electronic) properties?

Today the availability of enormous computing power could help in designing materials with the proper functional behaviour through the use of first-principles computational modelling which uses a bottom up approach starting from the atomistic scale. Such modelling has proven to be of great added value to understand experimental observations and to design better materials for specific applications. In this PhD research we have used such computational modelling to better understand the photocatalytic properties of MOFs and COFs. The photocatalytic activity of a material can be retrieved from its electronic structure, which describes how electrons occupy the electronic states within a material. Knowledge of the electronic structure indicates, for example, how a material interacts with light as well as with the reagents through reduction or oxidation processes during the photocatalytic process. Computational techniques were therefore used within this PhD research to determine the electronic structure of modular materials belonging to the MOF and COF family. However, the computational load of electronic structure calculations on the materials of interest and the large number of possible materials for MOFs and COFs makes comprehensive screenings unfeasible even with today's computational resources.

The overall aim of this PhD research is therefore the development of a strategy to rationally design the electronic structure of MOFs and COFs in a more effective and systematic way. We introduced the idea of *Orthogonal Electronic Structure Engineering* (*OESE*), in which the electronic structure of modular frameworks can be seen as a sum of independent (orthogonal) contributions of their building blocks. This principle makes it possible to deduce the electronic structure of the framework material from its building blocks, and could pave the way to a wide-scope screening of materials and design criteria for a specific application, while using much less computational power.

The validity of the OESE principle was investigated for two modular nanoporous materials (UiO-66 and CTF), a modular molecular complex ($Ru(II)L_3$) and a COF namely a CTF generating a photocatalytic active scaffold ($Ru(II)L_3$-CTF). We started with UiO-66(Zr), a MOF that consists of octahedrally coordinated Zr atoms, forming $Zr_6O_4(OH)_4$ nodes, connected via benzene dicarboxylate (BDC) linkers. UiO-66 is a very stable MOF that allows the inclusion of genuinely different linkers and metals and is increasingly considered as a potential photocatalytic material. Within this PhD thesis we found that the electronic structure of UiO-66(Zr) can indeed be found by superposition of the electronic contributions of its constituents. Quasiparticle energy levels associated with metallic nodes and organic linkers could clearly be distinguished, and the electronic structure could be described as a sum of independent constituents. The case of UiO-66 is thus a clear proof for the

OESE principle.

The photocatalytic activity of UiO-66(Zr) is determined by two processes, the energy needed to excite an electron at the linker and the efficiency of the transfer of this excited electron to the metal node, i.e. the ligand-to-metal charge transfer (LMCT). These two processes can be characterized from the electronic structure by two energy gaps, ΔE_{abs} and ΔE_{LMCT}, i.e. respectively the energy needed to excite an electron and subsequent LMCT of the excited electron. In order to obtain an efficient electron transfer to the Zr node and thus a high activity, ΔE_{LMCT} should be close to zero or or even negative. This is not the case for the pristine UiO-66(Zr) material restricting its activity. In addition, ΔE_{abs} of UiO-66(Zr) is too large and is therefore not suited for the direct use of sunlight. The unfunctionalized, defect-free material UiO-66(Zr) is thus not the holy grail in photocatalysis. However, thanks to its modular nature, it can be functionalized to pursue better photocatalytic properties, as was also seen in experiments.

In line with the OESE principle both problems could be targeted separately. ΔE_{abs} can be efficiently reduced by incorporation of amino functionalized linkers (electron donating groups), while the efficiency of LMCT can be increased by incorporating different metals within the inorganic node, effectively reducing ΔE_{LMCT}. The latter was investigated by incorporation of isovalent atoms (Zr, Hf, Ti) where it was concluded that only Ti improves the LMCT, in line with experimental results. We furthermore extended the search towards the incorporation of lanthanides, known for their interesting light-based and catalytic properties. When theoretically evaluating these Ln-doped materials, cerium insertion in the node was found to introduce an empty 4f band within the pristine UiO-66 band gap, which could also give rise to an efficient LMCT. Based on the invariance of the lanthanide series on its chemical environment similar charge-state transition levels were deduced for Yb and Eu, suggesting that these lanthanides can be used to increase the photocatalytic activity as well.

Defects are known to be omnipresent in materials and are know to have a significant effect on the functional behaviour of nanomaterials. This is particularly true for MOFs. In particular UiO-66(Zr) has shown to contain missing-linker defects which can be included by the synthetic procedure while retaining its stability. These defects create unsaturated metal sites interesting for catalysis. We therefore studied the effects of defects on the electronic structure of UiO-66(Zr) and related them to its photocatalytic activity. First, a clear notation was introduced to classify these missing-linker defect structures, indicating the altered node configurations within the defect structure introduced by the missing linkers. We subsequently showed that the behaviour of the Zr unoccupied d-orbitals, which control

the efficiency of the LMCT, can be deduced to a large extent from the types of nodes present in the defect structure. Moreover, the more linkers per node are removed, the more these orbitals lower in energy and the more the electron becomes localized near the site of the missing linkers. The observed lowering of the energy of localized Zr d-orbitals at the defect site effectively decreases ΔE_{LMCT} and improves the charge transfer to the node and therefore its photocatalytic activity. On the other hand, the linker states remain almost constant for all defect structures, preserving the absorption characteristics (ΔE_{abs}). The effect of missing linkers therefore corroborated the OESE principle where the electronic structure can be deduced from the building blocks.

To test the broader applicability of the OESE principle we also investigated the electronic structure of COFs. COFs are a very recent class of nanoporous materials solely composed of organic building blocks. Their properties are induced by their strong, fully covalent nature causing both a high stability and electronic coupling. The latter provides a major challenge for the OESE principle and is therefore an ideal case to test its broader applicability. Pristine COF frameworks are also being explored for photocatalysis, more in particular for the splitting of water. Although they lack an inorganic catalytic center, which seems to limit their activity compared to MOFs, their activity can be increased by incorporation of photocatalytic complexes. We therefore considered covalent triazine frameworks (CTFs) and examined how their building blocks affect the CTF's electronic structure. Furthermore, the CTFs were functionalised with Ru-polypyridyl complexes, well-known homogeneous photocatalysts, to construct heterogeneous photocatalysts with well defined active sites. These heterogeneous scaffolds are an ideal case to test the OESE principle. To this end the electronic structure of the isolated photoactive Ru-polypyridyl complexes, CTFs and the finally obtained scaffolds were investigated.

CTFs are an especially promising class of COFs as they are thermally and chemically stable. CTFs are 2D nanoporous frameworks made upon the trimerization of aromatic nitriles. Especially interesting are CTFs where nitrogen containing heterocyclic linkers are included in the structure, as these nitrogen sites can act as docking sites for different molecular complexes and more importantly the Ru-polypyridyl complex under investigation here. The Ru-polypyridyl complexes, Ru(II)L_3, consist of a Ru(II) cation chelated by three heteroaromatic azines (L_3) - with bipyridine the most studied ligand - and are interesting photoactive catalysts. The bidentate ligands, part of the polypyridyl class, make them particularly attractive as they can easily be introduced inside the CTF. The photoactivity of these complexes is caused by their long-lived metal-to-ligand charge-transfer (MLCT) state induced by

light absorption. This MLCT and resulting availability of the excited electron on the ligands is the origin of its good performance as photocatalyst for oxidation or reduction reactions.

Within this PhD thesis we investigated the electronic structure of both the unfunctionalized CTFs and the Ru(II)L_3 complexes and found that also for these systems the electronic structure can to a large extent be deduced from the individual components. This indicates that the principle of OESE is to a certain extent applicable to CTFs (COFs) and Ru-polypyridyl complexes (molecular complexes). To obtain insight into the CTF-anchored Ru-polypyridyl complex (Ru(II)L_3@CTF), we considered a wide range of different polypyridyl-based CTF monolayers and Ru(II)L_3 complexes and demonstrated that it is energetically favourable to anchor the Ru complexes onto the CTF. However, an essential condition for an efficient heterogeneous photocatalyst is that the photoredox properties of the Ru-polypyridyl complex do not deteriorate when incorporated into the CTF scaffold. We confirmed that the electronic structure of both the Ru(II)L_3 complex and CTF stay mostly unaltered upon combining the two systems and that the redox potential of the photocatalytic complex remains largely the same. This is again a confirmation of the OESE principle, but now for the combination of a COF and a molecular complex.

The Ru(II)L_3@CTF based scaffold is an interesting case for the design of modular heterogeneous photocatalytic systems, as it shows that the system can be tuned in a broader sense by varying the framework itself but also the anchored photocalytic complex. It might be interesting for future studies to explore the broader applicability of the OESE principle to a wider range of systems. For the Ru(II)L_3@CTF it was deduced that band gaps, charge-transfer reactions and redox potentials are all strongly adaptable by changing the nitrogen content of the different components of the catalyst. A higher nitrogen content typically lowers the energy of unoccupied polypyridyl levels and occupied Ru t_{2g} levels, while occupied linker or ligand states change only little. This behaviour makes it possible to guide the light-induced charge transfer to either the framework (framework-directed MLCT) or the pore (pore-directed MLCT) by increasing the nitrogen content of respectively the CTF or the dangling Ru ligands. The versatility of CTF-anchored Ru(II)L_3 complexes therefore endows them with the capability to display a high photoredox activity for a wide range of target reactions and catalytic set-ups. The obtained insights may therefore significantly advance electronic structure engineering of modular systems consisting of a heterogeneous support which is in itself modular, but can be further functionalized by photoactive modular complexes.

We can conclude that within this PhD research we have coined the con-

cept of orthogonal electronic structure engineering (OESE) stating that the electronic structure of modular materials can be deduced from decoupled contributions of their components. Proof of principle for the OESE was found in UiO-66 and Covalent Triazine Frameworks as well as the molecular Ru-polypyridyl complexes. Furthermore, the anchoring of Ru-polypyridyl complexes on CTFs showed the principle to be valid when considering the complex and the scaffold as its building blocks. It yields a potential heterogeneous photocatalyst with large versatility. The OESE paradigm provides a rational design strategy to tune the building blocks of these modular materials to make them more suited for photocatalytic applications.

List of Symbols

Throughout this dissertation, italicized variables indicate scalars and bold-faced variables indicate vectors.

Latin symbols	
A	Electron affinity
b_1	First reciprocal unit cell vector
b_2	Second reciprocal unit cell vector
b_3	Third reciprocal unit cell vector
D	Density of states
E	Energy
E_b	Exciton binding energy
E_g	Fundamental / band gap
E_H	Hartree energy
E_{opt}	Optical gap
E_{xc}	Exchange-correlation energy
h	Planck constant
$\hbar$	Reduced Planck constant
$\widehat{H}$	Hamiltonian
I	Ionization energy
$\mathbf{k}$	Wave vector
n	Electron density / band index
$\mathbf{r}$	Electronic coordinates
$\mathbf{R}$	Nuclear coordinates
$\widehat{T}_e$	Kinetic energy operator of the electrons
$\widehat{T}_s$	Kinetic energy operator of non-interacting system
$\widehat{T}_N$	Kinetic energy operator of the nuclei
$\widehat{V}$	Potential energy operator
$\widehat{V}_{ee}$	Coulomb repulsion operator between the electrons

v_{eff}	Effective potential
v_{ext}	External potential
v_H	Hartree potential
$\overline{V}_n$	The average electrostatic potential of a core electron around atom n
$\widehat{V}_{Ne}$	Coulomb attraction operator between the electrons and the nuclei
$\widehat{V}_{NN}$	Coulomb repulsion operator between the nuclei
v_{xc}	Exchange-correlation potential
V_∞	Vacuum potential / level
$\mathbf{x}$	General set of variables

Greek symbols

ν	Frequency
$\boldsymbol{\sigma}$	Spin of electrons
$\phi_{\alpha,\mu}$	Atomic orbital with μ its quantum numbers and α the atom around which it is centred
ϕ_j	Single-particle wave function
χ	Nuclear wave function
Ψ	Nuclear and electronic wave function
ψ	Electronic wave function
$\psi_{n,\mathbf{k}}$	Bloch wave function
Ω_{cell}	Unit cell volume

List of Abbreviations

ARPES	Angle-resolved photoemission spectroscopy
ATA	Aminoterephthalate
B3LYP	Becke three-parameter Lee-Yang-Parr
BDC	Benzene dicarboxylate
CAM	Coulomb-attenuating method
CN	Coordination number
COF	Covalent organic framework
CT	Charge-transfer
CTF	Covalent triazine frameworks
DFT	Density-functional theory
DLTS	Deep-level transient spectroscopy
DOS	Density of states
GGA	Generalized gradient approximation
GITT	Galvanostatic intermittent titration technique
GKS	Generalized Kohn-Sham
HOCO	Highest occupied crystal orbital
HOMO	Highest occupied molecular orbital
HRBE	Host-referred binding energy
HRTEM	High-resolution transmission electron microscopy
HSE06	Heyd-Scuseria-Ernzerhof '06
IBZ	Irreducible brilouine zone
IUPAC	International union of pure and applied chemistry
KS	Kohn-Sham
LAPW	Linearized Augmented Plane Wave
LDA	Local density approximation
LDOS	Local density of states
LMCT	Ligand-to-metal charge transfer
Ln	Lanthanide
LUCO	Lowest unoccupied crystal orbital
LUMO	Lowest unoccupied molecular orbital
MM	Molecular mechanics

MOF	Metal-organic framework
M06	Minnesota '06
NTA	Nitroterephthalate
OCV	Open-circuit voltage
OESE	Orthogonal electronic structure engineering
PAW	Projector-augmented wave
PBE	Perdew-Burke-Ernzerhof
PhD	Philosophiae doctor
PL	Photoluminescence
QM	Quantum mechanical
SBU	Secondary building unit
SE	Self-interaction error
TD-DFT	Time-dependent density-functional theory
TD-DFPT	Time-dependent density-functional perturbation theory
UiO	Universitetet i Oslo
VASP	Vienna ab initio simulation package
VRBE	Vacuum-referred binding energy
XC	Exchange-correlation

Part I

Orthogonal Electronic Structure Engineering in Nanoporous Frameworks

1

Introduction

It's a dangerous business, Frodo, going out your door. You step onto the road, and if you don't keep your feet, there's no knowing where you might be swept off to. (J. R. R. Tolkien (1892 – 1973))

Sustaining the growing global population requires a more efficient and environmentally friendly harvesting of energy, materials and chemicals. It is one of the main challenges of our time to find better chemicals and novel processes that reduce the overall footprint of the production industry.[1, 2] Climate change is only one (big) example of how devastating non-sustainable solutions are. Fortunately, we have witnessed tremendous advances in sciences, offering new technological solutions which may help to sustain in our daily energy, chemicals and other basic substances. Driven by these major societal challenges we are facing today, there is a relentless strive to search for sustainable and environmentally friendly solutions for processes which have a negative footprint on the future generations.

Chemical transformations by means of catalysis is certainly one of the main drivers in the search of improved sustainability.[3] Catalysts speed up reactions, lower the energy input for the transformation and reduce unwanted by-products. Conversion of pollutants in exhaust gases and synthesis of complex medicines from simple molecular building blocks are just two examples of its potential.[4, 5] Improving existing catalysts to obtain, for example, a higher selectivity can stepwise enhance the energy efficiency, raw material usage and sustainability of the transformation. However, with the quest for

conversion of new feedstock, such as biomass or the quest to harvest energy from sunlight more efficiently, new catalysts will have to be designed in the coming years and decades. Such technological developments are urgently needed to design green and sustainable chemical routes and a clean energy system.

Nanoporous materials are omnipresent within catalysis and provide a platform for a broad variety of chemical conversions.[6–8] According to the International Union of Pure and Applied Chemistry (IUPAC),[9] nanoporous materials can be categorized into microporous (diameter < 2 nm), mesoporous (diameter from 2 to 50 nm) or macroporous materials (diameter > 50 nm), and are tractable due their high surface area, porosity and chemical versatility.[10, 11] They behave as crystalline sponges (see Figure 1.1) with nanoscale apertures making them very attractive for catalysis.

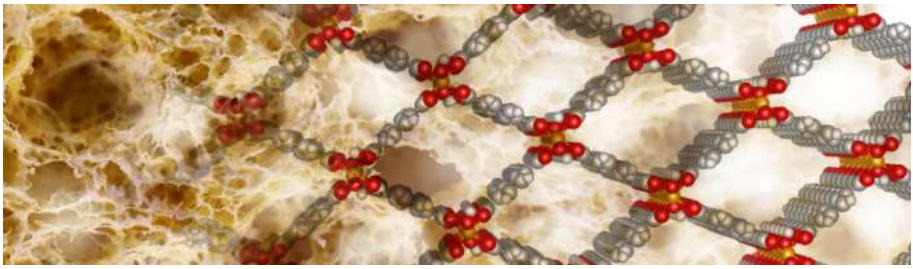

Figure 1.1: Artistic impression of nanoporous materials compared to macroscopic sponges. The nanoporous material shown at the right is MIL-53, a Metal-Organic Framework (MOF). Figure made by Wim Dewitte see Ref. [12].

Zeolites are to date the most studied nanoporous materials. They where discovered by the Swedish mineralogist Alex Frederic Cronstedt[13] in the 18th century and first synthesized in 1862.[14] Zeolites are combinations of purely inorganic building blocks – tetrahedral M-O_4 with M = Al, Si – forming a crystalline framework.[15] Around 200 zeolites are known and they are vital for the petrochemical industry.[16] Althrough zeolites are mostly used to convert non-renewable fossil fuels, they will maintain to play an important role in the conversion of new feedstock thanks to their high stability and versatility to design complicated active sites.[17–20]

However, in the last decades a whole new series of nanoporous materials were experimentally synthesized based on a building block concept.[21–27] The concept of Reticular Design or Reticular Chemistry was introduced in 2003 (see Figure 1.2).[28, 29] It is inspired by nature's ability to create complex systems with advanced functionalities using atomic-level assembly and evolutionized

the field as a broad variety of framework materials could be made with different pore size, surface area and chemical functionalities.

Metal-organic frameworks (MOFs) are the showcase example of this concept where organic building blocks are combined with inorganic fragments.[26, 30–32] The number of materials that can be created in this way is enormous and to date over 70000 have been experimentally synthesized whereas only a few have been found to naturally occur.[33]

In 2005, Omar Yaghi discovered that it is also possible to combine solely organic building blocks towards crystalline nanoporous materials creating covalent organic frameworks (COFs).[34] While the creation of structures based on merely organic (metal-free) monomers is common in polymers, the creation of crystalline nanoporous frameworks was a new concept.[18, 35] The strong covalent bonds in COFs provide a very high chemical and thermal stability[36–38] which MOF sometimes lack.[39–41] The absence of metals in COFs makes them much lighter than most other nanoporous materials while still possessing very high surface areas. Since their early days increasingly more COFs are being synthesized and the new materials can be made with a large tunability in terms of functionality and porosity. Furthermore, COFs have extended, conjugated structures which are not present in zeolites or MOFs making them attractive as nanoporous organic (photo)catalysts and electronic materials.[18, 36, 37, 42–44]

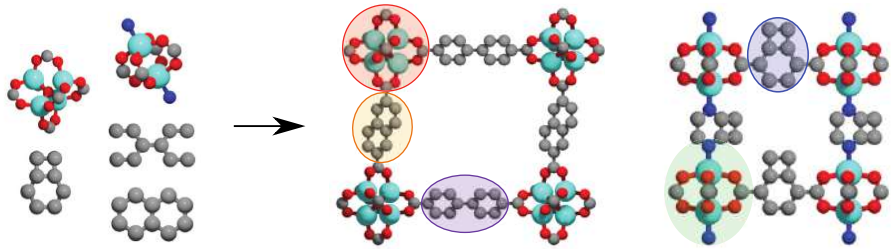

Figure 1.2: Reticular Chemistry: The playground for material chemistry is comparable to building with Lego® bricks, but, on the nanoscale. Adapted from Ref. [31] with permission from the Nature Publishing Group.

The three classes of nanoporous frameworks yield a complete cycle of crystalline nanoporous frameworks formed by solely inorganic (zeolites), hybrid (MOF) and solely organic building blocks (COFs) (see Figure 1.3).[42] Due to the concept of reticular chemistry used within MOFs and COFs, engineering nanoporous materials is like playing with Lego®, at least from a graphical/computational perspective. As these building blocks can be combined in a multitude of ways, they can be tailored for a specific application.

Consequently, their great designablility makes them suited for many applications. In the next sections we restrict ourselves to MOFs and COFs, the nanoporous frameworks of interest within this PhD thesis, for which applications such as photocatalysis are still largely unexplored.

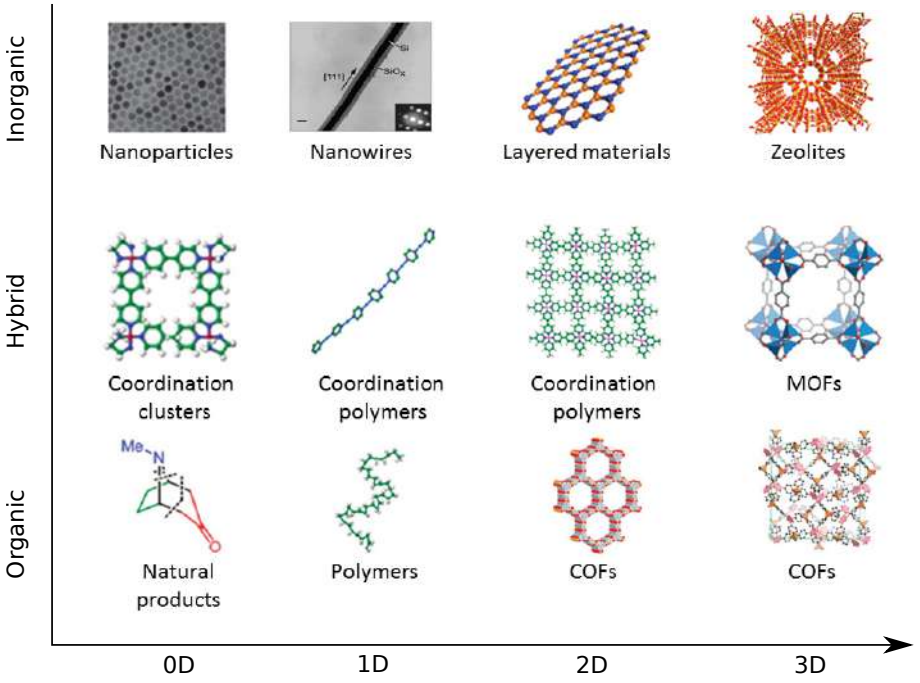

Figure 1.3: Assembly of building blocks to construct inorganic, hybrid and fully organic scaffolds, ranging from 0D to extended 3D structures. Adapted from Ref. [42] with permission of the American Chemical Society.

1.1 Applications of Nanoporous Frameworks

The high tuneability of MOFs and COFs offers opportunities to design materials for specific applications with perfectly tuned characteristics (see Figure 1.4). Due to this high tuneability MOFs and COFs can be used in very different fields of research and their number of applications is very broad. Here we merely give some examples of interesting applications. The interested reader is referred to thematic issues where novel applications are extensively discussed.[18, 26, 42, 45–47]

As MOFs and COFs are like molecular sponges one straight forward applications lies in gas sorption and storage. There enormous surface area surpasses

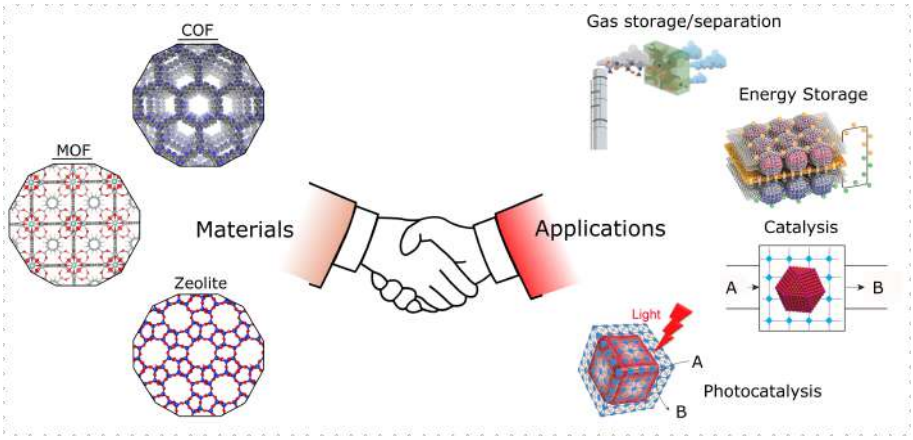

Figure 1.4: The high tuneability of nanoporous frameworks allows these materials to be designed for specific applications requiring specific characteristics.

that of Zeolites (500-1000 m^2/g) by a significant margin (> 10000 m^2/g).[48] Mitigate the amount of CO_2 inside our atmosphere by sequestration or the removal of toxic gases are just two examples in which they could enable new technological developments in the search for a more sustainable society. Storage for energy related gases like hydrogen, on the other hand, can be important for the transformation towards a sustainable automotive industry. Also in medical applications these materials are growing in importance where their porosity can serve as nanoencapsulators or as controlled-release agents.[49, 50]

The use of their sponge like behavior can also be addressed when using them for energy storage or electronic applications. Here particles captured in their pores combined with the framework metal, nitrogen or carbon sites makes them interesting for batteries (e.g. lithium-ion), fuel cells and supercapacitors.[51, 52] Further they can also be applied for solid-state microelectronics,[53, 54] chemical sensing[55] and light-based applications.[56–59]

Last but not least MOFs and COFs are explored to a growing extent within the field of catalysis where they can open totally new perspectives.[44, 60–70] It is certainly one of the main drivers in the search for sustainable applications.[3] Harvesting of alternative energy sources through photocatalytic reactions could address the global energy demand and thus the environmental issues of today. Therefore within this PhD thesis we will explore the photocatalytic properties in the field of heterogeneous catalysis of a selection of MOFs and COFs (see Section 1.3). Furthermore, the possibility to use COFs as host material to anchor photocatalytic complexes known from homogeneous

catalysis will be investigated too (see Figure 1.5). To that end we will discuss the basic concepts of heterogeneous catalysis and photocatalysis in the next sections.

1.1.1 Heterogeneous Catalysis

Heterogeneous catalysis is, in contrast to homogeneous catalysis, a type of catalysis where the phases between the catalyst and the reactants differ, for example a solid versus a liquid phase. In homogeneous catalysis the separation of the catalyst from its products often result in an environmentally unfriendly cycle. However, due to the difference in phase in heterogeneous catalysis this can be, quite naturally, avoided leading to an improved green catalytic route. Similar as in homogeneous catalysis, heterogeneous catalysis, strives to achieve a large contact area between the catalyst and the reagents. MOFs[60–67] and COFs[44, 68, 69] are increasingly explored in heterogeneous catalysis as they posses both the high surface area and have a broad chemical versatility and functionality.

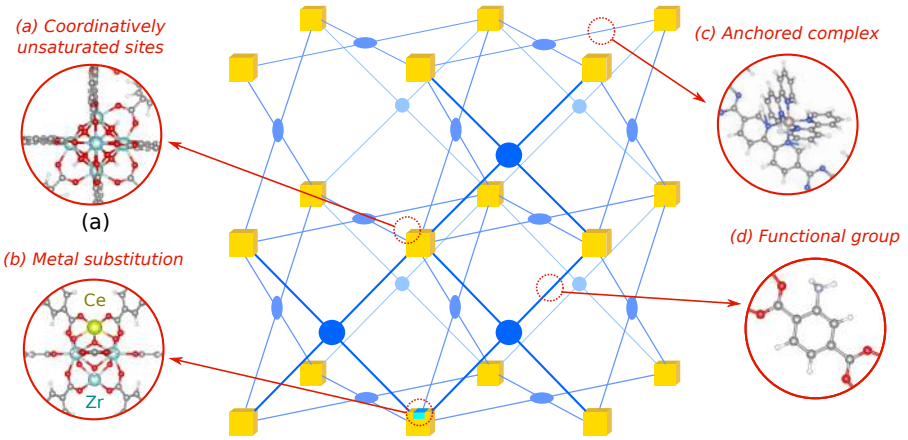

Figure 1.5: The different positions in nanoporous framework where single-site catalytic reactions can take place. Adapted from Ref. [70] with permission of the The Royal Society of Chemistry.

As for all catalysis, catalysis in MOFs and COFs requires robust catalytic/active sites, high thermal and chemical stability as well as efficient mass transport.[64, 68, 70–72] These active sites could be incorporated within the framework at different positions (see Figure 1.5). Coordinatively unsaturated metal sites in MOFs, for example, can be utilised as active sites and by synthesizing the MOF with different metal clusters (e.g. Ag, Zr, Co, Ti, Fe, Cu, etc.) their catalytic activity can be tuned (see Figure 1.5a,b). In UiO-66

these unsaturated metal sites can be included by the synthetic procedure, while retaining its stability, through what is called defect engineering (see further).[71, 73–75] Furthermore, even lanthanide, known for their light-based properties, can be incorporated in UiO-66 (see Figure 1.5b). This structural inclusion of metals causes high metal loadings and reusability of the catalyst which are big advantages. Besides the inorganic node of MOFs also their organic linkers can be altered to improve the catalytic activity (see Figure 1.5d).[76–78]

COFs, on the other hand, do not contain these reactive metals and despite having some intrinsic catalytic activity[70, 79, 80] their activity can be increased by including inorganic moieties within the COF. This can be performed by guest inclusion within the pore, however, this would reduce the porosity which is undesirable. A more efficient way is to functionalise COFs with well-known homogeneous catalysts, such as metal complexes, which may enhance their reactive power (see Figure 1.5c). As such, the specific catalytic properties of some homogeneous complexes could be combined with the advantage of a heterogeneous support, i.e. avoiding unwanted separation processes, possible high metal loading and reusability. Furthermore, well-known deactivation routes by complexation of several organometallic complexes would be avoided.

To conclude, MOFs and COFs are an interesting playground for catalysis as they are chemically versatile due to their tuneability. They offer a lot of potential to induce a transformation from energy intensive and polluting processes to green and sustainable alternatives.

1.1.2 Heterogeneous Photocatalysis

One of the main goals within this PhD thesis is to study the electronic structure of MOFs and COFs for its application within the field of photocatalysis. Photocatalysis may offer a more sustainable alternative to activate chemical transformations, as its energy is directly harvested from sunlight.[81–84] Furthermore, photocatalysis may be performed with a continuous flow set-up having the advantage of better penetration by light and higher photon fluxes trough the material compared to a batch reactor, see Figure 1.6 (left).[85–88] Yet visible light heterogeneous photocatalysis has to date not found its breakthrough in industry.[89] The great difficulty lies in designing a material that is highly active, efficient, robust, uses a large part of the solar spectrum and has a reasonable cost.[56]

The versatility of MOFs and COFs offers the opportunity to tune the materials towards photocatalytic applications, however, this requires a fun-

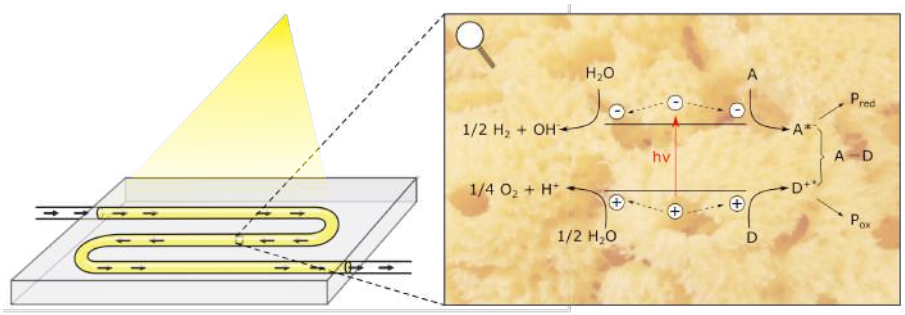

Figure 1.6: Experimental set-up of continuous flow heterogeneous photocatalysis (left). The light interacts with the crystalline solid material in which an electron-hole pair is created. These charge carriers are subsequently separated and cause two reactions, for example generating hydrogen and oxygen from water (right).

damental understanding of the three fundamental steps that take place in transforming solar in chemical energy (a photocatalytic reaction):[90]

- 1st step: Absorption of light creates an electron and hole
- 2nd step: Separation and migration of charge carriers (electron and hole)
- 3rd step: Charge carriers initiate two reactions at different active sites

All three steps require understanding the electronic structure of the photocatalyst. Within this PhD thesis we therefore studied the electronic properties of a subset of MOFs and COFs to obtain a fundamental understanding in the three steps of photocatalysis. To that end we give a brief summary on the basic concepts of the electronic structure of both extended materials and molecules.

In an extended, periodic material electrons are confined to continuous energy bands and forbidden regions. Between the highest occupied energy band, the valence band, and the lowest unoccupied band, the conduction band, a forbidden region can occur which is called the band gap. In standard solid-state terminology materials are classified based on this gap in three groups: metals, insulators and semiconductors (see Figure 1.7). A molecule, on the other hand, which is spatially constrained, has a completely different electronic spectrum. A discrete, spectral density is observed, in contrast to the band representation of solids (see Figure 1.7). Still they have a highest occupied molecular orbital (HOMO) and a lowest unoccupied molecular orbital (LUMO) between which a gap is observed.

In both solid-state semiconductors and molecular systems an electron can be excited from an occupied to an unoccupied state. In photocatalysis this

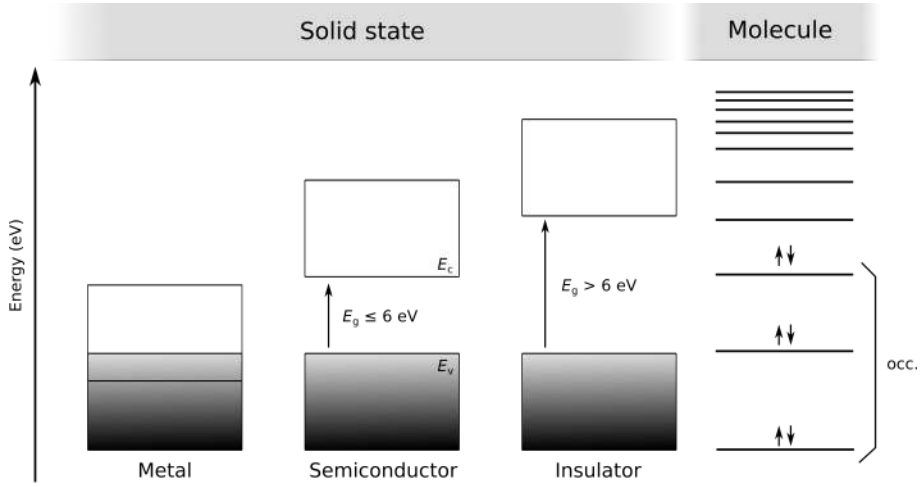

Figure 1.7: Schematic representation of the electronic structure of different kinds of materials. Adapted from Ref. [90] with permission of the Wiley Publishing Group.

energy ($h\nu$) is supplied, ideally, by visible light (ν part of the solar spectrum) and causes an exciton, an electron-hole pair (1st step). The band gap or HOMO-LUMO gap quantifies the energy necessary to create it. The second step is the separation of both electron and hole, the charge transfer. The charge transfer decreases the chance of a fast recombination which would destroy the catalytic activity. Separating the electron-hole pair circumvents it and the electron and hole can migrate through the materials towards the active site, a surface or metal (see Section 1.1.1). There they interact with the reactants initiating the photocatalytic reaction. Photocatalytic water splitting represents such a promising reaction, see Figure 1.6 (right), in which clean energy is produced from water by generating hydrogen and oxygen using only sunlight.[79, 91–95]

Natural photosynthesis is the prototype example of an efficient process based on solar energy. It uses a highly complex set of hierarchically assembled units to convert solar into chemical energy by combining the three steps. Nanoporous frameworks, more particularly MOFs[53, 56, 57, 96–98] and COFs,[99, 100] also represent such an assembled photosystem by its distinct building blocks. They are emerging classes to be used as heterogeneous photoactive materials as they are highly tunable, have large surfaces and can combine a photosensitizer and catalytically active centers into one material.[53]

An important problem when designing photocatalysts is the lifetime of the

photogenerated charge carriers (step 2). Indeed, the activity of the material, when excited, is highly determined by it.[101] To increase the lifetime, the created exciton has to be separated, to prevent fast recombination of its composing electron-hole pair.[102] The modular nature of MOFs allows to achieve this by e.g. a fast migration of an electron excited at the linker to the node or the other way round, see Chapter 3 for UiO-66. This ligand-to-metal charge transfer (LMCT)[58, 101] has been discussed as one of the main mechanisms underlying the photocatalytic activity of MOFs.[57] An alternative solution to create photoactive centers in nanoporous frameworks is to introduce additional components to the framework, either anchored or contained in the pore.[18, 53, 70, 72, 103–106] In both cases tuning the framework/framework-complex allows the alteration of a directional energy transfer along a predefined pathway beneficial for photocatalysis.

Within this PhD thesis molecular modelling will be used to obtain a deep understanding of the electronic properties of a selected set of MOFs and COFs. Furthermore, it will be studied in how far modifications to molecular building blocks alter the electronic properties of the assembly framework. The study of this subject may finally lead to engineered nanoporous frameworks optimal for photocatalytic applications.

1.2 Computational Modeling

From an experimental viewpoint one can deduce the macroscopic properties of a material by measurements, however, it is extremely difficult to unravel the atomic-level triggers causing them. Computational modelling, on the other hand, starts from a bottom up approach using atomistic models which should be representative for the material's function observed experimentally.[107] Such modelling has proven to be a great added value to understand experimental observations and to help designing better materials for specific applications.[108–113]

Additionally, computational modelling can be very fast, which makes large-scale (high-throughput) screening of materials possible[114, 115] and has contributed to the large material database and tools available today.[116–122] They allow the discovery of materials that would not have been found with the generally slower experimental studies that most often take place through trial and error or a stepwise optimization of existing materials. CO_2 capture,[123] hydrogen,[124, 125] methane[126] and oxygen storage,[127] as well as Li-ion batteries,[128–132] and electrocatalytic materials for hydrogen evolution[133] are just a few examples of studies where high-throughput screening allowed to identify new structures that outperform current materials.

Lastly modelling has also the advantage to construct materials in a methodological way, for example by changing only one constituent, and inspecting how their properties depend on it. The acquired insight can subsequently lead to design criteria and therefore towards both a more rational screening and design.[134–136]

Besides all its advantages molecular modelling has its drawbacks just as experiments. The finally obtained accuracy i.e. the correspondence with experiments, of a model depends on the approximations made. The more accurate, the more computational demanding the used physical model typically is. Such a more complicated physical model, where less approximations are made, is only applicable to systems of smaller size containing less atoms. In this sense it is impossible to determine every property of a large set of materials - existing or hypothetical - from theoretical point of view with very high accuracy.

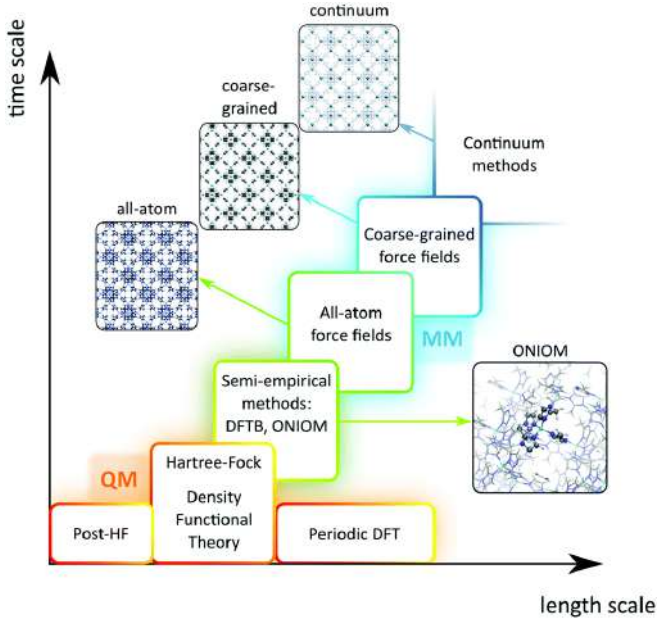

Figure 1.8: Schematic overview of length and time scales of methods going from purely quantum mechanical (QM) based to molecular mechanics (MM). Adapted from Ref. [70] with permission of The Royal Society of Chemistry.

This idea is illustrated in Figure 1.8 where a typical length-time scale plot is shown, indicating that the most accurate methods are only feasible to apply on systems of small to moderate size and can only be followed during a

limited timespan during a molecular dynamics run. The larger the time scales the coarser the models become, eventually leading to continuum models.

Force fields may be categorized into computationally inexpensive models as they neglect the electrons by considering an effective potential in which the nuclei move. They therefore reduce the computational resources significantly. Using this methodology record breaking system sizes with more than a billion of atoms have been simulated.[137] Evidently they are not suited to describe electronic properties as they neglect the electrons and are therefore not suited for the purpose of this PhD thesis.

Quantum mechanically based methods are necessary to model the electronic structure of a material. Such methods are also computationally much more expensive. Density-functional theory (DFT) is one of the most prominent many-body techniques used in literature,[138, 139] see Chapter 2 for a detailed description. It provides a methodology with a good trade-off between between speed and accuracy[140] and is widely used in a variety of molecular modelling situations. However, based on the choice of method within DFT, the accuracy may vary and the results may not necessarily be in good agreement with experiment.[12, 141] Dedicated studies on error estimation for various DFT based methods are available in literature.[140, 142–144] An important observation is that the mismatch between theory an experiments is less pronounced when investigating qualitative trends, due to error cancellation.[101, 110, 111, 145–147] This is an important observation in the context of this PhD research, as our results mainly focus on trends and variations when modifying candidate photocatalyst structures.

Note that besides DFT, other more accurate methods exist to investigate the electronic structure (see Figure 1.8), such as Green function based methods.[141, 148] However, these methods are computationally very demanding and quickly become unfeasible for our system sizes of 100-500 atoms. Apart from the specific goals of this PhD thesis namely calculating the electronic structure of framework materials, DFT has been successfully used to describe the anisotropic elastic properties[149] and mechanical stability[150] as well as the dielectric response[151] and the band gap changes in MOFs.[152] The interested reader is referred to Refs. [107, 153] for a more extensive overview of the applications of DFT within the field of nanoporous materials.

1.3 Goals of this PhD Research

This PhD research focuses on the electronic structure of MOFs and COFs, which offer an enormous opportunity to design due to their modular build-up. Engineering these materials in a constructive way requires choosing its

building blocks such that their combination yields the desired properties. The number of possible materials constructed in this way scales exponentially with the number of building blocks. Exploring all these materials can be performed by high-throughput calculations, for example done for gas storage,[135, 136, 154–156] but a more comprehensive screening, for example by including the electronic structure properties, becomes unfeasible even with today's computational resources. In this PhD thesis we are therefore interested in how the electronic structure of framework materials are affected by modifying their constituents.

To illustrate the impractical size of possible materials for a screening study we give the example for the UiO-66 material, one of the most stable MOFs available today (see Figure 1.9 (left)). Suppose we consider the UiO-66 type MOFs with 10 different linkers, 15 nodes (lanthanides, Zr, Hf and Ti) and the possibility of 42 missing linker defects configurations. The total number of materials that can be generated would already exceed 7500 only for this one MOF. In addition, a single electronic structure calculations at the DFT level would already consume more than 2500 CPU hours, a calculation of typically a few days on current supercomputers. From this example it becomes immediately clear that such procedure becomes unfeasible to use for screening purposes. In this respect, the number of calculations can be drastically decreased if we understand how the properties of the constituents transfer to the parent material (67 calculations in the above-mentioned example). If it would be possible to deduce the electronic structure of the framework material from its building blocks, this could pave the way to a wide-scope screening of materials and to design materials for a specific application, albeit using much less computational power. The development of such a strategy to rationally design the electronic structure of MOFs and COFs in a more effective and systematic way is precisely the goal of this PhD thesis.

In literature, earlier studies already noted that the electronic properties of modular materials may be derived from their building blocks. Such observations were predominantly made in MOFs but also in some other modular materials where a lack of electronic coupling or hybridization between constituents[152, 157–159] as well as a lack of conductivity was observed.[157] This inspired us to propose the idea of *Orthogonal Electronic Structure Engineering* (*OESE*), in which the electronic structure of modular frameworks can be seen as a sum of independent (orthogonal) contributions of its building blocks (see Section 3.1 of Chapter 3).

This concept should be most evident in MOFs and we will therefore start by investigating it in the UiO-66 type framework (see Figure 1.9 (left)). UiO-66 is a experimentally and computationally well studied MOF which gives us the additional advantage that it provides a good basis to benchmark the

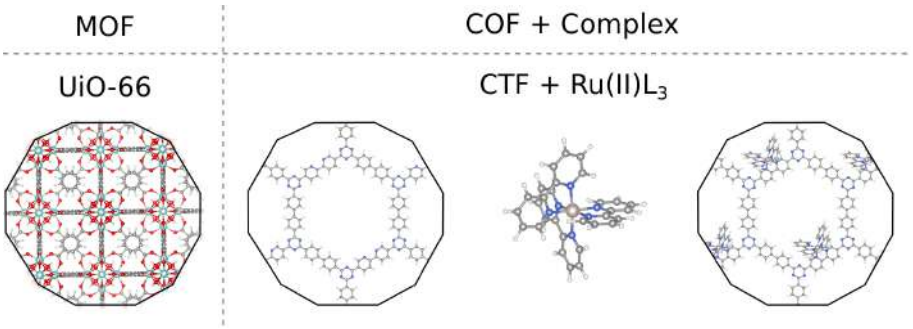

Figure 1.9: Overview of the considered materials to demonstrate the concept of *Orthogonal Electronic Structure Engineering* (*OESE*). The study of UiO-66, our proof-of-concept MOF material, resulted in **Papers I, II** while everything after the dashed line (the COF, complex and their combination) is discussed in **Papers III, IV**.

calculations performed in this PhD thesis with literature data. UiO-66 can be systematic altered by changing its linker or node (see Figure 1.10) for which already some literature was available at the start of this PhD research. We have extended the calculations from literature to include also the lanthanides and study the effect of missing linkers on the electronic structure. The work on the lanthanides was inspired by experimental work performed at LumiLab where they examine them for light-based properties.[160–162] However, the lanthanide series is also an interesting set of atoms for its catalytic applications,[163–165] making them highly attractive for incorporation in UiO-66 for photocatalytic applications (see Figure 1.5b).

As all crystals contain defects this is also the case for MOFs and particular for UiO-66. In UiO-66 missing linkers can be included by the synthetic procedure, while retaining its stability, through what is called defect engineering.[73–75] These defects create unsaturated metal sites which can be utilised as active sites (see Figure 1.5a). It is therefore important to know how these defects alter the electronic structure and if they can even open new opportunities. We therefore studied the effects of defects on the electronic structure of UiO-66 and relate it to its photocatalytic activity. All considered variations, both on the inorganic as organic building blocks of UiO-66 (see Figure 1.5) will serve as a benchmark and proof of concept for the OESE paradigm.

At second instance after carefully testing of the OESE principle, we aim to use the OESE principle to obtain design criteria for photocatalysis. The intention is to identify building blocks that increase the efficiency of UiO-66 for which the unaltered pristine material has only a limited photocatalytic activity. In

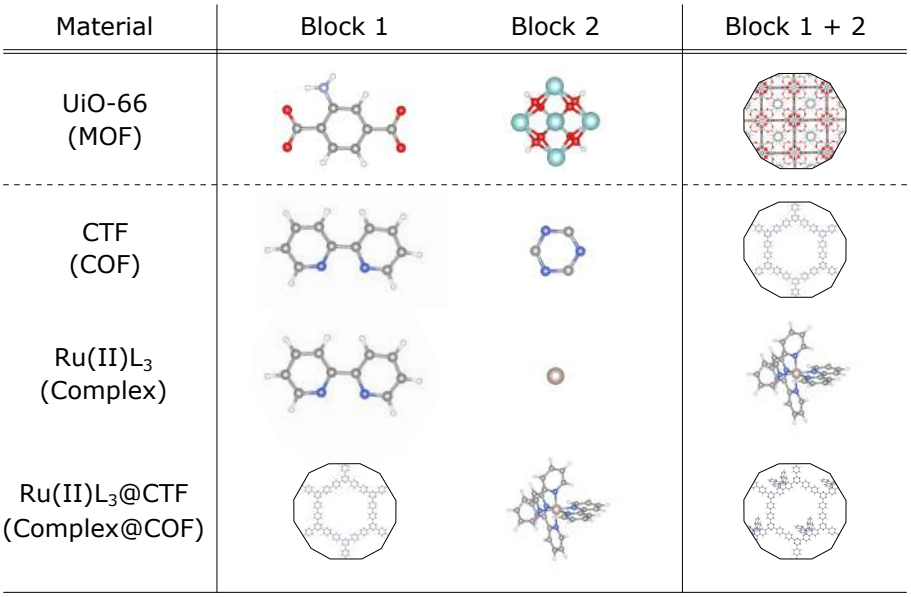

Figure 1.10: Overview of the considered materials and their building blocks to demonstrate the concept of *Orthogonal Electronic Structure Engineering* (*OESE*). The study of UiO-66, our proof-of-concept MOF material, resulted in **Papers I, II** while everything below the dashed line (the COF, complex and their combination) is discussed in **Papers III, IV**.

literature, for example, it is seen that Ti substitution increases the photocatalytic activity of UiO-66. Lanthanide substitution might increase it as well. Furthermore, the incorporation of the missing-linker defects i.e. linkers missing between the nodes of UiO-66, will alter the node configurations and create more accessible active sites. It is therefore investigated in how far defects alter the electronic structure to be more suited for photocatalytic applications.

At third instance, again inspired by an ongoing collaboration with the experimental group of Prof. Van Der Voort, the principle of OESE is explored for covalent triazine frameworks (CTFs), a group of frameworks belonging to the class of COFs (Figure 1.9 (right)). These frameworks, like all COFs, are formed by purely covalent bonding and therefore possess a stronger hybridization or electronic coupling between their constituents, a challenge for our OESE principle. We will examine the effects on the CTF's electronic structure by altering its building blocks (see Figure 1.10) in a similar way as was done for UiO-66. However, as COFs do not contain reactive metals they have been seen to only possess a limited catalytic activity.[70, 79, 80] We will therefore

functionalise the CTF with a well-known homogeneous photocatalyst, the Ru-polypiridyl complex (Figure 1.9 (right)). This complex itself is modular as various ligands can be used to coordinate to the ruthenium center. The OESE is therefore investigated on the isolated Ru-complex for these different building blocks (see Figure 1.10). In a next step, the OESE principle will be applied to the hybrid inorganic-organic scaffold, where the inorganic complex is anchored to the organic framework material. The COF materials are very stable materials and provide a versatile platform for electronic structure engineering. We aim to investigate in how far the OESE principle works when using these broad variety of building blocks. The conclusions may be used to rationally design the Complex@COF compound for photocatalysis in a similar way as was done for UiO-66.

To summarize the aim of the PhD thesis consists in introducing the concept of OESE and using it to systematically investigate the electronic structure of modular materials. We will assess to what extend it is valid by applying it to different materials (MOF, COF, Coordination Complex) where the resulting insights will allow us to construct design criteria and bring rational design of the electronic structure of modular materials within reach.

1.4 Outline

The remainder of this PhD thesis is organized as follows:

- In Chapter 2, the computational methods which are used in this PhD thesis are introduced to investigate the electronic structure of nanoporous frameworks.
- In Chapter 3, the major research results obtained during this PhD are presented. Most of these results were published in international peer-reviewed journals, which can be found in **Part II**.
- In Chapter 4, the main conclusions of this PhD research and an outlook to future research is given.

2

Computational Methods to Study the Electronic Structure

I have been impressed with the urgency of doing. Knowing is not enough; we must apply. Being willing is not enough; we must do.

Leonardo Da Vinci (1452 - 1519)

As discussed in the previous chapter computational modelling allows to deduce molecular level insight in material properties. It therefore offers information that is hard to assess through experiments. The electronic structure, the property of interest within this PhD research, is exactly of this nature. In this chapter we outline the computational methods used in this PhD thesis and elucidate which theory and strategies are used to obtain the results of Chapter 3. We do not provide a complete overview and the interested reader is referred to additional references and textbooks mentioned in the various sections.

2.1 Quantum Theory

We start this chapter with the main theory used in this PhD thesis which is quantum theory. Quantum theory has revolutionized our understanding of molecules and solid-state materials by its success in describing many properties. The theory is embodied by the time-dependent Schrödinger

equation[166]

$$i\hbar\frac{\partial}{\partial t}\Psi(\mathbf{x},t) = \widehat{H}\Psi(\mathbf{x},t) \tag{2.1}$$

with $\widehat{H}$ the Hamiltonian, describing all fundamental interactions of the physical quantum system and $\Psi(\mathbf{x},t)$ the wave function. The latter encompasses all the information of the system, specified by the former, as a function of time (t) and a general set of variables ($\mathbf{x}$). For molecules and solid-state materials it contains the fundamental interactions between electrons (e) and nuclei (N). They correspond to both attractive ($\widehat{V}_{Ne}$) and repulsive ($\widehat{V}_{ee}$, $\widehat{V}_{NN}$) Coulomb potentials ($\widehat{V}$) as a function of the electronic and nuclear coordinates ($\mathbf{r}$ and $\mathbf{R}$, respectively) as well as their kinetic energy ($\widehat{T}_e$, $\widehat{T}_N$). When the Hamiltonian contains no time dependence it further enables a set of stationary solutions found by solving the time-independent Hamiltonian

$$\left[\widehat{T}_e + \widehat{T}_N + \widehat{V}(\mathbf{r},\mathbf{R})\right]\Psi(\mathbf{r},\boldsymbol{\sigma},\mathbf{R}) = E\Psi(\mathbf{r},\boldsymbol{\sigma},\mathbf{R}), \tag{2.2}$$

$$\widehat{V} = \widehat{V}_{ee} + \widehat{V}_{NN} + \widehat{V}_{Ne}. \tag{2.3}$$

where $\boldsymbol{\sigma}$ indicates the spin of the electrons.

When obtaining the wave function $\Psi(\mathbf{r},\boldsymbol{\sigma},\mathbf{R})$ of Eq. 2.2 one can deduce all material properties and finally molecular level insight. However, the complexity makes assumptions necessary. The first approximation is called the Born-Oppenheimer approximation[167] in which the coupling between the motion of the nuclei and the electrons is at first instance neglected based on the large difference in mass between the two types of particles. This transforms the Schrödinger equation in two independent equations, a part depending on the nuclear coordinates ($\mathbf{R}$), see Eq. 2.4, and a part depending on the electronic coordinates and spin ($\mathbf{r},\boldsymbol{\sigma}$), see Eq. 2.5, where the nuclear configuration is considered as a parameter

$$\left[\widehat{T}_N + E(\mathbf{R})\right]\chi_{nm}(\mathbf{R}) = E_n\chi_{nm}(\mathbf{R}), \tag{2.4}$$

$$\left[\widehat{T}_e + \widehat{V}(\mathbf{r},\mathbf{R})\right]\psi_n(\mathbf{r},\boldsymbol{\sigma},\mathbf{R}) = E_n(\mathbf{R})\psi_n(\mathbf{r},\boldsymbol{\sigma},\mathbf{R}). \tag{2.5}$$

To obtain the electronic properties of a material we need to solve the electronic part of the Schrödinger equation (see Eq. 2.5). The most straightforward approach is to try to find the electronic wave function. The big downside of this strategy is that the number of variables to describe the wave function increases exponentially with the number of electrons, i.e. an exponential wall is observed.[168] To mitigate this phenomenon a wide range of approximations exist, such as (post-)Hartree-Fock (HF), coupled-cluster[169] (CC) or more recently the Density Matrix Renormalization Group[170] (DMRG)

and Tree Tensor Networks (TTNS).[171–174] The overall advantage of these methods is their high accuracy. However, due to their complexity they cause an immense increase in computation load and are therefore unfeasible on large system sizes, such as MOFs and COFs.[175] We conclude that trying to find the wave function is not a good approach for the materials we want to consider.

2.2 Density-Functional Theory

Here density-functional theory (DFT) comes in, providing a simpler way to solve the many-body problem (Eq. 2.5). DFT exploits the fact that the ground-state density contains as much information as the ground-state many-body wave function. The advantage is that the density is a function of just three spatial variables, which in comparison to the ground-state wave function, does not increase in complexity when increasing the particle number N. The exponential wall is thus avoided.

Note that in its most general form, the density can be separated into up and down spin contributions. However, for clarity, we will limit our explanation to a spin-unpolarized formalism. For more information on how to treat the dependence on spin, we refer to the book of Martin et al.[176]

The theory is founded on the Hohenberg-Kohn theorems[138] which prove a one-to-one mapping between the ground-state electronic density $n(\mathbf{r})$, the ground-state electronic wave function $\psi(\mathbf{x})$ and the external potential $\widehat{V}_{eN}(\mathbf{r}, \mathbf{R})$. Furthermore, it provides a formal way to variationally derive this ground-state electronic density by writing the ground-state energy as a functional of the density,

$$E = E[n] = \langle \psi[n] | \widehat{T}_e + \widehat{U} + \widehat{V}_{Ne} | \psi[n] \rangle, \tag{2.6}$$

$$\widehat{U} = \widehat{V}_{ee} + \widehat{V}_{NN}, \tag{2.7}$$

and minimizing this expression. However, the interaction term $\widehat{U}$ and the electronic kinetic energy $\widehat{T}_e$ are not known as a functional of the density and to obtain a solution approximations are needed.

The most common approximation is to replace the true unknown electronic kinetic energy ($\widehat{T}_e$) by that of a non-interacting system ($\widehat{T}_s$), and the repulsive electronic Coulomb interaction ($\widehat{V}_{ee}$) by the Hartree energy (E_H), the mean-field electrostatic interaction energy of the charge distribution $n(\mathbf{r})$. The remaining correction terms, which can be viewed as a small perturbation, are then grouped in an unknown exchange-correlation (XC) term E_{xc}

$$E[n] = T_s[n] + V_{Ne}[n] + E_H[n] + E_{xc}[n]. \tag{2.8}$$

Many approximations exists for the XC functional. In principle if we would be able to estimate the exact form of the XC functional, DFT would be an exact theory, however, in practice one needs to make approximations for this functional. The XC term can in a first approximation be estimated from the uniform electron gas which is referred to as the local density approximations (LDAs). Further improvements in the XC functional include terms that also depend on the gradient of the density and are called generalized gradient approximations (GGAs). The particular choice of the used approximation for the XC functional determines the accuracy of the predicted material properties and the field of developing better functionals is very active.[177–179] Nowadays a wealth of functionals exist with over 200 functionals present. In this sense large-scale tests are available for a variety of systems.[180–182] Last but not least the choice of the XC functional always has to balance its computational cost versus the desired accuracy (see Chapter 1, Section 1.2).

Irrespective of the approximation for the XC functional the energy minimisation problem as a function of the density (see Eq. 2.6) is also hard to solve. The Kohn-Sham (KS) scheme simplifies this minimisation procedure. The scheme goes one step back by reintroducing a wave function-like quantity. Instead of applying the variational principle directly to the ground-state density, the density is expressed in terms of single-particle orbitals in a non-interacting system. This is achieved by reinterpreting Eq. 2.8 as the energy functional of a non-interacting system. The effective potential v_{eff} of that system contains the functional derivative of respectively the XC functional (v_{xc}), the Hartree energy (v_H) and the external potential (v_{ext}),

$$v_{eff} = v_{ext} + v_H + v_{xc}, \tag{2.9}$$

whereas the single-particle wave functions are found based on the following equation

$$\left[-\frac{1}{2}\bigtriangledown^2 + v_{eff}[n](\mathbf{r}) - \epsilon_j\right]\phi_j(\mathbf{r}) = 0. \tag{2.10}$$

The density is then derived from the single-particle wave functions of the non-interacting system as

$$n(\mathbf{r}) = \sum_{j}^{occ} |\phi_j(\mathbf{r})|^2. \tag{2.11}$$

Eq. 2.10 also explicitly indicates that the effective potential, v_{eff}, depends on the density, which results from the Kohn-Sham orbitals that the equations aim to solve for. The problem therefore has to be solved self-consistently.

Practically these coupled Kohn-Sham equations are solved by proposing a – well chosen – basis set in which the Kohn-Sham Hamiltonian is diagonalized. This last part is computationally demanding and in order to reduce the computational effort a good basis set is essential. A good basis set means that it is able to accurately describe the density of the system with only a limited number of basis functions. In a periodic solid, which is an infinitely extended material, the plane-wave basis set arises naturally through symmetry arguments whereas for molecules a localized basis set is most often used. In both cases the core-state wave functions are very localized, and in case of a plane-wave basis set a large number of plane waves are necessary to describe them. On the other hand in both cases these core states are less mandatory to describe the chemical binding and luminescent properties. Making use of both observations these core states can be treated in a different way than the valence electrons in order to reduce the number of basis functions. In all-electron methods this is handled explicitly by constructing basis functions that are restricted to a specific energy range, such as linearized augmented plane wave (LAPW),[183–186] or basis functions treating core and valence states on equal footing (e.g., by using numerical atomic-like orbitals). In contrast pseudization approaches, such as pseudopotentials[187] and the projector-augmented wave (PAW) method[188, 189] derive a (valence) problem where fewer basis functions are needed. These methods reduce the computational load significantly.

The periodic simulations in this PhD thesis were performed with VASP[190] in the PAW formalism.[189] Cluster models were calculated using the Gaussian 16 software[191] using various localized basis sets and pseudopotentials.

2.3 Time-Dependent Density-Functional Theory

The interaction of a material with a time-dependent electromagnetic field, such as light, can not be studied by DFT as it is a time-independent theory. DFT provides an, in principle, exact solution to the time-independent Schrödinger equation and time-dependent density-functional theory (TD-DFT) provides its extension to the time-dependent Schrödinger equation.[192] TD-DFT can therefore be used to study the properties and dynamics of many-body systems in the presence of time-dependent potentials, such as light, and is able to extract excitation energies, response properties and photoabsorption spectra. Furthermore, it can calculate the transition probability, commonly known as the oscillator strength, which expresses the probability of absorption or emission of electromagnetic radiation.

TD-DFT is founded on the Runge-Gross theorem[193] and similar to the first Hohenberg-Kohn theorem in DFT it establishes a one-to-one mapping between the time-dependent density and the time-dependent external potential. This time-dependent external potential can be attributed to a time-dependent electric or magnetic field for which the response properties are determined. Excitation and emission spectrum can therefore be determined by deducing the resonant frequencies of such a field together with their oscillation strength. These are determined by a time-dependent variant of the Kohn-Sham equation and applying linear-response theory to it, most commonly implemented following the formulation of Casida.[192]

Similarly to DFT, TD-DFT has proven an attractive technique thanks to its acceptable computational cost for relatively large-size systems. Approaches such as Green's function theory[194] are much more expensive (see Section 2.5.4). However, whereas the latter provides similar accuracies in extended[195] and finite systems,[196, 197] TD-DFT for periodic materials remains a challenge.[198, 199] The big hurdle for periodic or extended materials is not only due to the increased computational cost but more fundamentally due to the breakdown of the Runge-Gross theorem.[200, 201] TD-DFT is therefore mainly applied to molecular systems[202] where it is able to reasonably reproduce the shape of the excitation spectra. The main offset between theory and experiment originates from the used functional.[203, 204] In this PhD thesis we will therefore use TD-DFT for molecules, complexes and cluster models, in order to deduce the oscillator strengths as well as the photoabsorption spectrum to extend our DFT calculations (see Section 3.4).

Excited states have been investigated with the Gaussian 16 software[191] adopting the time-dependent DFT scheme (TD-DFT)[193] within the linear-response approach due to Casida.[205]

2.4 The Electronic Structure

In an extended, periodic material electrons are confined to continuous energy bands separated by forbidden regions. In contrast, for a molecule a discrete spectrum is observed (see Section 1.1.2). The electronic structure of a material, a solid or a molecule, represents the energies of these states as a function of the wave vector of the electronic wave. It is commonly displayed among lines in that wave-vector space (see Figure 2.1) representing a band of accessible energies, the band structure. Nevertheless, this picture is based on an approximate description of the solid under study. The approximation consists in replacing the complicated many-body system (Eq. 2.5) by an independent-

particle model of quasi-particles i.e. weakly interacting particles which behave quasi independently. For example, an electron within a semiconductor behaves like an independent electron with a different mass (effective mass), a quasi-particle, travelling unperturbed through the semiconductor.

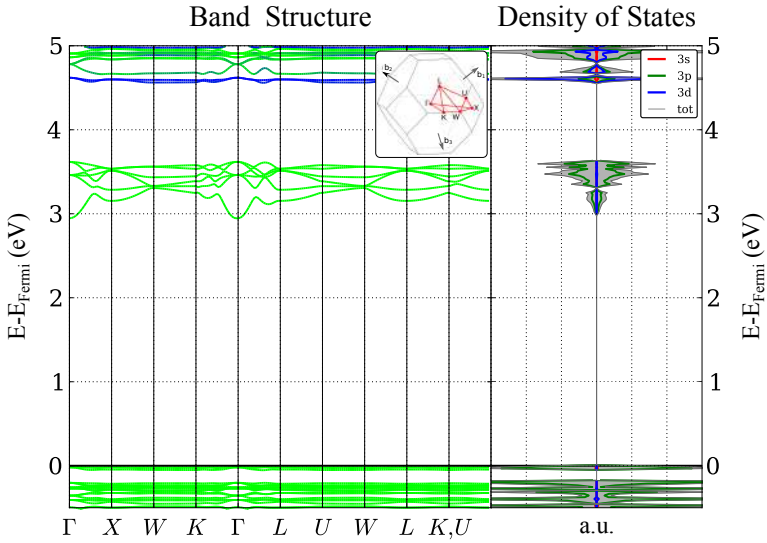

Figure 2.1: Band structure and density of states of UiO-66(Zr) calculated with the PBE functional. The 1st Irreducible Brilouine Zone (IBZ) is given in the inset (left) indicating the lines along which the dispersion relation is plotted. The projections of the band structure and density of states on the atomic orbitals is shown by color (see legend) and represents respectively the local band structure and local density of states.

2.4.1 Electronic Band Structure

In DFT it is the Kohn-Sham effective potential that generates this independent-particle model. When solving the Kohn-Sham equation in a periodic solid the symmetry of the Kohn-Sham Hamiltonian corresponds to its lattice and for such a Hamiltonian the eigenstates are so-called Bloch wave functions

$$\psi_{n,\mathbf{k}}(\mathbf{r}) = u_{n,\mathbf{k}}(\mathbf{r})e^{i\mathbf{k}\cdot\mathbf{r}}, \tag{2.12}$$

where the function $u_{n,\mathbf{k}}(\mathbf{r})$ fulfills the translational symmetry of the lattice and $\mathbf{k}$ and n are respectively a continuous and discrete quantum number called the wave vector and the band index. Applying these eigenstates to the

Kohn-Sham equation (Eq. 2.10) gives

$$\left[\frac{1}{2}(\frac{\overline{\nabla}}{i}+\mathbf{k})^2+v_{eff}(\mathbf{r})\right]u_{\mathbf{k},n}(\mathbf{r})=E_{\mathbf{k},n}u_{\mathbf{k},n}(\mathbf{r}). \tag{2.13}$$

The energies of these Bloch wave functions therefore show the dispersion relation ($E_{\mathbf{k},n}$) mentioned above as a function of $\mathbf{k}$ and n. The symmetry of the material under consideration further restricts the wave vectors $\mathbf{k}$ that we need to consider to the 1st Irreducible Brilouine Zone (IBZ) (see the inset of Figure 2.1 (left)). For visualization purposes this dispersion relation is not displayed for all $\mathbf{k}$ values but only along the border lines of the 1st IBZ (high-symmetry lines) representing the band structure (see Figure 2.1).

The band structure can also be measured experimentally by using Angle-Resolved Photoemission Spectroscopy (ARPES)[206, 207] and probes these quasi-particle states. Note, however, that for MOFs and COFs, the materials of interest within this PhD thesis, ARPES measurements are hindered due to the lack of large, high-quality single crystals. For materials where ARPES measurements are possible, the assumption is now that the Kohn-Sham scheme for the electrons is a reasonable approximation for the ARPES quasi-particle states, as both should provide a good approximation for the density. Consequently the Kohn-Sham electronic band structure is assumed to be a good approximation for the experimentally determined band structure.[208] Until today there is still a lot of research ongoing on the meaning of Kohn-Sham orbitals and whereas they were once completely considered as just a mathematical tool it is now believed that they do possess these physical properties (see also Section 2.5).[209, 210]

2.4.2 Density and Local Density of States

The band structure contains more information than is often necessary. In many cases, it is sufficient to know up to what energy level the possible states are filled. This information can be retrieved from the dispersion relation $E_{\mathbf{k},n}$ and is called the density of states (DOS). It represents the number of states within an energy interval $[E, E+dE]$ per unit cell volume (Ω_{cell}) as

$$D(E)=\frac{\Omega_{cell}}{(2\pi)^3}\sum_n\int d\mathbf{k}\delta(E-E(\mathbf{k},n)). \tag{2.14}$$

The electron density corresponding to an energy range within the DOS can be related to it by only considering those $\psi_{n,\mathbf{k}}$ in that energy range. Using the Bloch functions, this becomes

$$n(\mathbf{r})=\frac{\Omega_{cell}}{(2\pi)^3}\sum_n\int d\mathbf{k}|\psi_{n,\mathbf{k}}(\mathbf{r})|^2. \tag{2.15}$$

Therefore the density corresponding to a peak observed in the DOS can be plotted by summing over the corresponding squared moduli of the orbitals in the energy interval of such a peak (see Figure 2.2).

However, the DOS is a very condensed form of a material's electronic structure and additional knowledge can be acquired by considering the local density of states (LDOS). It expresses how many states are accessible in an atom-like orbital $\phi_{\alpha,\mu}$ with μ its quantum numbers and α the atom around which it is centred. Properties related to atomic orbitals allow for a much easier interpretation of chemical concepts. Furthermore, by considering the summed orbital densities centred on specific atoms we can deduce where the electron is localized across the structure (see Figure 2.2). To obtain the LDOS per unit cell, we write Eq. 2.14 as

$$D(E) = \sum_{\alpha,\mu} D_{\alpha,\mu}(E), \tag{2.16}$$

where

$$D_{\alpha,\mu}(E) = \frac{\Omega_{cell}}{(2\pi)^3} \sum_n \int |\langle \psi_{n,\mathbf{k}} | \phi_{\alpha,\mu} \rangle|^2 \delta(E - E(n,\mathbf{k})) d\mathbf{k}. \tag{2.17}$$

In this expression $\langle \psi_{n,\mathbf{k}} | \phi_{\alpha,\mu} \rangle$ is the projection of the Kohn-Sham wave function $\psi_{n,\mathbf{k}}$ onto the atomic orbital $\phi_{\alpha,\mu}$ where its modulus squared gives a measure of the orbital-like character.

The density and local density of states were calculated with VASP.[190] The post-processing was performed using both HIVE[211] and the Pymatgen software packages.[122]

2.5 Theoretical and Experimental Electronic Levels

The easiest way to probe the electronic structure of a material is by investigating how it interacts with an incident light beam. When light with sufficient energy hits the material it can cause electrons to transition between two electronic states. The excited state is what is called an excitation (see Section 1.1.2). This excitation can subsequently relax and transition back to its original state where in the process light can be emitted. In this last section of Chapter 2, we discuss the link of the characteristics of these processes with the results obtained out of the DFT calculations. In particular we identify and discuss energy levels and excitations with an important physical significance.

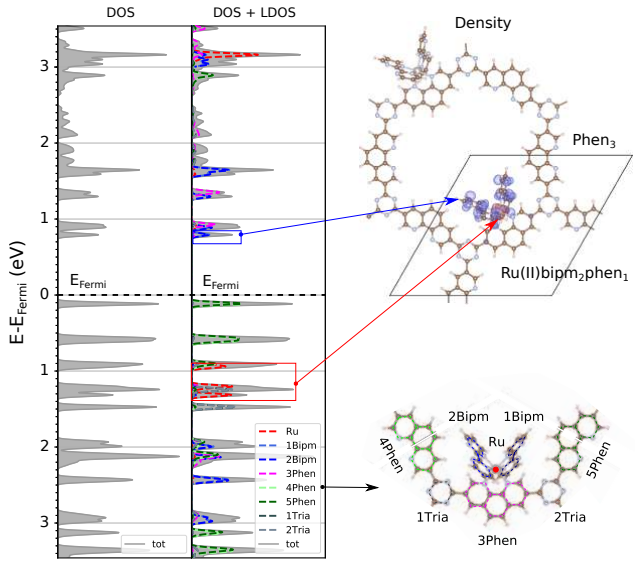

Figure 2.2: Density and local density of states shown for a Ru(II)bipm$_2$phen$_1$ complex anchored on a phen$_3$ framework (left). The local density of state is calculated based on the site DOS of the building blocks of both the framework and the complex (right, bottom). The local density of states therefore elucidates the character of the lowest unoccupied state centred on the ligands within the pore of the framework and the highest occupied state of the ruthenium complex. Its corresponding density is visualized in the top right pane. Adapted from **Paper I [Ref. 146]** with permission of the Royal Society of Chemistry.

2.5.1 Energy Gaps

The electronic structure of a material expresses which states are accessible within the material. A discrete spectrum, continuous energy bands and forbidden regions can be observed (see Section 1.1.2). These forbidden regions indicate gaps of energy where no states are accessible. However, these energy gaps can be bridged by supplying the correct amount of energy to the material, most commonly through a light source. This process illustrates that the required energy for excitations of the material corresponds to the magnitude of energy gaps within the electronic structure.

However, dependent on the physical process underlying such a transition different gaps need to be considered. Two such different gaps are of both theoretical and practical importance.[212, 213] The first energy gap is called

the band gap or fundamental gap (E_g, see Figure 2.3), which is defined as the difference between the ionization energy and the electron affinity. It considers the addition of an excited electron or the removal of a ground-state electron without coupling the two situations. A second energy gap is the optical gap and takes into account the electrostatic attraction energy between the excited electron and the newly generated hole. Both quantities are accessible experimentally: the fundamental gap can be determined as the difference of two observables, I and A, e.g., by using photoemission and inverse photoemission spectroscopy, while the optical gap can be measured from the absorption spectrum. For UiO-66, a material studied within this PhD thesis (see Chapter 3), an optical gap was measured in such a way by Musho et al.[214]

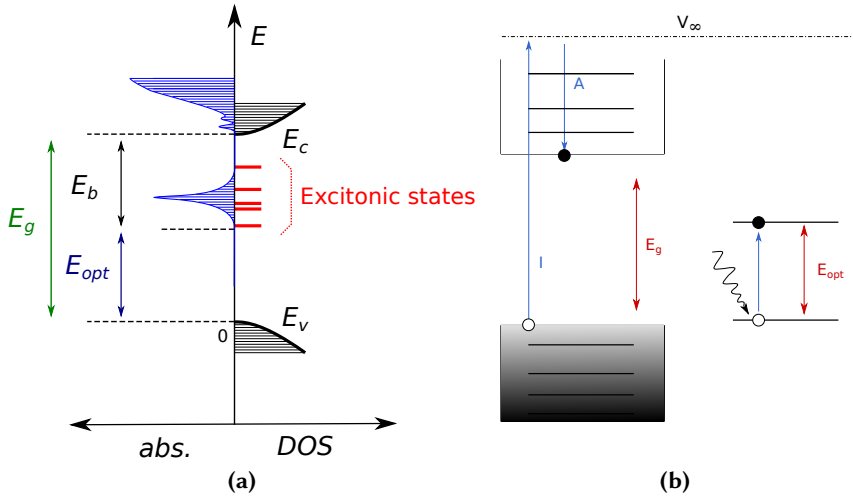

Figure 2.3: Schematic figure illustrating how the optical and fundamental band gap, respectively E_{opt} and E_g, are observed in the absorption spectrum (abs.) and density of states (DOS). The excitonic state are indicated in red and cause the optical gap to be smaller than the fundamental band gap (a). In (b) the additional relation is given with respect to the ionization and affinity.

These two physically different energy gaps can be related to each other by considering the concept of quasi-particles.[215] As an electron is inserted, or ejected, all other electrons in the system respond through the interelectronic repulsion. However, by considering the rearranged electronic configuration as quasi-electrons or quasi-holes we can consider them as independent particles. The ionization potential and electron affinity can then be considered as the quasi-hole excitation with the smallest energy or quasi-electron ex-

citation with the largest energy (see Figure 2.3b) and the fundamental gap being the difference between both. The simultaneous creation of both quasi-particles can be considered as an excitation where an attractive interaction between both takes place. The optical gap therefore differs from the fundamental gap by this attractive interaction, called the exciton binding energy E_b (see Figure 2.3a). It causes the optical gap to be smaller than the fundamental gap (see Figure 2.3).[209, 216] In semiconductors the exciton binding energy is often negligible compared to the band gap and optical and fundamental gap are approximately equal. In contrast, for molecules this exciton binding energy is most often not negligible, explaining why here the optical band gap is in most cases much lower than the fundamental band gap.[216]

Now how do we relate the electronic structure of DFT with both quantities? The Franck-Condon principle states, in a similar way as the Born-Oppenheimer approximation, that the motion of the nuclei is much slower than that of the electrons. This means that most electronic excitations happen without any immediate nuclear relaxations, such that absorption or emission energies can be estimated from different electronic energies at a fixed atomic geometry. Such excitations are often referred to as "vertical" transitions, because they take place in a purely vertical fashion when plotted with respect to the nuclear degrees of freedom (see Eq. 2.5).

Because the electronic structure of DFT assumes a quasi-particle character, we may compare band gaps in the DFT electronic structure with experimentally accessible energy gaps. However, when directly interpreting such differences between DFT energy levels as excitation energies, we attribute a physical meaning to them. This is not straightforward, as Kohn-Sham orbitals are one-particle wave functions of an auxiliary system and thus not physical. Even now, this point remains a topic of considerable research and even controversy in the literature.[209, 210, 212, 216–235] However, nowadays it has been accepted that the Kohn-Sham orbitals and their energies computed with local and semi-local functionals are an ideal basis for the description of (molecular) excitation and differences between Kohn-Sham energies can be seen as vertical excitations that take into account the exciton binding energy. Kohn-Sham energy gaps therefore approximate optical gaps.[209, 210, 233] It is furthermore assumed that the accuracy of Kohn-Sham gaps also depends on the functional used (see Section 2.5.4), where a non-local contribution to the XC potential yields a better description for the fundamental band gap.[217] Therefore Kohn-Sham energy gaps can give a qualitative measure of these energy gap in the band structure or density of states (see Figure 2.1 and 2.2) depending on the functional (see Section 2.5.4).

A more accurate approximation of the excitation and emission spectrum can be retrieved by TD-DFT (see Section 2.3). Here the interaction with light

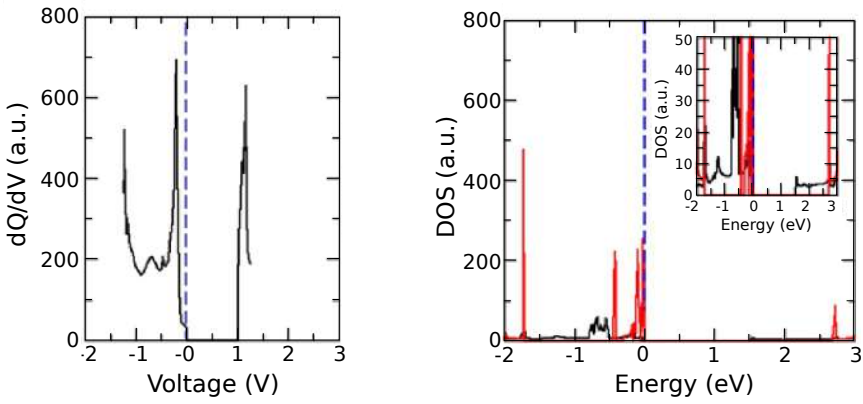

(a) Experiment **(b)** Theory

Figure 2.4: (a) Measurement of the DOS as a function of the voltage for CTF-1. (b) Theoretical DOS for ideal CTF-1 in the case of a single layer (red) and bulk (black), obtained from *ab initio* calculations. The inset presents the same data in a more illustrative fashion. The voltage (a) and energy (b) are given with respect to the Fermi level (dashed blue line). Adapted from Ref. [236] with permission of the American Chemical Society.

is directly modelled and the energy of the first dipole-allowed transition calculated by TD-DFT, which is defined as the difference between the energy of the ground state and lowest dipole-allowed excited state, is in theory an approximation to the optical gap. This energy gap in the linear-response TD-DFT can be written as a sum of the energy differences of the Kohn-Sham eigenvalues and a coupling term that is, especially in molecules, small. These transitions can therefore often be described as single excitation within the Kohn-Sham scheme again justifying this interpretation of the Kohn-Sham orbitals as excitations. However, TD-DFT also provides a way to directly consider the excited state and optimize it for its minimum energy, it can therefore be used to describing emission which DFT is not directly capable of.

The interpretation of the electronic structure is not solely limited to optical experiments. The fundamental gap is in essence an electrochemical property and it has been seen that the density of states can also be deduced by redox experiments. This was most recently done by Sakaushi et al. by measuring the open-circuit voltage (OCV) curves through the galvanostatic intermittent titration technique (GITT) for CTF-1 (see Figure 2.4).[52, 236] The calculated density of states using DFT was in close agreement with the experimen-

tally measured one. This demonstrates that the electronic structure also determines redox properties (see Chapter 1) and therefore also qualitatively indicates the fundamental gap.

Densities of states were calculated with VASP.[190] These densities of states were used to extract qualitative approximations of both the optical and fundamental gap.

2.5.2 Charge-State Transition Levels

The energy levels of impurities or defects can be qualitatively extracted from the band structure or density of states.[237] However, defect levels are typically associated with electron transfers between the defect and the valence or conduction band of the bulk material. The energy required for such a transfer is then referred to as a charge-state transition level. Here an excitation and emission is interpreted as the energy needed to transfer an electron between defect and bulk material. Optical charge-state transition levels correspond to excitations without structural reorganization, (vertical excitations) for example ligand-to-metal charge-transfer transitions which are often found in the excitation spectra. The thermodynamic charge-state transition levels, on the other hand, describe the shift in charge state between relaxed geometries and are observed in persistent luminescence, energy storage or mechanoluminescence. These energy levels are probed experimentally through deep-level transient spectroscopy (DLTS) or charge-transfer (CT) luminescence.

From a theoretical point of view, charge-state transition levels assume the conduction and valence band to provide a reservoir of holes or electrons, which move freely like quasi-particles (see earlier). Charge-state transition levels are therefore calculated as the location of the Fermi level at which the thermodynamically most favourable charge state of the considered defect or impurity changes. They can be accurately determined from defect formation energies obtained out of DFT.[112, 238–244] Explicitly the charge-state transition levels $\epsilon(Q/Q')$ can be calculated as the Fermi level locations at which two charge states Q and Q' of the defect have the same formation energy.[112, 238–244] Taking into account the linear dependence of the formation energy on the Fermi energy, we can therefore derive the charge-state transition levels as

$$\epsilon(Q/Q') = \frac{1}{Q-Q'}(E^f(A:X^{Q'})\mid_{E_F=E_V} - E^f(A:X^{Q})\mid_{E_F=E_V}) \quad (2.18)$$

where Q denotes the Kröger-Vink charge state of the impurity X created in the host material A with a formation energy $E^f(A:X^Q)$. E_F is the Fermi

energy, i.e. the electron chemical potential at absolute zero temperature, referred with respect to the valence band maximum, E_V.

The Kohn-Sham energy eigenvalues can also be used to deduce qualitative trends for the charge-state transition levels, although such results should be dealt with with care.[237] Normally the eigenvalues, obtained out of the Kohn-Sham equations show dispersion as a function of the wave vector (see Eq. 2.13). However, energy levels of defects or impurities show limited dispersion and discrete levels rather than bands are observed. These discrete levels can, as a first approximation, be considered as physical impurity levels, provided that both multiplet effects and geometric reorganization are negligible.[244] Again the lower computational cost of this approximation is the driving factor compared to the use of full defect formation energies as described above.

Charge-state transition levels, i.e. impurity levels, were calculated from defect formation energies for the different possible charge states of the dopant using defective supercells.[244]

2.5.3 Alignment of Electronic Structures

Within this PhD thesis we considered the electronic structure of different materials constructed by modifying a model framework, more specifically UiO-66(Zr) and CTF-1-2R (see Chapter 3). To compare these electronic structures on an absolute scale, a common reference is required. This procedure is called energy level alignment, which is frequently used in the domain of heterojunctions and electronics in general.[245–247] The energy of an electron at vacuum, the vacuum energy, is such a reference energy.[248] This vacuum level can be calculated for uncharged slabs with a large vacuum region by DFT and corresponds to the local one-electron potential at a point far from the surface where it becomes constant.[142]

In practice the alignment is done by referring the DFT band positions of different materials with respect to their respective vacuum levels. This is equivalent to considering the Kohn-Sham energies of the valence band maximum and conduction band minimum as ionization energy and electron affinity, as discussed previously (see Figure 2.3b). Some argumentation can be given for this procedure as for periodic systems in the limit of an infinite solid the vertical ionization potential and electron affinity are equal to the corresponding Kohn-Sham eigenvalues for any functional.[231, 232] This method is therefore extensively exploited to perform the band alignment in MOFs.[249, 250] We used this approach ourselves in the case of the lanthanide doped UiO-66 and the CTF frameworks (see Chapter 3, Figure 3.4, 3.13 and

3.18). The additional advantage of alignment based on an absolute reference, such as the vacuum energy, is that it also gives a qualitative measure of its redox properties and therefore its catalytic activity. However, it should be kept in mind that this is only valid for diffuse Kohn-Sham states and it is therefore merely an approximation that in practice gives good results.

If we want to compare the electronic structures of systems with different charges, the vacuum energy is an unsuitable energy reference as the potential in the vacuum scales with the charge and the distance to the surface of the material. Different materials can instead be aligned using either a judiciously chosen energy or a potential reference. The potential reference was, for example, used when comparing the electronic structure of a charged Ru(II)L_3 complex with its neutral linkers or the neutral scaffold with the charged Ru(II)L_3-CTF catalyst (see Chapter 3, Figure 3.16 and 3.17). In those cases the electrostatic potential at an ion is calculated by placing a well-confined test charge

$$\overline{V}_n = \int V(\mathbf{r})\rho_{test}(|\mathbf{r} - \mathbf{R_n}|)d^3\mathbf{r} \tag{2.19}$$

i.e., the average electrostatic potential a typical core electron would experience. In contrast, a judiciously chosen energy reference was used for UiO-66 where the electronic structure was aligned based on a localised node state present in all structures (see Chapter 3, Figure 3.2, 3.3, 3.6, 3.8 and 3.9). This reference has no physical equivalent, but serves to intuitively visualize changes induced in the electronic structure.

Depending on the feature of interest, different densities of states were aligned using either a judiciously chosen energy or potential reference,[111, 146] or by quantitatively positioning them with respect to the vacuum potential.[146]

2.5.4 Influence of the Exchange-Correlation Functional

As discussed in Section 2.2 the approximation made for the XC functional determines the accuracy of the predicted material properties. Local- and semi-local functionals, such as LDA and GGA, have worked quite well for cohesive and structural properties. However, in literature it has been often stated that they underestimate the fundamental band gap in semiconductors. This has caused a lot of confusion in literature.[209] The fundamental gap is a ground state property and is therefore accessible using DFT. However, in literature this fundamental gap is deduced from the difference between the Kohn-Sham highest occupied and lowest unoccupied states which is theoretically not equal to the fundamental gap. This follows from the properties of the

exact XC functional, which is known to display a discontinuity Δ_{xc} at integer electron numbers. This property is closely related to the self-interaction error (SE) which incorporates the non-physical interaction of an electron with itself in DFT.[251–253] (Semi-)local funtionals do not possess such a discontinuity, so the difference between the Kohn-Sham eigenvalues does not provide an accurate description of the fundamental gap and an offset equal to the XC discontinuity is present. Nowadays it has been accepted that the LDA and GGA functionals are better descriptions for the optical gap, which is indeed smaller than the fundamental gap.[209]

To approximate the fundamental gap with the energy difference of the Kohn-Sham eigenvalues the functional and therefore the Kohn-Sham auxiliary system should be altered. The idea is to incorporate the XC discontinuity by making the Hamiltonian dependent on the occupation of the single-particle orbitals, an idea theoretically enabled by the generalized Kohn-Sham (GKS) scheme.[254, 255] It represents an extension to the Kohn-Sham equations where the condition of a non-interacting model system is relaxed. Explicitly this is done by the introduction of non-local/orbital-dependent density functionals.[213] Typical examples are created by including an amount of full, screened or long-range corrected Hartree-Fock-like exchange in the functional. It was observed that the use of these functionals, such as HSE06,[148, 256–258] have resulted in theoretical fundamental band gaps which are in better agreement with experiment.[148, 244, 256, 259] It has now moreover been proven that in the GKS theory the difference between the lowest unoccupied and highest occupied energies for extended systems equals the fundamental gap for the approximate functional if the potential operator is continuous and the density change is delocalized when an electron or hole is added.[231, 232, 255] Therefore the interpretation of energy gaps in the DFT band structure or density of states as optical or fundamental (see Figure 2.1 and 2.2) depends on the functional. Note, however, that non-local contributions significantly increase the required computational resources.

Another approach to solve the band gap problem is not to use DFT and start from an explicit quasi-particles model based on Green's function theory,[194] such as the GW approximation (where G is the Green's function and W is the dynamically screened Coulomb interaction).[260] GW dynamically screens the Coulomb interaction such that electrons move in a potential screened by all other electrons directly taking into account the right physics.[261] This approach thus mimics the electron-hole quasi-particle behaviour. Instead of an XC functional a non-local and screened self-energy is introduced, including all electron-electron interactions. The resulting equations for the quasi-particles are very similar to the GKS system in DFT, where the non-local self-energy in the many-body GW theory resembles a non-local functional in

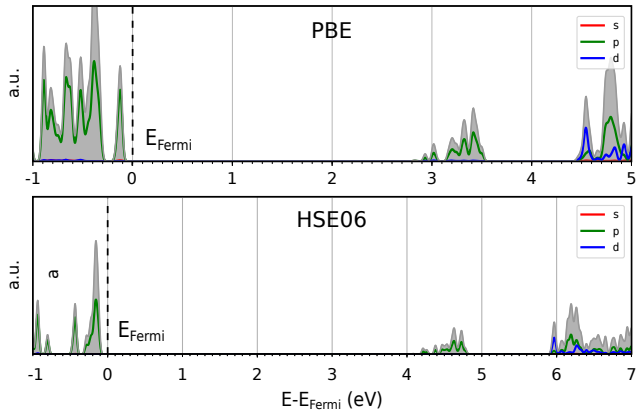

(a) UiO-66(Zr)

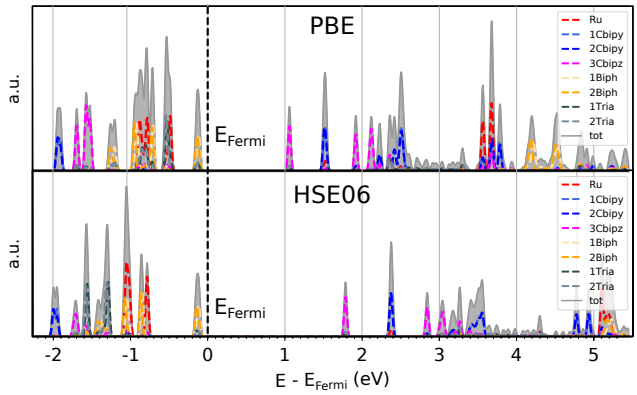

(b) Ru(II)L_3@CTF

Figure 2.5: PBE and HSE06 functional for UiO-66(Zr) (a) and a Ruthenium complex (Ru(II)cbipy$_2$cbipz$_1$) anchored on a CTF framework (Cbipz$_1$biph2) (b) (see Chapter 3).

DFT.[212, 255, 260, 262–264] This is further supported by the observation that HSE06 single-particle orbitals provide a good starting point for perturbative GW corrections.[233, 265, 266] The downside of these methods is that they are even more demanding than DFT with non-local functionals and become less or non-feasible for large systems, such as MOFs and COFs.

During this PhD thesis we have frequently tested the difference between PBE and HSE06 functionals, see Figure 2.5 for two examples. The most prominent effect is the increase in the band gap which is expected when using a hybrid functional (see explained above). However, relative trends in the band gap are typically maintained and the locations of individual peaks

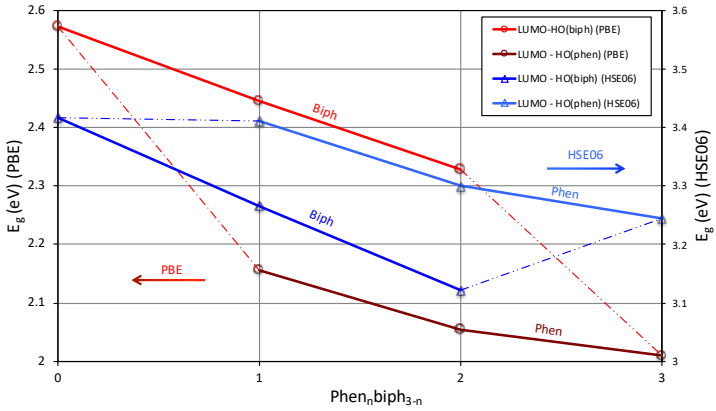

Figure 2.6: Energy gaps for PBE (red) and HSE06 (blue) calculations of phen$_n$biph$_{3-n}$, $n = 0, 1, 2, 3$. The energy gaps are defined between the LUMO, which has a delocalized character, and the highest occupied (HO) state localized on either a phen or biph linker. Adapted from the supporting information of **Paper I [Ref. 146]** with permission of the Royal Society of Chemistry.

and the vacuum potential are mostly shifted in energy with minor alteration to the relative trends. When states do change order, their character across different structures still follows the same trend between both functionals (see Figure 2.6). Semi-local functionals therefore display similar trends as HSE06 at a fraction of the computational cost. We therefore mainly limited ourselves to these functionals. GW calculations, on the other hand, were not performed due to the computational cost.

In this PhD thesis we extensively used the PBE[267] semi-local functional. However, non-local functionals were also used, such as the hybrid B3LYP,[268] long-range corrected CAM-B3LYP,[269] metahybrid M06[270] as well as the HSE06 functional.[256, 271]

3

Major Research Results

I begin with an idea and then it becomes something else.
Pablo Picasso (1881 – 1973)

3.1 Orthogonal Electronic Structure Engineering

The modular nature of nanoporous frameworks entails an enormous opportunity to design their properties (see Chapter 1). To design optimal photocatalytic materials, the property to modulate is the electronic structure (see Section 1.1.2). Electronically engineering of these materials requires a proper choice of the building blocks such that their combination yields the desired photocatalytic activity. Numerous ways exist to construct modular materials with a fixed number of variable building blocks. For example, UiO-66 can be constructed with 10 different linkers, 15 nodes (lanthanides, Zr, Hf and Ti) and the possibility of 42 missing-linker defects configurations giving a total of 7500 materials. The number of materials therefore surpasses the finite number of building blocks by more than an order of magnitude, as it scales exponentially. Even with current computational resources, it is unfeasible to calculate all these structures from first principles at a high level of accuracy. However, if we understand how the electronic properties of a modular material change as a function of its building blocks, a more efficient and rational material design comes within reach. One could therefore imagine an efficient screening of the electronic properties of modular materials,

based on the concept of *Orthogonal Electronic Structure Engineering (OESE)*, where the properties of the material are determined by the properties of its building blocks. Apart from the computational efficiency, the concept could also yield more chemical insight into which factors determine the overall electronic properties of the material.

On a fundamental level, the OESE concept requires knowledge on how the electronic structure is altered when two components are joined. In solid-state heterojunctions a similar phenomenon occurs. Far from the interface between both components/semiconductors their corresponding electronic structure is maintained whereas only locally, at the boundary between the two phases, a difference is observed. When both the electronic structure of the semiconductors are expressed relative to vacuum potential, assumed equal across the entire structure (see Section 2.5.3), the total electronic structure can, to a large extent be deduced from the individual components/semiconductors.[248]

In this PhD thesis we examine to what extend a similar principle is valid for modular framework materials with nanoporous properties. In literature, earlier studies already suggested into what extend the behavior of separate building blocks may be present in the parent modular material. Most papers originate from MOF research, where both experimental and computational work has been performed. Experimentally, for example, the group of Gascon showed that in the MIL-125(Ti) series MOFs should be seen as an array of self-assembled molecules.[272] Computations, on the other hand, by the group of Walsh et al. on MOF-5 showed no appreciable band dispersion in its electronic structure.[273] Moreover, prior work done in our own group revealed that linker and node states exhibit a low overlap in UiO-66.[110] These papers illustrate the general lack of electronic coupling or hybridization between the building blocks in MOFs.[274, 275] Furthermore, they demonstrate that the traditional solid state view of MOFs as semiconductors, characterized by delocalized conduction and valence bands, is inadequate (see Chapter 1). Instead the molecular terminology of highest occupied crystal orbital (HOCO) and lowest unoccupied crystal orbital (LUCO)[152, 272, 275] is more appropriate (see Figure 3.1).

These literature data led us to introduce the *Orthogonal Electronic Structure Engineering (OESE)* paradigm in which the electronic structure of nanoporous frameworks can be seen as a sum of independent (orthogonal) contributions of their building blocks. In what follows a validation is given for a number of modular nanoporous materials (see also Chapter 4, Section 4.2).

To investigate the principle of the OESE within MOFs, where it is expected to hold (vide supra), we studied the zirconium-based MOFs developed at Oslo

University (UiO) by Lillerud and coworkers.[74] These nanoporous materials are very stable,[40, 41, 150] have a fairly robust synthesis and even allow for an efficient upscaling from the lab to a pilot scale plant.[276] Moreover they favor the inclusion of genuinely different linkers[73, 277–281] and metals,[109, 282–284] which resulted in a plethora of functionalized materials with the UiO crystal structure. Finally, UiO-type MOFs are increasingly considered as potential photocatalytic materials,[285–291] the main application of interest in this PhD thesis. These properties make UiO-66 an ideal candidate to serve as a proof of concept for the OESE principle. Design of the different building blocks via OESE will allow us to optimize UiO-66-type materials for photocatalytic applications in a more efficient and rational way (see Section 3.2).

To examine the wider applicability of the OESE principle we will consider covalent organic frameworks (COFs), another subclass of nanoporous materials. COFs are a very recent class of nanoporous materials solely composed of organic building blocks connected by strong covalent bonds. It is expected that these materials exhibit a stronger hybridization or electronic coupling between their constituents.[18] It remains to be investigated in how far the OESE principle holds. Specifically we will look into covalent triazine frameworks (CTFs) and examine how, in a similar way as was done for UiO-66, their building blocks affects the CTF's electronic structure. Pristine COFs have only showed a limited catalytic activity but may be used as supports for molecular catalysts.[70, 79, 80] Therefore we will functionalise CTFs with Ru-polypyridyl complexes, well-known homogeneous photocatalysts, to make heterogeneous photocatalysts with well defined active sites. Additionally the isolated Ru-polypyridyl complex can by itself be regarded as a modular system with varying ligands. The applicability of the OESE principle towards molecular complexes will therefore be analyzed as well. Our end goal is again to rationally design better photocatalytic complexes and (functionalized) CTFs based on the OESE principle.

The above modular materials serve as benchmark studies for the OESE principle. In spite that these studies focus on a particular example of MOFs (UiO-66) and COFs (CTFs) we believe that the OESE is more generally applicable to modular materials. This will also be seen in its applicability to the anchored molecular complex as building block on the COF scaffold as well as within the modular Ru-polypyridyl complex itself. Furthermore, literature contains some justification that the decoupling between building blocks is also observed in other modular materials. Zeolitic imidazolate frameworks (ZIFs) with structures similar to conventional aluminosilicate zeolites, show a similar decoupling between its building blocks.[158, 159] Outside the class of nanopourous materials the concept of OESE might also be applicable. As an example we mention Metal halide perovskites (MHPs) which have emerged

as a promising, novel class of semiconductors. So far, they have mainly been explored within the field of solar cells, but perovskites are extremely versatile and possess an untapped potential for many other high-tech applications. They are modular by the versatility of the metal and halide for which a similar decoupling can be observed.[292–295] Organic electrodes on the other hand, organic structures in some sense related to the COF we examined, could also benefit from the OESE principle.[296–299] It is therefore clear that the OESE principle could have a wider range of applicability than MOFs or COFs. In the next section, we start with a thorough investigation on how the principle of OESE holds for MOFs and COFs. In the perspectives of Chapter 4 we will briefly reflect on the possibilities to use and extend the OESE principle in a broader context.

3.2 Application to MOFs: UiO-66

Most of the Zr-based frameworks and specifically UiO-66 have been subjected to extensive research in a broad domain of applications.[300] UiO-66(Zr) consists of octahedrally coordinated Zr atoms, forming $Zr_6O_4(OH)_4$ nodes, which are connected via 12 benzene dicarboxylate (BDC) linkers per node (see Figure 3.1). Recently its amino-functionalized UiO-66(Zr), both in its pure and mixed-linker form, showed reasonable photocatalytic activity in several chemical transformations.[285–291, 301] This indicates that through isoreticular alterations UiO-type MOFs can be tuned to function as a photocatalyst.

The electronic structure of pristine UiO-66(Zr) is presented in Figure 3.1. This electronic structure is calculated with the PBE functional (see Chapter 2), as well as all further structures, unless stated otherwise. The electronic structure of pristine UiO-66(Zr) is composed of a sum of contributions centred on the linkers and the nodes. Therefore, similarly to literature we observe localized states, referred to as crystal orbitals, rather than bands.[152] More importantly the electronic structure indicates why, despite the promise of UiO-66(Zr) for chemical conversions, the pristine material has only a limited photocatalytic activity. For its photocatalytic activity two energy gaps (see Chapter 2, Section 2.5.1) are relevant, ΔE_{abs} and ΔE_{LMCT} (see Figure 3.1). ΔE_{abs} corresponds to the energy required to excite the linker and ΔE_{LMCT} corresponds to the energy needed to transfer the excited linker's electron to the node's unoccupied d-orbitals, i.e. the ligand-to-metal charge transfer (LMCT). These processes are also summarized in Figure 3.1 (left). In order to obtain an efficient electron transfer to the Zr node and thus a high activity, ΔE_{LMCT} should be close to zero or or even negative i.e. overlapping or below

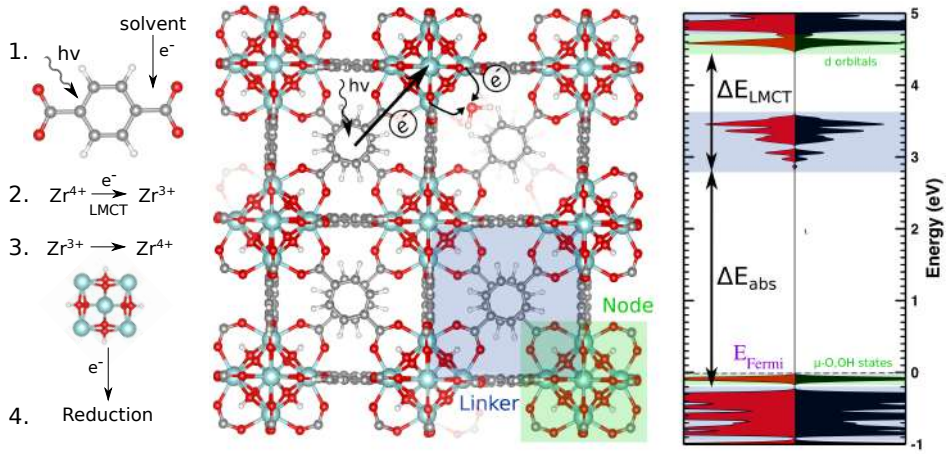

Figure 3.1: Photocatalytic process in UiO-66(Zr) in terms of its building blocks (left), defect crystal structure (middle) and density of states of the pristine UiO-66(Zr) (right), where red and black curves represent different spin channels and blue and green indicate linker and node states, respectively. The linker is excited by an incident photon (excitation energy ΔE_{abs}), after which the electron is transferred to the node, reducing a Zr atom (energy barrier ΔE_{LMCT}). The excited electron is then available to reduce reactants near the active site. Zr atoms are represented in blue, O atoms in red, C atoms in grey and H atoms in white. Adapted from **Paper I [Ref. 111]** with permission of the American Chemical Society.

the unoccupied linker states. However, as seen in the Figure 3.1 (right) this is not the case for pure UiO-66(Zr), restricting its activity. This hindered charge transfer has been confirmed both in experiment[286–288, 302, 303] and in theory[110] (TD-DFT cluster calculations). In addition the band gap of UiO-66(Zr) is too large and is prohibitive for the direct use of sunlight.

The unfunctionalized, defect-free material UiO-66(Zr) is thus not the holy grail in photocatalysis. However, thanks to its modular nature, it can be functionalized to pursue better photocatalytic properties, as was also seen in experiments.[57, 275, 285–291, 302] One can alter both its nodes and linkers to achieve an increased photocatalytic activity. To explore this, we start studying the electronic structure of pristine UiO-66(Zr) and we show how its electronic properties are altered when we systematically change its linkers and/or nodes. Most of these calculation were already performed in literature, however, we aim to reinterpret them in view of the OESE concept. Further-

more, the materials are extended towards incorporation of lanthanide ions, which are interesting for light-based and catalytic applications, and towards incorporation of missing-linker defects. Indeed within the MOF community it has been acknowledged that defects determine to a large extent the functionality of the MOF materials offering new interesting opportunities.

3.2.1 Linker Alterations

The first modifications we consider are based on a **linker alteration**.[73, 277–280, 304] By adding organic functional groups to the linkers (see Figure 3.2), or by increasing the linker length, the absorption wavelength of the system ΔE_{abs}, a linker based quantity, can be changed.[214] Effectively reducing ΔE_{abs} requires the introduction of an electron-donating group, which can shift the absorption peak deep into the visible spectrum. This reduction is caused by the introduction of filled states within the first band gap as seen in Figure 3.2. Electron-withdrawing groups (e.g. NO_2) or changes in linker length have a much more limited effect (see Figure 3.2 and **Paper I [Ref. 111]** including its supporting information for a more detailed assessment).

Additionally we see that the electronic states centered on the node are not changed by linker alteration (see Figure 3.2, green region), a first conformation of the OESE principle. This implies that, in the case of UiO-66(Zr), the absorption wavelength decreases, but that ΔE_{LMCT}, which plays a dominant role in the photocatalytic activity, does not. This was also confirmed in other computational[110] and experimental studies.[286, 302] Computationally it was shown that although several electron-donating groups change the theoretical charge-transfer efficiency, this change remains limited due to the high energy of the Zr d-orbitals with respect to the excited linker states (ΔE_{LMCT}).[110] Experimentally several groups investigated the charge transfer confirming that pristine and linker-functionalized UiO-66(Zr) materials have no efficient transfer (ΔE_{LMCT}).[286, 302] These conclusions can be explained and to a certain point predicted by considering the pristine UiO-66(Zr) electronic structure and the concept of OESE.

3.2.2 Node Alterations

The problem of inefficient charge transfer (ΔE_{LMCT}) can be tackled by a second pathway: **altering the metal node**. As the problem is essentially created by the high energy of the Zr d-orbitals with respect to the excited linker states this solution can, to a certain point, be expected. The introduction of Ti^{4+} in the Zr-node,[301, 304–309] for example, strongly improves the catalytic

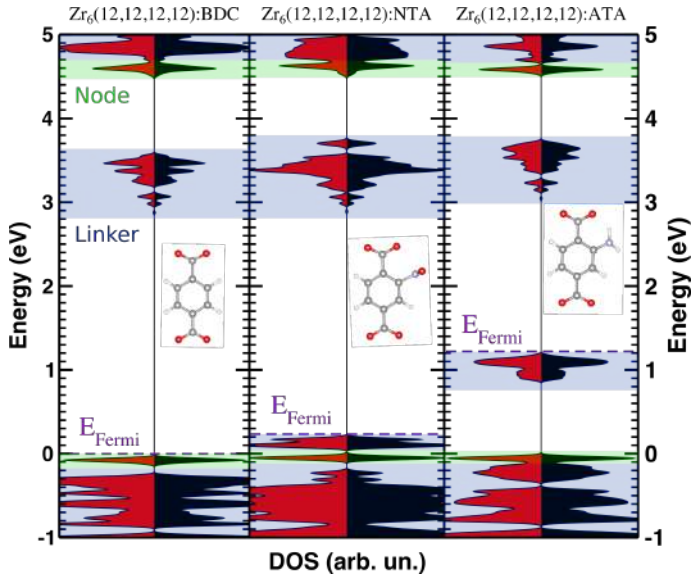

Figure 3.2: Densities of states for linker functionalized UiO-66 type materials. BDC, NTA and ATA are respectively benzene dicarboxylate, nitroterephthalate and aminoterephthalate. Red and black curves represent different spin channels and all DOS are aligned with respect to the pristine μ-OH,O states. Blue and green indicate linker and node states, respectively. Adapted from the supporting information of **Paper I [Ref. 111]** with permission of the American Chemical Society.

activity of the material.[282, 310] Gascon and coworkers[302] discussed three existing MOFs composed of d^0 metals (Ti^{4+}, Zr^{4+} and Hf^{4+}) and confirmed that only the titanium mixed-metal material shows a large LMCT. Also computationally, Ti materials have been shown to possess a much smaller ΔE_{LMCT},[308, 311] and shown more recently, an associated longer lifetime of the excited state.[101]

Figure 3.3 shows our own calculations of UiO-66 with purely Ti, Zr or Hf nodes. The low lying Ti 3d states overlap with the linker-based LUCO, increasing the electron-transfer efficiency. It also illustrates the OESE principle as the node alterations only change the nodes states and cause an overlap with the unaltered linker states. However, the inclusion of Ti is not the only possibility to increase the charge transfer, the decrease of ΔE_{LMCT}, in UiO-66 (see further).

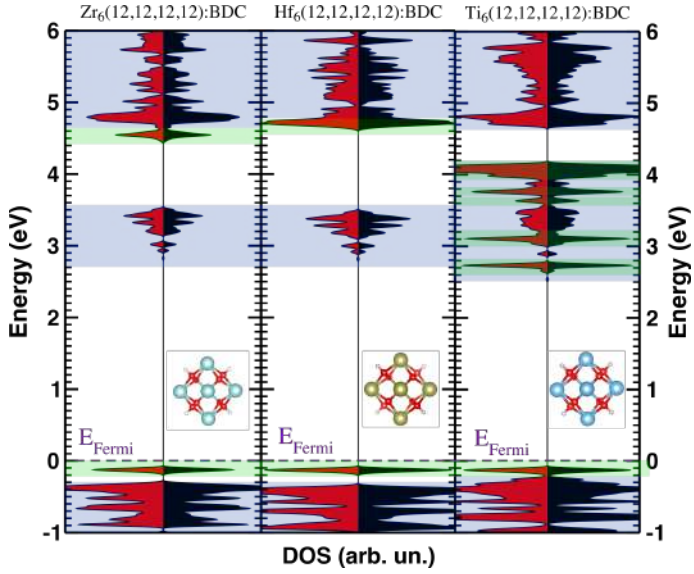

Figure 3.3: Densities of states of UiO-66(Zr), UiO-66(Hf) and UiO-66(Ti). Red and black curves represent different spin channels and all DOS are aligned with respect to the pristine μ-OH,O states. Blue and green indicate linker and node states, respectively. Adapted from the supporting information of **Paper I [Ref. 111]** with permission of the American Chemical Society.

I. Lanthanides

The lanthanide (Ln) series is an interesting set of atoms for both light-based[160–162] and catalytic applications[163–165] making them highly attractive for photocatalytic applications. Nowadays Ln-based materials have made their way into MOF research.[312–314] The inclusion of small amount of lanthanides within a MOF, in this case UiO-66(Zr), creates a set of advanced materials that combine both unique characteristics of lanthanides and the high stability of UiO-66(Zr). However, despite that some Ln MOFs had already been proposed in literature they most often lack in stability and/or are very difficult to synthesize.[315]

In **Paper II [Ref. 109]** this difficulty and limited stability was overcome by an approach inspired by solid-state lanthanide chemistry. A stable robust carrier material, in this case UiO-66(Zr), is doped with a small amount of lanthanide ions in a high-temperature process. Here a microwave-based methodology was adopted to dope UiO-66(Zr) with several lanthanide and transition metal ions, a strategy which had only been used to introduce isovalent atoms at that time.[307, 316] The electronic properties of these new materials were

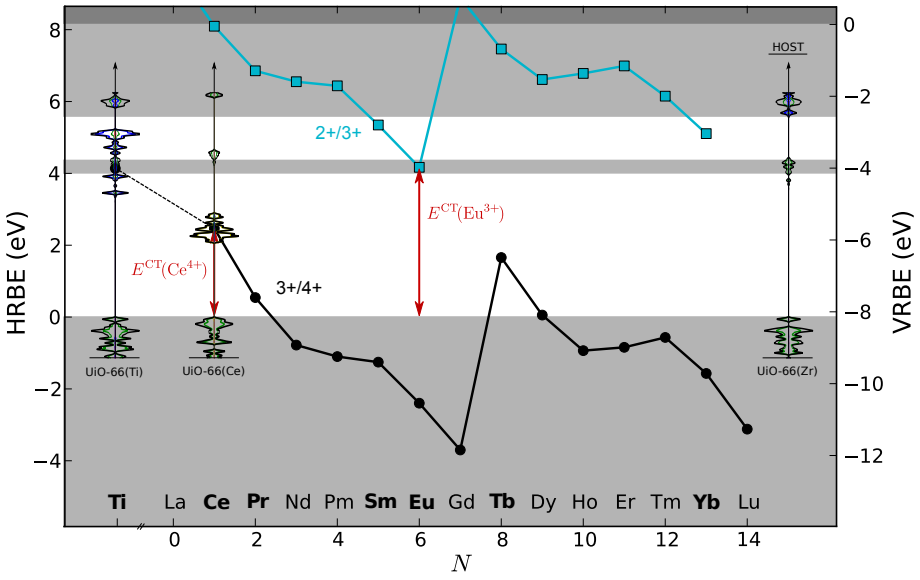

Figure 3.4: Overlay of the electronic structure of UiO-66(Zr), the host material, (grey) with both the (3+/4+) (black dots) and (2+/3+) charge-state transition levels (blue squares) for the lanthanide series incorporated as impurities. Elements with an interesting transition level for photocatalysis are printed in bold. Values are referred to the vacuum (VRBE, vacuum-referred binding energy) or to the host material (HRBE, host-referred binding energy). The DOS insets are calculated with PBE functional and rescaled to align with UiO-66(Zr) host material, they therefore merely indicating the qualitative trend. Adapted from **Paper II [Ref. 109]** with permission of the American Chemical Society.

subsequently investigated both by theory and experiments. Here we restrict ourselves to an overview of the DFT calculations on periodic MOF structures. More information, about both synthesis and experimental characterization as well as additional insights in the charge transfer using TD-DFT on cluster models, can be found in **Paper II [Ref. 109]**. The experiments for this work were done by Dr. Hendrickx, whereas the periodic calculations mentioned in Paper **Paper II [Ref. 109]** were performed by myself.

As seen previously the inclusion of Ti in UiO-66 creates an increase in charge transfer due to their low lying 3d states, decreasing ΔE_{LMCT}. Lanthanides have, similar as Ti, such low lying states, in this case 4f states. Moreover, these states behave chemically very similarly independent of the chemical environment.[317–319] Therefore when a material is doped with a lanthanide

the charge-state transition levels (see Chapter 2, Section 2.5.2) show a typical zigzag line. This line can be predicted, due to its invariance, if one knows the location of at least one such level for one lanthanide ion on that line.[317–319] Figure 3.4 shows this zigzag line for all fourteen Ln (2+/3+) and (3+/4+) charge-state transition levels, based on a small set of experimental absorption and photoluminescence (PL) spectra within the UiO-66(Zr) host material (see **Paper II [Ref. 109]** for more details).

The insets of Figure 3.4 shows the results of the periodic calculations performed in the framework of this PhD thesis. Since the behaviour of the localized electrons of the Ln ions is notoriously difficult to predict with DFT, we only performed UiO-66(Ln) calculations with Ce^{4+}, for which DFT has been shown to provide reasonable qualitative results.[320, 321] The calculations confirm that the UiO-66(Ce) framework contains low lying 4f states, qualitatively agreeing with the predication of the empirical model. In the case of Ce^{4+}, for example, these low lying 4f states or charge-state transition levels (3+/4+) lie below the unaltered unoccupied linker states, corresponding to a negative ΔE_{LMCT}. This creates an additional, more favourable pathway for ligand-to-metal charge transfer, in which an excited linker electron (present in the unoccupied linker states) relaxes to the lower lying 4f metal states. Figure 3.4 additionally shows the Ln in bold that may result in a more efficient charge transfer, i.e. with a charge-state transition level below, such as Ce^{4+} or overlapping with, such as Ti, the unoccupied linker states i.e. $\Delta E_{LMCT} \leq 0$ as well as those with a reduced ΔE_{LMCT} compared to the host material.

II. Missing-Linker Defects

While the photocatalytic activity of UiO-66(Zr) may be enhanced by the subsitution of Zr by Ti[302] or Ln[109] and the introduction of new components into the framework, such as guests,[64, 65, 72] we explored the possibility of defect engineering to alter the photocatalytic properties of the framework. It is inspired by the fact that also in non-modular materials, defects may have a strong effect on the photocatalytic activity.[322, 323] Defects can, for example, introduce band gap states, as was observed in our earlier work on antisite defects in $ZnGa_2O_4$:Cr, which significantly alter the electronic structure.[237] Within the MOF community, a lot of research has been performed on so-called defect engineering, as it has been observed that defects - ether localized or exhibiting spatial order/disorder - may substantially alter the properties of the material and may even be necessary to create the desired functional behaviour.[71, 75, 324, 325]

In UiO both missing-linker (see Figure 3.5) and missing-node defects can occur yielding stable frameworks. Lillerud et al. showed that defects are

inherently present in UiO-66 frameworks under normal synthesis conditions. They moreover succeeded in designing synthesis procedures to obtain a defect-free UiO-66(Zr)[326] or to incorporate additional defects.[327] These defects have also been recently observed by low-dose high-resolution transmission electron microscopy (HRTEM).[328] Here we considered (missing-linker) defect structures by removing one, two or three benzene dicarboxylate acid linkers, H_2BDC, from the pristine UiO-66 (see Figure 3.1), modeled in a 4-node unit cell. Note that we do not focus on missing nodes, but show at the end of this section that they exhibit, to a large extent, the same properties as missing linkers.

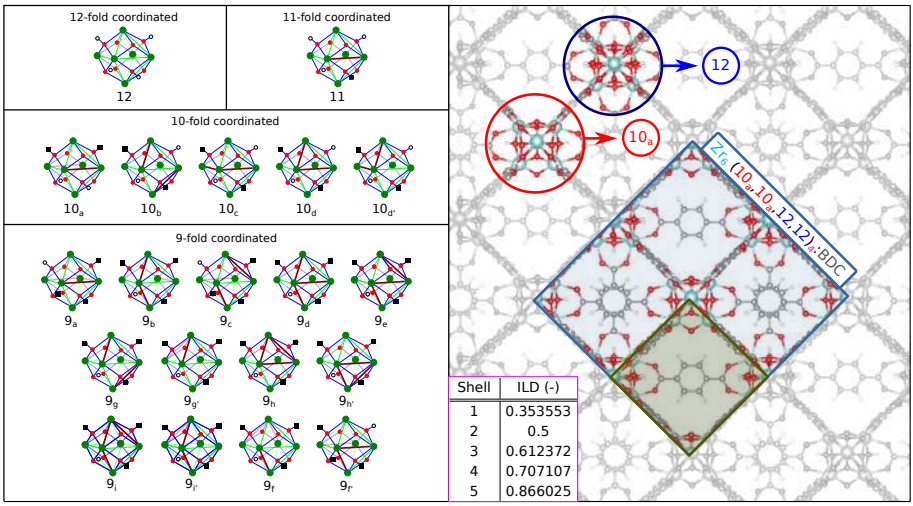

Figure 3.5: (right) Cross section of UiO-66(Zr) where two linkers are removed from a 4-brick unit cell (right, blue square). One of these missing linkers is enclosed in the transparent green square. The table represents the interlinker distances (ILD) between the centres of the removed linkers normalized with respect to the lattice constant of the four-node unit cell and serves to remove any remaining ambiguity. (left) The possible node configurations created when introducing one-, two- or three-missing-linker defect structures.

The removal of missing linkers from a UiO-66 crystal can be done in many ways. The number of symmetrically inequivalent ways that linkers can be removed depends on the number of removed linkers and the size of the modelled unit cell. To investigate the effect that linker removal has on the electronic structure, it is important to be able to characterize each defect structure with a transparent notation. We therefore introduced a general notation, extending the limited notations already present in literature.[329–331]

Our notation depends on the size of the unit cell and thus accounts for the periodicity of the defect structure. It is also easily extended towards larger unit cells and yields insight into the corresponding defect structure. In the following we discuss this notation when l linkers are removed from a n-node unit cell.

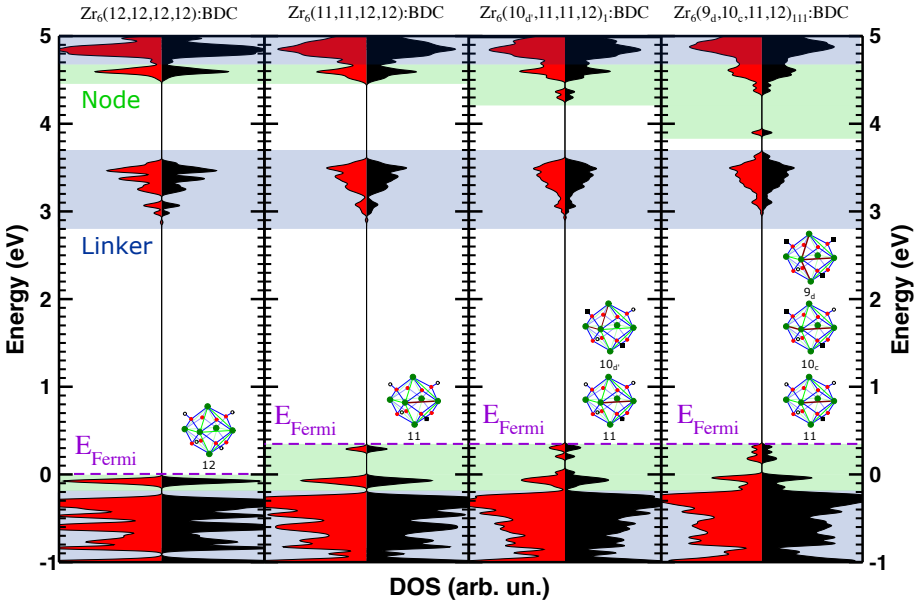

Figure 3.6: Density of states of the pristine, one-, two- and three-missing-linker defect structure where an increasing amount of linkers is removed from a single node. Red and black curves represent different spin channels and all DOS are aligned with respect to the pristine μ-OH,O states. Blue and green indicate linker and node states, respectively. Adapted from **Paper I [Ref. 111]** with permission of the American Chemical Society.

When l linkers are removed from a n-node unit cell we can note the resulting defect structure as $(CN(1)_\alpha, CN(2)_\beta, ..., CN(n)_\nu)_{\{i\}}$, representing the structure of the material from the point of view of the nodes (see Figure 3.5). Each node configuration, CN_α, is described by its coordination number CN, to which a subscript (α, ..., ν) is added to differentiate between nodes with the same coordination number but with a different symmetry. The subscript set $\{i\}$ indicates the $\binom{l}{2}$ interlinker distances (ILD) between the centres of the l removed linkers normalised with respect to the unit cell parameter (see Figure 3.5) and serves to remove any remaining ambiguity. Furthermore, these indices are expressed in terms of coordination shell numbers. Because our notation fully determines the defect structure, the order of the

node configurations does not matter. By convention, we propose to order by increasing coordination number and then by alphabetical subscript. An example of a modeled $Zr_6(10_a,10_a,12,12)_4$:BDC defect structure is shown in Figure 3.5. Here the notation indicates that 2 linkers are removed from a 4-node unit cell of Zr-nodes (Zr_6) connected by BDC linkers. The second linker is positioned in the fourth coordination shell of the first, leaving nodes of both 12 and 10_a configurations.

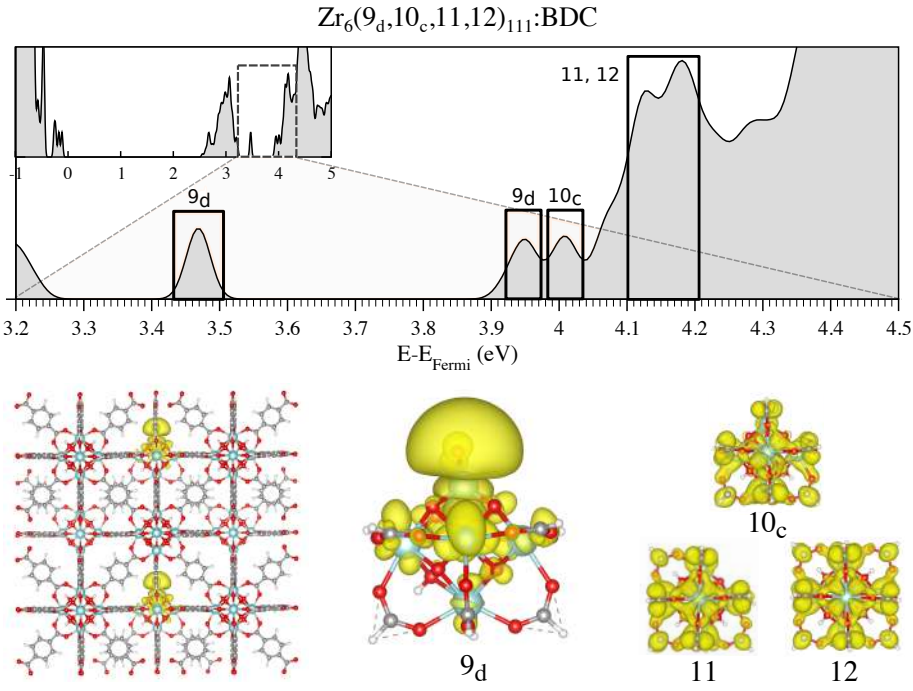

Figure 3.7: (top) Density of states of the $Zr_6(9_d,10_c,11,12)$:BDC defect structure, decomposed in terms of the Zr unoccupied d-orbitals. (bottom) Contour plots of the lowest-energy d-orbital centred on the 9_d node (left) and the singly occupied molecular orbital of formate-capped 9_d, 10_c, 11, 12 nodes (right). Adapted from **Paper I [Ref. 111]** with permission of the American Chemical Society.

In **Paper I [Ref. 146]**, we showed that these defects indeed alter the electronic structure (see Figure 3.6 and 3.7). In particular, removing linkers can provide an alternative way to tune the LMCT, since it alters the structure of the nodes. We showed that the local environment of the nodes affects the Zr unoccupied d-orbitals. The behavior of the d-orbitals can therefore be deduced to a large extent from the type of nodes present in the defect structure. Our notation, helpful in this deduction, is therefore immediately

inspired by the OESE principle as it characterizes the building block, the altered node configurations, within the defect structure. Moreover the more linkers per node are removed, the more the d-orbitals are lowered in energy, with the electron localized near the site of the missing linkers (see Figure 3.6 and 3.7). The observed lowering of the energy of localized Zr d-orbitals at the defect site effectively decreases ΔE_{LMCT} and improves the charge transfer to the node (see Figure 3.6). Therefore this work suggest that defects improve the photocatalytic activity. On the other hand these results are in line with the OESE principle as the inclusion of missing linkers does not affect the linker states and can be seen as a node alteration. Nowedays also experimental results show that missing-linker defect indeed increase the catalytic activity.[332]

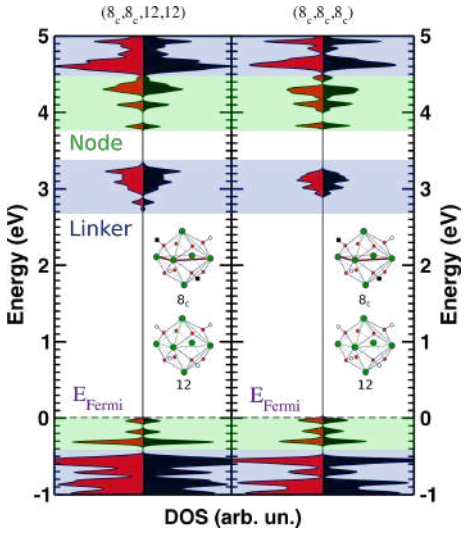

Figure 3.8: Removal of a node from the 4-node unit cell (right) compared to a 4-defect structure in which the linkers are removed to create the node configurations present in a missing-node defect structure (left). Red and black curves represent different spin channels and all DOS are aligned with respect to the pristine μ-OH,O node states. Blue and green indicate linker and node states, respectively. Adapted from the supporting information of **Paper I [Ref. 111]** with permission of the American Chemical Society.

The presence of missing-linker defects might (partially) explain why a good photocatalytic activity was experimentally found for some functionalized UiO-66(Zr) materials.[285–290] Rational design of the number and types of defects in the material is therefore a promising approach to improve the

photocatalytic activity of the material. Such specialized defect engineering is possible through different synthesis procedures.[324–326, 333] Besides missing linkers, Lillerud et al. recently discussed the presence of missing nodes as one of the major defect types in UiO-66(Zr).[327] However, removing a complete node has a similar effect on the electronic structure as removing linkers (see Figure 3.8), since the removed node itself does not affect the electronic structure and only creates defective nodes in its surroundings.

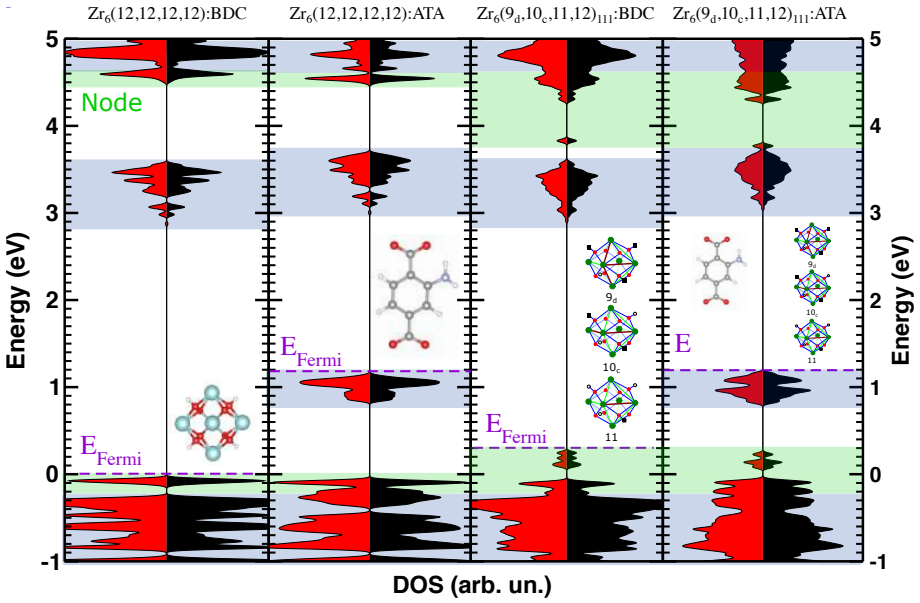

Figure 3.9: The electronic structure of UiO-66(Zr) with both aminoterephthalate (ATA) and 3 missing linkers can be deduced from the superposition of an ATA-functionalized UiO-66(Zr) and the defect structure of unfunctionalized UiO-66(Zr). Red and black curves represent different spin channels and all DOS are aligned with respect to the pristine μ-OH,O node states. Blue and green indicate linker and node states, respectively. The charge density corresponding to the lowest unoccupied d-orbitals of $Zr_6(9_d,10_c,11,12)_{111}$:ATA and $Zr_6(9_d,10_c,11,12)_{111}$:BDC are found similar. Adapted from **Paper I [Ref. 111]** with permission of the American Chemical Society.

We conclude that designing a highly active MOF-based photocatalyst, using a broad range of the visible spectrum and exhibiting an efficient LMCT, requires both ΔE_{abs} and ΔE_{LMCT} to be tuned. The independence of nodes and linkers, in MOFs with a 0D inorganic sublattice, allows one to tune them in an orthogonal way, enabling a complete and precise control

of the electronic properties of these photocatalysts (OESE). The orthogonality of this alterations in the electronic structure is prominently supported by Figure 3.9 where both linker and node alteration, respectively through an amino functionalized group (ATA) and 3 missing-linker defects $(9_d,10_c,11,12)_{111}$, are displayed. These alterations are first shown separate and then combined and as seen the electronic structure of their combination, the $Zr_6(9_d,10_c,11,12)_{111}$:ATA, can indeed be predicted by its altered building block i.e. the combination of the $Zr_6(9_d,10_c,11,12)_{111}$:BDC and the Zr_6(12,12,12,12):ATA. Figure 3.9 is therefore our most significant proof of the OESE principle. The OESE principle can now also be used as a design tool to to determine how the UiO-66 can be altered to optimize its photocatalytic activity. First the absorption properties can be tuned by altering the linker, functionalizing the linker with an amino group is a viable procedure. Second the LMCT can be enhanced by altering the node itself. This can be done by direct metal substitution, such as the incorporation of Ti or some lanthanides or indirectly through the introduction of defects, for example the $Zr_6(9_d,10_c,11,12)$:BDC defect structure. The OESE principle predicts that both alterations are independent and orthogonally combined in the electronic structure to form a photocatalyst with all its advantages.

3.3 Application to COFs: Ru(II)L_3@CTF

To test the broader applicability of the OESE principle we considered COFs.[34, 43, 100] Similarly to MOFs[30] their modular nature, large surface area and porosity generate an enormous potential for energy storage, gas capture and heterogeneous catalysis (see Chapter 1).[34] In literature, these materials are currently explicitly investigated for their electronic properties and stability.[18, 39–41] Their properties are induced by their strong, fully covalent nature causing both a high stability and electronic coupling. The latter provides a major challenge for the OESE principle and is an ideal case to test the broader applicability of the OESE principle.

COFs are also interesting from a photocatalytic point of view. Although they lack an inorganic catalytic center, which seems to limit their activity compared to MOFs,[79, 99, 334–336] their activity can be increased by incorporation of photocatalytic complexes. Similar strategies can be applied for MOFs,[337] where photocatalytic complexes were already successfully anchored to both linkers[338, 339] and nodes.[340] The assembly of a COF and a photoactive complex could merge some of the most important features of both organic (e.g. stability)[38] and inorganic (i.e. catalytic) worlds. Furthermore, the heterogenized photoactive complex may lead toward more efficient, environ-

mentally friendly and robust heterogeneous photocatalysis (see Chapter 1, Section 1.1.2). Therefore, we will study this pathway by considering covalent triazine frameworks (CTFs) as a support for the Ru-polypyridyl complex, a well-known homogeneous photocatalyst.

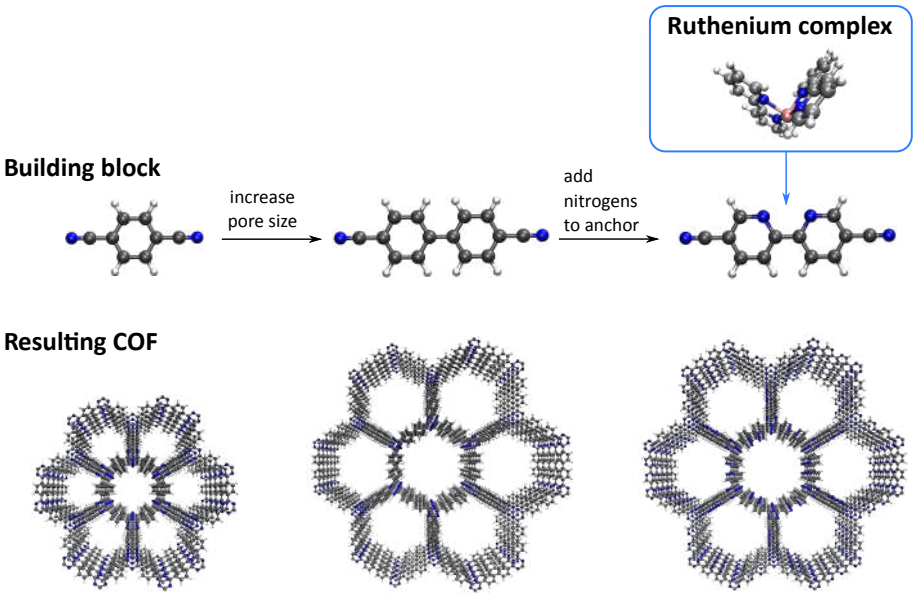

Figure 3.10: Covalent triazine frameworks, 2D type frameworks, and subclass of covalent organic frameworks. The introduction of bidentate ligands of the polypyridyl class, for example bipyridine, increases the channel size and creates anchor sites for metal complexes, such as the Ru-polypyridyl complex.

CTFs are an especially promising class of COFs known to be thermally and chemically stable.[35, 99, 341–353] They are 2D nanoporous frameworks made upon the trimerization of aromatic nitriles (see Figure 3.10).[351] CTFs are particularly interesting to anchor photocatalytic complexes, as they are much lighter than most other nanoporous materials and do not possess toxic or environmentally unfriendly elements. In addition, 2D heterostructures have attracted widespread attention thanks to their compelling properties, which are useful for many potential applications.[354]

The modular nature of the CTFs further allows to create suited anchor sites by incorporation of an attractive class of functional linkers, the polypyridyl class (see Figure 3.10 and 3.11). These linkers contain nitrogen moieties which can act as a docking site for different molecular complexes and more importantly our Ru-polypyridyl complex. The complexes can therefore be structurally anchored onto the scaffold, giving the advantage of potential

high metal loadings and reusability of the catalyst. Furthermore, the creation of such favorable docking sites – e.g. the bipyridine linker – within the covalent organic framework causes the molecular complexes to preferentially anchor on these sites, and hence be spatially separated.

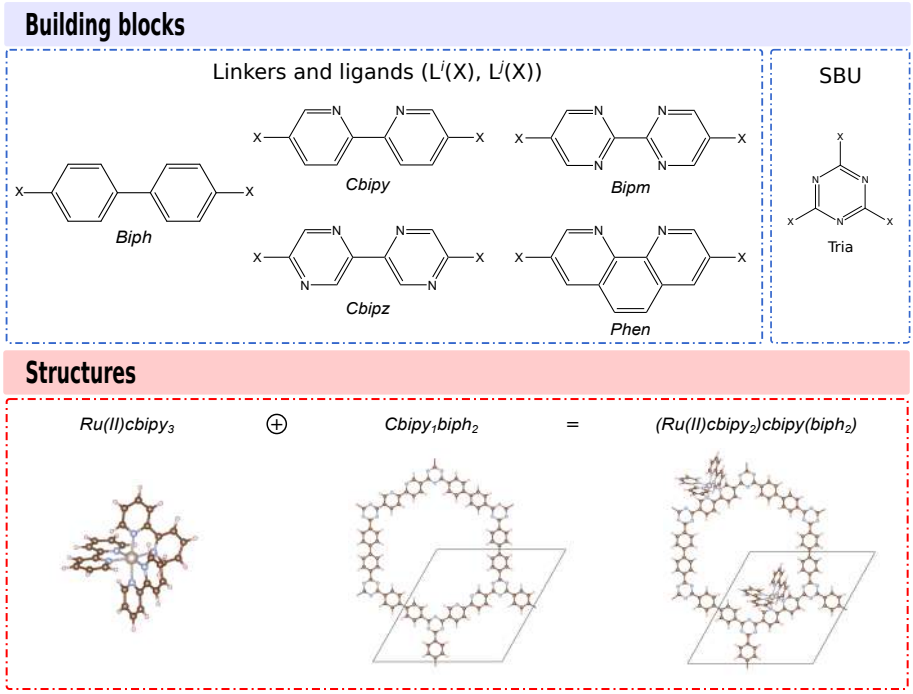

Figure 3.11: Covalent triazine frameworks where different polypyridyl linkers introduce appropriate anchor sites for the Ru-polypyridyl complexes. Four experimentally available bidentate nitrogen-containing linkers were considered, cis-bipyridine (cbipy), phenanthroline (phen), cis-bipyrazine (cbipz), and bipyrimidine (bipm), as well as their monodentate trans configurations (tbipy, tbipz). Adapted from **Paper III [Ref. 146]** with permission of the Royal Society of Chemistry.

The Ru-polypyridyl complexes, Ru(II)L$_3$, on the other hand, consists of a Ru(II) cation chelated by three hetero-aromatic azines (L$_3$) - bipyridine the most studied - and are interesting photoactive catalysts. The bidentate ligands, part of the polypyridyl class, make them particularly attractive as they can be easily introduced inside the CTF (see Figure 3.10 and 3.11). The photoactivity of these complexes, on the other hand, is caused by their long-lived metal-to-ligand charge-transfer (MLCT) state induced by light absorption (see Figure 3.12).[355] This MLCT and resulting availability of the

excited electron on the ligands enables its good performance as catalytic center, where it triggers oxidation or reduction reactions in surrounding systems.[39, 355–361] Proven photoredox applications include carbon dioxide reduction,[362, 363] solar cell development,[364] water splitting,[365–368] as well as Diels-Alder cycloadditions.[38]

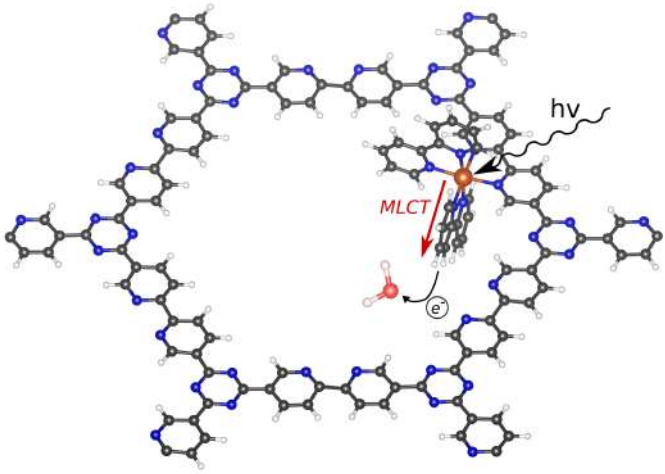

Figure 3.12: Possible charge transfer within the Ru(II)L_3@CTF heterogeneous photocatalyst. The photoactive Ru(II)L_3 is excited by light ($h\nu$) in which the excited electron is transferred toward its surrounding ligands, the metal-to-ligand charge transfer (MLCT). The excited electron on the ligands subsequently acts as a catalytic center, where it triggers oxidation or reduction reactions.

The combination of the Ru(II)L_3 complex and the CTF scaffold form the Ru(II)L_3@CTF heterogeneous photocatalyst which could contain the perfect ingredients for a heterogeneous photocatalyst: robust catalytic sites, high stability as well as efficient mass transport through it pores. Furthermore, the combined Ru(II)L_3@CTF heterogeneous photocatalyst has a larger versatility than the isolated complex as both the framework and the Ru(II)L_3 complex can be varied. In addition, it makes it possible to obtain asymmetrically surrounded Ru(II)L_3 complexes in a rather natural way.

We focussed on obtaining insight in the charge transfer (see Figure 3.12) as well as the light absorption and redox properties of the heterogeneous photocatalyst. To investigate this point, we first varied the bidentate moieties in both the isolated Ru(II)L_3 complex and the sole CTF support. The conducted research therefore assesses to what extend the OESE principle is valid

in both COFs and photoactive complexes. Furthermore, the heterogeneous photocatalyst Ru(II)L_3@CTF can be identified with a MOF-like structure where the inorganic nodes (the complexes) are connected by organic linkers (the framework). We will elucidate to what extent the OESE principle is observed when considering these as its building blocks and therefore deduce to what extent the favorable electronic properties of Ru(II)L_3 complexes are maintained upon anchoring. Lastly, we will use the OESE principle to predict that, depending on the composition of the system, the complex and the scaffold, the MLCT can be guided[369] either to the framework or to the pore of the material, producing a versatile photocatalyst for either interface- or pore-driven photocatalytic applications. The OESE principle is therefore used as a design tool, similar as in the case of UiO-66, to construct a better photocatalytic complex@COF compound in a more rational and efficient way.

3.3.1 The Scaffold: CTF

In order to use CTF as a support material, bidentate nitrogen-containing linkers similar to the chelating ligands of the Ru(II)L_3 complex should be present in the framework (see Figure 3.10 and 3.11). We start from a biphenyl-based CTF,[370] which we will refer to as CTF-1-2R[145] (the name CTF-2, which has also been used for this material[370] was originally proposed for a naphthalene-based structure[371]). Note that CTF-1-2R intrinsically has some photocatalytic activity.[370] We then replace a number of biphenyl (biph) linkers with polypyridyl ones suited to anchor the Ru(II)L_3 complex (see Figure 3.11 for their nomenclature within this PhD thesis). Hug et al. recently synthesized such a CTF-1-2R containing a 2-2'-bipyridine (bipy) linker.[343]

We modeled the resulting nitrogen-containing CTFs by considering single CTF-1-2R monolayers, which contains three biph linkers and two triazine (tria) secondary building blocks (SBU) per unit cell (see Figure 3.11). The influence of multilayer stacking is therefore not taken into account. We replaced in each layer one, two or three of the biph linkers by a particular polypyridyl one (L^i), forming a modified CTF-1-2R suitable to anchor the Ru(II)L_3 complex. We will refer to a given CTF in terms of its constituent linkers, e.g. $biph_3$ for CTF-1-2R and $L^i_n biph_{3-n}$ for the modified systems with n the number of replaced biph linkers. The systematic and controlled inclusion of polypyridyl linkers within the CTF allows us to assess the influence of the nitrogen content and the specific building blocks included on the CTF's electronic structure. The work of Wang *et al.* moreover indicates that it is indeed possible to make such mixed-linker CTFs.[372]

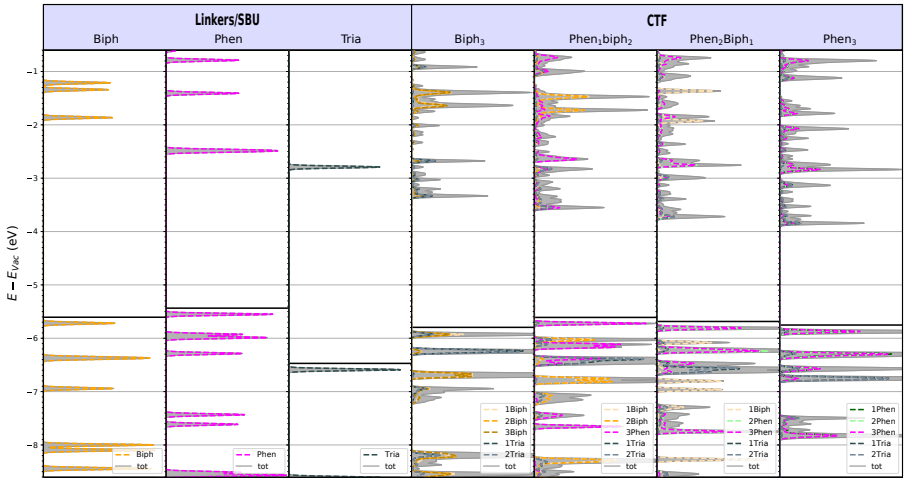

Figure 3.13: Densities of states of CTF-1-2R doped with 1, 2 or 3 phenanthroline linkers ($\text{phen}_n\text{biph}_{3-n}, n = 0, 1, 2, 3$) compared to the electronic structure of the hydrogen-terminated constituents (biph, phen, tria). The DOS are aligned with respect to the vacuum energy. Adapted from **Paper III [Ref. 146]** with permission of the Royal Society of Chemistry.

The electronic structure for a few considered CTFs are shown in the right panel of Figure 3.13 (see **Paper III [Ref. 146]** and its supporting information for a full overview). The decomposition with respect to the building blocks shows the appearance of both localized and delocalized states. The delocalized states, which include the conduction band minimum (CBM), are spread out over the entire structure and agree well with the traditional solid-state concept of an energy band (see Chapter 1, Section 1.1.2). In contrast, there are also localized states, such as the top of the valence band, which are characterized by sharp peaks in the DOS. The corresponding orbitals are confined to individual components of the CTF and retain a more discrete, molecular character.[57, 111, 152] The top of the valence band is therefore classified as a HOCO (see Section 3.1). Strikingly, the energy and shape of these localized electron levels are very similar to those in the CTF constituents (see Figure 3.13, left panel). This suggests that some features of the linkers are maintained when incorporating them into the aromatic system of the CTF. Hence we observe to some extend the OESE principle for COFs in a similar way as for MOFs,[110, 111] i.e. the ability to tune the overall electronic structure by independently varying the different constituents.

Finally, Figure 3.13 illustrates that the electronic structure of CTF-1-2R can

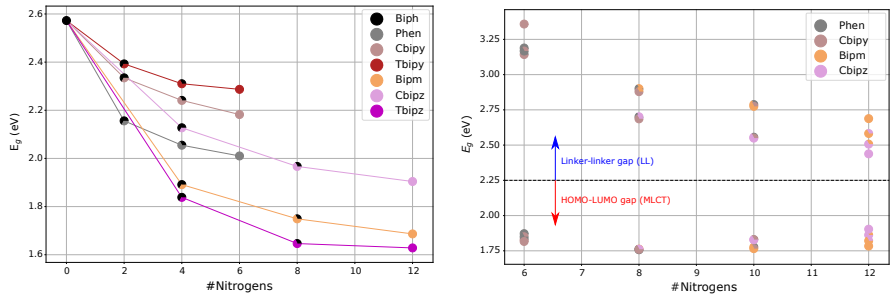

(a) CTF **(b)** Ru(II)L$_3$

Figure 3.14: Band gap of the CTF as a function of the number of linker nitrogen atoms per unit cell (a). HOMO-LUMO gap (LMCT) and analogous linker-linker gap (LL) of the Ru(II)L$_3$ complex with respect to the number of nitrogen atoms in the complex (b). Each data point is colored in three parts, which represent the composition of the CTF scaffold or Ru(II)L$_3$ complex. Adapted from **Paper III [Ref. 146]** with permission of the Royal Society of Chemistry.

be modified by doping it with nitrogen-containing linkers. Although the position of the HOCO relative to the vacuum energy remains fairly independent of the nitrogenous character of the framework, the CBM systematically lowers if it is increased (see Figure 3.13). As a result the band gap decreases. The band gap is plotted for the various materials in terms of the nitrogen content in Figure 3.14a. The behaviour of the conduction band minimum is found to be inherited from the individual linkers, indicating that the OESE principle even count for the delocalized band, which is in line with current literature on similar nitrogen-based organic frameworks.[52, 79, 373] It is caused by the inclusion of nitrogen atoms within the aromatic ring which leads to a π-electron-deficient system. The framework (or linker) will therefore accept electrons more easily. The resulting band gap may be more suitable for photocatalysis compared to its non-functionalized analogue.[52, 79, 335, 336, 370, 371] In addition, the dependence of the band gap on the nitrogen content may be relevant during photocatalysis as it could favor the transport of excited electrons from the photocatalytic complex to the framework (see further).

3.3.2 The Photoactive Complex: Ru(II)L$_3$

Essential to the photocatalytic performance of the envisioned heterogeneous photocatalyst is the activity of the Ru(II)L$_3$ complex. Similar to the CTF

scaffold, several nitrogen-containing ligands can be considered to further tune the properties of this complex (see Figure 3.11). Ru(II)L_3 complexes used for homogeneous photocatalysis consist of three bidentate nitrogen-containing ligands for which generally two or three are equal.[39, 355, 357–359] We will denote these complexes as Ru(II)$L_2^j L_1^i$, with the most prominent example being Ru(II)cbipy$_3$. When embedded into the CTF, the L^i linker is shared between the framework and the complex, while the other two chelating ligands L^j extend into the pore. Therefore such mixed-ligand complexes are here almost introduced in a natural way and allow us to tune the photocatalytic activity in much more detail.

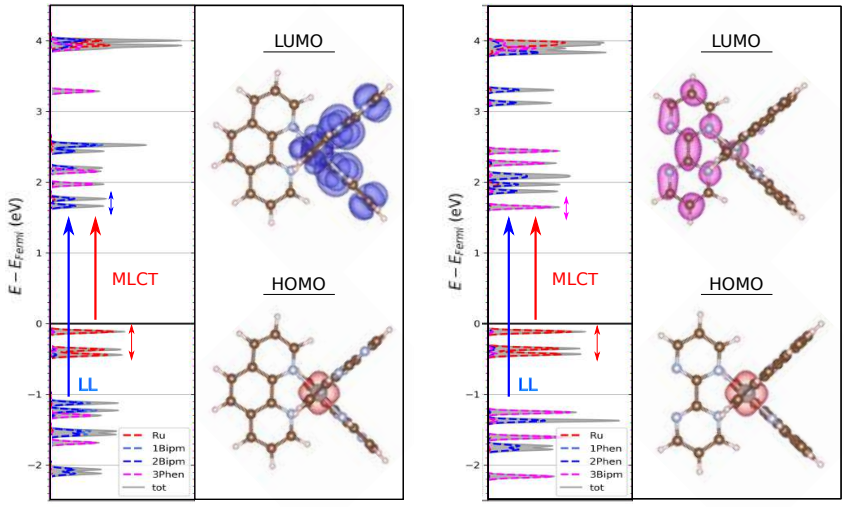

(a) Ru(II)bipm$_2$phen$_1$ **(b)** Ru(II)phen$_2$bipm$_1$

Figure 3.15: Metal-to-ligand (MLCT) and ligand-ligand (LL) transitions in Ru(II)bipm$_2$phen$_1$ (a) and Ru(II)phen$_2$bipm$_1$ (b) together with the corresponding orbitals. Adapted from **Paper III [Ref. 146]** with permission of the Royal Society of Chemistry.

The electronic structure of such Ru(II)L_3 complexes (see Figure 3.15) indicates that the HOMO is centered on the Ru^{2+} ion and corresponds to a t_{2g} state of an octahedrally surrounded complex. The LUMO, on the other hand, is located on the chelating ligands with the highest nitrogen content and thus highest electron affinity (see **Paper III [Ref. 146]** and its supporting information for a full overview). The HOMO-LUMO gap therefore represents a qualitative measure of the MLCT, which is one of the key properties in the photocatalytic process. The nitrogen dependence of the LUMO's location moreover allows tuning the MLCT to a specific ligand, which is of interest

when anchoring the complex to a CTF. Furthermore, this larger reduction potential of Ru(II)L_3 complexes with increasing nitrogen content was also observed experimentally.[355]

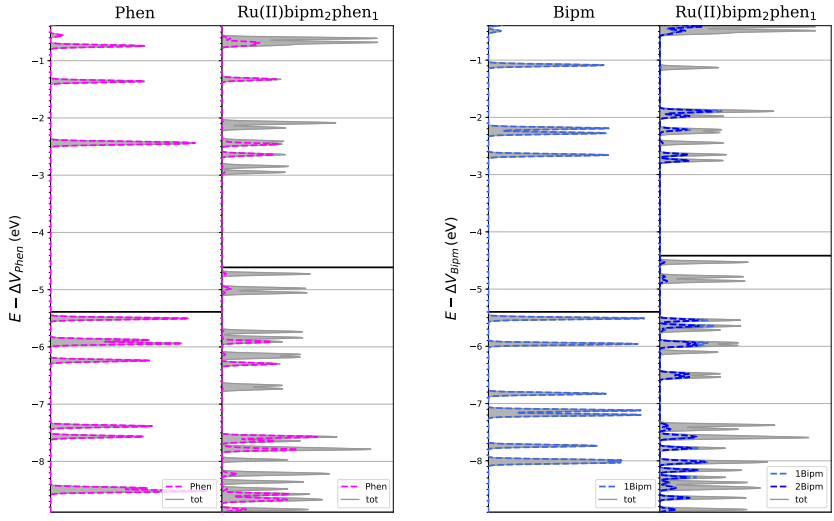

(a) Phen vs. Ru(II)bipm$_2$phen$_1$ **(b)** Bipm vs. Ru(II)bipm$_2$phen$_1$

Figure 3.16: Densities of states displaying how the properties of the chelating ligands are transferred to the Ru(II)L_3 complex. The electronic structures are aligned based on the average core potential of the phen (a) or bipm (b) ligands/linkers respectively. Adapted from the supporting information of **Paper III [Ref. 146]** with permission of the Royal Society of Chemistry.

When we further compare the electronic structure of the Ru(II)L_3 complex to its building blocks (see Figure 3.16) we see that, similar to CTFs (see Figure 3.13), its electronic structure can to a large extent be considered as a superposition of them. Therefore, even here the concept of OESE can be introduced. As the Ru(II)L_3 complex contains the same type of ligands/linkers as the CTF, its electronic structure moreover evolves in a similar way as a function of the nitrogen content. Indeed, the lowest unoccupied linker state lowers as the nitrogen content increases, while the highest occupied linker state remains rather constant. This leads to an overall decrease of the ligand-ligand (LL) gap with increasing nitrogen content (see Figure 3.14b and 3.15). On the other hand, the HOMO is now a Ru-based state and lowers as much in energy with nitrogen content as the LUMO. As shown in Figure 3.14b, this gives rise to a fairly constant HOMO-LUMO gap. Hence, the absorption

behaviour is similar across the different mixed Ru(II)L_3 complexes, although the redox potential is changing. This feature makes our Ru(II)L_3 complexes an interesting set for photocatalysis as it allows adapting both the direction of the MLCT and the chemical activity while targeting the same range of absorption wavelengths.

3.3.3 The Heterogeneous Photocatalyst: Ru(II)L_3@CTF

Both the CTF scaffold and the homogeneous Ru(II)L_3 photocatalyst display interesting properties for photocatalytic purposes. They can be combined in numerous ways, which enables fine-tuning the material beyond what is possible in the individual constituents. Such metal-functionalized COFs may be produced either post-synthetically or by using prefunctionalized linkers during the CTF synthesis.[39, 374] We therefore consider the electronic properties of a systematic subset of heterogeneous photocatalysts, (Ru(II)L_2^j)L_1^i(L_n^ibiph$_{2-n}$) with $n = 0, 1, 2$ combined out of a Ru(II)$L_2^j L_1^i$ complex anchored on a L_{n+1}^ibiph$_{2-n}$ CTF (see **Paper III [Ref. 146]** for more details).

The electronic structures of Ru(II)L_3 complexes show that they combine a band gap in the visible spectrum with an intrinsic charge transfer by light absorption. The combined Ru(II)L_3@CTF photocatalyst will only be promising if these advantages remain intact. A first requirement is that the electronic structure of the complex within the photocatalyst should not differ too much from that of the isolated one. Figure 3.17b and 3.18 illustrates that the energy levels of the isolated Ru(II)bipm$_2$phen$_1$ complex (left panel) are indeed retrieved when anchoring it onto a phenanthroline-containing framework (right panel) (see the supporting information of **Paper III [Ref. 146]** for further examples). Furthermore, Figure 3.18 shows that the redox potential of the complex remains almost unaltered, indicating that the heterogeneous photocatalyst may be applied to the same reactions as the homogeneous one. Moreover, besides the states of the Ru(II)L_3 complex, also those of the CTF are recovered (see Figure 3.17a). This demonstrates that the principle of OESE is also applicable on the combined Ru(II)L_3@CTF catalyst where the building blocks are considered to be the CTF and the Ru(II)L_3 complex.

A second point of attention is the electronic structure near the band gap. We showed in section 3.3.2 that the Ru(II)L_3 complex has a Ru-centered HOMO and a ligand-based LUMO. When anchored, the HOCO moves toward a non-anchoring CTF linker state (see Figure 3.18). Excitation from this level towards the complex's surrounding ligands, which we called crystal-to-crystal charge-transfer (CCCT) or crystal-to-ligand charge-transfer (CLCT) type, are spatially separated from the Ru^{2+} ion. More elaborate studies showed that

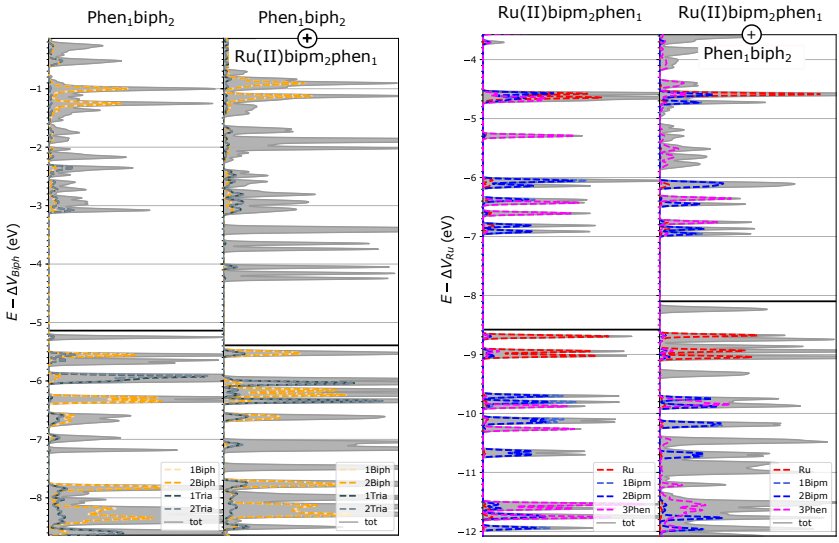

(a) CTF vs. CTF+Ru **(b)** Ru vs. CTF+Ru

Figure 3.17: Densities of states displaying how the properties of the CTF (a) and the Ru(II)L$_3$ complex (b) are transferred to the combined Ru(II)L$_3$@CTF heterogeneous catalyst. The electronic structures are aligned based on the average core potential of the biph linkers (a) or the Ru atom (b), respectively. Adapted from the supporting information of **Paper III [Ref. 146]** with permission of the Royal Society of Chemistry.

they have a possibility of occurring (see Paper **Paper IV [Ref. 146]** for more details) and are discussed in Section 3.4. Here, however, we instead focus on MLCT excitations of the anchored Ru(II)L$_3$ separately, which we find to display the same trends as the isolated Ru(II)L$_3$ complex further confirming the OESE principle. Indeed the LUCO and the Ru levels again decrease as a function of the nitrogen content of the Ru ligands while the highest occupied ligand states remain more or less fixed (see **Paper III [Ref. 146]** for more details). As a result, the MLCT gap remains fairly independent of the used ligands, while the LL gap decreases with nitrogen content. These findings again suggest that the Ru(II)L$_3$ complex retains its photoredox properties when it is heterogenized in the CTF. The heterogenized photocatalyst may therefore be suited for similar reactions as the isolated complex.

Although the general electronic properties of the Ru(II)L$_3$ complex are maintained, heterogenizing the Ru(II)L$_3$ complex onto the CTF does have some interesting consequences that can not be explained solely form the isolated

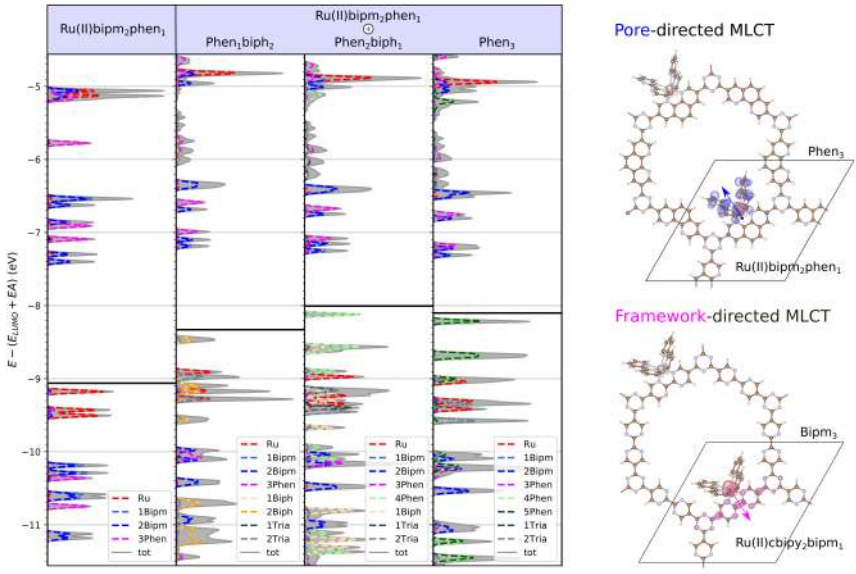

Figure 3.18: Electronic states of the Ru(II)bipm$_2$phen$_1$ complex in vacuo and when anchored on a phen$_n$biph$_{3-n}, n = 1, 2, 3$ framework (left). Depending on the Ru(II)L$_3$ complex and CTF scaffold, the charge transfer upon light absorption can be directed toward the pore or the framework (right). Adapted from **Paper III [Ref. 146]** with permission of the Royal Society of Chemistry.

constituents (Ru(II)L$_3$and CTF). These effects represent deviations from the ideal OESE principle. The most prominent effect is the introduction of a CTF-centered HOCO, as mentioned above. A second result is visible for the unoccupied states (see Figure 3.18a). Not only is the electron affinity increased as a function of the CTF nitrogen content, but this affects the anchoring linker differently from the linkers dangling into the pore. It may even lead to a change in energy ordering between the different unoccupied ligand orbitals (see the supporting information of **Paper III [Ref. 146**] for such examples). In that case, an MLCT-excited electron from the Ru(II)L$_3$ complex may change its charge-transfer direction compared to the isolated cluster, i.e. toward the framework rather than the other two (pore) ligands.

Anchoring the Ru(II)L$_3$ complex to a CTF does not appear to undermine its photoactivity nor the redox potential and thus the redox reactions to which it can be applied. On the contrary, modifying the CTF linkers provides an addi-

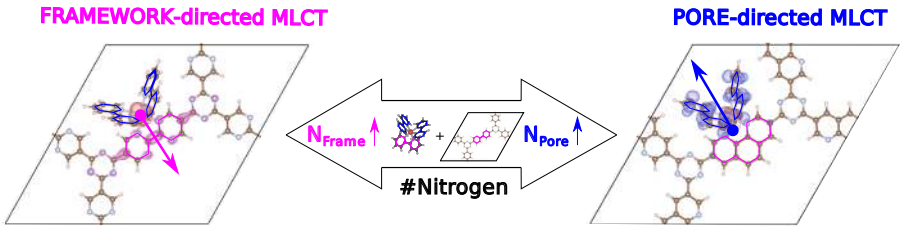

Figure 3.19: The charge transfer of light-excited electrons can be guided towards the framework or the pore by rationally designing the nitrogen content of the scaffold linkers and complex ligands. Adapted from **Paper I [Ref. 111]** with permission of the American Chemical Society.

tional degree of freedom to tune the electronic response of the photocatalyst. By varying the polypyridyl linkers in the CTF or the corresponding ligands in the Ru(II)L_3 complex, the redox potential of the catalyst can be altered by about 1 eV. This versatility is useful to further optimize Ru(II)L_3 complexes for sustainable applications, such as water splitting[368] and carbon dioxide reduction.[363] In addition, carefully selecting both the complex and CTF components allows the design of a guided metal-to-ligand charge-transfer (see Figure 3.18). In a mixed Ru(II)L_3 complex the MLCT is directed toward the ligand with the highest nitrogen content (see Figure 3.19). When combined with the CTF, a higher nitrogen content of the framework favors a MLCT toward the anchoring linker. If the photocatalytic operation requires excitation to the framework, the nitrogen content should therefore be high in the CTF and low for the ligands in the pore (e.g. (Ru(II)cbipy$_2$)bipm(bipm$_2$)). In contrast, MLCT toward the pore can be achieved by keeping the nitrogen content of the framework at a minimum and using highly nitrogenous moieties for the pore ligands (e.g. (Ru(II)bipm$_2$)phen(phen$_2$)) (see **Paper III [Ref. 146]** for more details).

3.4 Extension: Exited-State Properties

In this last section we discuss how insights on the electronic structure obtained from regular DFT calculations can be complemented by performing TD-DFT calculations (see Chaper 2, Section 2.3). TD-DFT calculations allow to investigate materials in the presence of time-dependent electric or magnetic fields.[192] It is therefore able to extract the excitation energies, response properties and photoabsorption spectra of molecules and solids as well as the oscillation strength in a more rigorous framework. This makes TD-DFT

calculations interesting for our photocatalytic systems. However, literature as well as our own calculations (see further) have shown that DFT electronic structures, such as those discussed previously, display qualitatively the same trends as TD-DFT. Nevertheless, to extract the excited-state properties more quantitatively TD-DFT should be used. The downside of TD-DFT is that it is computationally more demanding and calculations on periodic materials remain difficult even with current progress in algorithms.[375, 376] Only recent advances, such as time-dependent density-functional perturbation theory (TD-DFPT) have been able to quantitatively calculate the excitation spectrum of periodic materials.[101] Within the framework of this PhD thesis, additional TD-DFT calculations were performed on isolated clusters of the material, which were validated to be sufficiently large to give a reliable representation of the periodic structure.

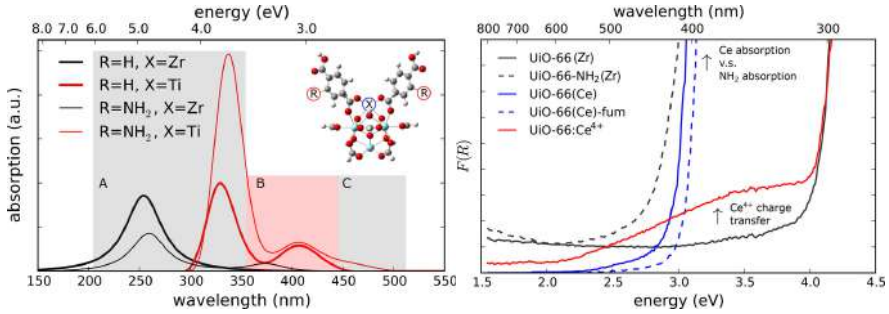

Figure 3.20: (a) TD-DFT absorption spectra (B3LYP/6-311+G(d,p), 30 states) for extended cluster models. The basic cluster model has a stoichiometry of $Zr_5XO_4(OH)_4(HCOO)_10(BDC\text{-}R)_2$ with R = H and NH_2 and X = Zr and Ti (inset). (b) UV/vis spectra in Kubelka–Munk units of a series of different Ce^{4+} UiO samples compared to pristine UiO-66(Zr) and UiO-66-NH_2(Zr). Adapted from **Paper II [Ref. 109]** with permission of the American Chemical Society.

In prior work performed by Hendrickx et al.[110] such cluster calculations on the building blocks of UiO-66(Zr) were already performed. There it was observed that the DFT and TD-DFT results qualitatively agreed with each other as well as with the DFT calculations performed in **Paper I [Ref. 111]**. In **Paper II [Ref. 109]** we extended this work by performing TD-DFT calculations on the building blocks of UiO-66 where both lanthanide, titanium and hafnium were incorporated within the inorganic node as well as amino functionalized linkers (see Figure 3.20a for Ti and Zr). More specifically these TD-DFT calculations resulted in the excitation spectrum and the transition

probabilities which were used to investigate the charge transfer within these materials. Corresponding experiments were conducted by the group of Prof. Van Der Voort which whom we have an ongoing collaboration. Note that we assume that the dopant ions are inserted in the metal node. However, whether dopant ions are inserted on a Zr position or are adsorbed at a defect site is still subject of much debate.[377] Direct proof however is very hard to obtain and this matter still remains open for discussion.

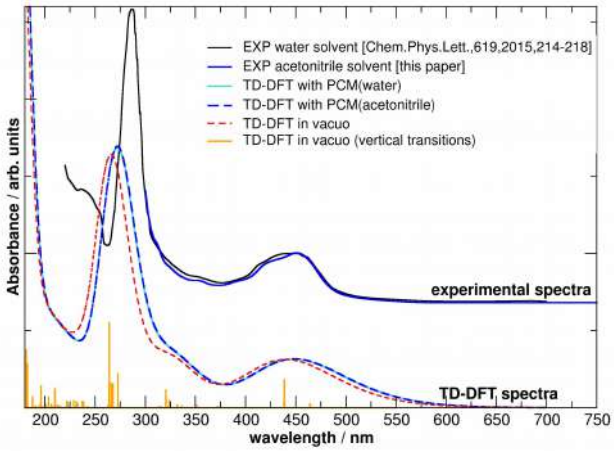

Figure 3.21: Experimental and computational UV-vis absorption spectra (bottom) of Ru(II)bipy$_3$. Vertical excitations for the in vacuo TD-DFT spectrum are reported as orange spikes. Computed spectra using TD-DFT have been smoothed using Gaussian functions of half-width at half-height of 0.333 eV (default value of Gaussview). Adapted from **Paper IV [Ref. 378]** with permission of the American Chemical Society.

When we look at the TD-DFT spectra of inorganic Hf-doped node we see an almost identical spectrum as that of the pristine Zr node. Furthermore, the insertion of Ti caused a shift to lower excitation energy in the TD-DFT spectrum which agreed well with the experimental shift in the absorption edges. The oscillator strength of this transition further increased when more Ti atoms are incorporated within the cluster. Finally, in the amino-functionalized material a transition between the aromatic ring of the linker and a Ti 3d orbital was observed in an extended cluster model (see Figure 3.20a). This transition can be seen as a long-range charge transfer and gives an indication as to why amine-functionalized UiO-66:Ti^{4+} system shows the largest photocatalytic activity reported in literature.[301, 310] These observations were in line with previous DFT calculations in **Paper I [Ref. 111]** as well as those in **Paper II [Ref. 109]** where

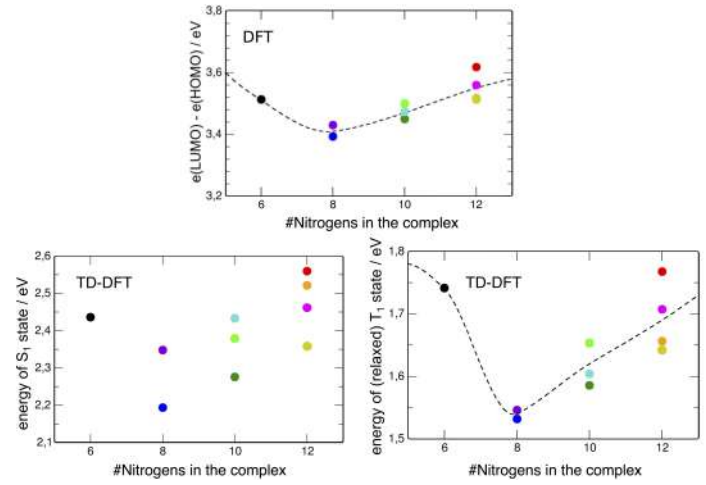

(a) Ru(II)L_3

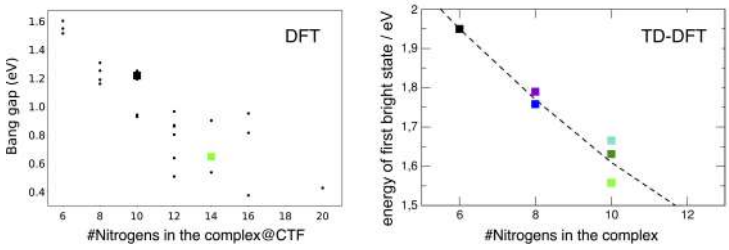

(b) Ru(II)L_3@CTF

Figure 3.22: Comparison between the DFT and TD-DFT calculations. (a) The Ru(II)L_3 complex, the HOMO-LUMO gaps (DFT), the vertical energies of the S1 states (TD-DFT, left) and the optimized T1 states (TD-DFT, right) as a function of the number of nitrogen atoms in the complex. (b) The Ru(II)L_3@CTF, the HOCO-LUCO gaps (DFT) and the strongest excitation energy (TD-DFT) shown as a function of the number of nitrogen atoms in respectively the complex and the complex@CTF. Calculation carried out at the M06/LanL2DZ level of theory. Adapted from **Paper IV [Ref. 378]** with permission of the American Chemical Society.

the inclusion of Ti causes an overlap between the Ti 3d and the linker orbitals, suggesting a better charge transfer and lower excitation energy. This remains true when the Ti is absorbed as a defect site as seen in the work by Santaclara et al.[377] The amine-functionalized linker introduces additional occupied linker state in the band gap which facilitate this transition even

further.

Additionally UiO-66 was examined both computational and experimentally when doped with lanthanides. However, since the behavior of Ln ions is notoriously difficult to predict with DFT, we only performed UiO-66(Ln) calculations with Ce^{4+} where it has been shown to provide reasonable qualitative results.[320, 321] No TD-DFT calculations were performed for UiO-66 doped with Ce, however, the experimental UV/vis spectra of a series of different Ce^{4+} were measured (see Figure 3.20b). As seen a reduction of the excitation energy is seen which can be linked to the DFT results where a band, which consists of the 4f orbitals, is introduced within the band gap of UiO-66 (see Section 3.2.2, I.). The occurrence of these 4f levels in the band gap of UiO-66 indicates that Ce can take different charge states depending on the Fermi level location and that a charge-transfer, measurable by optical spectroscopy, is to be expected. Indeed, the empty 4f band within the band gap of the pristine UiO-66 is energetically reachable for an electron that has been excited to the linker's LUCO via an energy-transfer process. The predicted location of the 4f band shows a good correspondence with the thermodynamic (3+/4+) charge-state transition level (see Section 3.2.2).

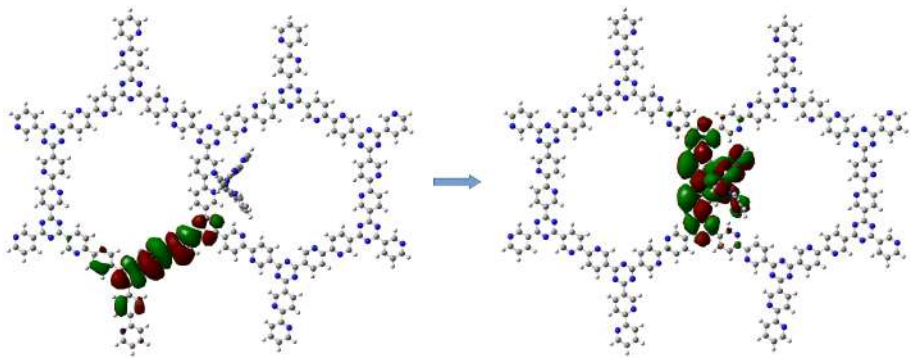

Figure 3.23: Orbitals involved in the first allowed transition in Ru(II)L_3@CTF, more specifically, a Ru(II)cbipy$_3$ complex anchored on a cbipy$_2$tbipy$_1$ framework. Calculation carried out at the M06/LanL2DZ level of theory. A crystal-to-crystal charge transfer (CCCT) or crystal-to-ligand charge transfer (CLCT) type is seen with nonvanishing oscillator strength. Adapted from **Paper IV [Ref. 378]** with permission of the American Chemical Society.

The fact that TD-DFT is able to extract the excitation energies was also used in **Paper IV [Ref. 378]** to deduce the absorption spectrum of Ru(II)L_3 (see Figure 3.21) where a good correspondence with the experimental spectrum

is observed. Furthermore, the same complexes were calculated as in Section 3.3.2 but with an other level of theory, M06/LanL2DZ, displaying the same trends as in **Paper III [Ref. 146]** and therefore additionally confirming it. DFT calculation were also compared to TD-DFT calculations for the isolated ruthenium complex (see Figure 3.22a). Similar as for UiO-66 the results of the TD-DFT calculation showed a similar trend with those of DFT.

The heterogeneous catalyst Ru(II)L_3@CTF was also studied in **Paper IV [Ref. 378]** by means of TD-DFT. Here cluster models were constructed using the periodic optimized structures of **Paper III [Ref. 146]**. Only a subset of the structures were examined using TD-DFT for which the general trend is similar to the one predicted by DFT (see Figure 3.22b). Furthermore, the non-vanishing oscillation strengths of excitations for crystal-to-crystal charge-transfer (CCCT) or crystal-to-ligand charge-transfer (CLCT) transitions (see Figure 3.23 and Section 3.3.3), also observed in our DFT calculation of **Paper III [Ref. 146]**, shows that they are accessible (see Figure 3.23).

4

Conclusions and Perspectives

Begin thus from the first act, and proceed; and, in conclusion, at the ill which thou hast done, be troubled, and rejoice for the good.

Pythagoras of Samos (570 – 495 BC)

4.1 Conclusions

Our society is confronted with the major challenge of providing a more sustainable and clean energy system in view of the growing population and climate change. Sunlight is abundantly present and freely available as energy source, however, its efficient use in photocatalytic devices is today hampered by the lack of materials which can operate in a large part of the solar spectrum, which are efficient, robust and highly active. However, the design of photoactive devices that efficiently harness sunlight is a cornerstone in the transition to a sustainable economy, for example to generate hydrogen gas through water splitting or reduce carbon dioxide.

Nanoporous materials with well-defined pores and active sites which allow efficient diffusion of reactant and products are very important in the field of heterogeneous catalysis. They can potentially play a very important role in the development of next generation photocatalytic materials, provided that their electronic structure can be engineered to yield the desired optical

properties. Within this PhD thesis we studied modular nanoporous frameworks, which are built from distinct chemical building blocks that can be tuned or replaced at will. This allows the introduction of several specialized functionalities. Moreover, the modular structure of these materials gives rise to an astronomical number of possible design choices. In this sense, nanoporous frameworks are extremely interesting for the design of next generation photocatalytic devices. However, the huge combinatorial space associated with nanoporous frameworks is also prohibitive for any sort of rational design. Therefore, within this PhD thesis we have unravelled how the electronic properties can be tuned based on the knowledge of their building blocks. This new strategy to regulate the electronic properties was coined *Orthogonal Electronic Structure Engineering* (*OESE*) and is based on the observed decoupled contributions of the electronic structure of the building blocks, where altering one part of the structure does not influence the electronic response to the other part, allowing modular tuning. This new paradigm brings us closer to a rational design of new high-efficiency photocatalysts.

Proof of concept for the OESE principle was given for the UiO-66 metal-organic framework (MOF). MOFs are modular materials that have attracted enormous attention from the scientific community in the last decades thanks to their versatility of construction from various inorganic (nodes) and organic (linkers) building blocks. UiO-66(Zr) is a zirconium based MOF with high connectivity, which attracted a lot of attention as it is very stable under various conditions. For UiO-66(Zr) we showed that the electronic contributions of the various components could essentially be superposed. Quasiparticle energy levels associated with metallic nodes and organic linkers could clearly be distinguished, and the electronic structure of the material could be described as a sum of independent constituents. Several observations in literature support this conclusion, indicating a lack of electronic coupling between components in MOFs and in modular materials in general.

Furthermore, the OESE principle allows a substantially more efficient design of potential photocatalytic materials, as information on the electronic structure of the target material can be predicted from its building blocks. In this respect we focused on both the light absorption as well as the photocatalytic activity. In the case of UiO-66 the pristine material shows a too large band gap for visible light absorption and an inefficient ligand-to-metal charge transfer (LMCT). Due to the orthogonality of the electronic structure in the building blocks of this modular material, both problems can be targeted separately. The band gap can be efficiently reduced by incorporation of amino functionalized linkers (electron donating groups), effectively reducing the absorption energy ΔE_{abs}, while the efficiency of LMCT, determining its catalytic activity after excitation, can be increased by

incorporating different metals within the inorganic node, effectively reducing ΔE_{LMCT}. The latter was investigated by incorporation of isovalent atoms (Zr, Hf, Ti). It was concluded that only Ti improves the LMCT due to the overlap between the Ti 3d orbitals with the unoccupied linker states. This is in line with experimental results. Furthermore, we extended the search towards the incorporation of lanthanides, known for their interesting light-based and catalytic properties. Our experimental partners at the COMOC group developed a microwave-assisted metal-exchange methodology to construct a series of doped UiO-66 frameworks (Hf, Eu, Yb, Nd, Ce) allowing post-synthetic metal-exchange much faster than with conventional methods, from 5 days to 4 hours. When theoretically evaluating these Ln-doped materials, cerium insertion in the node was found to introduce an empty 4f band within the pristine UiO-66(Zr) band gap, which also gives rise to an efficient LMCT. Based on the invariance of the lanthanide series on its chemical environment similar charge-state transition levels were deduced for Yb and Eu, suggesting that these lanthanides can be used to increase the photocatalytic activity as well. However, the use of such lanthanide doped UiO frameworks for photocatalysis is still in its infancy. Only a few experimental studies have measured the photocatalytic activity of Ce doped MOFs where an increase of activity was seen.[379, 380] In addition it was very recently discovered that the photocatalytic activity, and thus the LMCT, can be further increased by mixed Ti^{+4}/Ce^{+4} clusters due to the synergy of the low lying 4f states of Ce^{+4} and the large overlap of Ti^{+4} with the unoccupied linkers states in UiO-66.[381] Therefore, we suspect an even more increased photocatalytic activity of the proposed lanthanides co-doped with Ti^{+4}. This hypothesis is interesting for further research.

As all crystals contain defects this is also the case for metal-organic frameworks and particularly for UiO-66. In general, a whole field developed within the MOF community about defect engineering, as it was found that defects are extremely important for the finally observed functional behaviour of MOFs. In particular for UiO-66 missing-linker defects can be intentionally created by the synthetic procedure, while retaining its stability. Within the field of defect engineering, the material's properties can be tuned by introducing defects in a controlled way. In the case of UiO-66 missing linkers create unsaturated metal sites which can be utilized as catalytic sites. For the development of next generation photocatalytic devices it is therefore important to know how defects alter the electronic structure. In this PhD thesis, we investigated in a systematic way how missing linkers alter the electronic structure and how they can be used to increase the photocatalytic activity. First, a clear notation was introduced to classify missing-linker defect structures, providing a transparent way of ordering

them. This notation characterizes altered node configurations within the defect structure introduced by missing linkers. Second, we showed that the local environment of the nodes affects the Zr unoccupied d-orbitals. The behaviour of the d-orbitals can therefore be deduced to a large extent from the node configurations present in the defect structure, helpfully indicated by our newly introduced notation. Moreover, the more linkers per node are removed, the more the d-orbitals lower in energy and the more the electron becomes localized near the site of the missing linkers. The observed lowering of the energy of localized Zr d-orbitals at the defect site effectively decreases ΔE_{LMCT} and improves the charge transfer to the node and therefore its photocatalytic activity. On the other hand, the linker states remain almost constant for all defect structures, preserving the absorption characteristics ΔE_{abs}. The effect of missing-linkers therefore corroborates the OESE principle.

To test the broader applicability of the OESE principle we considered another subclass of nanoporous materials, namely covalent organic frameworks (COFs), which was also inspired by the collaboration with our experimental partners at the COMOC and the SynBIOC group. COFs are a fairly new class of nanoporous materials which are also built in a modular way but solely from organic building blocks. These materials are currently explicitly investigated in literature for their electronic properties and stability. Their properties are induced by their strong, fully covalent nature causing both a high stability and electronic coupling. The latter provides a major challenge for the OESE principle and can therefore test to what extent it is valid. COFs are also interesting from a photocatalytic point of view. Although they lack an inorganic catalytic center, which seems to limit their activity compared to MOFs, their activity can be increased by incorporation of photocatalytic complexes. The assembly of a COF and a photoactive complex could merge some of the most important features of both organic framework (e.g. stability) and inorganic photocatalytic complex (i.e. catalytic properties). Furthermore, the thus created heterogeneous photocatalyst may open a new route toward the development of more efficient, environmentally friendly and robust heterogeneous photocatalysis.

To examine this concept, we have studied the heterogenization of Ru-polypyridyl complexes (Ru(II)L_3), a well known and efficient class of photocatalytic complexes, to covalent triazine frameworks (CTFs), which provide a robust and light-weight support, forming the heterogeneous photocatalyst (Ru(II)L_3@CTF). The anchoring of the molecular photoactive complex on the 2D nanoporous substrates creates a more sustainable catalytic system and may be tuned to the redox reaction of interest. CTF-anchored complexes therefore not only offer a large accessible surface, but also a promising

versatility toward functional catalyst design. We considered a wide range of different polypyridyl-based CTF monolayers and Ru(II)L_3 complexes and demonstrated that it is indeed energetically favourable to anchor the Ru complexes onto the CTF. However, an essential condition for an efficient heterogeneous photocatalyst is that the photoredox properties of the Ru-polypyridyl complex do not deteriorate when incorporated into the CTF scaffold. We confirmed that the electronic structure of both the Ru(II)L_3 complex and CTF stay mostly unaltered upon combining the two systems and that the redox potential of the photocatalytic complex remains largely the same. This behaviour was shown to be even more generally valid: the energy levels of both the unfunctionalized CTF and the Ru(II)L_3 complex are to a large extent made up of contributions from their individual components. This indicates that the principle of OESE is applicable within the CTF (COF) and Ru-polypyridyl complexes (molecular complexes) as well as for their combination.

Although the heterogenization of photocatalytic Ru(II)L_3 complexes is a valuable target as such, our study additionally showed that anchoring onto a CTF scaffold provides the system with an even broader tunability than before. Band gaps, charge-transfer reactions and redox potentials are all strongly adaptable by changing the nitrogen content of the different components of the photocatalyst. A higher nitrogen content typically lowers the energy of unoccupied polypyridyl levels and occupied Ru t_{2g} levels, while occupied linker or ligand states change only little. This behavior makes it possible to guide the light-induced charge transfer by increasing the nitrogen content of either the CTF (framework-directed MLCT) or the dangling Ru ligands (pore-directed MLCT). The versatility of CTF-anchored Ru(II)L_3 complexes therefore endows them with the capability to display a high photoredox activity for a wide range of target reactions and catalytic set-ups. The attained knowledge may therefore guide further research towards electronic structure engineering of anchored molecular species on a heterogeneous support generating a scaffold with desired functional properties.

To conclude, within this PhD we have coined the concept of orthogonal electronic structure engineering (OESE) stating that the electronic structure of modular materials can be deduced from decoupled contributions of their components. Proof of principle for the OESE was found in UiO-66 and covalent triazine frameworks as well as the molecular Ru-polypyridyl complexes. This paradigm furthermore provided a rational design strategy to tune the building blocks of these modular materials to increase their photocatalytic activity.

4.2 Perspectives

In this PhD thesis we have unravelled the electronic structure of two modular nanoporous frameworks (UiO-66 and CTF), a modular molecular complex (Ru(II)L_3) and the anchoring of such a complex on a scaffold (Ru(II)L3–CTF) based on the OESE principle. The OESE principle, therefore, offers a lot of perspectives for future rational design of electronic engineered materials.

The OESE principle disentangles the electronic effects of different parts of a modular structure into contributions from its building blocks and could make advanced levels of theory, such as Green's function theory, tractable for much larger sets of materials than is nowadays possible. The procedure, based on the OESE principle, could consist of performing high level calculations for the building blocks and using this information to obtain also the electronic structure of the composed crystal with high accuracy. This PhD thesis has introduced the OESE principle, but to use the principle to obtain high level electronic structures for a broad set of materials, we need accurate alignment and reconstruction procedures. Some techniques are already available to align band structures, but more advanced developments will most likely be necessary.

In addition to more accurate levels of theory for the electronic structures the OESE principle could be extended on a more fundamental level e.g. towards different theories/properties. In this PhD thesis the main theory used was density-functional theory (DFT). However, it would be highly valuable to investigate this principle for time-dependent density-functional theory (TD-DFT), focussing more on the optical response of the system. In this thesis we have observed that DFT and TD-DFT give qualitatively the same trend as also indicated in recent literature[382] and therefore this would be a first obvious extension. The independent effect of different building blocks might even be directly considered for the prediction of catalytic activity. Some of the present literature already indicated such trends in the form of a linear free-energy relationship (LFER).[76] These examples or ideas indicate that the OESE principle is more broadly applicable than only to the electronic structure and can guide further research to understand simple design rules to tune the properties of modular materials. However, considerable research is still necessary to achieve this.

Furthermore, the OESE principle formulated within this PhD thesis is based on a limited set of materials. Nevertheless, we envision that it can be generalized towards a broader class of modular materials. A first obvious

extension based on our proof-of-concept material UiO-66 would be MOFs with a 0D inorganic sublattice.[27] ZIFs, metal-organic frameworks with a topology similar as zeolites, have, for example, already shown to possess a relation between its linker and the band gap.[158] This property can be directly related to the OESE principle. As a second example, the applicability of OESE to CTFs could have a strong impact in the field of organic electronics. CTFs could be seen as an extension into a second dimension of one-dimensional conductive conjugated polymers that are at the hart of organic electronic. Very recently, the electronic structure of such two-dimensional π-conjugated organic frameworks, were theoretically investigated by Simil et al.[299] They showed, based on tight-binding theory, that non-dispersive flat levels are introduced similar as those seen in the CTF. However, they also showed that common knowledge in organic electrodes is not easily transferable to these periodic two-dimensional structures. Further research is therefore of high importance to understand these materials and their relation to the OESE principle. Thirdly hybrid organic-inorganic perovskites (HOIPs) form a very interesting class of modular materials for photocatalytic applications. They are mostly known for their record-high solar-cell efficiencies. Their 2D variants, which overcome the detrimental stability problems of 3D HOIPs, have been shown to exhibit a composite nature as a function of the inorganic layers and organic spacers. Similar as MOFs, which could be considered as a composite, it is observed that in these materials the electronic structure can be deduced from the electronic structure of its building block.[293–295] This therefore resembles the OESE principle which we have outlined within this PhD thesis. Each of these materials would benefit considerably from the rational design strategy offered by the OESE principle. We expect that design tools like the OESE principle, used to predict and tune the properties of modular materials, will be much more common in the materials of the future. This is especially the case for novel materials engineered using nano technology and made from building blocks.

Irrespectively of the large potential of the OESE principle it will not be valid for all modular materials. When the coupling between electronic levels in material's building blocks is strong, such as seen in the CTF framework, delocalized bands arise which can not be explained from the OESE principle. The OESE principle therefore works best if the electronic levels are to an extent decoupled and if clear building blocks can be defined. MOFs naturally fulfill these conditions, however, within CTFs this is less straightforward. Nonetheless, we have seen that even in these fully conjugated frameworks properties are still transferred if sufficiently isolated entities can be distinguished. The major problem is that the reconstruction of the electronic structure from the building blocks is less well defined. In any case the OESE

principle shows a lot of potential but needs to be investigated on a larger scale. Additionally, it would be interesting to test the validity of the OESE principle with experimental results obtained from ultraviolet and inverse photoemission spectroscopy to deduce absolute band positions. A complete electronic structure using angle-resolved photoemission spectroscopy (ARPES) or electrochemical experiments could give further insight whereas time-resolved spectroscopy could be used to deduce how the materials behave when excited. These experiments would allow us to better understand the processes taking place.

The OESE principle is interesting to elucidate the electronic structure of a modular material, but besides, also other properties are important to deduce or predict the complete photocatalytic activity of a (modular) material. A first property that is also relevant is the carrier lifetime and recombination pathways. In this PhD thesis, we have qualitatively discussed this by investigating the electronic structure. The overlap between and the order of the orbitals were used to qualitatively deduce how the charge-transfer efficiency, related to this lifetime and photocatalytic activity, changes. However, a more appropriate way would be to deduce this lifetime and corresponding recombination pathways directly by modelling. This has recently been performed by Syzgantseva et al.[101] where they modelled the lifetime of charge carriers within UiO-66. Their results qualitatively agreed with the conclusion in this PhD thesis, and with experiments. A second property that was not considered yet, is the role of sacrificial donors. Sacrificial donors are chemical agents that serve to replenish the electron level of the reducing photocatalyst. Although we did not directly study them within this PhD research, it is possible to include their effect by comparing the redox potential of the framework and the sacrificial donor.[382] Unfortunately, the presence of such species limits the sustainability of the photocatalytic reaction.[383] Ideally, the framework's oxidation and reduction potential are aligned with the redox levels of both half reactions triggered by the photocatalyst,[384] removing the need for sacrificial donors altogether. Although much more challenging, the OESE principle may also prove useful in designing such fully sustainable catalysts.

5

Bibliography

Bibliography

[1] "World energy outlook 2019," Tech. Rep. (U.S. Energy Information Administration, 2019).

[2] "Tracking SDG 7 : The Energy Progress Report 2019," Tech. Rep. (International Energy Agency, International Renewable Energy Agency, United Nations Statistics Division, World Bank, World Health Organization, 2019).

[3] P. T. Anastas, M. M. Kirchhoff, and T. C. Williamson, "Catalysis as a foundational pillar of Green Chem." *Appl. Catal., A*, **221**, 3 (2001).

[4] S. A. Axon and A. Zwijnenburg, "Special issue on Industrial Catalysis," *Catal. Today*, **163**, 1 (2011).

[5] C. A. Busacca, D. R. Fandrick, J. J. Song, and C. H. Senanayake, "The Growing Impact of Catalysis in the Pharmaceutical Industry," *Advanced Synthesis & Catalysis*, **353**, 1825 (2011).

[6] T. Ennaert, J. Van Aelst, J. Dijkmans, R. De Clercq, W. Schutyser, M. Dusselier, D. Verboekend, and B. F. Sels, "Potential and challenges of zeolite chemistry in the catalytic conversion of biomass," *Chem. Soc. Rev.*, **45**, 584 (2016).

[7] S. M. J. Rogge, *Derivation and Application of a Reliable Procedure to Computationally Model the Mechanical Stabilitry of Rigid and Flexible Metal-Organic Frameworks*, Ph.D. thesis, Ghent University (2018).

[8] A. Dhakshinamoorthy, Z. Li, and H. Garcia, "Catalysis and photocatalysis by metal organic frameworks," *Chem. Soc. Rev.*, **47**, 8134 (2018).

[9] L. B. McCusker, F. Liebau, and G. Engelhardt, "Nomenclature of structural and compositional characteristics of ordered Microporous Mesoporous Mater. with inorganic hosts: (IUPAC recommendations 2001)," *Microporous Mesoporous Mater.*, **58**, 3 (2003).

[10] J. Jiang, Y. Zhao, and O. M. Yaghi, "Covalent Chemistry beyond Molecules," *J. Am. Chem. Soc.*, **138**, 3255 (2016).

[11] A. Corma and H. García, "Lewis Acids From Conventional Homogeneous to Green Homogeneous and Heterogeneous Catalysis," *Chem. Rev.*, **103**, 4307 (2003).

[12] J. Wieme, K. Lejaeghere, G. Kresse, and V. Van Speybroeck, "Tuning the balance between dispersion and entropy to design temperature-responsive flexible metal-organic frameworks," *Nat. Commun.*, **9**, 4899 (2018).

[13] A. F. Cronstedt, "Natural zeolite and minerals," *Svenska Vetenskaps Akademiens Handlingar Stockholm*, **17**, 120 (1756).

[14] V. de St. Claire-Deville, "Reproduction de la levyne," *Comptes Rendus*, **54**, 324 (1862).

[15] V. Van Speybroeck, K. Hemelsoet, L. Joos, M. Waroquier, R. G. Bell, and C. R. A. Catlow, "Advances in theory and their application within the field of zeolite chemistry," *Chem. Soc. Rev.*, **44**, 7044 (2015).

[16] A. Primo and H. Garcia, "Zeolites as catalysts in oil refining," *Chem. Soc. Rev.*, **43**, 7548 (2014).

[17] B. Lebeau, A. Galarneau, and M. Linden, "Introduction for 20 years of research on ordered mesoporous materials," *Chem. Soc. Rev.*, **42**, 3661 (2013).

[18] A. G. Slater and A. I. Cooper, "Function-led design of new porous materials," *Science*, **348** (2015), 10.1126/science.aaa8075.

[19] J. Liang, Z. Liang, R. Zou, and Y. Zhao, "Heterogeneous Catalysis in Zeolites, Mesoporous Silica, and Metal-Organic Frameworks," *Adv. Mater.*, **29**, 1701139 (2017).

[20] P. Sudarsanam, E. Peeters, E. V. Makshina, V. I. Parvulescu, and B. F. Sels, "Advances in porous and nanoscale catalysts for viable biomass conversion," *Chem. Soc. Rev.*, **48**, 2366 (2019).

[21] Y. Kinoshita, I. Matsubara, T. Higuchi, and Y. Saito, "The Crystal Structure of Bis(adiponitrilo)copper(I) Nitrate," *Bull. Chem. Soc. Jpn.*, **32**, 1221 (1959).

[22] C. Biondi, M. Bonamico, L. Torelli, and A. Vaciago, "On the structure and water content of copper(II) tricyanomethanide," *Chem. Commun. Lond.*, 191 (1965).

[23] E. A. Tomic, "Thermal stability of coordination polymers," *J. Appl. Polym. Sci.*, **9**, 3745 (1965).

[24] B. F. Hoskins and R. Robson, "Infinite polymeric frameworks consisting of three dimensionally linked rod-like segments," *J. Am. Chem. Soc.*, **111**, 5962 (1989).

[25] H. Li, M. Eddaoudi, M. O'Keeffe, and O. M. Yaghi, "Design and synthesis of an exceptionally stable and highly porous metal-organic framework," *Nature*, **402**, 276 (1999).

[26] S. Kitagawa, R. Kitaura, and S.-i. Noro, "Functional Porous Coordination Polymers," *Angew. Chem. Int. Ed.*, **43**, 2334 (2004).

[27] G. Frey, "Hybrid porous solids: past, present, future," *Chem. Soc. Rev.*, **37**, 191 (2008).

[28] O. M. Yaghi, M. O'Keeffe, N. W. Ockwig, H. K. Chae, M. Eddaoudi, and J. Kim, "Reticular synthesis and the design of new materials," *Nature*, **423**, 705 (2003).

[29] M. Eddaoudi, J. Kim, N. Rosi, D. Vodak, J. Wachter, M. O'Keeffe, and O. M. Yaghi, "Systematic Design of Pore Size and Functionality in Isoreticular MOFs and Their Application in Methane Storage," *Science*, **295**, 469 (2002).

[30] J. R. Long and O. M. Yaghi, "Thematic issue: Metal-Organic Frameworks," *Chem. Soc. Rev.*, **38**, 1201 (2009).

[31] C. E. Wilmer, M. Leaf, C. Y. Lee, O. K. Farha, B. G. Hauser, J. T. Hupp, and R. Q. Snurr, "Large-scale screening of hypothetical metal–organic frameworks," *Nat. Chem.*, **4**, 83 EP (2011).

[32] H.-C. Zhou, J. R. Long, and O. M. Yaghi, "Introduction to Metal–Organic Frameworks," *Chem. Rev.*, **112**, 673 (2012).

[33] I. Huskić, I. V. Pekov, S. V. Krivovichev, and T. Friščić, "Minerals with metal-organic framework structures," *Sci. Adv.*, **2**, e1600621 (2016).

[34] A. P. Côté, A. I. Benin, N. W. Ockwig, M. O'Keeffe, A. J. Matzger, and O. M. Yaghi, "Porous, Crystalline, Covalent Organic Frameworks," *Science*, **310**, 1166 (2005).

[35] S. Ren, M. J. Bojdys, R. Dawson, A. Laybourn, Y. Z. Khimyak, D. J. Adams, and A. I. Cooper, "Porous, Fluorescent, Covalent Triazine-Based Frameworks Via Room-Temperature and Microwave-Assisted Synthesis," *Adv. Mater.*, **24**, 2357 (2012).

[36] P. J. Waller, F. Gándara, and O. M. Yaghi, "Chemistry of Covalent Organic Frameworks," *Acc. Chem. Res.*, **48**, 3053 (2015).

[37] X. Feng, X. Ding, and D. Jiang, "Covalent organic frameworks," *Chem. Soc. Rev.*, **41**, 6010 (2012).

[38] S. Lin, M. A. Ischay, C. G. Fry, and T. P. Yoon, "Radical Cation Diels-Alder Cycloadditions by Visible Light Photocatalysis," *J. Am. Chem. Soc.*, **133**, 19350 (2011).

[39] C. Wang, Z. Xie, K. E. deKrafft, and W. Lin, "Doping Metal-Organic Frameworks for Water Oxidation, Carbon Dioxide Reduction, and Organic Photocatalysis," *J. Am. Chem. Soc.*, **133**, 13445 (2011).

[40] N. C. Burtch, H. Jasuja, and K. S. Walton, "Water Stability and Adsorption in Metal-Organic Frameworks," *Chem. Rev.*, **114**, 10575 (2014).

[41] K. Leus, T. Bogaerts, J. De Decker, H. Depauw, K. Hendrickx, H. Vrielinck, V. Van Speybroeck, and P. Van Der Voort, "Systematic study of the chemical and hydrothermal stability of selected stable Metal Organic Frameworks," *Microporous Mesoporous Mater.*, **226**, 110 (2016).

[42] S.-Y. Ding and W. Wang, "Covalent organic frameworks (COFs): from design to applications," *Chem. Soc. Rev.*, **42**, 548 (2013).

[43] M. S. Lohse and T. Bein, "Covalent Organic Frameworks: Structures, Synthesis, and Applications," *Adv. Func. Mater.*, **28**, 1705553 (2018).

[44] R. K. Sharma, P. Yadav, M. Yadav, R. Gupta, P. Rana, A. Srivastava, R. Zbořil, R. S. Varma, M. Antonietti, and M. B. Gawande, "Recent development of covalent organic frameworks (COFs): synthesis and catalytic (organic-electro-photo) applications," *Mater. Horiz.*, **7**, 411 (2020).

[45] C. Janiak, "Engineering coordination polymers towards applications," *Dalton Trans.*, 2781 (2003).

[46] C. Serre, S. Bourrelly, A. Vimont, N. Ramsahye, G. Maurin, P. Llewellyn, M. Daturi, Y. Filinchuk, O. Leynaud, P. Barnes, and G. Férey, "An Explanation for the Very Large Breathing Effect of a Metal-Organic Framework during CO2 Adsorption," *Adv. Mater.*, **19**, 2246 (2007).

[47] G. Férey, C. Serre, T. Devic, G. Maurin, H. Jobic, P. L. Llewellyn, G. De Weireld, A. Vimont, M. Daturi, and J.-S. Chang, "Why hybrid porous solids capture greenhouse gases?" *Chem. Soc. Rev.*, **40**, 550 (2011).

[48] O. K. Farha, I. Eryazici, N. C. Jeong, B. G. Hauser, C. E. Wilmer, A. A. Sarjeant, R. Q. Snurr, S. T. Nguyen, A. o. Yazaydın, and J. T. Hupp, "Metal-Organic Framework Materials with Ultrahigh Surface Areas: Is the Sky the Limit?" *J. Am. Chem. Soc.*, **134**, 15016 (2012).

[49] A. C. McKinlay, R. E. Morris, P. Horcajada, G. Férey, R. Gref, P. Couvreur, and C. Serre, "BioMOFs: Metal-Organic Frameworks for Biological and Medical Applications," *Angew. Chem. Int. Ed.*, **49**, 6260 (2010).

[50] S. Keskin and S. Kızılel, "Biomedical Applications of Metal Organic Frameworks," *Ind. Eng. Chem. Res.*, **50**, 1799 (2011).

[51] Y. Zhao, Z. Song, X. Li, Q. Sun, N. Cheng, S. Lawes, and X. Sun, "Metal organic frameworks for energy storage and conversion," *Energy Storage Materials*, **2**, 35 (2016).

[52] K. Sakaushi and M. Antonietti, "Carbon- and Nitrogen-Based Organic Frameworks," *Acc. Chem. Res.*, **48**, 1591 (2015).

[53] E. A. Dolgopolova and N. B. Shustova, "Metal-organic framework photophysics: Optoelectronic devices, photoswitches, sensors, and photocatalysts," *MRS Bull.*, **41**, 890 (2016).

[54] I. Stassen, N. Burtch, A. Talin, P. Falcaro, M. Allendorf, and R. Ameloot, "An updated roadmap for the integration of metal-organic frameworks with electronic devices and chemical sensors," *Chem. Soc. Rev.*, **46**, 3185 (2017).

[55] D. Liu, K. Lu, C. Poon, and W. Lin, "Metal-organic frameworks as sensory materials and imaging agents." *Inorg. Chem.*, **53**, 1916 (2013).

[56] J.-L. Wang, C. Wang, and W. Lin, "Metal-Organic Frameworks for Light Harvesting and Photocatalysis," *ACS Catal.*, **2**, 2630 (2012).

[57] M. A. Nasalevich, M. A. van der Veen, F. Kapteijn, and J. Gascon, "Metal-organic frameworks as heterogeneous photocatalysts: advantages and challenges," *CrystEngComm*, **16**, 4919 (2014).

[58] M. D. Allendorf, C. A. Bauer, R. K. Bhakta, and R. J. T. Houk, "Luminescent metal-organic frameworks," *Chem. Soc. Rev.*, **38**, 1330 (2009).

[59] Y. Cui, B. Chen, and G. Qian, in *Metal-Organic Frameworks for Photonics Applications*, Struct. Bond., Vol. 157, edited by B. Chen and G. Qian (2014) pp. 27–88.

[60] D. Farrusseng, S. Aguado, and C. Pinel, "Metal-Organic Frameworks: Opportunities for Catalysis," *Angew. Chem. Int. Ed.*, **48**, 7502 (2009).

[61] A. Corma, H. García, and F. X. Llabrés i Xamena, "Engineering Metal Organic Frameworks for Heterogeneous Catalysis," *Chem. Rev.*, **110**, 4606 (2010).

[62] M. Ranocchiari and J. A. v. Bokhoven, "Catalysis by metal-organic frameworks: fundamentals and opportunities," *Phys. Chem. Chem. Phys.*, **13**, 6388 (2011).

[63] F. Vermoortele, R. Ameloot, A. Vimont, C. Serre, and D. De Vos, "An amino-modified Zr-terephthalate metal-organic framework as an acid-base catalyst for cross-aldol condensation," *Chem. Commun.*, **47**, 1521 (2011).

[64] A. Dhakshinamoorthy and H. Garcia, "Catalysis by metal nanoparticles embedded on metal-organic frameworks," *Chem. Soc. Rev.*, **41**, 5262 (2012).

[65] A. Dhakshinamoorthy, A. M. Asiri, and H. García, "Metal-Organic Framework (MOF) Compounds: Photocatalysts for Redox Reactions and Solar Fuel Production." *Angew. Chem. Int. Ed. Engl.*, **55**, 5414 (2016).

[66] J. Gascon, A. Corma, F. Kapteijn, and F. X. Llabrés i Xamena, "Metal Organic Framework Catalysis: Quo vadis?" *ACS Catal.*, **4**, 361 (2014).

[67] J. Liu, L. Chen, H. Cui, J. Zhang, L. Zhang, and C.-Y. Su, "Applications of metal-organic frameworks in heterogeneous supramolecular catalysis," *Chem. Soc. Rev.*, **43**, 6011 (2014).

[68] Y. Zhang and J. Y. Ying, "Main-Chain Organic Frameworks with Advanced Catalytic Functionalities," *ACS Catal.*, **5**, 2681 (2015).

[69] R. S. B. Goncalves, A. B. V. de Oliveira, H. C. Sindra, B. S. Archanjo, M. E. Mendoza, L. S. A. Carneiro, C. D. Buarque, and P. M. Esteves, "Heterogeneous Catalysis by Covalent Organic Frameworks (COF): Pd(OAc)2@COF-300 in Cross-Coupling Reactions," *ChemCatChem*, **8**, 743 (2016).

[70] S. M. J. Rogge, A. Bavykina, J. Hajek, H. Garcia, A. I. Olivos-Suarez, A. Sepúlveda-Escribano, A. Vimont, G. Clet, P. Bazin, F. Kapteijn, M. Daturi, E. V. Ramos-Fernandez, F. X. Llabrés i Xamena, V. Van Speybroeck, and J. Gascon, "Metal-organic and covalent organic frameworks as single-site catalysts," *Chem. Soc. Rev.*, **46**, 3134 (2017).

[71] F. Vermoortele, B. Bueken, G. Le Bars, B. Van de Voorde, M. Vandichel, K. Houthoofd, A. Vimont, M. Daturi, M. Waroquier, V. Van Speybroeck,

C. Kirschhock, and D. E. De Vos, "Synthesis Modulation as a Tool To Increase the Catalytic Activity of Metal-Organic Frameworks: The Unique Case of UiO-66(Zr)," *J. Am. Chem. Soc.*, **135**, 11465 (2013).

[72] M. D. Allendorf, M. E. Foster, F. Léonard, V. Stavila, P. L. Feng, F. P. Doty, K. Leong, E. Y. Ma, S. R. Johnston, and A. A. Talin, "Guest-Induced Emergent Properties in Metal-Organic Frameworks," *The J. Phys. Chem. Lett.*, **6**, 1182 (2015).

[73] M. Kandiah, M. Nilsen, S. Usseglio, S. Jakobsen, U. Olsbye, M. Tilset, C. Larabi, E. Quadrelli, F. Bonino, and K. Lillerud, "Synthesis and Stability of Tagged UiO-66 Zr-MOFs," *Chem. Mater.*, **22**, 6632 (2010).

[74] J. H. Cavka, S. Jakobsen, U. Olsbye, N. Guillou, C. Lamberti, S. Bordiga, and K. P. Lillerud, "A new zirconium inorganic building brick forming metal organic frameworks with exceptional stability." *J. Am. Chem. Soc.*, **130**, 13850 (2008).

[75] M. Vandichel, J. Hajek, F. Vermoortele, M. Waroquier, D. E. De Vos, and V. Van Speybroeck, "Active site engineering in UiO-66 type metal-organic frameworks by intentional creation of defects: a theoretical rationalization," *CrystEngComm*, **17**, 395 (2015).

[76] F. Vermoortele, M. Vandichel, B. Van de Voorde, R. Ameloot, M. Waroquier, V. Van Speybroeck, and D. E. De Vos, "Electronic Effects of Linker Substitution on Lewis Acid Catalysis with Metal-Organic Frameworks," *Angew. Chem. Int. Ed.*, **51**, 4887 (2012).

[77] M. N. Timofeeva, V. N. Panchenko, J. W. Jun, Z. Hasan, M. M. Matrosova, and S. H. Jhung, "Effects of linker substitution on catalytic properties of porous zirconium terephthalate UiO-66 in acetalization of benzaldehyde with methanol," *Appl. Catal., A*, **471**, 91 (2014).

[78] F. Cirujano, A. Corma, and F. L. i Xamena, "Conversion of levulinic acid into chemicals: Synthesis of biomass derived levulinate esters over Zr-containing MOFs," *Chem. Eng. Sci.*, **124**, 52 (2015).

[79] V. S. Vyas, F. Haase, L. Stegbauer, G. Savasci, C. Podjaski, F. Ochsenfeld, and B. V. Lotsch, "A tunable azine covalent organic framework platform for visible light-induced hydrogen generation," *Nat. Commun.*, **6**, 8508 (2015).

[80] T. Banerjee and B. V. Lotsch, "The wetter the better," *Nat. Chem.*, **10**, 1175 (2018).

[81] J. Barber, "Photosynthetic energy conversion: natural and artificial," *Chem. Soc. Rev.*, **38**, 185 (2009).

[82] D. Gust, T. A. Moore, and A. L. Moore, "Solar Fuels via Artificial Photosynthesis," *Acc. Chem. Res.*, **42**, 1890 (2009).

[83] H. J. M. Hou, S. I. Allakhverdiev, M. M. Najafpour, and Govindjee, "Current challenges in photosynthesis: from natural to artificial," *Front. Plant Sci.*, **5**, 232 (2014).

[84] M. R. Hoffmann, S. T. Martin, W. Choi, and D. W. Bahnemann, "Environmental Applications of Semiconductor Photocatalysis," *Chem. Rev.*, **95**, 69 (1995).

[85] K. Gilmore and P. H. Seeberger, "Continuous Flow Photochemistry," *The Chem. Rec.*, **14**, 410 (2014).

[86] Y. Su, N. J. W. Straathof, V. Hessel, and T. Noël, "Photochemical Transformations Accelerated in Continuous-Flow Reactors: Basic Concepts and Applications," *Chemistry - A European Journal*, **20**, 10562 (2014).

[87] D. Cantillo, O. de Frutos, J. A. Rincón, C. Mateos, and C. O. Kappe, "A Continuous-Flow Protocol for Light-Induced Benzylic Fluorinations," *The J. Org. Chem.*, **79**, 8486 (2014).

[88] D. Rackl, P. Kreitmeier, and O. Reiser, "Synthesis of a polyisobutylene-tagged fac-Ir(ppy)3 complex and its application as recyclable visible-light photocatalyst in a continuous flow process," *Green Chem.*, **18**, 214 (2016).

[89] M. Oelgemöller and N. Hoffmann, "Studies in organic and physical photochemistry - an interdisciplinary approach," *Org. Biomol. Chem.*, **14**, 7392 (2016).

[90] H. Kisch, *Semiconductor Photocatalysis: Principles and Applications* (2015) pp. 1–249.

[91] A. Kudo and Y. Miseki, "Heterogeneous photocatalyst materials for water splitting," *Chem. Soc. Rev.*, **38**, 253 (2009).

[92] K. Maeda and K. Domen, "Photocatalytic Water Splitting: Recent Progress and Future Challenges," *The J. Phys. Chem. Lett.*, **1**, 2655 (2010).

[93] M. G. Walter, E. L. Warren, J. R. McKone, S. W. Boettcher, Q. Mi, E. A. Santori, and N. S. Lewis, "Solar Water Splitting Cells," *Chem. Rev.*, **110**, 6446 (2010).

[94] T. Hisatomi, J. Kubota, and K. Domen, "Recent advances in semiconductors for photocatalytic and photoelectrochemical water splitting," *Chem. Soc. Rev.*, **43**, 7520 (2014).

[95] R. S. Sprick, J.-X. Jiang, B. Bonillo, S. Ren, T. Ratvijitvech, P. Guiglion, M. A. Zwijnenburg, D. J. Adams, and A. I. Cooper, "Tunable Organic Photocatalysts for Visible-Light-Driven Hydrogen Evolution," *J. Am. Chem. Soc.*, **137**, 3265 (2015).

[96] D. Shi, C. He, B. Qi, C. Chen, J. Niu, and C. Duan, "Merging of the photocatalysis and copper catalysis in metal-organic frameworks for oxidative CC bond formation," *Chem. Sci.*, **6**, 1035 (2015).

[97] S. Wang and X. Wang, "Multifunctional Metal-Organic Frameworks for Photocatalysis," *Small*, **11**, 3097 (2015).

[98] Y. Li, H. Xu, S. Ouyang, and J. Ye, "Metal-organic frameworks for photocatalysis," *Phys. Chem. Chem. Phys.*, **18**, 7563 (2016).

[99] X. Jiang, P. Wang, and J. Zhao, "2D covalent triazine framework: a new class of organic photocatalyst for water splitting," *J. Mater. Chem. A*, **3**, 7750 (2015).

[100] C. S. Diercks and O. M. Yaghi, "The atom, the molecule, and the covalent organic framework," *Science*, **355**, eaal1585 (2017).

[101] M. A. Syzgantseva, N. F. Stepanov, and O. A. Syzgantseva, "Carrier Lifetimes and Recombination Pathways in Metal-Organic Frameworks," *The J. Phys. Chem. Lett.*, **2019**, 5041 (0).

[102] S.-n. Zhao, G. Wang, D. Poelman, and P. Van Der Voort, "Metal organic frameworks based materials for heterogeneous photocatalysis," *MOLECULES*, **23**, 23 (2018).

[103] T. Bogaerts, A. Van Yperen-De Deyne, Y.-Y. Liu, F. Lynen, V. Van Speybroeck, and P. Van Der Voort, "Mn-salen@MIL101(Al): a heterogeneous, enantioselective catalyst synthesized using a 'bottle around the ship' approach," *Chem. Commun.*, **49**, 8021 (2013).

[104] K. Leus, G. Vanhaelewyn, T. Bogaerts, Y.-Y. Liu, D. Esquivel, F. Callens, G. B. Marin, V. V. Speybroeck], H. Vrielinck, and P. V. D. Voort], "Ti-functionalized NH2-MIL-47: An effective and stable epoxidation catalyst," *Catal. Today*, **208**, 97 (2013).

[105] Y.-Y. Liu, K. Leus, T. Bogaerts, K. Hemelsoet, E. Bruneel, V. Van Speybroeck, and P. Van Der Voort, "Bimetallic-Organic Framework as a

Zero-Leaching Catalyst in the Aerobic Oxidation of Cyclohexene," *ChemCatChem*, **5**, 3657 (2013).

[106] H. Takeda, M. Ohashi, Y. Goto, T. Ohsuna, T. Tani, and S. Inagaki, "A Versatile Solid Photosensitizer: Periodic Mesoporous Organosilicas with Ruthenium Tris(bipyridine) Complexes Embedded in the Pore Walls," *Adv. Func. Mater.*, **26**, 5068 (2016).

[107] F.-X. Coudert and A. H. Fuchs, "Computational characterization and prediction of metal-organic framework properties," *Coord. Chem. Rev.*, **307**, 211 (2016).

[108] J. A. Steele, H. Jin, I. Dovgaliuk, R. F. Berger, T. Braeckevelt, H. Yuan, C. Martin, E. Solano, K. Lejaeghere, S. M. J. Rogge, C. Notebaert, W. Vandezande, K. P. F. Janssen, B. Goderis, E. Debroye, Y.-K. Wang, Y. Dong, D. Ma, M. Saidaminov, H. Tan, Z. Lu, V. Dyadkin, D. Chernyshov, V. Van Speybroeck, E. H. Sargent, J. Hofkens, and M. B. J. Roeffaers, "Thermal unequilibrium of strained black CsPbI3 thin films," *Science*, **365**, 679 (2019).

[109] K. Hendrickx, J. J. Joos, A. De Vos, D. Poelman, P. F. Smet, V. Van Speybroeck, P. Van Der Voort, and K. Lejaeghere, "Exploring Lanthanide Doping in UiO-66: A Combined Experimental and Computational Study of the Electronic Structure," *Inorg. Chem.*, **57**, 5463 (2018).

[110] K. Hendrickx, D. E. P. Vanpoucke, K. Leus, K. Lejaeghere, A. Van Yperen-De Deyne, V. Van Speybroeck, P. Van Der Voort, and K. Hemelsoet, "Understanding Intrinsic Light Absorption Properties of UiO-66 Frameworks: A Combined Theoretical and Experimental Study." *Inorg. Chem.*, **54**, 10701 (2015).

[111] A. De Vos, K. Hendrickx, P. Van Der Voort, V. Van Speybroeck, and K. Lejaeghere, "Missing Linkers: An Alternative Pathway to UiO-66 Electronic Structure Engineering," *Chem. Mater*, **29**, 3006 (2017).

[112] J. J. Joos, K. Lejaeghere, K. Korthout, A. Feng, D. Poelman, and P. F. Smet, "Charge transfer induced energy storage in CaZnOS:Mn - insight from experimental and computational spectroscopy," *Phys. Chem. Chem. Phys.*, **19**, 9075 (2017).

[113] Z. W. Seh, J. Kibsgaard, C. F. Dickens, I. Chorkendorff, J. K. Nørskov, and T. F. Jaramillo, "Combining theory and experiment in electrocatalysis: Insights into materials design," *Science*, **355**, eaad4998 (2017).

[114] S. Curtarolo, G. L. W. Hart, M. B. Nardelli, N. Mingo, S. Sanvito, and O. Levy, "The high-throughput highway to computational materials design," *Nat. Mater.*, **12**, 191 EP .

[115] D. Morgan, G. Ceder, and S. Curtarolo, "High-throughput and data mining with ab initio methods," *Meas. Sci. Technol.*, **16**, 296 (2004).

[116] L. M. Ghiringhelli, C. Carbogno, S. Levchenko, F. Mohamed, G. Huhs, M. Lüders, M. Oliveira, and M. Scheffler, "Towards efficient data exchange and sharing for big-data driven materials science: metadata and data formats," *Npj Comput. Mater.*, **3**, 46 (2017).

[117] C. Draxl, F. Illas, and M. Scheffler, "Open data settled in materials theory," *Nature*, **548**, 523 (2017).

[118] C. Draxl and M. Scheffler, "NOMAD: The FAIR concept for Big Data-driven Mater. Sci." *MRS Bull.*, **43**, 676 (2018).

[119] R. J. García-Hernández and D. Kranzlmüller, "NOMAD VR: Multiplatform virtual reality viewer for chemistry simulations," *Comput. Phys. Commun.*, **237**, 230 (2019).

[120] N. Science and T. C. (US), *Materials genome initiative for global competitiveness* (Executive Office of the President, National Science and Technology Council, 2011).

[121] A. Jain, S. P. Ong, G. Hautier, W. Chen, W. D. Richards, S. Dacek, S. Cholia, D. Gunter, D. Skinner, G. Ceder, and K. A. Persson, "Commentary: The Materials Project: A materials genome approach to accelerating materials innovation," *APL Mater.*, **1**, 011002 (2013).

[122] S. P. Ong, W. D. Richards, A. Jain, G. Hautier, M. Kocher, S. Cholia, D. Gunter, V. L. Chevrier, K. A. Persson, and G. Ceder, "Python Materials Genomics (pymatgen): A robust, open-source python library for materials analysis," *Computational Mater. Sci.*, **68**, 314 (2013).

[123] P. G. Boyd, A. Chidambaram, E. García-Díez, C. P. Ireland, T. D. Daff, R. Bounds, A. Gładysiak, P. Schouwink, S. M. Moosavi, M. M. Maroto-Valer, J. A. Reimer, J. A. R. Navarro, T. K. Woo, S. Garcia, K. C. Stylianou, and B. Smit, "Data-driven design of metal–organic frameworks for wet flue gas CO2 capture," *Nature*, **576**, 253 (2019).

[124] S. V. Alapati, J. K. Johnson, and D. S. Sholl, "Identification of Destabilized Metal Hydrides for Hydrogen Storage Using First Principles Calculations," *The J. Phys. Chem. B*, **110**, 8769 (2006).

[125] J. Lu, Z. Z. Fang, Y. J. Choi, and H. Y. Sohn, "Potential of Binary Lithium Magnesium Nitride for Hydrogen Storage Applications," *J. Phys. Chem. C*, **111**, 12129 (2007).

[126] C. M. Simon, J. Kim, D. A. Gomez-Gualdron, J. S. Carno, Y. G. Chung, R. L. Martin, R. Mercado, M. W. Deem, D. Gunger, M. Haranczyk, D. S. Sholl, R. Q. Snurr, and B. Smit, "The materials genome in action: identifying the performance limits for methane storage," *Energy Environ. Sci.*, **8**, 1190 (2015).

[127] P. Z. Moghadam, T. Islamoglu, S. Goswami, J. Exley, M. Fantham, C. F. Kaminski, R. Q. Snurr, O. K. Farha, and D. Fairen-Jimenez, "Computer-aided discovery of a metal-organic framework with superior oxygen uptake," *Nat. Commun.*, **9**, 1378 (2018).

[128] H. Chen, G. Hautier, A. Jain, C. Moore, B. Kang, R. Doe, L. Wu, Y. Zhu, Y. Tang, and G. Ceder, "Carbonophosphates: A New Family of Cathode Materials for Li-Ion Batteries Identified Computationally," *Chem. Mater.*, **24**, 2009 (2012).

[129] G. Hautier, A. Jain, H. Chen, C. Moore, S. P. Ong, and G. Ceder, "Novel mixed polyanions lithium-ion battery cathode materials predicted by high-throughput ab initio computations," *J. Mater. Chem.*, **21**, 17147 (2011).

[130] H. Chen, G. Hautier, and G. Ceder, "Synthesis, Computed Stability, and Crystal Structure of a New Family of Inorganic Compounds: Carbonophosphates," *J. Am. Chem. Soc.*, **134**, 19619 (2012).

[131] J. C. Kim, C. J. Moore, B. Kang, G. Hautier, A. Jain, and G. Ceder, "Synthesis and Electrochemical Properties of Monoclinic LiMnBO[sub 3] as a Li Intercalation Material," *J. Electrochem. Soc.*, **158**, A309 (2011).

[132] A. Jain, G. Hautier, C. Moore, B. Kang, J. Lee, H. Chen, N. Twu, and G. Ceder, "A Computational Investigation of Li9M3(P2O7)3(PO4)2(M = V, Mo) as Cathodes for Li Ion Batteries," *J. Electrochem. Soc.*, **159**, A622 (2012).

[133] J. Greeley, T. F. Jaramillo, J. Bonde, I. Chorkendorff, and J. K. Nørskov, "Computational high-throughput screening of electrocatalytic materials for hydrogen evolution," *Nat. Mater.*, **5**, 909 (2006).

[134] S. M. Moosavi, A. Chidambaram, L. Talirz, M. Haranczyk, K. C. Stylianou, and B. Smit, "Capturing chemical intuition in synthesis of metal-organic frameworks," *Nat. Commun.*, **10**, 539 (2019).

[135] Y. Lee, S. D. Barthel, P. Dłotko, S. M. Moosavi, K. Hess, and B. Smit, "High-Throughput Screening Approach for Nanoporous Materials Genome Using Topological Data Analysis: Application to Zeolites," *J. Chem. Theory Comput.*, **14**, 4427 (2018).

[136] M. Witman, S. Ling, A. Gladysiak, K. C. Stylianou, B. Smit, B. Slater, and M. Haranczyk, "Rational Design of a Low-Cost, High-Performance Metal-Organic Framework for Hydrogen Storage and Carbon Capture," *J. Phys. Chem. C*, **121**, 1171 (2017).

[137] W. Eckhardt, A. Heinecke, R. Bader, M. Brehm, N. Hammer, H. Huber, H.-G. Kleinhenz, J. Vrabec, H. Hasse, M. Horsch, M. Bernreuther, C. W. Glass, C. Niethammer, A. Bode, and H.-J. Bungartz, "591 TFLOPS Multi-trillion Particles Simulation on SuperMUC," in *Supercomputing: 28th International Supercomputing Conference, ISC 2013, Leipzig, Germany, June 16-20, 2013. Proceedings*, edited by J. M. Kunkel, T. Ludwig, and H. W. Meuer (Springer Berlin Heidelberg, 2013) pp. 1–12.

[138] P. Hohenberg and W. Kohn, "Inhomogeneous Electron Gas," *Phys. Rev.*, **136**, B864 (1964).

[139] W. Kohn and L. J. Sham, "Self-Consistent Equations Including Exchange and Correlation Effects," *Phys. Rev.*, **140**, A1133 (1965).

[140] K. Lejaeghere, G. Bihlmayer, T. Björkman, P. Blaha, S. Blügel, V. Blum, D. Caliste, I. E. Castelli, S. J. Clark, A. Dal Corso, S. de Gironcoli, T. Deutsch, J. K. Dewhurst, I. Di Marco, C. Draxl, M. Dułak, O. Eriksson, J. A. Flores-Livas, K. F. Garrity, L. Genovese, P. Giannozzi, M. Giantomassi, S. Goedecker, X. Gonze, O. Grånäs, E. K. U. Gross, A. Gulans, F. Gygi, D. R. Hamann, P. J. Hasnip, N. A. W. Holzwarth, D. Iuşan, D. B. Jochym, F. Jollet, D. Jones, G. Kresse, K. Koepernik, E. Küçükbenli, Y. O. Kvashnin, I. L. M. Locht, S. Lubeck, M. Marsman, N. Marzari, U. Nitzsche, L. Nordström, T. Ozaki, L. Paulatto, C. J. Pickard, W. Poelmans, M. I. J. Probert, K. Refson, M. Richter, G.-M. Rignanese, S. Saha, M. Scheffler, M. Schlipf, K. Schwarz, S. Sharma, F. Tavazza, P. Thunström, A. Tkatchenko, M. Torrent, D. Vanderbilt, M. J. van Setten, V. Van Speybroeck, J. M. Wills, J. R. Yates, G.-X. Zhang, and S. Cottenier, "Reproducibility in density functional theory calculations of solids," *Science*, **351**, 1415 (2016).

[141] M. Shishkin, M. Marsman, and G. Kresse, "Accurate Quasiparticle Spectra from Self-Consistent GW Calculations with Vertex Corrections," *Phys. Rev. Lett.*, **99**, 246403 (2007).

[142] S. De Waele, K. Lejaeghere, M. Sluydts, and S. Cottenier, "Error estimates for density-functional theory predictions of surface energy and work function," *Phys. Rev. B*, **94**, 235418 (2016).

[143] K. Lejaeghere, V. Van Speybroeck, G. Van Oost, and S. Cottenier, "Error Estimates for Solid-State Density-Functional Theory Predictions: An Overview by Means of the Ground-State Elemental Crystals," *Crit. Rev. Solid State Mater. Sci.*, **39**, 1 (2014).

[144] K. Lejaeghere, L. Vanduyfhuys, T. Verstraelen, V. Van Speybroeck, and S. Cottenier, "Is the error on first-principles volume predictions absolute or relative?" *Computational Mater. Sci.*, **117**, 390 (2016).

[145] P. Zhu and V. Meunier, "Electronic properties of two-dimensional covalent organic frameworks," *J. Chem. Phys.*, **137**, 244703 (2012).

[146] A. De Vos, K. Lejaeghere, F. Muniz Miranda, C. V. Stevens, P. Van Der Voort, and V. Van Speybroeck, "Electronic properties of heterogenized Ru(ii) polypyridyl photoredox complexes on covalent triazine frameworks," *J. Mater. Chem. A*, **7**, 8433 (2019).

[147] D. Nazarian, P. Ganesh, and D. S. Sholl, "Benchmarking density functional theory predictions of framework structures and properties in a chemically diverse test set of metal-organic frameworks," *J. Mater. Chem. A*, **3**, 22432 (2015).

[148] J. Heyd, J. E. Peralta, G. E. Scuseria, and R. L. Martin, "Energy band gaps and lattice parameters evaluated with the Heyd-Scuseria-Ernzerhof screened hybrid functional," *J. Chem. Phys.*, **123**, 174101 (2005).

[149] A. U. Ortiz, A. Boutin, A. H. Fuchs, and F. m. c.-X. Coudert, "Anisotropic Elastic Properties of Flexible Metal-Organic Frameworks: How Soft are Soft Porous Crystals?" *Phys. Rev. Lett.*, **109**, 195502 (2012).

[150] H. Wu, T. Yildirim, and W. Zhou, "Exceptional Mechanical Stability of Highly Porous Zirconium Metal-Organic Framework UiO-66 and Its Important Implications," *The J. Phys. Chem. Lett.*, **4**, 925 (2013).

[151] M. R. Ryder, L. Doná, J. G. Vitillo, and B. Civalleri, "Understanding and Controlling the Dielectric Response of Metal-Organic Frameworks," *ChemPlusChem*, **83**, 308 (2018).

[152] S. Ling and B. Slater, "Unusually Large Band Gap Changes in Breathing Metal-Organic Framework Materials," *J. Phys. Chem. C*, **119**, 16667 (2015).

[153] S. O. Odoh, C. J. Cramer, D. G. Truhlar, and L. Gagliardi, "Quantum-Chemical Characterization of the Properties and Reactivities of Metal–Organic Frameworks," *Chem. Rev.*, **115**, 6051 (2015).

[154] R. Mercado, R.-S. Fu, A. V. Yakutovich, L. Talirz, M. Haranczyk, and B. Smit, "In Silico Design of 2D and 3D Covalent Organic Frameworks for Methane Storage Applications," *Chem. Mater.*, **30**, 5069 (2018).

[155] Y. G. Chung, J. Camp, M. Haranczyk, B. J. Sikora, W. Bury, V. Krungleviciute, T. Yildirim, O. K. Farha, D. S. Sholl, and R. Q. Snurr, "Computation-Ready, Experimental Metal-Organic Frameworks: A Tool To Enable High-Throughput Screening of Nanoporous Crystals," *Chem. Mater.*, **26**, 6185 (2014).

[156] J.-R. Li, R. J. Kuppler, and H.-C. Zhou, "Selective gas adsorption and separation in metal-organic frameworks," *Chem. Soc. Rev.*, **38**, 1477 (2009).

[157] L. Sun, M. G. Campbell, and M. Dincă, "Electrically Conductive Porous Metal-Organic Frameworks," *Angew. Chem. Int. Ed.*, **55**, 3566 (2016).

[158] R. Grau-Crespo, A. Aziz, A. W. Collins, R. Crespo-Otero, N. C. Hernández, L. M. Rodriguez-Albelo, A. R. Ruiz-Salvador, S. Calero, and S. Hamad, "Modelling a Linker Mix-and-Match Approach for Controlling the Optical Excitation Gaps and Band Alignment of Zeolitic Imidazolate Frameworks," *Angewandte Chemie (International ed. in English)*, **55**, 16012 (2016).

[159] K. T. Butler, S. D. Worrall, C. D. Molloy, C. H. Hendon, M. P. Attfield, R. A. W. Dryfe, and A. Walsh, "Electronic structure design for nanoporous, electrically conductive zeolitic imidazolate frameworks," *J. Mater. Chem. C*, **5**, 7726 (2017).

[160] K. Van den Eeckhout, P. F. Smet, and D. Poelman, "Persistent luminescence in Eu2+-doped compounds: a review," *Materials*, **3**, 2536 (2010).

[161] P. Smet, K. Korthout, J. V. Haecke, and D. Poelman, "Using rare earth doped thiosilicate phosphors in white light emitting LEDs: Towards low colour temperature and high colour rendering," *Mater. Sci. and Engineering: B*, **146**, 264 (2008).

[162] J. J. Joos, P. F. Smet, L. Seijo, and Z. Barandiarán, "Insights into the complexity of the excited states of Eu-doped luminescent materials," *Inorg. Chem. Front.*, **7**, 871 (2020).

[163] X. Qin, X. Liu, W. Huang, M. Bettinelli, and X. Liu, "Lanthanide-Activated Phosphors Based on 4f-5d Optical Transitions: Theoretical and Experimental Aspects," *Chem. Rev.*, **117**, 4488 (2017).

[164] G. S. Kumar and G. L. Devi, "Review on Modified TiO_2 Photocatalysis under UV/Visible Light: Selected Results and Related Mechanisms on Interfacial Charge Carrier Transfer Dynamics," *J. Phys. Chem. A*, **115**, 13211 (2011).

[165] Y. Yaoguang, C. Gang, Z. Yansong, and H. Zhonghui, "Recent advances in rare-earth elements modification of inorganic semiconductor-based photocatalysts for efficient Sol. Energy conversion: A review," *J. Rare Earth*, **33**, 453 (2015).

[166] E. Schrödinger, "An undulatory theory of the mechanics of atoms and molecules," *Phys. Rev.*, **28**, 1049 (1926).

[167] M. Born and R. Oppenheimer, "Zur Quantentheorie der Molekeln," *Ann. Phys.*, **389**, 457 (1927).

[168] A. J. Cohen, P. Mori-Sánchez, and W. Yang, "Challenges for Density Functional Theory," *Chem. Rev.*, **112**, 289 (2012).

[169] R. J. Bartlett and M. Musiał, "Coupled-cluster theory in quantum chemistry," *Rev. Mod. Phys.*, **79**, 291 (2007).

[170] S. R. White, "Density matrix formulation for quantum renormalization groups," *Phys. Rev. Lett.*, **69**, 2863 (1992).

[171] N. Nakatani and G. K.-L. Chan, "Efficient tree tensor network states (TTNS) for quantum chemistry: Generalizations of the density matrix renormalization group algorithm," *J. Chem. Phys.*, **138**, 134113 (2013).

[172] V. Murg, F. Verstraete, O. Legeza, and R. M. Noack, "Simulating strongly correlated quantum systems with tree tensor networks," *Phys. Rev. B*, **82** (2010), 10.1103/physrevb.82.205105.

[173] K. Gunst, F. Verstraete, S. Wouters, O. Legeza, and D. Van Neck, "T3NS: Three-Legged Tree Tensor Network States," *J. Chem. Theory Comput.*, **14**, 2026 (2018).

[174] K. Gunst, F. Verstraete, and D. Van Neck, "Three-Legged Tree Tensor Networks with SU(2) and Molecular Point Group Symmetry," *J. Chem. Theory Comput.*, **15**, 2996 (2019).

[175] B. Vlaisavljevich, J. Huck, Z. Hulvey, K. Lee, J. A. Mason, J. B. Neaton, J. R. Long, C. M. Brown, D. Alfè, A. Michaelides, and B. Smit, "Performance of van der Waals corrected functionals for guest adsorption in the M_2(dobdc) metal-organic frameworks," *J. Phys. Chem. A*, **4139-4151**, 121 (2017).

[176] R. M. Martin, *Electronic Structure: Basic Theory and Practical Methods* (Cambridge University Press, 2004).

[177] M. G. Medvedev, I. S. Bushmarinov, J. Sun, J. P. Perdew, and K. A. Lyssenko, "Density functional theory is straying from the path toward the exact functional," *Science*, **355**, 49 (2017).

[178] R. J. Maurer, C. Freysoldt, A. M. Reilly, J. G. Brandenburg, O. T. Hofmann, T. Björkman, S. Lebègue, and A. Tkatchenko, "Advances in density-functional calculations for materials modeling," *Annu. Rev. Mater. Res.*, **49** (2019).

[179] R. Peverati and D. G. Truhlar, "Quest for a universal density functional: the accuracy of density functionals across a broad spectrum of databases in chemistry and physics," *Philosophical Transactions of the Royal Society A: Mathematical, Physical and Eng. Sci.*, **372**, 20120476 (2014).

[180] N. Mardirossian and M. Head-Gordon, "Thirty years of density functional theory in computational chemistry: an overview and extensive assessment of 200 density functionals," *Mol. Phys.*, **115**, 2315 (2017).

[181] S. Kurth, J. P. Perdew, and P. Blaha, "Molecular and solid-state tests of density functional approximations: LSD, GGAs, and meta-GGAs," *Int. J. Quantum Chem.*, **75**, 889 (1999).

[182] F. Tran, J. Stelzl, and P. Blaha, "Rungs 1 to 4 of DFT Jacob's ladder: extensive test on the lattice constant, bulk modulus, and cohesive energy of solids," *J. Chem. Phys.*, **144**, 204120 (2016).

[183] J. C. Slater, "Wave Functions in a Periodic Potential," *Phys. Rev.*, **51**, 846 (1937).

[184] O. K. Andersen, "Linear methods in band theory," *Phys. Rev. B*, **12**, 3060 (1975).

[185] E. Sjöstedt, L. Nordström, and D. Singh, "An alternative way of linearizing the augmented plane-wave method," *Solid State Commun.*, **114**, 15 (2000).

[186] G. K. H. Madsen, P. Blaha, K. Schwarz, E. Sjöstedt, and L. Nordström, "Efficient linearization of the augmented plane-wave method," *Phys. Rev. B*, **64**, 195134 (2001).

[187] N. Troullier and J. L. Martins, "Efficient pseudopotentials for plane-wave calculations," *Phys. Rev. B*, **43**, 1993 (1991).

[188] P. E. Blöchl, "Projector augmented-wave method," *Phys. Rev. B*, **50**, 17953 (1994).

[189] G. Kresse and D. Joubert, "From ultrasoft pseudopotentials to the projector augmented-wave method," *Phys. Rev. B*, **59**, 1758 (1999).

[190] G. Kresse and J. Furthmüller, "Efficient iterative schemes for ab initio total-energy calculations using a plane-wave basis set," *Phys. Rev. B*, **54**, 11169 (1996).

[191] M. J. Frisch, G. W. Trucks, H. B. Schlegel, G. E. Scuseria, M. A. Robb, J. R. Cheeseman, G. Scalmani, V. Barone, G. A. Petersson, H. Nakatsuji, X. Li, M. Caricato, A. V. Marenich, J. Bloino, B. G. Janesko, R. Gomperts, B. Mennucci, H. P. Hratchian, J. V. Ortiz, A. F. Izmaylov, J. L. Sonnenberg, D. Williams-Young, F. Ding, F. Lipparini, F. Egidi, J. Goings, B. Peng, A. Petrone, T. Henderson, D. Ranasinghe, V. G. Zakrzewski, J. Gao, N. Rega, G. Zheng, W. Liang, M. Hada, M. Ehara, K. Toyota, R. Fukuda, J. Hasegawa, M. Ishida, T. Nakajima, Y. Honda, O. Kitao, H. Nakai, T. Vreven, K. Throssell, J. A. Montgomery, Jr., J. E. Peralta, F. Ogliaro, M. J. Bearpark, J. J. Heyd, E. N. Brothers, K. N. Kudin, V. N. Staroverov, T. A. Keith, R. Kobayashi, J. Normand, K. Raghavachari, A. P. Rendell, J. C. Burant, S. S. Iyengar, J. Tomasi, M. Cossi, J. M. Millam, M. Klene, C. Adamo, R. Cammi, J. W. Ochterski, R. L. Martin, K. Morokuma, O. Farkas, J. B. Foresman, and D. J. Fox, "Gaussian16 Revision C.01," (2016), gaussian Inc. Wallingford CT.

[192] M. A. L. Marques, C. A. Ullrich, F. Nogueira, A. Rubio, K. Burke, and E. K. U. Gross, *Time-Dependent Density Functional Theory*, Vol. 55 (Springer, 2004).

[193] E. Runge and E. K. U. Gross, "Density-functional theory for time-dependent systems," *Phys. Rev. Lett.*, **52**, 997 (1984).

[194] G. Strinati, "Application of the greens functions method to the study of the optical properties of semiconductors," *Rivista del Nuovo Cimento*, **11**, 1988 (1988).

[195] G. A. Wilfried, L. Jönsson, and J. W. Wilkins, "Quasiparticle calculations in solids," (Academic press, 1999).

[196] X. Blase and C. Attaccalite, "Charge-transfer excitations in molecular donor-acceptor complexes within the many-body Bethe-Salpeter approach," *Appl. Phys. Lett.*, **99**, 171909 (2011).

[197] C. Faber, I. Duchemin, T. Deutsch, C. Attaccalite, V. Olevano, and X. Blase, "Electron-phonon coupling and charge-transfer excitations in organic systems from many-body perturbation theory," *J. Mater. Sci.*, **47**, 7472 (2012).

[198] J. Hutter, "Excited state nuclear forces from the Tamm-Dancoff approximation to time-dependent density functional theory within the plane wave basis set framework," *J. Chem. Phys.*, **118**, 3928 (2003).

[199] X. Andrade, S. Botti, M. A. L. Marques, and A. Rubio, "Time-dependent density functional theory scheme for efficient calculations of dynamic (hyper)polarizabilities," *J. Chem. Phys.*, **126**, 184106 (2007).

[200] N. T. Maitra, I. Souza, and K. Burke, "Current-density functional theory of the response of solids," *Phys. Rev. B*, **68**, 045109 (2003).

[201] C. Attaccalite, "Non-linear response in extended systems: a real-time approach," (2016), arXiv:1609.09639 [cond-mat.mtrl-sci] .

[202] A. Dreuw and M. Head-Gordon, "Single-Reference ab Initio Methods for the Calculation of Excited States of Large Molecules," *Chem. Rev.*, **105**, 4009 (2005).

[203] V. Barone, M. Biczysko, J. Bloino, L. Carta, and A. Pedone, "Environmental and dynamical effects on the optical properties of molecular systems by time-independent and time-dependent approaches: Coumarin derivatives as test cases," *Comput. Theor. Chem.*, **1037**, 35 (2014).

[204] A. D. Laurent, C. Adamo, and D. Jacquemin, "Dye chemistry with time-dependent density functional theory," *Phys. Chem. Chem. Phys.*, **16**, 14334 (2014).

[205] M. E. Casida, C. Jamorski, K. C. Casida, and D. R. Salahub, "Molecular excitation energies to high-lying bound states from time-dependent density-functional response theory: Characterization and correction of the time-dependent local density approxination ionization threshold," *J. Chem. Phys.*, **108**, 4439 (1998).

[206] T.-C. Chiang, J. A. Knapp, M. Aono, and D. E. Eastman, "Angle-resolved photoemission, valence-band dispersions E($\overline{k}$), and electron and hole lifetimes for GaAs," *Phys. Rev. B*, **21**, 3513 (1980).

[207] A. Damascelli, "Probing the Electronic Structure of Complex Systems by ARPES," *Phys. Scr.*, **T109**, 61 (2004).

[208] K. C. Pandey and J. C. Phillips, "Nonlocal pseudopotentials for Ge and GaAs," *Phys. Rev. B*, **9**, 1552 (1974).

[209] E. J. Baerends, O. V. Gritsenko, and R. van Meer, "The Kohn-Sham gap, the fundamental gap and the optical gap: the physical meaning of occupied and virtual Kohn-Sham orbital energies," *Phys. Chem. Chem. Phys.*, **15**, 16408 (2013).

[210] R. van Meer, O. V. Gritsenko, and E. J. Baerends, "Physical Meaning of Virtual Kohn-Sham Orbitals and Orbital Energies: An Ideal Basis for the Description of Molecular Excitations," *J. Chem. Theory Comput.*, **10**, 4432 (2014).

[211] D. E. P. Vanpoucke, "*Hive*," *Version 3.x*, http://dannyvanpoucke.be (2015).

[212] G. Onida, L. Reining, and A. Rubio, "Electronic excitations: density-functional versus many-body Green's-function approaches," *Rev. Mod. Phys.*, **74**, 601 (2002).

[213] S. Kümmel and L. Kronik, "Orbital-dependent density functionals: Theory and applications," *Rev. Mod. Phys.*, **80**, 3 (2008).

[214] T. Musho, J. Li, and N. Wu, "Band gap modulation of functionalized metal-organic frameworks," *Phys. Chem. Chem. Phys.*, **16**, 23646 (2014).

[215] L. Landau, "Kinetic Equation Approach," *Sov. Phys. JETP*, **3**, 920 (1957).

[216] L. Kronik, T. Stein, S. Refaely-Abramson, and R. Baer, "Excitation Gaps of Finite-Sized Systems from Optimally Tuned Range-Separated Hybrid Functionals," *J. Chem. Theory Comput.*, **8**, 1515 (2012).

[217] A. J. Cohen, P. Mori-Sánchez, and W. Yang, "Fractional charge perspective on the band gap in density-functional theory," *Phys. Rev. B*, **77**, 115123 (2008).

[218] O. Gritsenko and E. J. Baerends, "The analog of Koopmans' theorem for virtual Kohn–Sham orbital energies," *Can. J. Chem.*, **87**, 1383 (2009).

[219] U. Salzner and R. Baer, "Koopmans' springs to life," *J. Chem. Phys.*, **131**, 231101 (2009).

[220] R. Baer, E. Livshits, and U. Salzner, "Tuned Range-Separated Hybrids in Density Functional Theory," *Annu. Rev. Phys. Chem.*, **61**, 85 (2010).

[221] I. Dabo, A. Ferretti, N. Poilvert, Y. Li, N. Marzari, and M. Cococcioni, "Koopmans' condition for density-functional theory," *Phys. Rev. B*, **82**, 115121 (2010).

[222] T. Tsuneda, J.-W. Song, S. Suzuki, and K. Hirao, "On Koopmans' theorem in density functional theory," *J. Chem. Phys.*, **133**, 174101 (2010).

[223] J. P. Perdew, R. G. Parr, M. Levy, and J. L. Balduz, "Density-Functional Theory for Fractional Particle Number: Derivative Discontinuities of the Energy," *Phys. Rev. Lett.*, **49**, 1691 (1982).

[224] J. P. Perdew and M. Levy, "Physical Content of the Exact Kohn-Sham Orbital Energies: Band Gaps and Derivative Discontinuities," *Phys. Rev. Lett.*, **51**, 1884 (1983).

[225] L. Kleinman, "Significance of the highest occupied Kohn-Sham eigenvalue," *Phys. Rev. B*, **56**, 12042 (1997).

[226] S. Hamel, P. Duffy, M. E. Casida, and D. R. Salahub, "Kohn–Sham orbitals and orbital energies: fictitious constructs but good approximations all the same," *J. Electron Spectrosc. Relat. Phenom.*, **123**, 345 (2002).

[227] R. Stowasser and R. Hoffmann, "What Do the Kohn-Sham Orbitals and Eigenvalues Mean?" *J. Am. Chem. Soc.*, **121**, 3414 (1999).

[228] P. Politzer and F. Abu-Awwad, "A comparative analysis of Hartree-Fock and Kohn-Sham orbital energies," *Theor. Chem. Acc.*, **99**, 83 (1998).

[229] J.-L. Bredas, "Mind the gap!" *Mater. Horiz.*, **1**, 17 (2014).

[230] G. Zhang and C. B. Musgrave, "Comparison of DFT Methods for Molecular Orbital Eigenvalue Calculations," *J. Phys. Chem. A*, **111**, 1554 (2007).

[231] E. J. Baerends, "Density functional approximations for orbital energies and total energies of molecules and solids," *J. Chem. Phys.*, **149**, 054105 (2018).

[232] J. P. Perdew, W. Yang, K. Burke, Z. Yang, E. K. U. Gross, M. Scheffler, G. E. Scuseria, T. M. Henderson, I. Y. Zhang, A. Ruzsinszky, H. Peng, J. Sun, E. Trushin, and A. Görling, "Understanding band gaps of solids in generalized Kohn–Sham theory," *Proceedings of the National Academy of Sciences*, **114**, 2801 (2017).

[233] B. G. Janesko, T. M. Henderson, and G. E. Scuseria, "Screened hybrid density functionals for solid-state chemistry and physics," *Phys Chem Chem Phys*, **11**, 443 (2009).

[234] P. Rinke, A. Qteish, J. Neugebauer, and M. Scheffler, "Exciting prospects for solids: Exact-exchange based functionals meet quasiparticle energy calculations," *physica status solidi (b)*, **245**, 929 (2008).

[235] D. P. Chong, O. V. Gritsenko, and E. J. Baerends, "Interpretation of the Kohn-Sham orbital energies as approximate vertical ionization potentials," *J. Chem. Phys.*, **116**, 1760 (2002).

[236] K. Sakaushi, G. Nickerl, H. C. Kandpal, L. Cano-Cortés, T. Gemming, J. Eckert, S. Kaskel, and J. van den Brink, "Polymeric Frameworks as Organic Semiconductors with Controlled Electronic Properties," *The J. Phys. Chem. Lett.*, **4**, 2977 (2013).

[237] A. De Vos, K. Lejaeghere, D. E. P. Vanpoucke, J. J. Joos, P. F. Smet, and K. Hemelsoet, "First-Principles Study of Antisite Defect Configurations in ZnGa2O4:Cr Persistent Phosphors," *Inorg. Chem.*, **55**, 2402 (2016).

[238] C. Persson, Y.-J. Zhao, S. Lany, and A. Zunger, "n-type doping of $\mathrm{CuInSe_2}$ and $\mathrm{CuGaSe_2}$," *Phys. Rev. B*, **72**, 035211 (2005).

[239] A. Janotti and C. G. Van de Walle, "Native point defects in ZnO," *Phys. Rev. B*, **76**, 165202 (2007).

[240] H. Raebiger, S. Lany, and A. Zunger, "Electronic structure, donor and acceptor transitions, and magnetism of $3d$ impurities in In_2O_3 and ZnO," *Phys. Rev. B*, **79**, 165202 (2009).

[241] E. M. Benecha and E. B. Lombardi, "Cr in diamond: A first-principles study," *Phys. Rev. B*, **84**, 235201 (2011).

[242] A. Chakrabarty and C. H. Patterson, "Transition levels of defects in ZnO: Total energy and Janak's theorem methods," *J. Chem. Phys.*, **137**, 054709 (2012).

[243] H. Dixit, N. Tandon, S. Cottenier, R. Saniz, D. Lamoen, and B. Partoens, "First-principles study of possible shallow donors in $ZnAl_2O_4$ spinel," *Phys. Rev. B*, **87**, 174101 (2013).

[244] C. Freysoldt, B. Grabowski, T. Hickel, J. Neugebauer, G. Kresse, A. Janotti, and C. G. Van de Walle, "First-principles calculations for point defects in solids," *Rev. Mod. Phys.*, **86**, 253 (2014).

[245] R. T. Tung, "The physics and chemistry of the Schottky barrier height," *Applied Physics Reviews*, **1**, 011304 (2014).

[246] W. Mönch, *Semiconductor surfaces and interfaces*, Vol. 26 (Springer Science & Business Media, 2013).

[247] Z. Zhang and J. T. Yates, "Band Bending in Semiconductors: Chemical and Physical Consequences at Surfaces and Interfaces," *Chem. Rev.*, **112**, 5520 (2012).

[248] R. L. Anderson, "Germanium-Gallium Arsenide Heterojunctions [Letter to the Editor]," *IBM J. Res. Dev.*, **4**, 283 (1960).

[249] K. T. Butler, C. H. Hendon, and A. Walsh, "Electronic Chemical Potentials of Porous Metal-Organic Frameworks," *J. Am. Chem. Soc.*, **136**, 2703 (2014).

[250] X.-P. Wu, L. Gagliardi, and D. G. Truhlar, "Cerium Metal–Organic Framework for Photocatalysis," *J. Am. Chem. Soc.*, **140**, 7904 (2018).

[251] L. J. Sham and M. Schlüter, "Density-Functional Theory of the Energy Gap," *Phys. Rev. Lett.*, **51**, 1888 (1983).

[252] I. E. Castelli, F. Hüser, M. Pandey, H. Li, K. S. Thygesen, B. Seger, A. Jain, K. A. Persson, G. Ceder, and K. W. Jacobsen, "New Light-Harvesting Materials Using Accurate and Efficient Bandgap Calculations," *Adv. Energy Mater.*, **5**, 1400915 (2015).

[253] J. L. Bao, L. Gagliardi, and D. G. Truhlar, "Self-Interaction Error in Density Functional Theory: An Appraisal," *The J. Phys. Chem. Lett.*, **9**, 2353 (2018).

[254] A. Görling and M. Levy, "Correlation-energy functional and its high-density limit obtained from a coupling-constant perturbation expansion," *Phys. Rev. B*, **47**, 13105 (1993).

[255] A. Seidl, A. Görling, P. Vogl, J. A. Majewski, and M. Levy, "Generalized Kohn-Sham schemes and the band-gap problem," *Phys. Rev. B*, **53**, 3764 (1996).

[256] J. Heyd, G. E. Scuseria, and M. Ernzerhof, "Hybrid functionals based on a screened Coulomb potential," *J. Chem. Phys.*, **118**, 8207 (2003).

[257] K. Hummer, J. Harl, and G. Kresse, "Heyd-Scuseria-Ernzerhof hybrid functional for calculating the lattice dynamics of semiconductors," *Phys. Rev. B*, **80**, 115205 (2009).

[258] C. Adamo and V. Barone, "Toward reliable density functional methods without adjustable parameters: The PBE0 model," *J. Chem. Phys.*, **110**, 6158 (1999).

[259] A. J. Garza and G. E. Scuseria, "Predicting Band Gaps with Hybrid Density Functionals," *The J. Phys. Chem. Lett.*, **7**, 4165 (2016).

[260] L. Hedin, "New Method for Calculating the One-Particle Green's Function with Application to the Electron-Gas Problem," *Phys. Rev.*, **139**, A796 (1965).

[261] M. S. Hybertsen and S. G. Louie, "Electron correlation in semiconductors and insulators: Band gaps and quasiparticle energies," *Phys. Rev. B*, **34**, 5390 (1986).

[262] D. M. Bylander and L. Kleinman, "Good semiconductor band gaps with a modified local-density approximation," *Phys. Rev. B*, **41**, 7868 (1990).

[263] F. Gygi and A. Baldereschi, "Quasiparticle energies in semiconductors: Self-energy correction to the local-density approximation," *Phys. Rev. Lett.*, **62**, 2160 (1989).

[264] P. Sánchez-Friera and R. W. Godby, "Efficient Total Energy Calculations from Self-Energy Models," *Phys. Rev. Lett.*, **85**, 5611 (2000).

[265] F. Fuchs, J. Furthmüller, F. Bechstedt, M. Shishkin, and G. Kresse, "Quasiparticle band structure based on a generalized Kohn-Sham scheme," *Phys. Rev. B*, **76**, 115109 (2007).

[266] A. Schleife, C. Rödl, F. Fuchs, J. Furthmüller, and F. Bechstedt, "Strain influence on valence-band ordering and excitons in ZnO: An ab initio study," *Appl. Phys. Lett.*, **91**, 241915 (2007).

[267] J. P. Perdew, K. Burke, and M. Ernzerhof, "Generalized gradient approximation made simple," *Phys. Rev. Lett.*, **77**, 3865 (1996).

[268] A. D. Becke, "Density-functional thermochemistry. III. The role of exact exchange," *J. Chem. Phys.*, **98**, 5648 (1993).

[269] T. Yanai, D. P. Tew, and N. C. Handy, "A new hybrid exchange–correlation functional using the Coulomb-attenuating method (CAM-B3LYP)," *Chem. Phys. Lett.*, **393**, 51 (2004).

[270] Y. Zhao and D. G. Truhlar, "The M06 suite of density functionals for main group thermochemistry, thermochemical kinetics, noncovalent

interactions, excited states, and transition elements: two new functionals and systematic testing of four M06-class functionals and 12 other functionals," *Theor. Chem. Acc.*, **120**, 215 (2008).

[271] J. Heyd, G. E. Scuseria, and M. Ernzerhof, "Erratum: "Hybrid functionals based on a screened Coulomb potential" [J. Chem. Phys. 118, 8207 (2003)]," *J. Chem. Phys.*, **124**, 219906 (2006).

[272] M. A. Nasalevich, M. G. Goesten, T. J. Savenije, F. Kapteijn, and J. Gascon, "Enhancing optical absorption of metal-organic frameworks for improved visible light photocatalysis," *Chem. Commun.*, **49**, 10575 (2013).

[273] C. H. Hendon, D. Tiana, and A. Walsh, "Conductive metal-organic frameworks and networks: fact or fantasy?" *Phys. Chem. Chem. Phys.*, **14**, 13120 (2012).

[274] T. Zhang and W. Lin, "Metal-organic frameworks for artificial photosynthesis and photocatalysis," *Chem. Soc. Rev.*, **43**, 5982 (2014).

[275] J. G. Santaclara, F. Kapteijn, J. Gascon, and M. A. van der Veen, "Understanding metal-organic frameworks for photocatalytic solar fuel production," *CrystEngComm*, **19**, 4118 (2017).

[276] S.-N. Kim, Y.-R. Lee, S.-H. Hong, M.-S. Jang, and W.-S. Ahn, "Pilot-scale synthesis of a zirconium-benzenedicarboxylate UiO-66 for CO_2 adsorption and catalysis," *Catal. Today*, **245**, 54 (2015).

[277] S. Biswas and P. Van Der Voort, "A General Strategy for the Synthesis of Functionalised UiO-66 Frameworks: Characterisation, Stability and CO_2 Adsorption Properties," *Eur. J. Inorg. Chem.*, **2013**, 2154 (2013).

[278] M. J. Katz, Z. J. Brown, Y. J. Colón, P. W. Siu, K. A. Scheidt, R. Q. Snurr, J. T. Hupp, and O. K. Farha, "A facile synthesis of UiO-66, UiO-67 and their derivatives," *Chem. Commun.*, **49**, 9449 (2013).

[279] S. M. Chavan, G. C. Shearer, S. Svelle, U. Olsbye, F. Bonino, J. Ethiraj, K. Lillerud, and S. Bordiga, "Synthesis and Characterization of Amine-Functionalized Mixed-Ligand Metal-Organic Frameworks of UiO-66 Topology," *Inorg. Chem.*, **53**, 9509 (2014).

[280] P. Deria, J. E. Mondloch, O. Karagiaridi, W. Bury, J. T. Hupp, and O. K. Farha, "Beyond post-synthesis modification: evolution of metal-organic frameworks via building block replacement." *Chem. Soc. Rev.*, **43**, 5896 (2014).

[281] B. Bueken, F. Vermoortele, M. J. Cliffe, M. T. Wharmby, D. Foucher, J. Wieme, L. Vanduyfhuys, C. Martineau, N. Stock, F. Taulelle, V. Van Speybroeck, A. L. Goodwin, and D. E. De Vos, "A Breathing Zirconium Metal-Organic Framework with Reversible Loss of Crystallinity by Correlated Nanodomain Formation," *Chem. Eur. J.*, **22**, 3264 (2016).

[282] A. Wang, Y. Zhou, Z. Wang, M. Chen, L. Sun, and X. Liu, "Titanium incorporated with UiO-66(Zr)-type Metal-Organic Framework (MOF) for photocatalytic application," *RSC Adv.*, **6**, 3671 (2015).

[283] M. Lammert, M. T. Wharmby, S. Smolders, B. Bueken, A. Lieb, K. A. Lomachenko, D. E. De Vos, and N. Stock, "Cerium-based metal organic frameworks with UiO-66 architecture: synthesis, properties and redox catalytic activity," *Chem. Commun.*, **51**, 12578 (2015).

[284] Z. Hu, A. Nalaparaju, Y. Peng, J. Jiang, and D. Zhao, "Modulated Hydrothermal Synthesis of UiO-66(Hf)-Type Metal-Organic Frameworks for Optimal Carbon Dioxide Separation," *Inorg. Chem.*, **55**, 1134 (2016).

[285] C. G. Silva, I. Luz, F. X. Llabrés i Xamena, A. Corma, and H. García, "Water Stable Zr-Benzenedicarboxylate Metal-Organic Frameworks as Photocatalysts for Hydrogen Generation," *Chem. Eur. J.*, **16**, 11133 (2010).

[286] J. Long, S. Wang, Z. Ding, S. Wang, Y. Zhou, L. Huang, and X. Wang, "Amine-functionalized zirconium metal-organic framework as efficient visible-light photocatalyst for aerobic organic transformations," *Chem. Commun.*, **48**, 11656 (2012).

[287] D. Sun, Y. Fu, W. Liu, L. Ye, D. Wang, L. Yang, X. Fu, and Z. Li, "Studies on Photocatalytic CO_2 Reduction over NH_2-UiO-66(Zr) and Its Derivatives: Towards a Better Understanding of Photocatalysis on Metal-Organic Frameworks," *Chem. Eur. J.*, **19**, 14279 (2013).

[288] L. Shen, S. Liang, W. Wu, R. Liang, and L. Wu, "Multifunctional NH_2-mediated zirconium metal-organic framework as an efficient visible-light-driven photocatalyst for selective oxidation of alcohols and reduction of aqueous Cr(VI)," *Dalton Trans.*, **42**, 13649 (2013).

[289] L. Shen, R. Liang, M. Luo, F. Jing, and L. Wu, "Electronic effects of ligand substitution on metal-organic framework photocatalysts: the case study of UiO-66," *Phys. Chem. Chem. Phys.*, **17**, 117 (2014).

[290] T. Goh, C. Xiao, M. Raghu, X. Li, and W. Huang, "Utilizing mixed-linker zirconium based metal-organic frameworks to enhance the visible light photocatalytic oxidation of alcohol," *Chem. Eng. Sci.*, **124**, 45 (2015).

[291] A. E. Kozlovac, V. N. Panchenko, Z. Hasan, N. A. Khan, M. N. Timofeeva, and S. H. J., "Photoreactivity of metal-organic frameworks in the decolorization of methylene blue in aqueous solution," *Catal. Today*, **266**, 136 (2016).

[292] W. Li, Z. Wang, F. Deschler, S. Gao, R. H. Friend, and A. K. Cheetham, "Chemically diverse and multifunctional hybrid organic–inorganic perovskites," *Nature Reviews Materials*, **2** (2017).

[293] J. Even, L. Pedesseau, and C. Katan, "Understanding Quantum Confinement of Charge Carriers in Layered 2D Hybrid Perovskites," *ChemPhysChem*, **15**, 3733 (2014).

[294] T. Braeckevelt, A. De Vos, K. Lejaeghere, and V. Van Speybroeck, *Designing 2D hybrid organic-inorganic perovskites for game-changing photovoltaics*, Master's thesis, Ghent University.

[295] C. Katan, N. Mercier, and J. Even, "Quantum and Dielectric Confinement Effects in Lower-Dimensional Hybrid Perovskite Semiconductors," *Chem. Rev.*, **119**, 3140 (2019).

[296] D. A. Egger, Z.-F. Liu, J. B. Neaton, and L. Kronik, "Reliable Energy Level Alignment at Physisorbed Molecule–Metal Interfaces from Density Functional Theory," *Nano Lett.*, **15**, 2448 (2015).

[297] Q. Fu, D. Nabok, and C. Draxl, "Energy-Level Alignment at the Interface of Graphene Fluoride and Boron Nitride Monolayers: An Investigation by Many-Body Perturbation Theory," *J. Phys. Chem. C*, **120**, 11671 (2016).

[298] M. T. Greiner, M. G. Helander, W.-M. Tang, Z.-B. Wang, J. Qiu, and Z.-H. Lu, "Universal energy-level alignment of molecules on metal oxides," *Nat. Mater.*, **11**, 76 EP (2011).

[299] S. Thomas, H. Li, C. Zhong, M. Matsumoto, W. R. Dichtel, and J.-L. Bredas, "Electronic Structure of Two-Dimensional π-Conjugated Covalent Organic Frameworks," *Chem. Mater.*, **31**, 3051 (2019).

[300] Y. Bai, Y. Dou, L.-H. Xie, W. Rutledge, J.-R. Li, and H.-C. Zhou, "Zr-based metal-organic frameworks: design, synthesis, structure, and applications," *Chem. Soc. Rev.*, **45**, 2327 (2016).

[301] Y. Lee, S. Kim, J. Kang, and S. M. Cohen, "Photocatalytic CO_2 reduction by a mixed metal (Zr/Ti), mixed ligand metal-organic framework under visible light irradiation," *Chem. Commun.*, **51**, 5735 (2015).

[302] M. Nasalevich, C. H. Hendon, J. G. Santaclara, K. Svane, B. van der Linden, S. L. Veber, M. V. Fedin, A. J. Houtepen, M. A. van der Veen, F. Kapteijn, A. Walsh, and J. Gascon, "Electronic origins of photocatalytic activity in d^0 metal organic frameworks," *Sci. Rep.*, **6**, 23676 (2016).

[303] Y. Horiuchi, T. Toyao, M. Saito, K. Mochizuki, M. Iwata, H. Higashimura, M. Anpo, and M. Matsuoka, "Visible-Light-Promoted Photocatalytic Hydrogen Production by Using an Amino-Functionalized Ti(IV) Metal-Organic Framework," *J. Phys. Chem. C.*, **116**, 20848 (2012).

[304] R. J. Marshall and R. S. Forgan, "Postsynthetic Modification of Zirconium Metal-Organic Frameworks," *Eur. J. Inorg. Chem.*, **2016**, 4310 (2016).

[305] M. Kim, J. F. Cahill, H. Fei, K. A. Prather, and S. M. Cohen, "Postsynthetic Ligand and Cation Exchange in Robust Metal-Organic Frameworks," *J. Am. Chem. Soc.*, **134**, 18082 (2012).

[306] S. J. Smith, B. P. Ladewig, A. J. Hill, C. Lau, and M. R. Hill, "Post-synthetic Ti Exchanged UiO-66 Metal-Organic Frameworks that Deliver Exceptional Gas Permeability in Mixed Matrix Membranes," *Sci. Rep.*, **5**, 7823 (2015).

[307] C. Lau, R. Babarao, and M. R. Hill, "A route to drastic increase of CO_2 uptake in Zr metal organic framework UiO-66," *Chem. Commun.*, **49**, 3634 (2013).

[308] A. Yasin, J. Li, N. Wu, and T. Musho, "Study of the inorganic substitution in a functionalized UiO-66 metal-organic framework," *Phys. Chem. Chem. Phys.*, **18**, 12748 (2016).

[309] A. Santiago-Portillo, H. Baldovi, T. García, S. Navalon, P. Atienzar, B. Ferrer, M. Alvaro, H. Garcia, and Z. Li, "Ti as Mediator in the Photoinduced Electron Transfer of Mixed-Metal NH_2-UiO66(Zr/Ti). Transient Absorption Spectroscopy Study and Application in Photovoltaic Cell," *J. Phys. Chem. C*, **121**, 7015 (2017).

[310] D. Sun, W. Liu, M. Qiu, Y. Zhang, and Z. Li, "Introduction of a mediator for enhancing photocatalytic performance via post-synthetic metal exchange in metal-organic frameworks (MOFs)," *Chem. Commun.*, **51**, 2056 (2015).

[311] L. Yang, E. Ganz, S. Svelle, and M. Tilset, "Computational exploration of newly synthesized zirconium metal-organic frameworks UiO-66, -67, -68 and analogues," *J. Mater. Chem. C*, **2**, 7111 (2014).

[312] P. Cheng, *Lanthanide Metal-Organic Frameworks*, Struct. Bond., Vol. 164 (Springer Berlin Heidelberg, 2014).

[313] H. Xu, C. Cao, X. Kang, and B. Zhao, "Lanthanide-based metal-organic frameworks as luminescent probes," *Dalton Trans.*, **45**, 18003 (2016).

[314] C. Pagis, M. Ferbinteanu, G. Rothenberg, and S. Tanase, "Lanthanide-Based Metal-Organic Frameworks: Synthetic Strategies and Catalytic Applications," *ACS Catal.*, **6**, 6063 (2016).

[315] Y. Liang, G. Yang, B. Liu, Y. Yan, Z. Xi, and Y. Wang, "Four super water-stable lanthanide-organic frameworks with active uncoordinated carboxylic and pyridyl groups for selective luminescence sensing of Fe^{3+}," *Dalton Trans.*, **44**, 13325 (2015).

[316] J. Tu, X. Zeng, F. Xu, X. Wu, Y. Tian, X. Hou, and Z. Long, "Microwave-induced fast incorporation of titanium into UiO-66 metal-organic frameworks for enhanced photocatalytic properties," *Chem. Commun.*, **53**, 3361 (2017).

[317] P. Dorenbos, "A Review on How Lanthanide Impurity Levels Change with Chemistry and Structure of Inorganic Compounds," *ECS J. Solid State Sci. Tech.*, **2**, R3001 (2013).

[318] J. J. Joos, D. Poelman, and P. F. Smet, "Energy level modeling of lanthanide materials: review and uncertainty analysis," *Phys. Chem. Chem. Phys.*, **17**, 19058 (2015).

[319] L. Seijo and Z. Barandiarán, *Ab Initio Calculations on Excited States of Lanthanide Containing Materials*, Handbook on the Physics and Chemistry of Rare Earths (Elsevier, 2016).

[320] J. R. Levin, W. L. Dorfner, A. X. Dai, P. J. Carroll, and E. J. Schelter, "Density Functional Theory as a Predictive Tool for Cerium Redox Properties in Nonaqueous Solvents." *Inorg. Chem.*, **55**, 12651 (2016).

[321] C. Loschen, A. Migani, S. T. Bromley, F. Illas, and K. M. Neyman, "Density functional studies of model cerium oxide nanoparticles," *Phys. Chem. Chem. Phys.*, **10**, 5730 (2008).

[322] A. A. Minnekhanov, N. T. Le, E. A. Konstantinova, and P. K. Kashkarov, "Influence of Defects on Photoconductivity and Photocatalytic Activity of Nitrogen-Doped Titania," *Appl. Magn. Reson.*, **48**, 335 (2017).

[323] D. Chen, Z. Wang, T. Ren, H. Ding, W. Yao, R. Zong, and Y. Zhu, "Influence of Defects on the Photocatalytic Activity of ZnO," *J. Phys. Chem. C*, **118**, 15300 (2014).

[324] D. S. Sholl and R. P. Lively, "Defects in Metal-Organic Frameworks: Challenge or Opportunity?" *J. Phys. Chem. Lett.*, **6**, 3437 (2015).

[325] Z. Fang, B. Bueken, D. E. De Vos, and R. A. Fischer, "Defect-Engineered Metal-Organic Frameworks." *Angew. Chem. Int. Ed.*, **54**, 7234 (2015).

[326] G. C. Shearer, S. Chavan, J. Ethiraj, J. G. Vitillo, S. Svelle, U. Olsbye, C. Lamberti, S. Bordiga, and K. Lillerud, "Tuned to Perfection: Ironing Out the Defects in Metal-Organic Framework UiO-66," *Chem. Mater.*, **26**, 4068 (2014).

[327] G. C. Shearer, S. Chavan, S. Bordiga, S. Svelle, U. Olsbye, and K. Lillerud, "Defect Engineering: Tuning the Porosity and Composition of the Metal-Organic Framework UiO-66 via Modulated Synthesis," *Chem. Mater.*, **28**, 3749 (2016).

[328] L. Liu, Z. Chen, J. Wang, D. Zhang, Y. Zhu, S. Ling, K.-W. Huang, Y. Belmabkhout, K. Adil, Y. Zhang, B. Slater, M. Eddaoudi, and Y. Han, "Imaging defects and their evolution in a metal–organic framework at sub-unit-cell resolution," *Nat. Chem.*, **11**, 622 (2019).

[329] S. M. J. Rogge, J. Wieme, L. Vanduyfhuys, S. Vandenbrande, G. Maurin, T. Verstraelen, M. Waroquier, and V. Van Speybroeck, "Thermodynamic Insight in the High-Pressure Behavior of UiO-66: Effect of Linker Defects and Linker Expansion," *Chem. Mater.*, **28**, 5721 (2016).

[330] J. K. Bristow, K. L. Svane, D. Tiana, J. M. Skelton, J. D. Gale, and A. Walsh, "Free Energy of Ligand Removal in the Metal-Organic Frameword UiO-66," *J. Phys. Chem. C*, **120**, 9276 (2016).

[331] M. Vandichel, J. Hajek, A. Ghysels, A. De Vos, M. Waroquier, and V. Van Speybroeck, "Water coordination and dehydration processes in defective UiO-66 type metal organic frameworks," *Cryst. Eng. Comm.*, **18**, 7056 (2016).

[332] Z. Xue, K. Liu, Q. Liu, Y. Li, M. Li, C.-Y. Su, N. Ogiwara, H. Kobayashi, H. Kitagawa, M. Liu, and G. Li, "Missing-linker metal-organic frameworks for oxygen evolution reaction," *Nat. Commun.*, **10**, 5048 (2019).

[333] O. V. Gutov, M. Hevia, E. C. Escudero-Adán, and A. Shafir, "Metal-Organic Framework (MOF) Defects under Control: Insights into

the Missing Linker Sites and Their Implication in the Reactivity of Zirconium-Based Frameworks," *Inorg. Chem.*, **54**, 8396 (2015).

[334] J. Lan, D. Cao, W. Wang, and B. Smit, "Doping of Alkali, Alkaline-Earth, and Transition Metals in Covalent-Organic Frameworks for Enhancing CO_2 Capture by First-Principles Calculations and Molecular Simulations," *ACS Nano*, **4**, 4225 (2010).

[335] L. Stegbauer, K. Schwinghammer, and B. V. Lotsch, "A hydrazone-based covalent organic framework for photocatalytic hydrogen production," *Chem. Sci.*, **5**, 2789 (2014).

[336] J. Xie, S. A. Shevlin, Q. Ruan, S. J. A. Moniz, Y. Liu, X. Liu, Y. Li, C. C. Lau, Z. X. Guo, and J. Tang, "Efficient visible light-driven water oxidation and proton reduction by an ordered covalent triazine-based framework," *Energy Environ. Sci.*, **11**, 1617 (2018).

[337] C. H. Hendon, J. Bonnefoy, E. A. Quadrelli, J. Canivet, M. B. Chambers, G. Rousse, A. Walsh, M. Fontecave, and C. Mellot-Draznieks, "A Simple and Non-Destructive Method for Assessing the Incorporation of Bipyridine Dicarboxylates as Linkers within Metal-Organic Frameworks," *Chem. Eur. J.*, **22**, 3713 (2016).

[338] W. A. Maza and A. J. Morris, "Photophysical Characterization of a Ruthenium(II) Tris(2,2'-bipyridine)-Doped Zirconium UiO-67 Metal-Organic Framework," *J. Phys. Chem. C*, **118**, 8803 (2014).

[339] C.-C. Hou, T.-T. Li, S. Cao, Y. Chen, and W.-F. Fu, "Incorporation of a $[Ru(dcbpy)(bpy)_2]^{2+}$ photosensitizer and a $Pt(dcbpy)Cl_2$ catalyst into metal-organic frameworks for photocatalytic hydrogen evolution from aqueous solution," *J. Mater. Chem. A*, **3**, 10386 (2015).

[340] D. Yang, S. O. Odoh, T. C. Wang, O. K. Farha, J. T. Hupp, C. J. Cramer, L. Gagliardi, and B. C. Gates, "Metal-Organic Framework Nodes as Nearly Ideal Supports for Molecular Catalysts: NU-1000- and UiO-66-Supported Iridium Complexes," *J. Am. Chem. Soc.*, **137**, 7391 (2015).

[341] R. Palkovits, M. Antonietti, P. Kuhn, A. Thomas, and F. Schüth, "Solid Catalysts for the Selective Low-Temperature Oxidation of Methane to Methanol," *Angew. Chem. Int. Ed.*, **48**, 6909 (2009).

[342] P. Kuhn, A. Thomas, and M. Antonietti, "Toward Tailorable Porous Organic Polymer Networks: A High-Temperature Dynamic Polymerization Scheme Based on Aromatic Nitriles," *Macromolecules*, **42**, 319 (2009).

[343] S. Hug, M. E. Tauchert, S. Li, U. E. Pachmayr, and B. V. Lotsch, "A functional triazine framework based on N-heterocyclic building blocks," *J. Mater. Chem.*, **22**, 13956 (2012).

[344] S. Hug, L. Stegbauer, H. Oh, M. Hirscher, and B. V. Lotsch, "Nitrogen-Rich Covalent Triazine Frameworks as High-Performance Platforms for Selective Carbon Capture and Storage," *Chem. Mater.*, **27**, 8001 (2015).

[345] K. Kamiya, R. Kamai, K. Hashimoto, and S. Nakanishi, "Platinum-modified covalent triazine frameworks hybridized with carbon nanoparticles as methanol-tolerant oxygen reduction electrocatalysts," *Nat. Commun.*, **5**, 5040 EP (2014).

[346] K. Iwase, T. Yoshioka, S. Nakanishi, K. Hashimoto, and K. Kamiya, "Copper-Modified Covalent Triazine Frameworks as Non-Noble-Metal Electrocatalysts for Oxygen Reduction," *Angew. Chem. Int. Ed.*, **54**, 11068 (2015).

[347] K. Park, G. H. Gunasekar, N. Prakash, K.-D. Jung, and S. Yoon, "A Highly Efficient Heterogenized Iridium Complex for the Catalytic Hydrogenation of Carbon Dioxide to Formate," *ChemSusChem*, **8**, 3410 (2015).

[348] A. V. Bavykina, M. G. Goesten, F. Kapteijn, M. Makkee, and J. Gascon, "Efficient production of hydrogen from formic acid using a Covalent Triazine Framework supported molecular catalyst," *ChemSusChem*, **8**, 809 (2015).

[349] P. Puthiaraj and K. Pitchumani, "Triazine-Based Mesoporous Covalent Imine Polymers as Solid Supports for Copper-Mediated Chan-Lam Cross-Coupling N-Arylation Reactions," *Chemistry - A European Journal*, **20**, 8761 (2014).

[350] N. Salam, S. K. Kundu, R. A. Molla, P. Mondal, A. Bhaumik, and S. M. Islam, "Ag-grafted covalent imine network material for one-pot three-component coupling and hydration of nitriles to amides in aqueous medium," *RSC Adv.*, **4**, 47593 (2014).

[351] P. Kuhn, M. Antonietti, and A. Thomas, "Porous, Covalent Triazine-Based Frameworks Prepared by Ionothermal Synthesis," *Angew. Chem. Int. Ed.*, **47**, 3450 (2008).

[352] S. Hug, M. B. Mesch, H. Oh, N. Popp, M. Hirscher, J. Senker, and B. V. Lotsch, "A fluorene based covalent triazine framework with high

CO_2 and H_2 capture and storage capacities," *J. Mater. Chem. A*, **2**, 5928 (2014).

[353] P. Kuhn, A. Forget, D. Su, A. Thomas, and M. Antonietti, "From Microporous Regular Frameworks to Mesoporous Materials with Ultrahigh Surface Area: Dynamic Reorganization of Porous Polymer Networks," *J. Am. Chem. Soc.*, **130**, 13333 (2008).

[354] S. Tongay, "Special Topic: 2D Mater. and Applications," *Applied Physics Reviews*, **5**, 010401 (2018).

[355] C. K. Prier, D. A. Rankic, and D. W. C. MacMillan, "Visible Light Photoredox Catalysis with Transition Metal Complexes: Applications in Organic Synthesis," *Chem. Rev.*, **113**, 5322 (2013).

[356] J. J. Concepcion, J. W. Jurss, M. K. Brennaman, P. G. Hoertz, A. O. T. Patrocinio, N. Y. Murakami Iha, J. L. Templeton, and T. J. Meyer, "Making Oxygen with Ruthenium Complexes," *Acc. Chem. Res.*, **42**, 1954 (2009).

[357] J. M. R. Narayanam, J. W. Tucker, and C. R. J. Stephenson, "Electron-Transfer Photoredox Catalysis: Development of a Tin-Free Reductive Dehalogenation Reaction," *J. Am. Chem. Soc.*, **131**, 8756 (2009).

[358] S. Fukuzumi, T. Kishi, H. K., Y.-M. Lee, and W. Nam, "Highly efficient photocatalytic oxygenation reactions using water as an oxygen source," *Nat. Chem.*, **3**, 38 (2010).

[359] D. A. Nicewicz and D. W. C. MacMillan, "Merging Photoredox Catalysis with Organocatalysis: The Direct Asymmetric Alkylation of Aldehydes," *Science*, **322**, 77 (2008).

[360] J.-M. Zen, S.-L. Liou, A. S. Kumar, and M.-S. Hsia, "An Efficient and Selective Photocatalytic System for the Oxidation of Sulfides to Sulfoxides," *Angew. Chem. Int. Ed.*, **42**, 577 (2003).

[361] W. Chen, F. N. Rein, and R. C. Rocha, "Homogeneous Photocatalytic Oxidation of Alcohols by a Chromophore-Catalyst Dyad of Ruthenium Complexes," *Angew. Chem. Int. Ed.*, **48**, 9672 (2009).

[362] H. Takeda and O. Ishitani, "Development of efficient photocatalytic systems for CO_2 reduction using mononuclear and multinuclear metal complexes based on mechanistic studies," *Coord. Chem. Rev.*, **254**, 346 (2010).

[363] T. J. Meyer, "Chemical approaches to artificial photosynthesis," *Acc. Chem. Res.*, **22**, 163 (1989).

[364] F. Gao, Y. Wang, J. Zhang, D. Shi, M. Wang, R. Humphry-Baker, P. Wang, S. M. Zakeeruddin, and M. Grätzel, "A new heteroleptic ruthenium sensitizer enhances the absorptivity of mesoporous titania film for a high efficiency dye-sensitized solar cell," *Chem. Commun.*, 2635 (2008).

[365] J. J. Concepcion, J. W. Jurss, J. L. Templeton, and T. J. Meyer, "One Site is Enough. Catalytic Water Oxidation by $[Ru(tpy)(bpm)(OH_2)]^{2+}$ and $[Ru(tpy)(bpz)(OH_2)]^{2+}$," *J. Am. Chem. Soc.*, **130**, 16462 (2008).

[366] N. Kaveevivitchai, R. Chitta, R. Zong, M. El Ojaimi, and R. P. Thummel, "A Molecular Light-Driven Water Oxidation Catalyst," *J. Am. Chem. Soc.*, **134**, 10721 (2012).

[367] K. Takanabe, "Photocatalytic Water Splitting: Quantitative Approaches toward Photocatalyst by Design," *ACS Catal.*, **7**, 8006 (2017).

[368] M. Graetzel, "Artificial photosynthesis: water cleavage into hydrogen and oxygen by visible light," *Acc. Chem. Res.*, **14**, 376 (1981).

[369] M. Jäger, L. Freitag, and L. González, "Using computational chemistry to design Ru photosensitizers with directional charge transfer," *Coord. Chem. Rev.*, **304-305**, 146 (2015).

[370] C. B. Meier, R. S. Sprick, A. Monti, P. Guiglion, J.-S. M. Lee, M. A. Zwijnenburg, and A. I. Cooper, "Structure-property relationships for covalent triazine-based frameworks: The effect of spacer length on photocatalytic hydrogen evolution from water," *Polymer*, **126**, 283 (2017).

[371] M. J. Bojdys, J. Jeromenok, A. Thomas, and M. Antonietti, "Rational Extension of the Family of Layered, Covalent, Triazine-Based Frameworks with Regular Porosity," *Adv. Mater.*, **22**, 2202 (2010).

[372] K. Wang, L.-M. Yang, X. Wang, L. Guo, G. Cheng, C. Zhang, S. Jin, B. Tan, and A. Cooper, "Covalent Triazine Frameworks via a Low-Temperature Polycondensation Approach," *Angew. Chem. Int. Ed.*, **56**, 14149 (2017).

[373] A. Karmakar, A. Kumar, A. K. Chaudhari, P. Samanta, A. V. Desai, R. Krishna, and S. K. Ghosh, "Bimodal Functionality in a Porous Covalent Triazine Framework by Rational Integration of an Electron-Rich and -Deficient Pore Surface," *Chem. Eur. J*, **22**, 4931 (2016).

[374] J.-X. Jiang, C. Wang, A. Laybourn, T. Hasell, R. Clowes, Y. Z. Khimyak, J. Xiao, S. J. Higgins, D. J. Adams, and A. I. Cooper, "Metal-Organic Conjugated Microporous Polymers," *Angew. Chem. Int. Ed.*, **50**, 1072 (2011).

[375] J. Hutter, M. Iannuzzi, F. Schiffmann, and J. VandeVondele, "cp2k: atomistic simulations of condensed matter systems," *WIREs Comput Mol Sci*, **4**, 15 (2014).

[376] A. Castro, H. Appel, M. Oliveira, C. A. Rozzi, X. Andrade, F. Lorenzen, M. A. L. Marques, E. K. U. Gross, and A. Rubio, "octopus: a tool for the application of time-dependent density functional theory," *physica status solidi (b)*, **243**, 2465 (2006).

[377] J. G. Santaclara, A. I. Olivos-Suarez, A. Gonzalez-Nelson, D. Osadchii, M. A. Nasalevich, M. A. van der Veen, F. Kapteijn, A. M. Sheveleva, S. L. Veber, M. V. Fedin, A. T. Murray, C. H. Hendon, A. Walsh, and J. Gascon, "Revisiting the Incorporation of Ti(IV) in UiO-type Metal–Organic Frameworks: Metal Exchange versus Grafting and Their Implications on Photocatalysis," *Chemistry of Materials*, **29**, 8963 (2017).

[378] F. Muniz-Miranda, L. De Bruecker, A. De Vos, F. Vanden Bussche, C. V. Stevens, P. Van Der Voort, K. Lejaeghere, and V. Van Speybroeck, "Optical Properties of Isolated and Covalent Organic Framework-Embedded Ruthenium Complexes," *J. Phys. Chem. A*, **123**, 6854 (2019).

[379] Z. Yang, X. Xu, X. Liang, C. Lei, L. Gao, R. Hao, D. Lu, and Z. Lei, "Fabrication of Ce doped UiO-66/graphene nanocomposites with enhanced visible light driven photoactivity for reduction of nitroaromatic compounds," *Applied Surf. Sci.*, **420**, 276 (2017).

[380] Y. An, Y. Liu, H. Bian, Z. Wang, P. Wang, Z. Zheng, Y. Dai, M.-H. Whangbo, and B. Huang, "Improving the photocatalytic hydrogen evolution of UiO-67 by incorporating Ce4+-coordinated bipyridinedicarboxylate ligands," *Science Bulletin*, **64**, 1502 (2019).

[381] Y. Zhang, H. Chen, Y. Pan, X. Zeng, X. Jiang, Z. Long, and X. Hou, "Cerium-based UiO-66 metal–organic frameworks explored as efficient redox catalysts: titanium incorporation and generation of abundant oxygen vacancies," *Chem. Commun*, **55**, 13959 (2019).

[382] M. Fumanal, G. Capano, S. Barthel, B. Smit, and I. Tavernelli, "Energy-based descriptors for photo-catalytically active metal–organic framework discovery," *J. Mater. Chem. A*, **8**, 4473 (2020).

[383] J. Schneider and D. W. Bahnemann, "Undesired Role of Sacrificial Reagents in Photocatalysis," *The J. Phys. Chem. Lett.*, **4**, 3479 (2013).

[384] S. Park, W. J. Chang, C. W. Lee, S. Park, H.-Y. Ahn, and K. T. Nam, "Photocatalytic hydrogen generation from hydriodic acid using methylammonium lead iodide in dynamic equilibrium with aqueous solution," *Nature Energy*, **2**, 16185 (2016).

Part II

Published Papers

A

Publications in International Peer–Reviewed Journals

Paper I

Missing Linkers: An Alternative Pathway to UiO-66 Electronic Structure Engineering

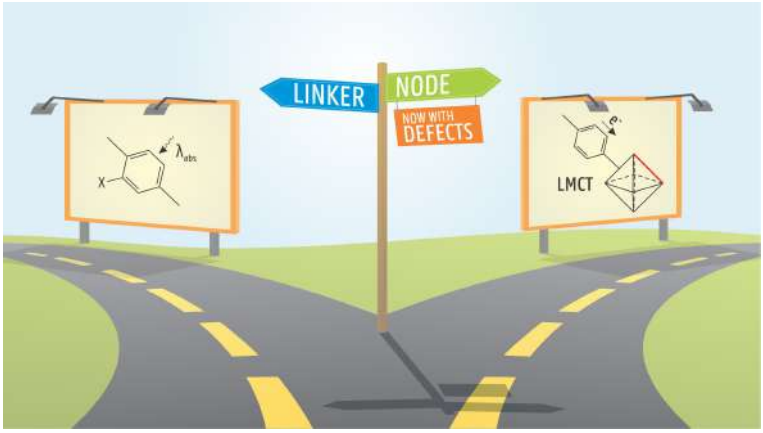

A. De Vos, K. Hendrickx, P. Van Der Voort,
V. Van Speybroeck, and K. Lejaeghere

Chemistry of Materials, **2017**, *29*, 3006–3019,

A. De Vos performed the research and wrote the manuscript.

CHEMISTRY OF MATERIALS

Article

pubs.acs.org/cm

Missing Linkers: An Alternative Pathway to UiO-66 Electronic Structure Engineering

Arthur De Vos,[†] Kevin Hendrickx,[†,‡] Pascal Van Der Voort,[‡] Veronique Van Speybroeck,*[,†] and Kurt Lejaeghere*[,†]

[†]Center for Molecular Modeling (CMM), Ghent University, Technologiepark 903, 9052 Zwijnaarde, Belgium

[‡]Center for Ordered Materials, Organometallics and Catalysis (COMOC), Department of Inorganic and Physical Chemistry, Ghent University, Krijgslaan 281 (S3), 9000 Ghent, Belgium

Supporting Information

ABSTRACT: UiO-66 is a promising metal–organic framework for photocatalytic applications. However, the ligand-to-metal charge transfer of an excited electron is inefficient in the pristine material. Herein, we assess the influence of missing linker defects on the electronic structure of UiO-66 and discuss their ability to improve ligand-to-metal charge transfer. Using a new defect classification system, which is transparent and easily extendable, we identify the most promising photocatalysts by considering both relative stability and electronic structure. We find that the properties of UiO-66 defect structures largely depend on the coordination of the constituent nodes and that the nodes with the strongest local distortions alter the electronic structure most. Defects hence provide an alternative pathway to tune UiO-66 for photocatalytic purposes, besides linker modification and node metal substitution. In addition, the decomposition of MOF properties into node- and linker-based behavior is more generally valid, so we propose orthogonal electronic structure tuning as a paradigm in MOF design.

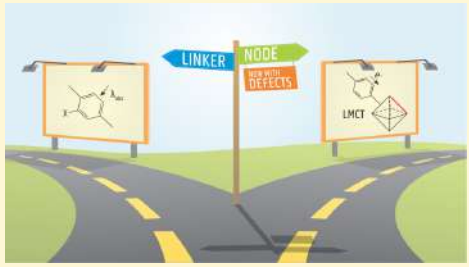

1. INTRODUCTION

One of the major scientific challenges of the 21st century is the change from energy intensive and polluting processes to green and sustainable alternatives. A promising approach is the conversion of solar energy, an abundant energy source, into chemical energy via photocatalytic processes.[1,2] Natural photosynthesis is the prototype example of an efficient process based on solar energy, using a highly complex set of hierarchically assembled units to convert the energy into chemical bonds.[1,3] The roots of the implementation of solar-driven chemical conversions in our daily technology lie in the seminal work of Honda and Fujishima, who studied photocatalytic water splitting on TiO_2.[4] Since then, novel materials have been developed for these processes, enabling many environmentally friendly applications and yielding a deep understanding of the fundamental physics of semiconductor-based photocatalysis.[5−9] It remains however challenging to design a system that is highly active, uses a broad range of the electromagnetic spectrum, is stable, and has a reasonable cost.

One emerging class of photoactive materials, combining molecular functionality and control in a solid state material, is that of metal–organic frameworks (MOFs). MOFs are versatile porous crystals that are constructed from inorganic clusters linked by organic moieties.[10] Their inherent modular nature, in a way resembling the naturally assembled photosystem, combined with their large internal surface and highly ordered pore structure make them interesting platforms for use in gas sorption,[11] heterogeneous catalysis,[12] biocompatible scaffolds,[13,14] chemical sensing,[15] and light-based applications.[16−19]

Regarding their electronic structure, MOFs are still mostly described with traditional solid state terminology. Nevertheless, in recent literature, this classical view of MOFs has been challenged and has attributed to these materials significantly different properties than typical insulators.[17,20] This difference in behavior is because MOFs retain many of their discrete, molecular characteristics. Instead of showing a delocalized valence and conduction band, a more localized highest occupied and lowest unoccupied crystal orbital (HOCO and LUCO) can be observed.

This discrete nature can be beneficial when designing MOFs for photocatalysis. The activity of a material is highly determined by the lifetime of the created charge carriers. To increase the lifetime, the created exciton has to be separated to prevent fast recombination of its composing electron–hole pair. The modular nature of MOFs allows for the optimization of their different constituents in order to achieve, e.g., a fast migration of an electron excited at the linker to the inorganic node. This ligand-to-metal charge transfer (LMCT)[18] has been

Received: December 23, 2016
Revised: March 10, 2017
Published: March 10, 2017

DOI: 10.1021/acs.chemmater.6b05444
Chem. Mater. 2017, 29, 3006−3019

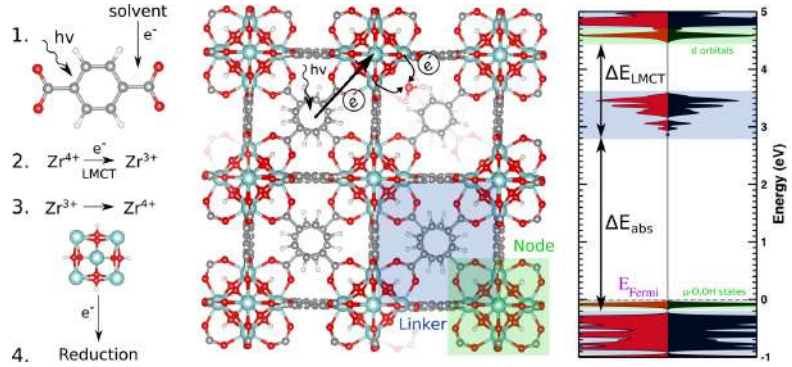

Figure 1. Photocatalytic process in UiO-66(Zr) in terms of its building blocks (left), defect crystal structure (middle), and density of states of the pristine UiO-66(Zr) (right), where red and black curves represent different spin channels and blue and green indicate linker and node states, respectively. The linker is excited by an incident photon (excitation energy ΔE_{abs}), after which the electron is transferred to the node, reducing a Zr atom (energy barrier ΔE_{LMCT}). The excited electron is then available to reduce reactants near the active site. Zr atoms are represented in blue, O atoms in red, C atoms in gray, and H atoms in white.

discussed in different materials as one of the main mechanisms underlying the photocatalytic activity of MOFs.[17]

Zr-based MOFs, and more specifically the series developed at Oslo University (UiO) by Lillerud and co-workers,[21] are an interesting class of frameworks with great possibilities for photocatalysis. They are very stable materials[22,23] and have a fairly robust synthesis, allowing the inclusion of genuinely different linkers and metals.[24] This resulted in a plethora of functionalized materials with the UiO crystal structure.[25−28] Moreover, the straightforward synthesis procedure allows for efficient upscaling from the lab scale to a pilot scale plant, as was demonstrated by Ahn et al.[29]

Most of the Zr-based frameworks have been subjected to extensive research in a broad domain of applications.[30] A particularly popular material is UiO-66(Zr). It consists of octahedrally coordinated Zr atoms, forming $Zr_6O_4(OH)_4$ nodes, which are connected via 12 benzene dicarboxylate (BDC^{2-}) linkers per node (see Figure 1). Recently, several examples in the literature have appeared on the use of this UiO-type MOF as a photocatalyst. More specifically, the amino-functionalized UiO-66(Zr), in both its pure and mixed-linker forms, showed reasonable activity in several chemical transformations. The considered transformations not only include proof-of-concept reactions, allowing understanding and optimization of the materials, but also more high-end organic transformations, which have now been successfully catalyzed.[31−37] Moreover, because of the versatility of the framework, numerous possibilities remain to be explored, such as tandem catalysis, using also the excellent Lewis acid−base features of the material for instance, or framework-controlled product selectivity. The inclusion of guest species inside the framework pores (dyes, metal complexes, nanoparticles, ...) offers an effective route to increase photocatalytic activity as well.[38,39]

Despite the promise of UiO-66(Zr) for chemical conversions, the pristine material has only limited photocatalytic activity. The reason for this is evident from the DOS, presented in Figure 1. In terms of the photocatalytic process, two energy gaps are relevant, ΔE_{abs} and ΔE_{LMCT}, indicated in the figure. ΔE_{abs} corresponds to the energy required to excite the linker, and ΔE_{LMCT} corresponds to the energy needed to transfer the excited linker's electron to the node's unoccupied d orbitals. In order to obtain an efficient electron transfer to the Zr node and thus a high activity, ΔE_{LMCT} should be close to zero or even negative. However, as seen in the figure, this is not the case for pure UiO-66(Zr), restricting its activity. Although some groups claim to have observed ligand-to-metal charge transfer (LMCT) in pristine UiO-66(Zr), nevertheless,[32,35,36] Nasalevich et al. recently confirmed the hindered charge transfer using transient absorption spectroscopy and EPR. They probed the formation of reduced Zr^{3+} species in the framework, as this indicates an electron transfer from the linker, with the unpaired electron resulting in an EPR signal.[40] The authors observed a very low signal for UiO-66(Zr), indicating the inefficient transfer. These results corroborate the findings by Matsuoka and co-workers attributing the low photocatalytic activity of the UiO-66(Zr) framework to the strongly negative redox potential of Zr^{4+}.[41] Some of the presenting authors also used time-dependent density-functional theory (TDDFT) calculations to confirm that the theoretical LMCT is only possible to a limited extent in the pristine UiO-66(Zr) frameworks.[42]

While the photocatalytic activity of UiO-66(Zr) may be enhanced by the subsitution of Zr by Ti[40] (see section 5) or by introducing new components into the framework,[38] we propose defect engineering as an alternative route. Defect engineering is a rising topic within MOF research and offers interesting new opportunities.[43,44] Both missing linker and missing cluster defects can occur in UiO and appear to yield stable frameworks. Lillerud et al. showed that defects are inherently present in UiO-66 frameworks under normal synthesis conditions. They moreover succeeded in designing synthesis procedures to obtain a defect-free UiO-66(Zr)[45] or to incorporate additional defects.[46] The incorporation of multiple types of defects in a highly controllable manner[45−47] was found to lead to different mechanical properties,[48] catalytic behavior,[49−53] and absorption properties.[54,55]

In this contribution, we discuss missing linker defects as an alternative pathway to engineer the electronic structure of UiO-66(Zr) and thus their photocatalytic activity. To the best of our knowledge, this work is the first thorough discussion of the

DOI: 10.1021/acs.chemmater.6b05444
Chem. Mater. 2017, 29, 3006−3019

influence of different defect structures on the electronic structure of MOFs and the intentional use of defects to engineer it. Note that we do not explicitly consider missing nodes but show at the end that they exhibit to a large extent the same properties as missing linkers (see section 5 and Supporting Information). This manuscript is organized as follows. In section 2, we present a new notation to unambiguously define different missing linker defect structures and compare this to the current literature. Section 3 contains the computational details of all calculations. Section 4 first discusses the energetics of the defect structures. Next, the electronic properties are discussed by means of an analysis of the periodic DOS (section 4.2.1) and via cluster calculations (section 4.2.2). The considered quantities are found to be related to a large extent to the local node environments present in the defect structure. We expand on this idea in section 5, connecting our research to the literature and reinterpreting current efforts to engineer the electronic structure of UiO.

2. DEFECT STRUCTURES

A (missing linker) defect structure is created by removing a number of benzene dicarboxylate linkers, BDC^{2-}, from the pristine UiO-66 (see Figure 1). In this work, we look at defect structures created by removing one, two, or three linkers from a four-node unit cell. Before describing the associated node configurations, we first introduce a general notation to uniquely define UiO-66 defect structures. Our notation improves upon previous classifications recently proposed in the literature,[48,56,57] to which we compare in the Supporting Information (see Table S2).

2.1. Classification of Missing Linker Defect Structures. There are many ways to remove linkers from a UiO-66 crystal. The number of symmetrically inequivalent ways that linkers can be removed depends on the number of removed linkers and the size of the unit cell. To investigate the effect that linker removal has on the electronic structure (see section 4.2), it is important to be able to characterize each defect structure with a transparent notation. We introduce a general notation here that depends on the size of the unit cell and thus accounts for the periodicity of the defect structure. It is also easily extended toward larger unit cells. Although some studies in the literature already introduced limited notations for missing linker defect structures,[48,56,57] a general scheme was not yet available.

When l linkers are removed from an n-node unit cell, we can note the resulting defect structure as $(CN(1)_{\alpha}, CN(2)_{\beta}, ..., CN(n)_{\nu})_{\{i\}}$, representing the structure of the material from the point of view of the nodes. Each node configuration, CN_{α}, is described by its coordination number (CN), to which a subscript is added (α, ..., ν) to differentiate between nodes with the same coordination number but with a different symmetry. The subscript set $\{i\}$ indicates the $\binom{l}{2}$ interlinker distances between the centers of the l removed linkers and serves to remove any remaining ambiguity. These indices are expressed in terms of coordination shell numbers: 245, for example, means that there are three missing linkers that are second-, fourth-, and fifth-nearest neighbors. Because our notation fully determines the defect structure, the order of the node configurations does not matter. By convention, we order by increasing coordination number and then by alphabetical subscript.

This work considers unit cells with four Zr nodes,[48,56,57] removing up to three linkers. The possible node configurations and interlinker distances are listed in Figure 2 and Table 1, respectively. Figure S2 displays all considered defect structures with our general notation, and in Table S2 the connection with previous notations[48,56,57] is shown. The B structure in the paper of Vandichel et al.,[56] for example, is equivalent to the 8/8 structure in the paper of Bristow et al.[57] and the type 6 defect structure of Rogge et al.[48] Neither of these notations yields insight into the corresponding defect structure. In contrast, our notation, $(10_a10_a12,12)_4$, shows two linkers to be removed from a four-node unit cell with the second linker in the fourth coordination shell of the first, leaving nodes of both 12 and 10_a node configurations.

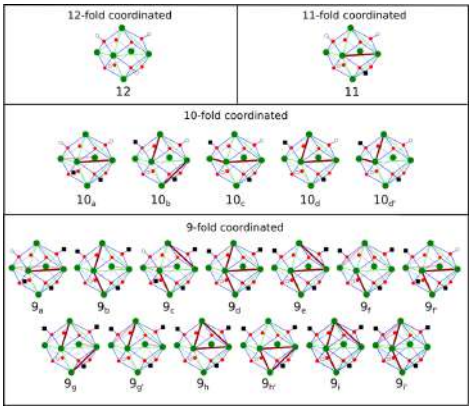

Figure 2. Different node configurations created by removing zero, one, two, or three linkers. Zr atoms are represented in green, O atoms in red, and H atoms in white. Red lines indicate where a linker is missing, and black squares indicate removed hydrogen atoms to ensure charge neutrality.

Table 1. Subscript Used in Our Defect Structure Notation to Indicate the Distance between the Centers of the Removed Linkers[a]

shell	ILD (−)
1	0.354
2	0.500
3	0.612
4	0.707
5	0.866

[a]This interlinker distance (ILD) has been normalized with respect to the lattice constant of the four-node unit cell of UiO-66. It does not take into account potential relaxation caused by removing linkers.

2.2. Node Relaxation. A missing linker defect structure is created by removing a number of BDC^{2-} linkers from the pristine UiO-66 framework. To ensure neutrality of the inorganic node, the removed negative charge can be compensated by adding a negative ligand[57,58] or by removing a positive proton from the node.[48,56,59] Bristow et al.[57] compared different charge compensation methods for the one-defect structure, (11,11,12,12), and concluded that the acetate capping mechanism (CH_3COO^-), which closely resembles the missing BDC^{2-} linker, was the most stable. However, the acetate cap effectively shields the Zr electrons from potential reactants. In contrast, undercoordinated Zr sites provide more efficient active sites for catalysis. They are created

DOI: 10.1021/acs.chemmater.6b05444
Chem. Mater. 2017, 29, 3006−3019

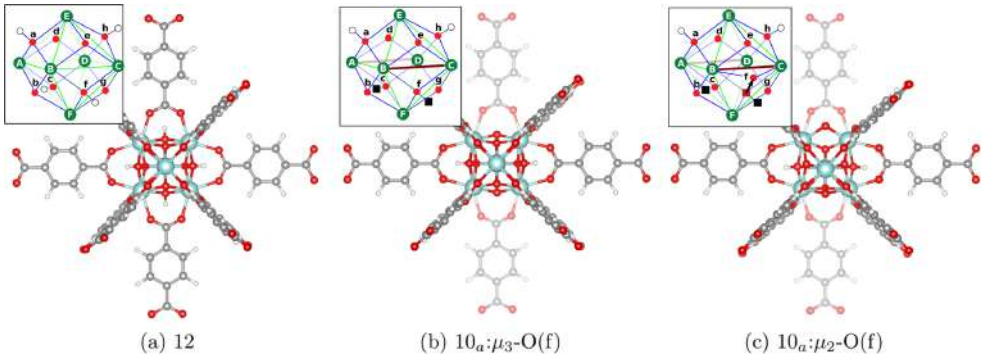

Figure 3. The 12-fold coordinated node (left), 10$_a$ node configuration without recoordinating oxygen atom (middle), and with recoordinating oxygen atom (right). The recoordinating oxygen atom, μ_2-O (f), lowers the charge imbalance on the Zr atom (F) and therefore stabilizes the node. The insets display the node geometry where A–F indicate the Zr atoms (see Table 2) and a–h indicate the oxygen atoms. Graphical conventions are the same as in Figures 1 and 2.

Table 2. Ionic Model for the Zr Charges q_{Zr} (Unit e) in the Pristine Node (a), the 10$_a$ Node Configuration without a Recoordinating Oxygen Atom (b), and the 10$_a$ Node Configuration with a Recoordinating Oxygen Atom (c) (see Figure 3)

	# μ_3-OH			# μ_3-O			# COO^-			# μ_2-O			q_{Zr}-4		
Zr	(a)	(b)	(c)	(a)	(b)	(c)	(a)	(b)	(c)	(a)	(b)	(c)	(a)	(b)	(c)
A	2	1	1	2	3	2	4	3	3	0	0	0	0	−1/6	−1/6
B	2	1	1	2	3	3	4	3	3	0	0	1	0	−1/6	1/6
C	2	1	1	2	3	3	4	3	3	0	0	1	0	−1/6	1/6
D	2	1	1	2	3	2	4	3	3	0	0	0	0	−1/6	−1/6
E	2	2	2	2	2	2	4	4	4	0	0	0	0	0	0
F	2	0	0	2	4	3	4	4	4	0	0	0	0	4/6	0

by removing a proton from the inorganic node, for example through reaction with the acetate termination, leaving the node free of both acetate cap and proton. During the process of alternating capping and decapping of the node, the bare node is expected to play the most important role in photocatalytic reactions. In this work, we will therefore only consider deprotonated nodes.

By removing linkers, the affected nodes will relax, causing bond lengths to adjust. Deprotonated μ_3-O atoms are pulled closer to the node, similar to the μ_3-O atoms originally present. The bond between a deprotonated μ_3-O and one of its three coordinating Zr atoms may even break, triggering a structural transition. Such a bond breaking was observed for the 10$_a$ (see Figure 3) and 9$_{f'}$ node configurations.

Molecular level insight suggests the recoordination of one of the oxygen atoms to be triggered by the increased number of μ_3-O atoms. By recoordinating one of these oxygen atoms, the overly electronegative environment can be remediated and the node stabilized. To understand the charge imbalance promoting such an oxygen recoordination, we constructed an ionic model to quantify the charges on O and Zr. In this ionic model, we assume oxygen atoms to adopt a noble gas configuration and all Zr atoms to be equivalent. In this way, a Zr atom in the 12-fold coordinated node loses two times 2/3 e^- to a μ_3-O atom, two times 1/3 e^- to a μ_3-OH group, and four times 1/2 e^- to the oxygen atoms of the four connected linkers. In defect-free (or acetate-capped[57]) nodes, all Zr atoms therefore have a +4 charge, in line with their expected oxidation number. In contrast, when linkers are removed from a node, the change in environment of the Zr atoms will alter the Zr charge. The deviation from an ideal +4 charge can be seen as a measure of the node's instability.

The ionic model can be used to qualitatively assess the driving force toward oxygen recoordination for a particular node configuration. When applying this model to a 10$_a$ node without structural transition, for example, a strong deviation in Zr charge is observed, associated with a high energy (see Table 2). Particularly, the Zr (F) connected to both deprotonated μ_3-O atoms (c,f) is highly positive due to its more electronegative environment (see Figure 3 and S1 for the classification of the individual Zr and O atoms). Breaking a bond with the deprotonated μ_3-O atoms enables a stabilization of the node as the number of surrounding μ_3-O atoms is reduced by one (b,c,g). Table 2 shows the improved charge balance, demonstrating a much smaller charge deviation of Zr (F) after recoordination of the oxygen. This predicted improvement of the node stability is also observed in our DFT calculations, which yield a stability increase of approximately 250 meV.

According to our ionic model, it is possible to reduce Zr charge deviations by oxygen recoordination in the 9$_a$, 9$_\beta$ and 9$_{f'}$ node configurations as well. These nodes all have a 10$_a$ configuration from which an additional linker is removed. In reality, however, not all of these node configurations undergo a transition. This shortcoming of our model can be attributed to the neglect of relaxation and repulsion effects. When breaking a bond, for example, the μ_2-O (f) moves away from the Zr octahedron while the μ_3-O (e) is simultaneously pulled closer.

DOI: 10.1021/acs.chemmater.6b05444
Chem. Mater. 2017, 29, 3006−3019

If the repulsion with the other μ_3-O atoms prevents the latter oxygen atom from entering the Zr octahedron, no bonds will break. This is the case in the 9_a and 9_f structures. On the other hand, the nonrelaxed deprotonated μ_3-O atom may also experience a strong repulsion with its neighboring μ_3-O atom when an adjacent linker is removed. This triggers a structural transition in the $9_{f'}$ node configuration. Only the $9_{f'}$ and 10_a nodes therefore exhibit oxygen recoordination.

Note that in a four-node unit cell a complication arises when more than one 10_a node is present. In this case, each node has two equivalent ways to generate a μ_2-O atom, but the relative orientation is not necessarily the same. Figure 4 shows two different defect structures, both missing three linkers and containing two 10_a nodes. However, because of the way the linkers are removed, a different relative orientation of the recoordinated oxygen atoms is preferred. In the case of the $(10_a,10_a,11,11)_{245}$ structure, the absence of a linker in the channel between the two 10_a nodes makes it more favorable (by approximately 50 meV) for both recoordinating O atoms to face each other.

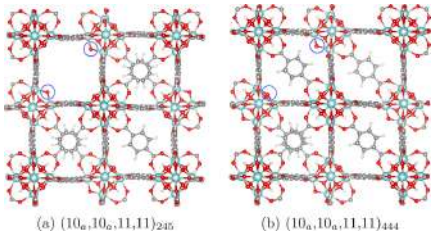

Figure 4. Different relative orientations of two recoordinating oxygen atoms (encircled) in a four-node unit cell containing two 10_a node configurations. Graphical conventions are the same as in Figure 1.

3. COMPUTATIONAL DETAILS

All periodic calculations were performed using density-functional theory (DFT) in the projector augmented wave (PAW) approach[60] with the VASP package[61−64] and employing the PBE functional.[65] Although the semilocal PBE functional is known to substantially underestimate band gaps, hybrid functional calculations on UiO-66(Zr) have shown PBE to display the correct trends.[42] In view of the large number of possible defect structures, containing up to 456 atoms per unit cell, the PBE functional should therefore yield the correct qualitative conclusions at an acceptable computational cost. The recommended GW PAW potentials were used because of their high precision.[66,67] In addition, a plane wave basis set was employed with a kinetic energy cutoff of 700 eV, and a Γ-point grid was used to sample the Brillouin zone. We imposed an electronic energy convergence criterion of 10^{-5} eV together with an ionic energy criterion of 10^{-4} eV. These settings allowed energy convergence up to 1 meV per unit cell and were used to fit a Rose-Vinet equation of state.[68] From the equation of state, the equilibrium volume was obtained, at which the structures were relaxed using a more stringent electronic energy convergence criterion of 10^{-7} eV. Density of states calculations were moreover performed with a 2 × 2 × 2 Γ-centered grid. To calculate the energy needed to remove a linker (eq 1), the energy of an isolated H_2BDC linker was calculated by placing the molecule in a 20 Å × 20 Å × 20 Å box.

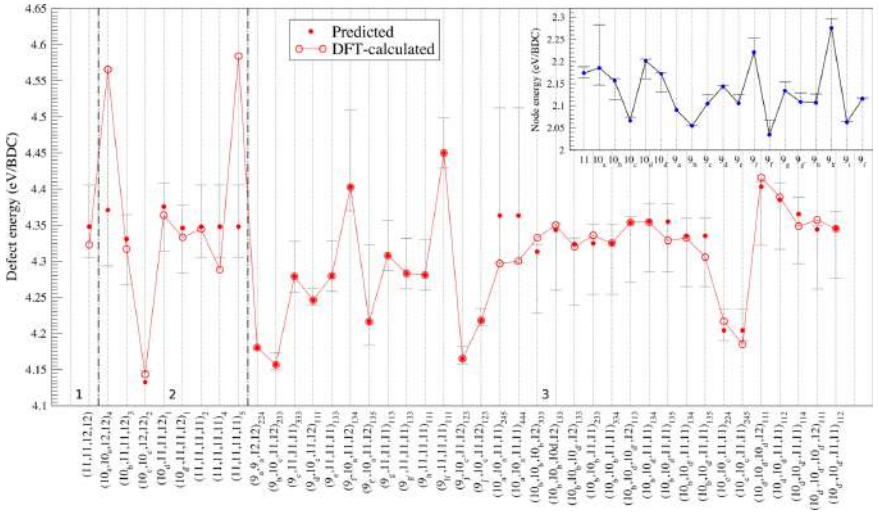

Figure 5. Defect energies for all missing linker defect structures normalized with respect to the number of missing linkers per unit cell. The connected open circles indicate the calculated values, and the solid markers represent the predicted defect energies from the least-squares fitted node energies. These fitted node energies, normalized to the number of missing linkers on each node, are shown in the inset. Error bars express the sensitivity of the fit and essentially represent the effect of different linker orientations. They are determined as the range of possible node energies when fitting to different sets of reference data (subsets of one-, two-, or three-defect structures separately and combinations of these subsets).

DOI: 10.1021/acs.chemmater.6b05444
Chem. Mater. 2017, 29, 3006−3019

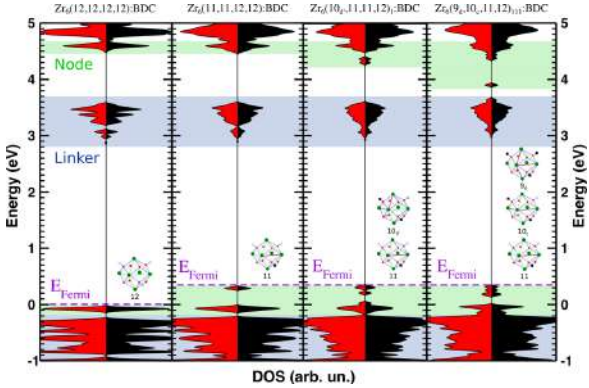

Figure 6. Density of states of the pristine, one-, two-, and three-defect structure where all missing linkers were connected to a single node. Red and black curves represent different spin channels, and all DOS are aligned with respect to the pristine μ-OH,O node states. Blue and green indicate linker and node states, respectively.

To demonstrate the effect of LMCT on the inorganic nodes, it is also instructive to complement the periodic calculations with cluster calculations for isolated nodes. These cluster calculations were performed with Gaussian 09 (G09).[69] Previous research[42] has shown that the combination of the B3LYP[70,71] functional with a triple-ζ Def2TZVP basis[72] set is a good choice for these cluster calculations, and therefore the same settings were applied in this work. Geometry optimization of the clusters was performed at the same level of theory by constraining the hydrogen atoms of the formate termination.

4. RESULTS AND DISCUSSIONS

Defects are inherently part of any material. Although producing defects requires energy, their formation is favored entropically. Depending on the conditions, the formation free energy of a defect at finite temperature can therefore be sufficiently low to enable its creation. While the synthesis of a defect-free UiO-66(Zr) crystal is possible[45] and can be an objective, defects may also be desirable as they introduce properties that the perfect crystalline material does not possess. Without missing linkers, the Zr atoms in the octahedral nodes are fully coordinated and are not as accessible as active sites. Moreover, missing linkers alter the node structure and thus the corresponding electronic properties. This is of interest for photocatalytic applications of UiO-66(Zr), which are mediated by the unoccupied d orbitals of the accessible Zr atoms. In this section, we first look at the stability of different defect structures. Afterward, we study the impact of missing linkers on the electronic properties with a particular focus on the energy of the unoccupied d orbitals. Ideally, defect structures would provide an enhancement of the photocatalytic activity and thus make defect engineering an alternative path to modulate the electronic structure of UiO-type materials.

4.1. Energetics. The energy necessary to remove linkers depends on the defect structures they create. Not only is the symmetry of the node lowered, but the removal of a linker (BDC^{2-}) is additionally charge compensated by the removal of a hydrogen atom from each connected node. The 0 K defect energy per linker, i.e., the energy cost per removed linker, can be calculated via

$$E_{\text{form}} = \frac{1}{l}(E[\text{host:}l] - (E[\text{host}] - l{\cdot}E[H_2BDC])) \quad (1)$$

where $E[\text{host:}l]$ is the energy of the defect structure missing l linkers, $E[\text{host}]$ is the energy of the pristine UiO-66, and $E[H_2BDC]$ is the energy of a H_2BDC linker.[73,74]

The removal of linkers introduces altered nodes into the UiO-66 host (see Figure 2), while the remaining linkers are largely unaffected. It is therefore interesting to assess whether the defect energy can be calculated as a sum of energies attributed to the different node configurations in the defect structure. To check this additivity principle, we extracted node energies from a least-squares fit to the defect energies of all defect structures (see Tables S3−S4 and inset of Figure 5). In this fit, all node energies are expressed relative to that of a 12-fold coordinated node, leaving the defect-free node with a zero energy by definition. Error bars are calculated as the range of possible node energies when fitting to different sets of reference data: we fitted to both the subsets of one-, two- or three-defect structures separately and to combinations of these subsets. The spread on the fitted node energies thus provides a measure of the sensitivity of the fit. These error bars capture the effect of different linker orientations on the nodes' energies and hence the extent to which our node-based model is valid. They do not take into account the influence of the chosen charge balancing mechanism, which also affects the relative stability of different defect structures[57] and, therefore, the fitted node energies as well. In Figure 5, the defect energies predicted from the fitted node energies (inset) are compared with the actual defect energies (main figure).

We first consider the 11-fold and 10-fold coordinated nodes. The inset of Figure 5 shows that the 11, 10_a, 10_b, 10_d, and $10_{d'}$ nodes all have similar energies, whereas the 10_c node is much more stable. This is also seen from the defect energies of the corresponding defect structures. There are however two exceptions. The $(10_a,10_a,12,12)_4$ structure has a significantly higher defect energy, suggesting that the 10_a nodes are more sensitive to the orientation of the surrounding linkers. In addition, the defect energy of the (11,11,11,11) defect structures strongly depends on the orientation of the linkers. Both linker−node and linker−linker interaction may therefore

DOI: 10.1021/acs.chemmater.6b05444
Chem. Mater. 2017, 29, 3006−3019

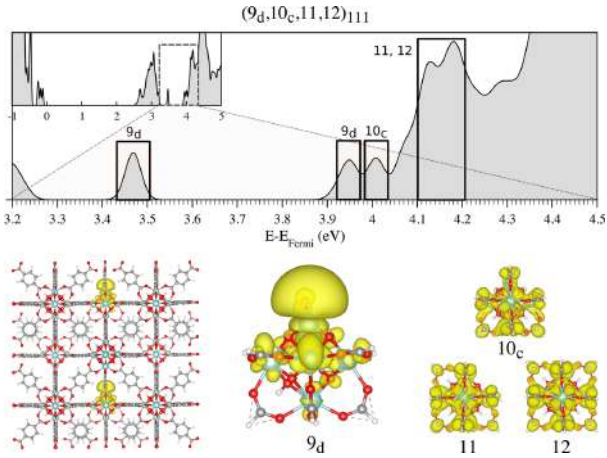

Figure 7. (Top) Density of states of the $(9_d,10_c,11,12)$ defect structure, decomposed in terms of the Zr unoccupied d orbitals. (Bottom) Contour plots of the lowest-energy d orbital centered on the 9_d node (left) and the SOMOs of formate capped 9_d, 10_c, 11, 12 nodes (right).

play an important role. However, for most defect structures, their effect is negligible.

Although the differences remain small, the energies of the 9-fold coordinated nodes and their associated defect energies are more broadly distributed (Figure 5). This is due to their larger structural diversity. The 9_a, 9_b, $9_{f'}$, and 9_i nodes have the lowest energies, three of which, 9_a, 9_b, and 9_i correspond to a 10_c node from which an extra linker has been removed. This confirms the stability of the 10_c node configuration. The largest error bars are observed for 9_f and $9_{f'}$, which can be explained by the presence of the 10_a node in $(9_f10_a11,12)_{134}$ and $(9_{f'},10_a,11,12)_{134}$.

Although our node-based model fails when linker orientations are important, assigning a fixed energy to each node configuration captures the most important trends of the defect energies. The model works particularly well for defect structures with a low defect energy, all of which contain 10_c-based nodes. In terms of the defect energies, a defect structure may therefore as a first approximation be seen as the sum of its constituting nodes' energies.

4.2. Electronic Properties. In an ideal photocatalyst, the excited linker electrons should be easily transferred to the node's unoccupied d orbitals. Such an efficient charge transfer requires reducing ΔE_{LMCT} (see Figure 1). One possible route is to substitute Zr by other metals. This approach has been extensively discussed in the literature,[75] emphasizing the favorable effect of Ti incorporation.[24,76−80] Because the removal of linkers alters the nodes, it may lower the unoccupied d orbitals as well. We therefore investigate the DOS of all defect structures created by removing one, two, or three linkers from a four-node unit cell, focusing on the change in the unoccupied d orbitals. To assess the impact of LMCT on the d orbitals, we also performed cluster calculations.

4.2.1. Density of States. An overview of all calculated DOS is presented in the Supporting Information (see Figures S3 and S4), and a selection is shown in Figure 6. Some trends among the different defect structures can be identified. The density of states of the one-defect structure, (11,11,12,12), is almost identical to that of the defect-free UiO-66(Zr), for example (see Figure 6). More importantly, the lowest unoccupied d orbitals in the DOS are unchanged. The environment of the Zr atoms in the 11-fold coordinated nodes is apparently not altered sufficiently to influence the character and position of the lowest unoccupied d orbitals, leaving ΔE_{LMCT} unaltered. This also follows from our ionic model (see section 2.2). Although the removal of one linker introduces charge fluctuations, there is no locally amplified effect between neighboring Zr atoms, with charge imbalances on each face of the node's octahedron canceling out (see Table S1). The only difference in electronic structure between the defect-free and the one-defect structure is seen at the top of the HOCO, where the exact ordering of linker and node states moreover depends slightly on the level of theory.[40,81,82] There, the μ_3-OH,O node states split off a filled gap state because the linker removal lifts the equivalence of the different oxygen atoms. Although this lowers the effective band gap of the material, it does not change the linker excitation energy, ΔE_{abs}, as the linker states are unaltered (see Figure 6).

The DOS of the two-defect structures show a similar μ_3-OH,O node state splitting, again leaving ΔE_{abs} unaltered. More importantly, however, some defect structures also exhibit modified unoccupied d orbitals, decreasing ΔE_{LMCT}. This is the case for all defect structures that contain a 10-fold coordinated node, while no change is seen when only 11-fold coordinated nodes are present. The largest shift of the lowest unoccupied d orbitals is seen for the $(10_{d'},11,11,12)_1$ (see Figure 6) and (10d,11,11,12)1 defect structures. For both 10_d and $10_{d'}$ nodes, the removed linkers are adjacent and connected to the same Zr atom. This suggests that a strongly localized distortion of the environment of the Zr atoms substantially lowers the energy of the d orbitals, potentially improving the photocatalytic activity. The corresponding charge imbalance can be quantified with our ionic model (see Table S1). For the 10_d and $10_{d'}$ nodes, the Zr atoms on the octahedral face formed by the two removed linkers experience a charge deviation of $(-e/6, -e/6, -e/3)$. In contrast to the 11-fold coordinated node, the charge differences on the octahedral face therefore amplify each other. Note that there are energetically more

DOI: 10.1021/acs.chemmater.6b05444
Chem. Mater. 2017, 29, 3006−3019

favorable nodes than the 10_d and $10_{d'}$ nodes. However, the more stable 10_c node also introduces lower d orbitals, albeit to a lesser extent. This suggests a correlation between the energy per node determined by the addition model and the lowering of d orbitals, as higher charge fluctuations correspond to lower d orbitals but also to a higher energy per node. Such a correlation is indeed observed for some (but not all) of the considered node types (see Figure 5 and Tables S3 and S4).

Finally, among three-defect structures, a lowering of the lowest unoccupied d orbitals is quite common, decreasing ΔE_{LMCT} while ΔE_{abs} remains constant. This is partly because many of these defect structures contain 10-fold coordinated nodes. The 9-fold coordinated nodes moreover affect the unoccupied d orbitals as well. Defect structures $(9_d,10_c,11,12)_{111}$ (see Figure 6) and $(9_{h'},11,11,11)_{111}$ show the lowest unoccupied d orbitals and smallest ΔE_{LMCT}, outperforming two-defect structures with 10_d or $10_{d'}$ nodes. These three-defect structures contain 9-fold coordinated nodes where the environment of the Zr atoms is locally strongly distorted. In the 9_d node, three linkers are missing from a single Zr atom, while for $9_{h'}$ the three linkers are removed from a single octahedral face of the node. Here, too, our ionic model indicates a large charge imbalance: for $9_{h'}$, Zr charges on the octahedral face formed by the three missing linkers change by $(-e/3, -e/3, -e/3)$ and for the 9_d node, a $-5e/6$ charge difference is found for the Zr atom connected to the three missing linkers. Energetically, the $9_{h'}$ node is very unstable, but the 9_d node belongs to the midenergy range (see Figure 5). Some more stable node configurations such as the 9_i node moreover lower the d orbitals as well.

The position of the unoccupied d orbitals in the DOS, related to ΔE_{LMCT}, is not the only relevant quantity. It is also interesting to see what these d orbitals look like in real space. Such a visualization gives a first impression of how electrons, transferred from the excited linker states, are localized on the target nodes. Figure 7 shows the example of a $(9_d,10_c,11,12)_{111}$ defect structure where the unoccupied d orbitals are localized on different node types. Both defect-free and 11-fold coordinated nodes are characterized by d-states spread over the entire node, while the d orbitals are much more localized in 10- and 9-fold coordinated nodes. In the latter case, the d orbitals are lower in energy and located at sites where the linkers have been removed, ideal for photocatalytic reaction.

The above observations show that changes in the Zr unoccupied d orbitals are driven by the local environment of the nodes. Similar to the defect energy (see section 4.1), the behavior of the d orbitals can therefore be deduced to a large extent from the type of nodes present in the defect structure. When only 11-fold coordinated nodes are available, almost no change is seen compared to pristine UiO-66(Zr). However, when more linkers per node are removed, the d orbitals lower in energy and the electron localizes near the site of the missing linkers. The observed energy lowering and electron localization moreover suggest an improved photocatalytic activity.

Note that the strongest effects are not necessarily seen for the lowest-energy node types. However, several low-energy nodes also display a noticeable change in the lowest unoccupied d orbitals. One could moreover wonder how important the role of nodes with multiple missing linkers is for photocatalysis, since removing a single linker already suffices to generate an active site. Indeed, the removal of each additional linker generates a supplementary energy cost, but it leads to nodes with increased charge transfer capabilities. In addition, specialized synthesis procedures exist to introduce more defects,[83] leading to lower coordinated nodes with more favorable properties. The 10-fold and 9-fold coordinated nodes are therefore expected to play an important role in the material's photocatalytic activity, be it by nature or by design.

4.2.2. Singly Occupied Molecular Orbitals. In an idealized process, a separation of the exciton occurs via a migration of the electron to the unoccupied Zr d orbitals. Although our periodic calculations provide much insight in the ground state electronic structure of UiO-66 materials, it is also instructive to consider what happens after this ligand-to-metal charge transfer occurs. To obtain more insight into the behavior of the system after charge transfer, calculations were performed on isolated nodes, replacing linkers by formate termination groups. Indeed, our periodic analysis shows that the properties of individual nodes are to a large extent indicative of the overall properties of the material. The excited cluster is mimicked via ground state DFT calculations, adding one extra electron to the cluster by artificially imposing a -1 charge and a doublet state. While the LUCO in periodic calculations is localized on the linkers (see Figure 1), these states are not present in a node cluster model, so the targeted Zr node orbitals become the lowest unoccupied states. This negatively charged model system therefore represents the idealized situation in the framework after excitation and charge transfer. Analysis of the orbital contributions to the newly created singly occupied molecular orbital (SOMO) gives information on the sites where the electron preferentially resides. For this analysis, we consider a representative set of node types, the 12, 11, $10_{a-d'}$, 9_d, and 9_h node configurations, to cover the most important structural features present in the different defect structures.

Figure 7 and Figure S12 allow us to identify the general trends in the changing orbital contributions. The node with only one defect shows almost no changes in orbital contributions compared to the perfect 12-fold configuration. The extra electron gets delocalized over the whole node. This means that transfer of the electron to a reactant approaching the defect will hardly be improved via a singly defected node. The node configurations with two missing linkers show larger differences in orbital contributions and a less uniform distribution throughout the inorganic node. The effect is again the most pronounced in nodes $10_{d-d'}$, where two linkers are missing from a single Zr atom (see Figure S12). The orbital contributions of the thrice defected Zr atoms to the SOMO, present in the 9-fold coordinated nodes, increase even further. These cluster-based SOMOs resemble the unoccupied d orbitals of the periodic calculations (see Figure 7), where d orbitals are highly localized on defected nodes with the highest contributions on the lowest coordinated Zr (see Figure 7 (left)).

One can calculate the contributions of an atomic orbital χ_μ to the SOMO via a Mulliken approach:

$$C_\mu^2 + C_\mu \sum_{\nu \neq \mu} C_\nu S_{\nu\mu} \tag{2}$$

with C_μ the expansion coefficient of the SOMO in terms of atomic orbital χ_μ, and $S_{\nu\mu}$ the overlap between two atomic orbitals χ_μ and χ_ν. The results for the 9- and 10-fold coordinated node models are shown in Table 3.

In general, we observe that the contributions from the Zr atoms, compared to the other atoms in the node, increase as the number of defects on the node becomes larger. If one looks at the calculated orbital contributions of node 9_d, for example,

DOI: 10.1021/acs.chemmater.6b05444
Chem. Mater. 2017, 29, 3006−3019

Table 3. Orbital Contributions of Zr-Centered Atomic Orbitals to the SOMO, Calculated via a Mulliken Approach (See eq 2)[a]

	$Zr^{3\times}$ (%)	$Zr^{2\times}$ (%)	$Zr^{1\times}$ (%)	$Zr^{0\times}$ (%)	Σ Zr (%)
12				6	38
11			5	7	36
10_a			4	17	49
10_b			16	8	64
10_c		2	5	7	32
10_d		27	19	8	88
$10_{d'}$		35	16	6	85
9_d	49		10	7	93
9_h		22		9	93

[a]Contributions from all Zr types in a given node configurations are shown per Zr atom with $Zr^{n\times}$ representing an *n*-fold defected Zr atom.

the thrice defected Zr atom accounts for half of the orbital contributions to the SOMO. Together with the singly defected Zr atoms in that node type, this amounts up to almost 80% of the SOMO contributions. This shows that when an electron can migrate to a defected node, it will preferably reside on the most defected Zr atom. This also appears from our ionic model (section 4.1), which assigned the most negative charge to the Zr with the lowest coordination (see Table S1). The preferential localization of the excited electron thus enhances the possibility for a reaction to occur at a defect site, since the electron will be more accessible for approaching reactants.

5. PERSPECTIVE: OTHOGONAL ELECTRONIC STRUCTURE ENGINEERING

MOFs are interesting platforms for photocatalytic applications. Their inherent modular nature allows the construction of systems with optimized constituent parts, resulting in tailored control and transfer of the absorbed energy in the system. One of the most studied materials is UiO-66, because of its stability, robust synthesis, and easy postsynthetic modification. However, it is by now accepted that the unfunctionalized, defect-free material is not the holy grail in photocatalysis. Thanks to the efforts of several groups, as well as the analysis above, we now understand the electronic structure and the possible pathways to alter UiO-66 toward specific photocatalytic applications. Indeed, the modular nature of the framework results in an almost independent contribution to the electronic structure by the different substructures of the framework, i.e., the nodes and the linkers, which can therefore be modified separately (see Figure 8). Hence, we would like to introduce the idea of orthogonal tuning of the electronic structure, which is transferable to all MOFs with a similar 0D inorganic sublattice[84] and quasi-localized bands: orthogonal, because altering one part of the structure does not influence the electronic response to the other part, allowing different effects to be superimposed (see Figures 9 and S9). The photocatalytic properties of UiO-66 can therefore be engineered by treating the nodes and linkers independently. Following this reasoning, we can now reassess the modification approaches for UiO-66 that have been proposed both in the literature and in this work, by repeating previous calculations and combining them with new insights. Because of the orthogonal character of UiO-66 electronic structure tuning, we distinguish two methods.

The first method is based on a **linker alteration** step. By adding organic functional groups to the linkers, or by increasing the linker length, the absorption wavelength of the system (ΔE_{abs}) can be changed. There are many examples of linker-altered UiO-66 frameworks in the literature, which are produced during synthesis, via a mixed-linker approach, or postsynthetically, by means of a ligand exchange.[25,85−88] Several authors have studied the resulting changes in electronic structure[81,89] and hence in catalytic activity,[31−33,35,36] both via experiments and computational modeling. Effectively reducing ΔE_{abs} requires the introduction of an electron-donating group, which can shift the absorption peak deep into the visible spectrum. This is caused by the introduction of filled states within the first band gap. Electron-withdrawing groups (e.g., NO_2) or changes in linker length have a much more limited effect (see Figures S7 and S8). It has also been shown[42] that

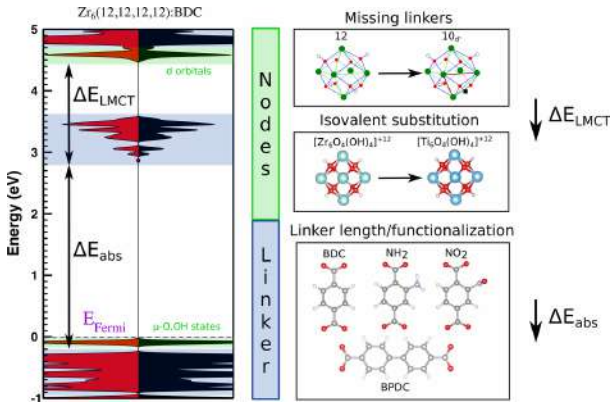

Figure 8. Orthogonal tuning of the electronic structure of UiO-66(Zr) (left) where red and black curves represent different spin channels and blue and green indicate linker and node states, respectively. Linker alteration affects the absorption wavelength, ΔE_{abs}, and therefore controls the energy needed to excite the linker (BPDC = biphenyl dicarboxylate). The position of the unoccupied d orbitals (ΔE_{LMCT}) is changed by node modification and is important for an efficient LMCT.

DOI: 10.1021/acs.chemmater.6b05444
Chem. Mater. 2017, 29, 3006−3019

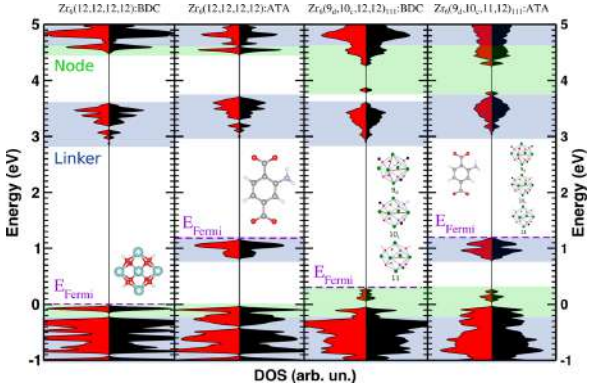

Figure 9. Electronic structure of UiO-66(Zr) with both aminoterephthalate (ATA) and three missing linkers. This can be deduced from the superposition of an ATA-functionalized UiO-66(Zr) and the defect structure of unfunctionalized UiO-66(Zr). Red and black curves represent different spin channels, and all DOS are aligned with respect to the pristine μ-OH,O node states. Blue and green indicate linker and node states, respectively. The charge density corresponding to the lowest unoccupied d orbitals of Zr6(9d,10c,11,12)111:ATA and $Zr_6(9_d10_\sigma11,12)_{111}$:BDC is found to be essentially equal (see Figure S10).

although several electron-donating groups change the theoretical charge transfer efficiency, this change remains limited due to the high energy of the Zr d orbitals with respect to the excited linker states (ΔE_{LMCT}). Several groups discussed the LMCT and performed EPR and other spectroscopic measurements to investigate the charge transfer experimentally.[36,40] They demonstrated the existence of Zr^{3+} species, but at very low concentrations and highly dependent on temperature and solvent, confirming that pristine and linker-functionalized UiO-66(Zr) materials have no efficient transfer. The limited increase in catalytic activity may either be caused by small electronic effects of functional groups or by the presence of inherent defects (see further).

The problem of inefficient charge transfer can be tackled by **altering the metal node**, reducing ΔE_{LMCT}. Introduction of Ti in the Zr node, via postsynthetic exchange,[90,91] strongly improves the catalytic activity of the material.[24,80] Nasalevich and co-workers[40] discussed three existing isostructural MOFs composed of d^0 metals (Ti^{4+}, Zr^{4+}, and Hf^{4+}) and confirmed that only the Ti mixed-metal material shows a large LMCT. Also computationally, Ti materials have been shown to possess a much smaller ΔE_{LMCT}.[77,79] Figure S6 shows our own calculations of UiO-66 with purely Ti, Zr, or Hf nodes. The low lying Ti 3d states overlap with the linker-based LUCO, increasing the electron transfer efficiency.

In this work, we showed that defects also alter the electronic structure. They provide an alternative way to tune the LMCT since removing linkers from the UiO-66 structure affects the nodes as well. This lowers the energy of localized Zr d orbitals at the defect site, effectively decreasing ΔE_{LMCT} and improving the charge transfer to the node. The presence of missing linker defects might (partially) explain why a good catalytic activity was still found for some functionalized UiO-66(Zr) materials.[31−36] The number and types of defects present in the material and hence ΔE_{LMCT} can be controlled by applying different syntheses.[43−45,47] Besides missing linkers, Lillerud et al. recently also discussed the presence of missing nodes as one of the major defect types in UiO-66(Zr).[46] However, removing a complete node has a similar effect on the electronic structure as removing linkers (see Figure S5), since the removed node itself does not affect the electronic structure and the edges of the defect consist of nodes with one additional linker missing.

Designing a highly active MOF-based photocatalyst, using a broad range of the visible spectrum and exhibiting an efficient LMCT, requires both ΔE_{abs} and ΔE_{LMCT} to be tuned. The independence of nodes and linkers, in MOFs with a 0D inorganic sublattice, allows one to tune them in an orthogonal way, enabling a complete and precise control of the electronic properties of these photocatalysts. Absorption properties can be tuned by the introduction of linker states. LMCT on the other hand, can be tuned by modifying the makeup of the node, be it directly through metal substitution or indirectly through the introduction of defects.

6. CONCLUSION

When designing UiO-66 frameworks for photocatalysis, different pathways are available to engineer their absorption and charge transfer capabilities. Moreover, the largely independent behavior of linkers and inorganic nodes enables the introduction of the concept of orthogonal electronic structure engineering. This work discusses the influence of missing linker defects on the electronic structure of UiO-66-type frameworks. Missing linker defects mostly affect the local node geometry and therefore offer an alternative route to node modification, which was thus far only achieved through metal substitution.

We first introduced a clear notation to classify missing linker defect structures, providing a more complete and transparent way of ordering these structures compared to currently available literature. The notation specifies for each defect structure the node coordinations in the unit cell and the interlinker distances, in line with the observed independence of nodes and linkers in UiO-66.

The energetics of different defect structures could be understood via a simple model, again assuming that linker−node and even linker−linker interactions only play a minor role in their relative stability. A unique energy could therefore be

DOI: 10.1021/acs.chemmater.6b05444
Chem. Mater. 2017, 29, 3006−3019

attributed to each node configuration in a defect structure, summing up to the total defect energy. Their geometry could be explained with an ionic model, which assumes complete electron transfer to the oxygen atoms. Using such a node-based energy approach, the most stable defect structures, typically containing 10_c nodes (see Figure 2), were successfully identified. Only the predictions for the high-energy defect structures sometimes deviated, since our assumption of independent nodes only holds if there is no interaction with the (missing) linkers.

The electronic properties were also shown to be determined by the node configurations present in the unit cell. Linker removal results in a change of the environment of the affected Zr atoms, which often lowers their unoccupied d orbitals (ΔE_{LMCT}) and increases charge transfer likelihood, therefore improving the photocatalytic activity. On the other hand, the linker states remain almost constant for all defect structures (ΔE_{abs}), corroborating the idea of orthogonal tuning of the electronic structure. We showed that the effect of missing linkers on the unoccupied d orbitals is highly dependent on the number of defects and their configuration. It was observed that only when two or more missing linkers are removed from the same node, a noticeable energy lowering of the d orbitals is obtained. This lowering was found to be the largest when the removed linkers are connected to a single Zr atom, as this drastically changes the environment of that atom. Furthermore, we investigated the localization of the excited electron after LMCT by means of a simple cluster model. We showed that for a sufficient number of missing linkers, the excited electron will preferentially be located on the lowest coordinated Zr atoms, in line with the periodic results, which is beneficial for further catalytic steps with the material.

Because of this striking decoupling between node- and linker-based effects on the energetic and electronic properties, we reinterpreted the known approaches to modify the UiO-66 electronic structure according to these two possible routes. From this perspective, we revisited and extended calculations on functionalized linker systems and isovalently substituted UiO-66(Ti, Hf). We concluded that a first approach, i.e., linker modification (linker functionalization, increasing linker length), targeted ΔE_{abs} and thus the absorptive properties of the materials. The second method, node alteration, could be achieved by metal substitution or via the newly proposed pathway of defect engineering and lowers the energy of the node's d orbitals relative to the linker states, ΔE_{LMCT}, to enhance charge transfer capabilities. This reasoning can be extended to MOFs with a clear separation of nodes and linkers in the DOS, providing an instructive approach to design new frameworks and opening possibilities for precisely tuned materials for high-end photocatalytic applications. In addition, the principle of orthogonal electronic structure engineering may also be of broader use in promising new fields such as semiconducting[92] or conductive MOFs[93] and dynamic magnetic frameworks.[94]

■ ASSOCIATED CONTENT

Supporting Information

The Supporting Information is available free of charge on the ACS Publications website at DOI: 10.1021/acs.chemmater.6b05444.

Ionic model applied to all node configurations; schematic structures and comparison of different notations for all one-, two-, and three-defect structures, UiO- 66(Hf), UiO-66(Ti), nitro and amino functionalized UiO-66, UiO-67 and UiO-68; examples corroborating the principle of UiO-66 orthogonal electronic structure engineering; values for ΔE_{LMCT} and ΔE_{abs}; orbital localization in the periodic structure and for the cluster models (PDF)

■ AUTHOR INFORMATION

Corresponding Authors

*E-mail: Veronique.VanSpeybroeck@UGent.be.
*E-mail: Kurt.Lejaeghere@UGent.be.

ORCID

Arthur De Vos: 0000-0002-4916-6066

Notes

The authors declare no competing financial interest.

■ ACKNOWLEDGMENTS

This project has received funding from the European Union's Horizon 2020 research and innovation programme under Marie Sklodowska-Curie grant agreement no. 641887 (project acronym: DEFNET), the Fund for Scientific Research-Flanders (FWO), the Research Board of Ghent University, the European Union Horizon 2020 research and innovation programme [consolidator ERC grant, agreement no. 647755-DYNPOR (2015-2020)], and BELSPO in the frame of IAP-PAI P7/05. Computational resources and services were provided by the Stevin Supercomputer Infrastructure of Ghent University and by the Flemish Supercomputer Center (VSC), funded by the Hercules Foundation and the Flemish Government - department EWI. The authors thank S. M. J. Rogge for fruitful discussions and W. Dewitte for technical support with the figures.

■ REFERENCES

(1) Barber, J. Photosynthetic energy conversion: natural and artificial. *Chem. Soc. Rev.* **2009**, *38*, 185−196.
(2) Gust, D.; Moore, T. A.; Moore, A. L. Solar fuels via artificial photosynthesis. *Acc. Chem. Res.* **2009**, *42*, 1890−1898.
(3) Hou, H. J. M.; Allakhverdiev, S. I.; Najafpour, M. M.; Govindjee. Current challenges in photosynthesis: from natural to artificial. *Front. Plant Sci.* **2014**, *5*, 232.
(4) Fujishima, A.; Honda, K. Electroctrochemical photolysis of water at a semiconductor. *Nature* **1972**, *238*, 37−38.
(5) Hennig, H. Semiconductor Photocatalysis: Principles and Applications. By Horst Kisch. *Angew. Chem., Int. Ed.* **2015**, *54*, 4429−4429.
(6) Hoffmann, M. R.; Martin, S.; Choi, W.; Bahnemann, D. W. Environmental Applications of Semiconductor Photocatalysis. *Chem. Rev.* **1995**, *95*, 69−96.
(7) Fox, M.; Dulay, M. T. Heterogeneous photocatalysis. *Chem. Rev.* **1993**, *93*, 341−357.
(8) Schultz, D. M.; Yoon, T. P. Solar Synthesis: Prospects in Visible Light Photocatalysis. *Science* **2014**, *343*, 1239176.
(9) Lang, X.; Chen, X.; Zhao, J. Heterogeneous visible light photocatalysis for selective organic transformations. *Chem. Soc. Rev.* **2014**, *43*, 473−486.
(10) Zhou, H.-C.; Long, J. R.; Yaghi, O. M. Thematic issue: Metal-Organic Frameworks. *Chem. Rev.* **2012**, *112*, 673−1268.
(11) Li, J.-R.; Kuppler, R. J.; Zhou, H.-C. Selective gas adsorption and separation in metal-organic frameworks. *Chem. Soc. Rev.* **2009**, *38*, 1477−1504.

DOI: 10.1021/acs.chemmater.6b05444
Chem. Mater. 2017, 29, 3006−3019

(12) Corma, A.; García, H.; Llabrés i Xamena, F. X. Engineering metal organic frameworks for heterogeneous catalysis. *Chem. Rev.* **2010**, *110*, 4606−4655.
(13) McKinlay, A.; Morris, R. E.; Horcajada, P.; Férey, G.; Gref, R.; et al. BioMOFs: Metal-Organic Frameworks for Biological and Medical Applications. *Angew. Chem., Int. Ed.* **2010**, *49*, 6260−6266.
(14) Keskin, S.; Kızılel, S. Biomedical Applications of Metal Organic Frameworks. *Ind. Eng. Chem. Res.* **2011**, *50*, 1799−1812.
(15) Liu, D.; Lu, K.; Poon, C.; Lin, W. Metal-organic frameworks as sensory materials and imaging agents. *Inorg. Chem.* **2013**, *53*, 1916−1924.
(16) Wang, J.-L.; Wang, C.; Lin, W. Metal-Organic Frameworks for Light Harvesting and Photocatalysis. *ACS Catal.* **2012**, *2*, 2630−2640.
(17) Nasalevich, M. A.; Van Der Veen, M.; Kapteijn, F.; Gascon, J. Metal-organic frameworks as heterogeneous photocatalysts: advantages and challenges. *CrystEngComm* **2014**, *16*, 4919−4926.
(18) Allendorf, M. D.; Bauer, C. A.; Bhakta, R. K.; Houk, R. J. T. Luminescent metal-organic frameworks. *Chem. Soc. Rev.* **2009**, *38*, 1330−1352.
(19) Cui, Y.; Chen, B.; Qian, G. In *Metal-Organic Frameworks for Photonics Applications*; Chen, B., Qian, G., Eds.; Structure and Bonding, Springer: Berlin, 2014; Vol. *157*, pp 27−88.
(20) Ling, S.; Slater, B. Unusually Large Band Gap Changes in Breathing Metal-Organic Framework Materials. *J. Phys. Chem. C* **2015**, *119*, 16667−16677.
(21) Cavka, J. H.; Jakobsen, S.; Olsbye, U.; Guillou, N.; Lamberti, C.; et al. A new zirconium inorganic building brick forming metal organic frameworks with exceptional stability. *J. Am. Chem. Soc.* **2008**, *130*, 13850−13851.
(22) Leus, K.; Bogaerts, T.; De Decker, J.; Depauw, H.; Hendrickx, K.; et al. Systematic study of the chemical and hydrothermal stability of selected stable Metal Organic Frameworks. *Microporous Mesoporous Mater.* **2016**, *226*, 110−116.
(23) Burtch, N. C.; Jasuja, H.; Walton, K. S. Water Stability and Adsorption in Metal-Organic Frameworks. *Chem. Rev.* **2014**, *114*, 10575−10612.
(24) Wang, A.; Zhou, Y.; Wang, Z.; Chen, M.; Sun, L.; Liu, X. Titanium incorporated with UiO-66(Zr)-type Metal-Organic Framework (MOF) for photocatalytic application. *RSC Adv.* **2015**, *6*, 3671−3679.
(25) Biswas, S.; Van Der Voort, P. A General Strategy for the Synthesis of Functionalised UiO-66 Frameworks: Characterisation, Stability and CO_2 Adsorption Properties. *Eur. J. Inorg. Chem.* **2013**, *2013*, 2154−2160.
(26) Bueken, B.; Vermoortele, F.; Cliffe, M. J.; Wharmby, M. T.; Foucher, D.; et al. A Breathing Zirconium Metal-Organic Framework with Reversible Loss of Crystallinity by Correlated Nanodomain Formation. *Chem. - Eur. J.* **2016**, *22*, 3264−3267.
(27) Lammert, M.; Wharmby, M. T.; Smolders, S.; Bueken, B.; Lieb, A.; et al. Cerium-based metal organic frameworks with UiO-66 architecture: synthesis, properties and redox catalytic activity. *Chem. Commun.* **2015**, *51*, 12578−12581.
(28) Hu, Z.; Nalaparaju, A.; Peng, Y.; Jiang, J.; Zhao, D. Modulated Hydrothermal Synthesis of UiO-66(Hf)-Type Metal-Organic Frameworks for Optimal Carbon Dioxide Separation. *Inorg. Chem.* **2016**, *55*, 1134−1141.
(29) Kim, S.-N.; Lee, Y.-R.; Hong, S.-H.; Jang, M.-S.; Ahn, W.-S. Pilot-scale synthesis of a zirconium-benzenedicarboxylate UiO-66 for CO_2 adsorption and catalysis. *Catal. Today* **2015**, *245*, 54−60.
(30) Bai, Y.; Dou, Y.; Xie, L.-H.; Rutledge, W.; Li, J.-R.; et al. Zr-based metal-organic frameworks: design, synthesis, structure, and applications. *Chem. Soc. Rev.* **2016**, *45*, 2327−2367.
(31) Gomes Silva, C.; Luz, I.; Llabrés i Xamena, F. X.; Corma, A.; García, H. Water Stable Zr-Benzenedicarboxylate Metal-Organic Frameworks as Photocatalysts for Hydrogen Generation. *Chem. - Eur. J.* **2010**, *16*, 11133−11138.
(32) Sun, D.; Fu, Y.; Liu, W.; Ye, L.; Wang, D.; et al. Studies on Photocatalytic CO_2 Reduction over NH_2-UiO-66(Zr) and Its Derivatives: Towards a Better Understanding of Photocatalysis on Metal-Organic Frameworks. *Chem. - Eur. J.* **2013**, *19*, 14279−14285.
(33) Shen, L.; Liang, R.; Luo, M.; Jing, F.; Wu, L. Electronic effects of ligand substitution on metal-organic framework photocatalysts: the case study of UiO-66. *Phys. Chem. Chem. Phys.* **2014**, *17*, 117−121.
(34) Goh, T.; Xiao, C.; Maligal-Ganesh, R. V.; Li, X.; Huang, W. Utilizing mixed-linker zirconium based metal-organic frameworks to enhance the visible light photocatalytic oxidation of alcohol. *Chem. Eng. Sci.* **2015**, *124*, 45−51.
(35) Shen, L.; Liang, S.; Wu, W.; Liang, R.; Wu, L. Multifunctional NH_2-mediated zirconium metal-organic framework as an efficient visible-light-driven photocatalyst for selective oxidation of alcohols and reduction of aqueous Cr(VI). *Dalton Trans.* **2013**, *42*, 13649−13658.
(36) Long, J.; Wang, S.; Ding, Z.; Wang, S.; Zhou, Y.; et al. Amine-functionalized zirconium metal-organic framework as efficient visible-light photocatalyst for aerobic organic transformations. *Chem. Commun.* **2012**, *48*, 11656−11658.
(37) Kozlova, A. E.; Panchenko, V. N.; Hasan, Z.; Khan, N. A.; Timofeeva, M. N.; Jhung, S. W. Photoreactivity of metal-organic frameworks in the decolorization of methylene blue in aqueous solution. *Catal. Today* **2016**, *266*, 136−143.
(38) Dhakshinamoorthy, A.; Asiri, A. M.; García, H. Metal-Organic Framework (MOF) Compounds: Photocatalysts for Redox Reactions and Solar Fuel Production. *Angew. Chem., Int. Ed.* **2016**, *55*, 5414−45.
(39) Dhakshinamoorthy, A.; Garcia, H. *Chem. Soc. Rev.* **2012**, *41*, 5262−5284.
(40) Nasalevich, M.; Hendon, C. H.; Santaclara, J. G.; Svane, K.; van der Linden, B.; et al. Electronic origins of photocatalytic activity in d^0 metal organic frameworks. *Sci. Rep.* **2016**, *6*, 23676.
(41) Horiuchi, Y.; Toyao, T.; Saito, M.; Mochizuki, K.; Iwata, M.; et al. Visible-Light-Promoted Photocatalytic Hydrogen Production by Using an Amino-Functionalized Ti(IV) Metal-Organic Framework. *J. Phys. Chem. C* **2012**, *116*, 20848−20853.
(42) Hendrickx, K.; Vanpoucke, D. E. P.; Leus, K.; Lejaeghere, K.; Van Yperen-De Deyne, A.; et al. Understanding Intrinsic Light Absorption Properties of UiO-66 Frameworks: A Combined Theoretical and Experimental Study. *Inorg. Chem.* **2015**, *54*, 10701−10710.
(43) Sholl, D. S.; Lively, R. P. Defects in Metal-Organic Frameworks: Challenge or Opportunity? *J. Phys. Chem. Lett.* **2015**, *6*, 3437−3444.
(44) Fang, Z.; Bueken, B.; De Vos, D. E.; Fischer, R. A. Defect-Engineered Metal-Organic Frameworks. *Angew. Chem., Int. Ed.* **2015**, *54*, 7234−7254.
(45) Shearer, G. C.; Chavan, S.; Ethiraj, J.; Vitillo, J. G.; Svelle, S.; et al. Tuned to Perfection: Ironing Out the Defects in Metal-Organic Framework UiO-66. *Chem. Mater.* **2014**, *26*, 4068−4071.
(46) Shearer, G. C.; Chavan, S.; Bordiga, S.; Svelle, S.; Olsbye, U.; et al. Defect Engineering: Tuning the Porosity and Composition of the Metal-Organic Framework UiO-66 via Modulated Synthesis. *Chem. Mater.* **2016**, *28*, 3749−3761.
(47) Gutov, O. V.; Hevia, M.; Escudero-Adán, E. C.; Shafir, A. Metal-Organic Framework (MOF) Defects under Control: Insights into the Missing Linker Sites and Their Implication in the Reactivity of Zirconium-Based Frameworks. *Inorg. Chem.* **2015**, *54*, 8396−8400.
(48) Rogge, S. M. J.; Wieme, J.; Vanduyfhuys, L.; Vandenbrande, S.; Maurin, G.; et al. Thermodynamic Insight in the High-Pressure Behavior of UiO-66: Effect of Linker Defects and Linker Expansion. *Chem. Mater.* **2016**, *28*, 5721−5732.
(49) Vandichel, M.; Hajek, J.; Vermoortele, F.; Waroquier, M.; De Vos, D. E.; Van Speybroeck, V. Active site engineering in UiO-66 type metal-organic frameworks by intentional creation of defects: a theoretical rationalization. *CrystEngComm* **2014**, *17*, 395−406.
(50) Vermoortele, F.; Bueken, B.; Le Bars, G.; Van de Voorde, B.; Vandichel, M.; et al. Synthesis Modulation as a Tool To Increase the Catalytic Activity of Metal-Organic Frameworks: The Unique Case of UiO-66(Zr). *J. Am. Chem. Soc.* **2013**, *135*, 11465−11468.
(51) Vermoortele, F.; Vandichel, M.; Van de Voorde, B.; Ameloot, R.; Waroquier, M.; et al. Electronic Effects of Linker Substitution on

DOI: 10.1021/acs.chemmater.6b05444
Chem. Mater. 2017, 29, 3006−3019

Lewis Acid Catalysis with Metal-Organic Frameworks. *Angew. Chem., Int. Ed.* **2012**, *51*, 4887−4890.
(52) Canivet, J.; Vandichel, M.; Farrusseng, D. Origin of highly active metal-organic framework catalysts: defects? Defects! *Dalton Trans.* **2016**, *45*, 4090−409.
(53) Yang, D.; Odoh, S. O.; Borycz, J.; Wang, T. C.; Farha, O. K.; et al. Tuning Zr_6 Metal-Organic Framework (MOF) Nodes as Catalyst Supports: Site Densities and Electron-Donor Properties Influence Molecular Iridium Complexes as Ethylene Conversion Catalysts. *ACS Catal.* **2016**, *6*, 235−247.
(54) Wu, H.; Chua, Y.; Krungleviciute, V.; Tyagi, M.; Chen, P.; et al. Unusual and Highly Tunable Missing-Linker Defects in Zirconium Metal-Organic Framework UiO-66 and Their Important Effects on Gas Adsorption. *J. Am. Chem. Soc.* **2013**, *135*, 10525−10532.
(55) Thornton, A. W.; Babarao, R.; Jain, A.; Trousselet, F.; Coudert, F.-X. Defects in metal-organic frameworks: a compromise between adsorption and stability? *Dalton Trans.* **2016**, *45*, 4352−4359.
(56) Vandichel, M.; Hajek, J.; Ghysels, A.; De Vos, A.; Waroquier, M.; et al. Water coordination and dehydration processes in defective UiO-66 type metal organic frameworks. *CrystEngComm* **2016**, *18*, 7056−7069.
(57) Bristow, J. K.; Svane, K. L.; Tiana, D.; Skelton, J. M.; Gale, J. D.; et al. Free Energy of Ligand Removal in the Metal-Organic Framework UiO-66. *J. Phys. Chem. C* **2016**, *120*, 9276−9281.
(58) Ling, S.; Slater, B. Dynamic acidity in defective UiO-66. *Chem. Sci.* **2016**, *7*, 4706−4712.
(59) Yang, D.; Odoh, S. O.; Wang, T. C.; Farha, O. K.; Hupp, J. T.; et al. Metal-Organic Framework Nodes as Nearly Ideal Supports for Molecular Catalysts: NU-1000- and UiO-66-Supported Iridium Complexes. *J. Am. Chem. Soc.* **2015**, *137*, 7391−7396.
(60) Kresse, G.; Joubert, D. From Ultrasoft Pseudopotentials to the Projector Augmented-Wave Method. *Phys. Rev. B: Condens. Matter Mater. Phys.* **1999**, *59*, 1758−1775.
(61) Kresse, G.; Hafner, J. Ab Initio Molecular Dynamics for Liquid Metals. *Phys. Rev. B: Condens. Matter Mater. Phys.* **1993**, *47*, 558−561.
(62) Kresse, G.; Hafner, J. Ab Initio Molecular-Dynamics Simulation of the Liquid-Metal-Amorphous-Semiconductor Transition in Germanium. *Phys. Rev. B: Condens. Matter Mater. Phys.* **1994**, *49*, 14251−14269.
(63) Kresse, G.; Furthmüller, J. Efficiency of Ab-Initio Total Energy Calculations for Metals and Semiconductors Using a Plane-Wave Basis Set. *Comput. Mater. Sci.* **1996**, *6*, 15−50.
(64) Kresse, G.; Furthmüller, J. Efficient Iterative Schemes for Ab Initio Total-Energy Calculations Using a Plane-Wave Basis Set. *Phys. Rev. B: Condens. Matter Mater. Phys.* **1996**, *54*, 11169−11186.
(65) Perdew, J. P.; Burke, K.; Ernzerhof, M. Generalized Gradient Approximation Made Simple. *Phys. Rev. Lett.* **1996**, *77*, 3865−3868.
(66) Lejaeghere, K.; Bihlmayer, G.; Björkman, T.; Blaha, P.; Blügel, S.; et al. Reproducibility in density functional theory calculations of solids. *Science* **2016**, *351*, 1415.
(67) Kresse, G.; Marsman, M.; Furthmüller, J. *VASP the GUIDE*; Computational Materials Physics, Faculty of Physics, Universität Wien: Vienna, Austria.
(68) Vinet, P.; Ferrante, J.; Rose, J. H.; Smith, J. R. Compressibility of solids. *J. Geophys. Res.* **1987**, *92*, 9319−9325.
(69) Frisch, M. J.; Trucks, G. W.; Schlegel, H. B.; Scuseria, G. E.; Robb, M. A. et al. *Gaussian 09*, revision D.01; Gaussian Inc.: Wallingford, CT, 2009.
(70) Lee, C.; Yang, W.; Parr, R. G. Development of the Colle-Salvetti correlation-energy formula into a functional of the electron density. *Phys. Rev. B: Condens. Matter Mater. Phys.* **1988**, *37*, 785−789.
(71) Becke, A. D. Density-functional thermochemistry. III. The role of exact exchange. *J. Chem. Phys.* **1993**, *98*, 5648−5652.
(72) Weigend, F.; Ahlrichs, R. Balanced basis sets of split valence, triple zeta valence and quadruple zeta valence quality for H to Rn: Design and assessment of accuracy. *Phys. Chem. Chem. Phys.* **2005**, *7*, 3297−3305.
(73) Freysoldt, C.; Grabowski, B.; Hickel, T.; Neugebauer, J.; Kresse, G.; et al. First-principles calculations for point defects in solids. *Rev. Mod. Phys.* **2014**, *86*, 253−305.
(74) De Vos, A.; Lejaeghere, K.; Vanpoucke, D. E. P.; Joos, J. J.; Smet, P. F.; et al. First-Principles Study of Antisite Defect Configurations in $ZnGa_2O_4$:Cr Persistent Phosphors. *Inorg. Chem.* **2016**, *55*, 2402−2412.
(75) Hu, Z.; Zhao, D. De facto methodologies toward the synthesis and scale-up production of UiO-66-type metal-organic frameworks and membrane materials. *Dalton Trans.* **2015**, *44*, 19018−19040.
(76) Hon Lau, C.; Babarao, R.; Hill, M. R. A route to drastic increase of CO_2 uptake in Zr metal organic framework UiO-66. *Chem. Commun.* **2013**, *49*, 3634−3636.
(77) Yasin, A.; Li, J.; Wu, N.; Musho, T. Study of the inorganic substitution in a functionalized UiO-66 metal-organic framework. *Phys. Chem. Chem. Phys.* **2016**, *18*, 12748−12754.
(78) Lee, Y.; Kim, S.; Kang, J.; Cohen, S. M. Photocatalytic CO_2 reduction by a mixed metal (Zr/Ti), mixed ligand metal-organic framework under visible light irradiation. *Chem. Commun.* **2015**, *51*, 5735−5738.
(79) Yang, L.; Ganz, E.; Svelle, S.; Tilset, M. Computational exploration of newly synthesized zirconium metal-organic frameworks UiO-66, −67, −68 and analogues. *J. Mater. Chem. C* **2014**, *2*, 7111−7125.
(80) Sun, D.; Liu, W.; Qiu, M.; Zhang, Y.; Li, Z. Introduction of a mediator for enhancing photocatalytic performance via post-synthetic metal exchange in metal-organic frameworks (MOFs). *Chem. Commun.* **2014**, *51*, 2056−2059.
(81) Flage-Larsen, E.; Røyset, A.; Cavka, J. H.; Thorshaug, K. Band Gap Modulations in UiO Metal-Organic Frameworks. *J. Phys. Chem. C* **2013**, *117*, 20610−20616.
(82) Walsh, A.; Butler, K. T.; Hendon, C. H. Chemical principles for electroactive metal-organic frameworks. *MRS Bull.* **2016**, *41*, 870−876.
(83) Vermoortele, F.; Vandichel, M.; Van de Voorde, B.; Ameloot, R.; Waroquier, M.; et al. Electronic Effects of Linker Substitution on Lewis Acid Catalysis with Metal-Organic Frameworks. *Angew. Chem., Int. Ed.* **2012**, *51*, 4887−4890.
(84) Ferey, G. Hybrid porous solids: past, present, future. *Chem. Soc. Rev.* **2008**, *37*, 191−214.
(85) Kandiah, M.; Nilsen, M.; Usseglio, S.; Jakobsen, S.; Olsbye, U.; et al. Synthesis and Stability of Tagged UiO-66 Zr-MOFs. *Chem. Mater.* **2010**, *22*, 6632−6640.
(86) Katz, M. J.; Brown, Z. J.; Colón, Y. J.; Siu, P. W.; Scheidt, K. A.; et al. A facile synthesis of UiO-66, UiO-67 and their derivatives. *Chem. Commun.* **2013**, *49*, 9449−9451.
(87) Chavan, S. M.; Shearer, G. C.; Svelle, S.; Olsbye, U.; Bonino, F.; et al. Synthesis and Characterization of Amine-Functionalized Mixed-Ligand Metal-Organic Frameworks of UiO-66 Topology. *Inorg. Chem.* **2014**, *53*, 9509−9515.
(88) Deria, P.; Mondloch, J. E.; Karagiaridi, O.; Bury, W.; Hupp, J. T.; et al. Beyond post-synthesis modification: evolution of metal-organic frameworks via building block replacement. *Chem. Soc. Rev.* **2014**, *43*, 5896−912.
(89) Musho, T.; Li, J.; Wu, N. Band gap modulation of functionalized metal-organic frameworks. *Phys. Chem. Chem. Phys.* **2014**, *16*, 23646−23653.
(90) Kim, M.; Cahill, J. F.; Fei, H.; Prather, K. A.; Cohen, S. M. Postsynthetic Ligand and Cation Exchange in Robust Metal-Organic Frameworks. *J. Am. Chem. Soc.* **2012**, *134*, 18082−18088.
(91) Smith, S. J.; Ladewig, B. P.; Hill, A. J.; Lau, C.; Hill, M. R. Post-synthetic Ti Exchanged UiO-66 Metal-Organic Frameworks that Deliver Exceptional Gas Permeability in Mixed Matrix Membranes. *Sci. Rep.* **2015**, *5*, 7823.
(92) Usman, M.; Mendiratta, S.; Lu, K.-L. Semiconductor Metal-Organic Frameworks: Future Low-Bandgap Materials. *Adv. Mater.* **2017**, *29*, 1605071.
(93) Sun, L.; Campbell, M. G.; Dincă, M. Electrically Conductive Porous Metal-Organic Frameworks. *Angew. Chem., Int. Ed.* **2016**, *55*, 3566−3579.

DOI: 10.1021/acs.chemmater.6b05444
Chem. Mater. 2017, 29, 3006−3019

(94) Coronado, E.; Minguez Espallargas, G. Dynamic magnetic MOFs. *Chem. Soc. Rev.* **2013**, *42*, 1525−1539.

DOI: 10.1021/acs.chemmater.6b05444
Chem. Mater. 2017, 29, 3006−3019

Paper II

Exploring Lanthanide Doping in UiO-66: A Combined Experimental and Computational Study of the Electronic Structure

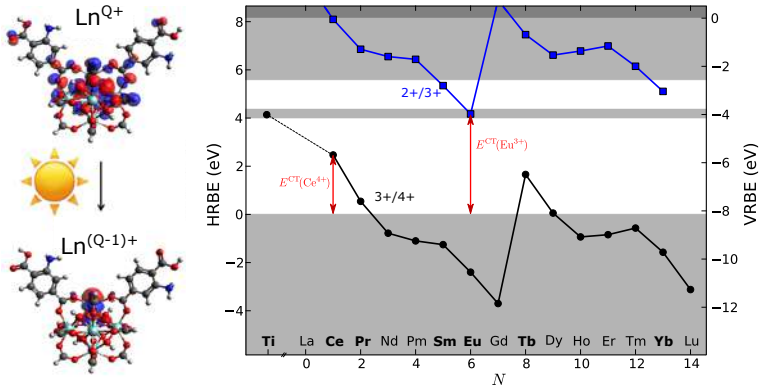

K. Hendrickx, J. J. Joos, A. De Vos,
D. Poelman, P. F. Smet, V. Van Speybroeck,
P. Van Der Voort and K. Lejaeghere

Inorganic Chemistry, **2018**, *57*, 5463–5474,

A. De Vos performed the periodic simulations and contributed in the interpretation as well as the preparation of the manuscript.

Inorganic Chemistry
Cite This: Inorg. Chem. 2018, 57, 5463−5474
Article
pubs.acs.org/IC

Exploring Lanthanide Doping in UiO-66: A Combined Experimental and Computational Study of the Electronic Structure

Kevin Hendrickx,[†,∥] Jonas J. Joos,[‡,§] Arthur De Vos,[∥] Dirk Poelman,[‡,§] Philippe F. Smet,[‡,§] Veronique Van Speybroeck,[*,∥] Pascal Van Der Voort,[*,†] and Kurt Lejaeghere[*,∥]

[†]Center for Ordered Materials, Organometallics and Catalysis (COMOC), Department of Inorganic and Physical Chemistry, Ghent University, Krijgslaan 281 (S3), 9000 Gent, Belgium
[‡]LumiLab, Department of Solid State Sciences, Ghent University, Krijgslaan 281 (S1), 9000 Gent, Belgium
[§]Center for Nano- and Biophotonics (NB Photonics), Ghent University, 9000 Gent, Belgium
[∥]Center for Molecular Modeling (CMM), Ghent University, Technologiepark 903, 9052 Zwijnaarde, Belgium

Supporting Information

ABSTRACT: Lanthanide-based metal−organic frameworks show very limited stabilities, which impedes their use in applications exploiting their extraordinary electronic properties, such as luminescence and photocatalysis. This study demonstrates a fast and easy microwave procedure to dope UiO-66, an exceptionally stable and tunable Zr-based metal−organic framework. The generally applicable synthesis methodology is used to incorporate different transition metal and lanthanide ions. Selected experiments on these newly synthesized materials allow us to construct an energy scheme of lanthanide energy levels with respect to the UiO-66 host. The model is confirmed via absolute intensity measurements and provides an intuitive way to understand charge transfer mechanisms in these doped UiO-66 materials. Density functional theory calculations on a subset of materials moreover improve our understanding of the electronic changes in doped UiO-66 and corroborate our empirical model.

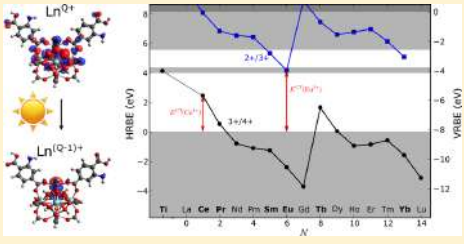

INTRODUCTION

Since their discovery, metal−organic frameworks (MOFs) have developed into a versatile platform for various applications, ranging from gas sorption and catalysis to sensing.[1−3] They owe this to their construction from inorganic clusters, linked together by organic bridges. This inherent modular nature makes it possible to design the materials at a molecular level and tune their properties for a specific application. Moreover, MOFs have recently emerged as photoactive materials, showing promising results in luminescence and photocatalytic applications.[4−8] One of the limiting factors in traditional semiconductor photocatalysts is the high electron−hole recombination rate. In MOFs, electrons are localized on distinct constituents. Hence, the organic linker may serve as the photoreceptive system (or antenna) and the inorganic node as the photocatalytically active center, which are separated entities within the same crystalline material. If the corresponding electronic bands are well-aligned, then an efficient separation and transfer between these sites can take place via a ligand-to-metal charge transfer (LMCT). Moreover, the modular setup of a MOF allows for an orthogonal engineering of the electronic structure, since linker and node contributions can be treated independently.[9]

In light-based applications, special attention goes to the series of lanthanide (Ln) metals. Their bright emission forms the basis of many lighting applications, and their specific electronic structure is ideally suited for catalytic fine chemistry.[10−12] Also within MOF research, Ln-based materials have emerged in recent years.[13−15] As Ln ions are inserted in a crystalline framework, they are heterogenized, facilitating the processing steps for several applications. Moreover, the orbital overlap between the antenna and the Ln ion can be ensured since they are part of the same rigid framework. The latter is of paramount importance to provide an efficient pathway for the charge carriers to move in the framework. Unfortunately, difficult syntheses and limited stability restrict the use of Ln MOFs.[16] To overcome this problem, we propose an approach inspired by solid-state lanthanide chemistry where a stable robust carrier material (e.g., a metal oxide) is doped with a small amount of lanthanide ions in a high-temperature process. Within this work, we adopt a microwave-based methodology to dope UiO-66, a robust MOF, with several lanthanide and transition metal ions and investigate the electronic properties of the new materials. So far, this doping strategy to alter the electronic properties was only used to introduce isovalent atoms.[17] However, thanks to the highly exchangeable nature of the constituents in MOF materials, we

Received: February 15, 2018
Published: April 16, 2018

DOI: 10.1021/acs.inorgchem.8b00425
Inorg. Chem. 2018, 57, 5463−5474

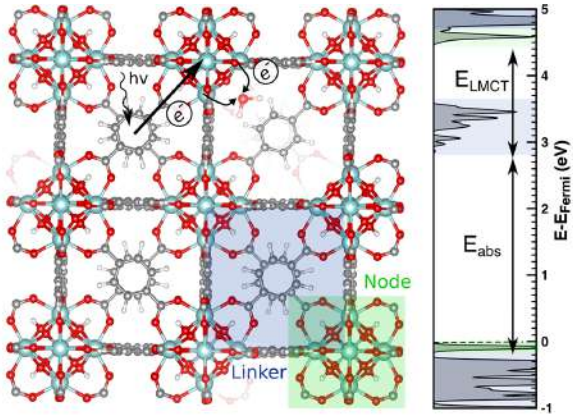

Figure 1. (left) Basic steps in a UiO-66 photocatalytic process: light absorption, LMCT and reduction process. (Right) Density of states of pristine UiO-66. Areas shaded in green indicate node contributions while areas shaded in blue indicate linker states.[9]

show that this methodology can be extended toward many more metals. The doping of a robust MOF with low concentrations of Ln dopant ions leads to a whole new series of materials which may advance a wide variety of applications, ranging from lighting to photocatalysis. Given the stability of the parent material, evaluation in different chemical environments and under different ambient conditions is possible while retaining the Ln-specific properties.

Challenges and Opportunities in Ln-Doping of UiO-66. UiO-66 is an often-used prototype MOF, also in light-based applications, due to its high tunability and unprecedented stability.[18] It is built out of 12-fold coordinated $Zr_6O_4(OH)_4$ inorganic bricks and benzene-1,4-dicarboxylate (BDC^{2-}) linkers.[19,20] The coordinative nature of the bonding in UiO-66 allows for an efficient postsynthetic exchange of both linkers and metals,[21] making UiO-66 the ideal platform for the exploration of new structures containing lanthanide dopant ions. Figure 1 represents the electronic structure of pristine UiO-66 and captures the basic idea of the LMCT process lying at the basis of the photocatalytic activity of the material. In an ideal situation, the aromatic BDC linker acts as an antenna to absorb light and generate an exciton. The excited electron should be able to move toward the inorganic node, reducing the zirconium from Zr^{4+} to Zr^{3+} which then becomes a redox active center.

UiO-66 in its pristine form is however poorly suited for photocatalysis. Besides its large band gap (4 eV), impeding excitation with light in the visible region of the spectrum, the major problem is the inefficient charge transfer between linker and node. Figure 1 shows that a transfer from the linker to the inorganic node will be very difficult, since the empty Zr d states lie more than 1 eV higher than the empty linker band (E_{LMCT}). This lack of overlap hinders the electron in traveling efficiently to the node.[9] In order to improve LMCT, changes to the LUCO states (lowest unoccupied crystalline orbital) are necessary. Introduction of Ti in the Zr node via postsynthetic exchange[22,23] was previously found to strongly improve the catalytic activity of the material due to a lowering of the d states.[24−30] Similarly, the 4f levels of Ln ions are expected to alter the HOCO−LUCO region of the material (HOCO: highest occupied crystal orbital).

Within this work we use for the first time a systematic experimental method to incorporate lanthanide ions in the UiO-66 framework and probe the electronic properties of these new materials. Although we provide insight into the electronic transitions (which result in their absorption/emission behavior) using demanding first-principles computational techniques, we also establish a more empirical model by exploiting recurrent features of the lanthanides. Indeed, systematic behavior emerges across the lanthanide series independent of the chemical environment, as all ions act chemically very similar. This behavior results in a typical zigzag curve for the charge state transition levels of lanthanide impurities in crystalline materials as a function of the used lanthanide. Thanks to the systematics, the location of the charge state transition levels for all lanthanides can be predicted when one knows the location of at least one such level for one lanthanide ion.[31−33] In this work, the systematic properties of the lanthanide ions are used to construct band diagrams of Ln-doped UiO-66, containing all 14 Ln (2+/3+) and (3+/4+) charge state transition levels, based on a small set of experimental absorption and photoluminescence (PL) spectra. To our knowledge, this is the first time a complex hybrid carrier material is evaluated using this methodology. Furthermore, a density functional theory (DFT) study of some of the selected materials corroborates the findings of the empirical model and helps to understand the electronic structure changes observed for the different doped frameworks. It bridges the gap between our novel Ln-MOFs and the existing isovalently doped materials.

EXPERIMENTAL AND COMPUTATIONAL DETAILS

Experimental Details. *Synthesis.* UiO-66 was synthesized based on a general procedure by Biswas and co-workers[34] (see Supporting Information section S1). The doping of the UiO-66 framework was performed using postsynthetic metal ion exchange inspired by a methodology developed by Lau et al. and Tu et al.[17] Materials were prepared doped with Ti^{4+}, Yb^{3+}, Eu^{3+}, Nd^{3+}, and Ce^{4+} and will be denoted as UiO-66:X^{n+}. To compare the spectroscopic properties of pure and doped UiO materials, a pure cerium-based UiO was also prepared. Synthesis of this UiO-66(Ce) was based on a procedure by Lammert et al.[35] Details of all syntheses are given in Supporting Information (section S1).

DOI: 10.1021/acs.inorgchem.8b00425
Inorg. Chem. 2018, 57, 5463−5474

Structural Characterization. Ambient-temperature powder X-ray diffraction (PXRD) patterns were recorded on a Thermo Scientific ARL XTra diffractometer operating at 40 kV and 40 mA using Cu Kα radiation (λ = 1.5406 Å). The sorption isotherms were measured on a Belsorp Mini apparatus, operating at 77 K. Before the measurements, samples were dried for 4h at 80 °C in dynamic vacuum. All X-ray photoelectron spectroscopy (XPS) measurements were recorded on a S-Probe XPS spectrometer from Surface Science Instruments (VG) with monochromated Al (1486 eV) exciting radiation. Powder was positioned on the holder using conducting tape. In order to minimize charging, an electron flood gun of 3 eV was used as a neutralizer. All spectra were calibrated toward a C 1s peak position of adventitious carbon at 284.6 eV. For elemental mapping, a field-emission scanning electron microscope (FEI Quanta 200) operating at low vacuum was used, equipped with an energy dispersive X-ray spectrometer (EDX). Samples were measured with an electron beam accelerating voltage of 15 kV. Bright-field scanning transmission electron microscopy (BF-STEM) and EDX measurements were performed on a JEOL JEM-2200FS high-resolution STEM equipped with an EDX spectrometer with a spatial resolution of 0.13 nm, image lens spherical aberration corrector, electron energy loss spectrometer (filter), and field-emission gun (FEG) operating at 200 keV.

Spectroscopy. Solid-state ultraviolet/visible light (UV/vis) measurements were done on a Varian Cary 500 dual-beam UV/vis/NIR spectrophotometer using an internal 110 mm $BaSO_4$-coated integrating sphere. Liquid experiments were carried out in solvent (dimethylformamide) on a PerkinElmer Lambda 900 UV/vis/NIR spectrometer. For both emission and excitation photoluminescence spectra, a FS920 of Edinburgh Instruments was used. A high-pressure xenon arc lamp of 450 W was used as light source. The excitation wavelength was selected through a double excitation monochromator.

Empirical Model for Charge State Transition Levels. Lanthanide ions show similar properties irrespective of their chemical environment.[36] When incorporated as impurities in a given host material, a typical zigzag curve can be constructed for their charge state transition levels as a function of the 4f occupation number using the energies of the charge transfer bands observed in experimental spectra. This methodology is reviewed in refs 31−33 and is known to give transition level locations of lanthanide impurities in inorganic crystals within accuracies of a few 100 meV. Recently, an extension of the empirical rules was proposed toward titanium.[37]

Computational Details. In addition to the empirical model used to construct the Ln charge state transition levels, we also opted to further unravel the electronic properties of a carefully selected subset of samples by using DFT and time-dependent DFT (TDDFT). Because excited state calculations on periodic systems are still challenging within current computational models, we first performed TDDFT calculations on some well-defined clusters. These calculations allowed us to study the possible excitations and yielded qualitative information on the orbitals involved. Afterward periodic DFT calculations revealed the ground state band structures of the pristine UiO-66, UiO-66(Ti), UiO-66(Hf), and UiO-66(Ce) material. Since the behavior of Ln ions is notoriously difficult to predict with DFT, we only performed UiO-66(Ln) calculations with Ce^{4+}. Because Ce^{4+} contains no 4f or 5d electrons, the electron correlation is limited and DFT has been shown to provide reasonable qualitative results.[38,39]

Calculations on Cluster Models. Calculations on cluster models were performed in Gaussian09[40] using DFT and TDDFT on a series of simplified model systems. Both clusters with stoichiometry $Zr_{6-x}X_xO_4(OH)_4(HCOO)_{12}$ and $Zr_{6-x}X_xO_4(OH)_4(HCOO)_{10}(HBDC)_2$ were used to investigate the influence of the dopant ion. Previous research[41] has shown that the combination of the B3LYP[42,43] functional with a triple-ζ Def2TZVP basis set[44] is a good choice for these cluster calculations and hence we applied the same settings in this work. Geometry optimization of the clusters was performed on the same level.

Two types of calculations were performed. In order to mimic the cluster after excitation and LMCT of the framework, we performed ground-state DFT calculations on the model cluster with one extra electron.[45] In this way, the system is forced in a doublet spin state and a charge of −1. This allowed us to look into the ideal case where the electron efficiently transfers to the inorganic node, and to study the potential preferential sites in these nodes for the electron to reside. Actual modeling of excited states is computationally much more demanding. TDDFT within its linear-response formulation offers a way to calculate vertical transition energies, which can be linked to experimental UV/vis spectra.[46−48] To visually improve the similarity with the experimental spectra, a Gaussian distribution (σ = 0.4 eV) was used to broaden the theoretical transition energies.

Periodic Models. Periodic calculations were performed on a 4-node unit cell within the VASP package,[49,50] using the Projector Augmented Wave approach (PAW)[51] with the recommended high-precision VASP 5.4 GW PAW potentials[52] and the PBE functional.[53] The plane-wave basis set had a kinetic energy cutoff of 700 eV, and a Γ-only grid was used to sample the first Brillouin zone. The equilibrium volume was obtained using a Rose-Vinet equation-of-state fit (9 points between −4 and 4% of the equilibrium volume),[54] and the structures were relaxed at this volume. An ionic energy criterion of 10^{-4} eV was used for all relaxations, and an electronic convergence criterion of 10^{-5} eV or 10^{-7} eV was applied for the equation of state points and equilibrium structures, respectively. Densities of states (DOS) were calculated using a Γ-centered 2 × 2 × 2 grid and a 10^{-7} eV electronic convergence threshold.

RESULTS AND DISCUSSION

The first part of this work provides an overview of our experimentally produced UiO-66 samples and describes their synthesis and structural characterization in detail. Second, spectroscopic techniques are used to probe the electronic structure of the samples. Using these experimental data, we then reconstruct the typical lanthanide "zigzag" curve of the (2+/3+) and (3+/4+) charge state transition levels relative to the UiO-66 band diagram. Finally, we use DFT calculations on cluster and periodic models to obtain more insight in the charge transfer processes in titanium- and lanthanide-doped materials.

Synthesis and Structural Characterization. We doped UiO-66 with 5 different lanthanide and transition metal ions using a postsynthetic cation exchange method (see Table 1). Postsynthetic cation exchange is a technique that allows the modification of existing stable materials and the production of systems with otherwise unreachable compositions.[21,22,55] It is only in the past decade that the cation techniques applied to other inorganic materials[56−58] came into use within MOF chemistry. We used a microwave-assisted approach inspired by

Table 1. Overview of Samples Studied in This Work[a]

sample name	metal ion concentrations	linker
UiO-66	100% Zr^{4+}	BDC
UiO-66(Ce)	100% Ce^{4+}	BDC
UiO-66(Ce)-fum	100% Ce^{4+}	Fum
UiO-66:Ce^{4+}	1−5% Ce^{4+}	BDC
UiO-66-NH_2:Ce^{4+}	1−5% Ce^{4+}	BDC-NH_2
UiO-66:Nd^{3+}	1−5% Nd^{3+}	BDC
UiO-66:Eu^{3+}	1−5% Eu^{3+}	BDC
UiO-66:Yb^{3+}	1−5% Yb^{3+}	BDC
UiO-66:Ti^{4+}	5% Ti^{4+}	BDC
UiO-66-NH_2:Ti^{4+}	5% Ti^{4+}	BDC-NH_2

[a]Doped samples are indicated as UiO-66:X^{n+}. Ion concentrations are obtained by fitting of the (TEM/SEM)-EDX results and are prone to large errors. However, similar loadings were obtained for all samples. The loading of the UiO-66:Ti^{4+} was verified via inductive coupled plasma optical emission spectroscopy (ICP-OES). BDC stands for benzene-1,4-dicarboyxlic acid, BDC-NH_2 is 2-amino-benzene-1,4-dicarboxylic acid and fum represents fumaric acid. Note that UiO-66-fum is more generally known as MOF-801.[59]

DOI: 10.1021/acs.inorgchem.8b00425
Inorg. Chem. 2018, 57, 5463−5474

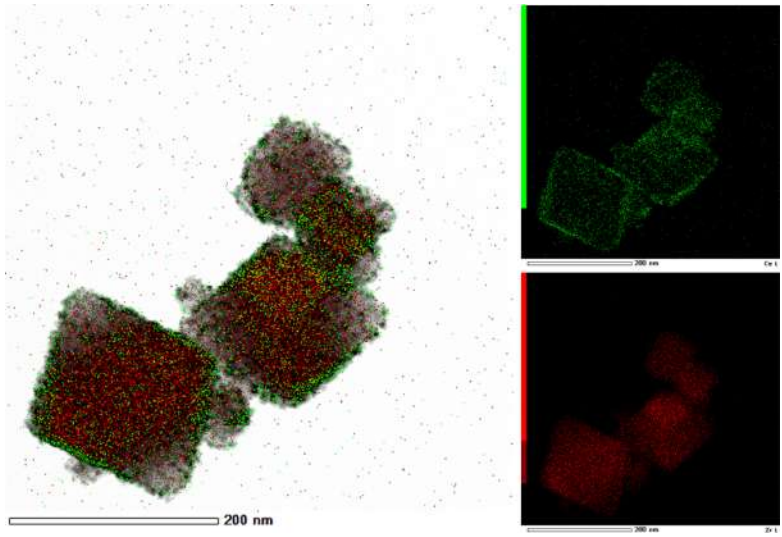

Figure 2. BF-STEM EDX profiles of Ce atoms (green) and Zr atoms (red) within a UiO-66:Ce^{4+} sample.

Tu et al.,[17] which compared to a conventional solvothermal approach allows for a drastic reduction in synthesis time from about a week to only a few hours to obtain a similar loading. We based our procedure on this doping strategy and extended its application to the incorporation of lanthanide ions as dopant in the framework.

A thorough experimental characterization was performed for all samples shown in Table 1, and the data are provided in Supporting Information (section S2). Our measurements show that after the cation exchange, all samples retained their crystallinity and porosity. Moreover, the shift of the low-angle diffraction peaks and the fact that no new peaks are observed in the XRD diffractogram seem to suggest that dopant ions are included on a Zr site and that no other Ti−O or Ln−O species are formed. However, whether dopant ions are inserted on a Zr position in the metal node or are adsorbed at a defect site is still subject to much debate.[60] Direct proof is very hard to obtain, and this matter remains open for discussion. Nitrogen sorption measurements (see Supporting Information) confirm that the UiO samples preserve a high surface area, but a partial blocking of the pores by adsorbed metal precursors cannot be a priori excluded. A combination of the two effects may also occur.

The distribution of the dopant ions was verified using BF-STEM EDX measurements. Figure 2 shows that the Ce^{4+} ions are distributed quite homogeneously and no cluster formation is observed. We however notice that some surface enrichment can be seen, probably due to diffusion limitations of the precursor in the material. Similar measurements were performed on Eu^{3+}- and Yb^{3+}-doped samples (see Figures S2 and S3). In the following sections, our focus will be mainly on the Ce^{4+}- and Eu^{3+}-doped materials. This gives sufficient information to construct the charge state transition zigzag curve for both (2+/3+) and (3+/4+) transitions. Results will be compared to either experiments or DFT calculations on pristine UiO-66 and Ti- or Hf-containing materials. For completeness spectra of all doped samples are provided in the Supporting Information.

Spectroscopy. UV/vis and photoluminescence (PL) measurements were performed to probe the electronic structure of the UiO materials. The former give information on direct transitions, directly related to the band gap of the material. Interpretation of the latter is more involved, since excited-state relaxations and intersystem conversions can occur before a photon is emitted by the material. Combination of the two techniques allows to understand the electronic structure of the materials on a fundamental level and provides the necessary information for the construction of the Ln zigzag curve.

UV/Vis Measurements of Doped UiO-66:X^{n+}. When assessing the electronic properties of photoactive doped UiO materials, it is instructive to compare the new materials to the known titanium-doped UiO-66. Figure 3 shows the UV/vis Kubelka−Munk function obtained from diffuse reflectance measurements for pristine UiO-66 and UiO-66:Ti^{4+} and for their amino-functionalized counterparts. As was previously established, the amine group of the linker-functionalized material has a large effect on the absorption edge (region **B** in Figure 3).[41] In comparison, the introduction of Ti leads to a shift and broadening of the UV edge due to the strong Ti−O−Zr interactions (region **A** in Figure 3). The interaction of the metal node with the linker also leads to a shift of the NH_2 absorption for the amine-functionalized materials (region **C** in Figure 3). The influence of the nearby metal node on the absorption maximum of the linker (regions **A** and **C**) has been observed in literature[24,26] and will be discussed in more detail later in the "Computational Assessment" section of this work.

Figure 4 shows the UV/vis spectra of UiO-66:Ce^{4+} and UiO-66-X(Ce) (X = BDC and fumaric acid (fum)) compared to pristine UiO-66 and UiO-66-NH_2. UV/vis spectra of the other lanthanide-doped materials are provided in the Supporting Information. We find that independent of the chosen linker

DOI: 10.1021/acs.inorgchem.8b00425
Inorg. Chem. 2018, 57, 5463−5474

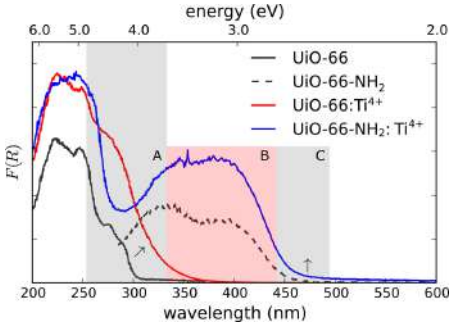

Figure 3. UV/vis spectra in Kubelka–Munk units of pristine UiO-66 and UiO-66-NH_2 materials compared to Ti-doped frameworks. Band **A** shows how the excitation of the aromatic system is influenced by the metal node. The black arrow indicates the shift caused by the changing environment of the linker. Band **B** corresponds to the absorption of the NH_2 group. Band **C** shows the change in the NH_2 absorption due to the interaction with Ti. Here again, the arrow indicates the shift caused by titanium.

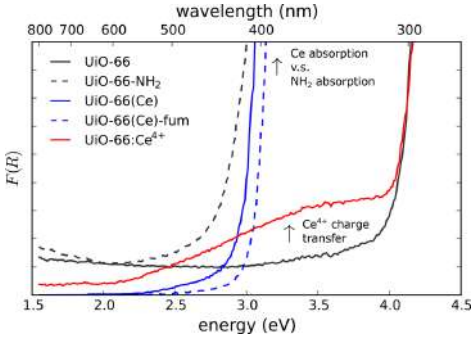

Figure 4. UV/vis spectra in Kubelka–Munk units of a series of different Ce^{4+} UiO samples compared to pristine UiO-66 and UiO-66-NH_2. For the nomenclature, see Table 1.

(fumaric acid or BDC), the absorption edge of UiO-66-X(Ce) is the same. This indicates that the main absorption in this material is due to a node-based transition rather than a linker transition like in pristine UiO-66. Moreover, the change in band gap is coincidentally about the same as induced by addition of a NH_2 functional group to the linker. We will show in the "Computational Assessment" section that this is because insertion of cerium in the inorganic node introduces a new band within the band gap of the pristine UiO-66, similar to what happens in amino-functionalized UiO-66.

Contrary to the pure cerium materials, the doped UiO-66:Ce^{4+} shows an edge at 4 eV. This transition is similar to the one in pristine UiO and corresponds to the BDC linker. However, a new broad band arises in the spectrum, starting at 2.5 eV, which we attribute to a charge transfer process. This band is most likely due to the O^{2-}–Ce^{4+} LMCT process, and we will refer to the corresponding energy as E_{CT} to avoid confusion with E_{LMCT} as defined in Figure 1 ($E_{CT} = E_{gap} + E_{LMCT}$ with $E_{LMCT} < 0$ for UiO-66:Ce^{4+}). The position of this band will be used to construct the charge state transition level curve for the (3+/4+) transition further on.

Photoluminescence Measurements. Eu^{3+} represents one of the spectroscopically most investigated lanthanide ions due to its characteristic red luminescence lines.[61] A typical Jablonski diagram of a generic Eu^{3+}-doped material is presented in Figure 5 and shows the different pathways that can occur after

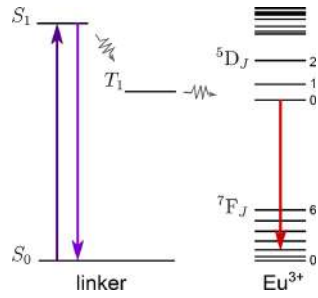

Figure 5. Simplified Jablonski diagram showing the energy transfer processes in a generic Eu^{3+}-doped material. Solid lines indicate the absorption or emission of a photon and curved lines are nonradiative transitions.

absorption of a photon by the material. The excited linker can quickly decay to its ground state (fluorescence) or the electron can be transferred via an intersystem crossing to a triplet state and then to the Eu^{3+} impurity. From there it decays to different low-lying Eu^{3+} levels, giving rise to characteristic peaks in the emission spectrum.

Figure 6 shows the emission and excitation spectra of the UiO-66:Eu^{3+} sample. The red line shows a broad linker emission band

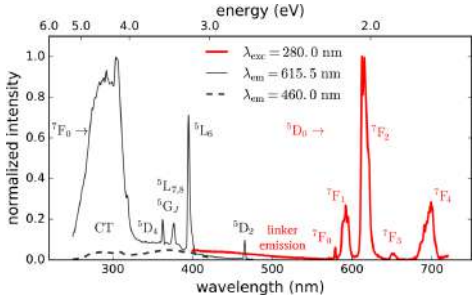

Figure 6. Emission and excitation spectrum of UiO-66:Eu^{3+} measured at 230 K.

ranging to about 550 nm (see Supporting Information section S3) followed by the characteristic Eu^{3+} intraconfigurational $4f^6$ lines.[61,62] By measuring the excitation spectrum for emission at wavelengths in these two different regions, we can investigate the mechanisms leading to this specific emission. At 460 nm, only linker emission is found and no Eu^{3+} emission. The excitation spectrum for emission at this wavelength hence shows the characteristic broad band absorption which is also observed for pristine UiO-66 (Supporting Information section S3) and which corresponds to photon absorption of the linker followed by

DOI: 10.1021/acs.inorgchem.8b00425
Inorg. Chem. 2018, 57, 5463–5474

fluorescent decay. If we however look at the spectrum measured at an emission of 615.5 nm, corresponding to the $^5D_0 \rightarrow {}^7F_2$ transition of Eu^{3+}, then more features arise. The narrow lines correspond to direct excitation channels of the Eu atoms with following fluorescent decay. In addition, we observe a broad band which we associate with a charge transfer band. We attribute this excitation to the O^{2-}–Eu^{3+} CT and the value of the edge (300 nm, 4.1 eV) will be used to position the (2+/3+) transition levels of all other lanthanides in the next section.

Charge State Transition Levels. The limited sensitivity of lanthanides to the chemical environment leads to a systematic behavior of various physical properties across the lanthanide series, resulting in a typical zigzag curve. Such curves are often constructed in Ln-doped oxides to predict the charge state transition energies of the whole series by means of only a few experimental data points. These levels are usually compared to the band edges of the host electronic structure (host-referred binding energy, HRBE). The CT offset obtained from the UV/vis data positions the Ce(3+/4+) level at 2.5 eV with respect to the HOCO. The position of this data point fixes the relative energies of the other lanthanides (black line in Figure 7).

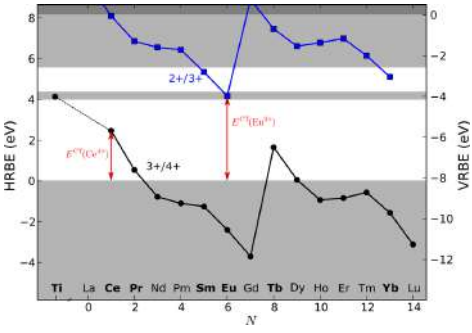

Figure 7. Overlay of the band diagram of UiO-66 (gray) with both the (3+/4+) (black dots) and (2+/3+) charge state transition levels (blue squares) for the lanthanide series incorporated as impurities in the UiO-66 host. Elements with a potentially interesting transition level for photocatalysis are printed in bold. The curves are calibrated using the CT absorption edges obtained for UiO-66:Ce^{4+} (3+/4+) and UiO-66:Eu^{3+} (2+/3+) as indicated by the red arrows. Titanium can also be included using a recently proposed expansion of the empirical model.[37] Values are referred to the vacuum (VRBE, vacuum-referred binding energy) or relative to the host material (HRBE, host-referred binding energy).

Positioning of the (2+/3+) transition curve was possible from the PL measurements performed on UiO-66:Eu^{3+}. The associated CT was found to occur at 4.1 eV, which fixes the Eu(2+/3+) charge state transition energy and as a result the complete (2+/3+) curve (blue line in Figure 7). Rogers et al. moreover found that the $Ti^{(3+/4+)}$ transition level can be found at approximately the same binding energy value as the $Eu^{(2+/3+)}$ transition level.[37] Because of the relevance of Ti-doped UiO-66, this transition level was also added to Figure 7.

Note that the Coulomb correlation energy U, defined as the difference between two successive charge state transition levels, amounts to 6.87 eV for Eu. This is a typical value for Eu in oxides (e.g., Dorenbos et al.[63]), which confirms our correct interpretation of the excitation/emission spectra. We can moreover use U to determine the vacuum level in the band diagram via the chemical shift of Eu^{2+}.[31] It allows the expression of all binding energies relative to this value (vacuum-referred binding energy, VRBE).

From the diagram in Figure 7, it is observed that the $Ti^{(3+/4+)}$ level and hence the CT of Ti^{4+} is resonant with the material's HOCO–LUCO gap, explaining the improved electron mobility of UiO-66:Ti^{4+} after excitation. The overlap between the $Ti^{(3+/4+)}$ level and the LUCO of UiO-66 is believed to be the cause for the increased photocatalytic activity for UiO-66:Ti^{4+}, since an excited electron of the linker has sufficient energy to move to the dopant ion. Following the same reasoning, all Ln ions with (3+/4+) or (2+/3+) charge state transition levels near or below the UiO-66 LUCO region could potentially be the target of an LMCT process upon excitation of the UiO host (e.g., Pr, Sm, or Tb). In order to validate this assumption, the transfer is investigated in the next section via absolute luminescence intensity measurements. Furthermore, DFT calculations will be performed on Ti- and Ce-doped samples to corroborate our findings.

Absolute Intensities. From the PL measurements, we know that the unfunctionalized linker shows a broad band emission centered around 400 nm (see Supporting Information section S3). This band is due to the recombination of the exciton, centered on the linker, with emission of a photon. The doped UiO materials aim to impede this direct recombination pathway by inducing energy transfer to the metal ions. The opening of the new decay channel competes with the direct recombination, resulting in a decrease of the linker emission band. The more efficient the LMCT process, the stronger the reduction of the linker emission, offering a method to assess the efficiency of the energy transfer via LMCT.

The most simple semiquantitative method to compare absolute emission intensities of powder samples consists of measuring an "infinitely" thick sample. This is done by using a filled cup that is placed in the standard PL setup. Since the incident light beam illuminates the entire sample, the emission can be compared among different samples in the same setup.

Table 2 shows the integrated intensities of the linker emission band of the different doped UiO samples. They are normalized to

Table 2. Integrated Intensities of the Linker Emission Band between 350 and 500 nm Excited at 300 nm[a]

sample	integrated intensity (%)
UiO-66	100
UiO-66:Ce^{4+}	6
UiO-66:Nd^{3+}	71
UiO-66:Eu^{3+}	12
UiO-66:Yb^{3+}	14
UiO-66:Ti^{4+}	31

[a]The results are normalized to the UiO-66 emission.

the pure UiO-66 emission and are based on the emission spectra provided in Supporting Information (section S3). One can observe that by doping the material, the resulting linker emission diminishes, suggesting that it is now in competition with alternative pathways. We see that Ti^{4+}, Eu^{3+}, Yb^{3+}, and Ce^{4+} all lead to a drastic decrease in intensity. For Ti and Eu, we already discussed their beneficial influence on the charge transfer pathway in UiO-66. Indeed, Table 2 corroborates that an efficient LMCT can take place and the emission intensity drops substantially. For the Ce^{4+} sample, almost a complete loss of the

DOI: 10.1021/acs.inorgchem.8b00425
Inorg. Chem. 2018, 57, 5463–5474

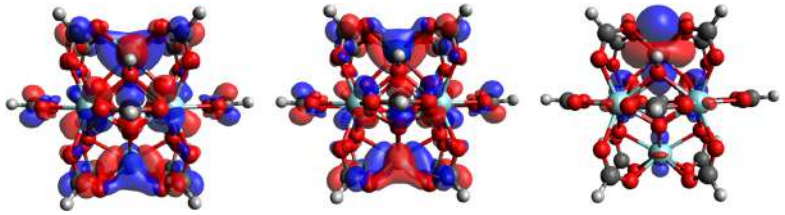

Figure 8. Cluster models of $Zr_6O_4(OH)_4(HCOO)_{12}$ (left), $Zr_5Hf_1O_4(OH)_4(HCOO)_{12}$ (middle, Hf is the top metal atom), and $Zr_5Ti_1O_4(OH)_4(HCOO)_{12}$ (right, Ti is the top metal atom) calculated at the B3LYP/DEF2TZVP level with a −1 charge and doublet spin state. The models show the localization of the additional electron on the titanium 3d shell (right).

emission peak is found. This could also be attributed to a fast energy transfer but possibly followed by fast energy dissipation via nonradiative pathways, for which Ce^{4+} is notorious.[64,65]

We also have a look at the other lanthanides not thoroughly discussed in the previous sections. About the same drop in intensity as for Eu^{3+} and Ce^{4+} can be found for Yb^{3+}. Figure 7 shows that the interband transition of the host material resonates with the (2+/3+) charge state transition level of the Yb ion, opening a decay pathway via this channel and hence lowering the linker-based emission peak. However, incorporation of Nd^{3+} leads to a much smaller decrease in intensity. This behavior is because the $Nd^{(2+/3+)}$ charge state transition occurs at a too high energy with respect to the LUCO (Figure 7), implying that a Nd charge transition will likely not occur.

Figure 7 shows that many more possibilities arise for an efficient LMCT, since Sm and Tb also show charge state transition levels within the UiO-66 band gap. Further investigation of the different Ln-doped UiO-66 materials can yield more insight in the decay pathways and could lead to materials with improved luminescent properties or increased photocatalytic activity. However, as the results show, the resonance of the Eu or Yb charge state transitions with the HOCO-LUCO energy gap indicates that these doped materials would be first of choice for a further study.

Computational Assessment. In order to gain more insight at a fundamental level, a selected subset of the samples was assessed from first principles. Excited-state calculations are still challenging for periodic systems, so we performed TDDFT calculations on some well-defined clusters. We focused on isovalent dopant ions (Ti or Hf), which do not offer computational difficulties and may serve as a reference. In addition, ground state calculations were used to simulate isovalently substituted UiO-66 with a single negative charge (and doublet spin state). This model represents the cluster after charge transfer from the linker. Observation of the singly occupied molecular orbital (SOMO) then yields insight in the localization of this excess negative charge. Periodic data are presented afterward and offer insights in the ground state electronic structure, which can be qualitatively linked to the observed changes in the experimental data.

Cluster Models. First, we performed calculations on a series of simplified cluster models, consisting of one inorganic node terminated with formic acid. These clusters result in a total stoichiometry of $Zr_{6-n}M_nO_4(OH)_4(HCOO)_6$ (M = Ti^{4+} or Hf^{4+}). Three particular geometries are shown in Figure 8. The SOMO of both the pristine Zr node (left) and a Hf-doped one (middle) indicate that an extra electron is uniformly distributed over the whole node. If we however insert a titanium atom (right), then the electron is localized on the empty 3d orbitals of the Ti atom.

Even though these small clusters do not contain any aromatic linkers, and are therefore severely simplified model systems, inspection of the TDDFT spectra shows some interesting results (Figure 9). The Hf-doped node shows an almost identical

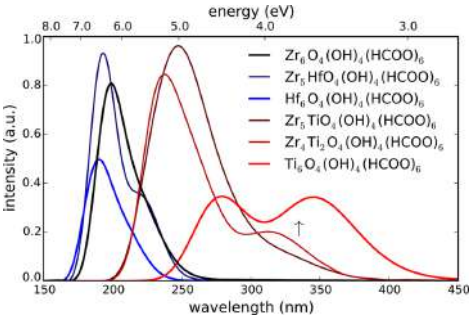

Figure 9. TDDFT spectra for simple formic acid terminated clusters with 1 or more Zr replaced by Hf of Ti. The arrow indicates the new peak rising as a function of the number of Ti atoms in the cluster and corresponds to an O^{2-}-Ti^{4+} excitation.

spectrum as the pristine Zr node. In contrast, a peak arises around 320 nm caused by the inserted Ti. As the number of Ti atoms in the cluster increases, both the oscillator strength of this transition and the absorption in the spectrum rise. Closer investigation learns that it concerns a transition from oxygen-centered p-orbitals (oxygen from the formate anions) toward the Ti 3d orbitals. It can be linked to the shift observed experimentally in the A region of Figure 3. Moreover, the predicted position of this CT band agrees well with both experimental (Figure 3) and empirical results (Figure 7). As a final remark, it should be noted that the 100% titanium UiO has not yet been synthesized as such and has to be considered as a limiting case.

The simple cluster models allow to identify the absorption pathways that arise upon doping the UiO material. However, the artificial replacement of the linkers by formate anions results in a loss of linker states and is thus a severe approximation. We therefore studied more complex Ti-containing clusters, in which two formate capping molecules were replaced by BDC linkers, terminated by a hydrogen to secure charge balance. Since much interest has gone to the amine-functionalized variants, showing an even larger increase in photocatalytic activity, we also include

DOI: 10.1021/acs.inorgchem.8b00425
Inorg. Chem. 2018, 57, 5463−5474

an amine-modified cluster model in our calculations. The general cluster structure is shown in Figure 10 (inset), where atom X indicates the dopant and the *R*-group can be H or NH_2. The resulting spectra are shown in Figure 10.

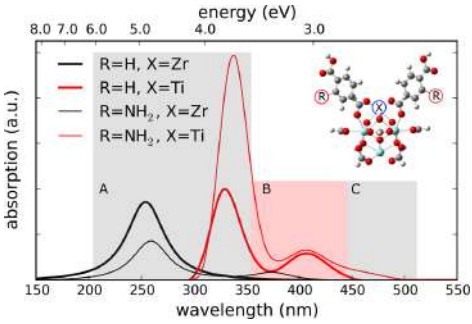

Figure 10. TDDFT absorption spectra (B3LYP/6-311+G(d,p), 30 states) for extended cluster models. The basic cluster model has a stoichiometry of $Zr_5XO_4(OH)_4(HCOO)_{10}(BDC\text{-}R)_2$ with R = H and NH_2 and X = Zr and Ti (inset). The meaning of shaded regions **A**, **B**, and **C** is described in the text.

We notice that the results are qualitatively similar to those of Figure 9. A more detailed view on the three main features in the spectrum can be obtained by considering the related orbital transitions (see Figure 11). Region **A** of Figure 10 corresponds to the classical HOMO−LUMO excitation of the linker. The shift of this peak upon inclusion of a titanium atom agrees with the shift of absorption edges observed experimentally (indicated as region A in Figure 3). In region **B**, the BDC-NH_2 absorption arises as a small peak just below 400 nm, and there is a clear absorption caused by the included Ti. In this transition the most important contribution to the orbitals is moved from the p-orbitals of the oxygen atoms of the surrounding carboxylate groups to the Ti 3d orbitals (Figure 11B). This transition is similar to the one observed in the small cluster models shown in Figure 9. Finally, region **C** in Figure 10 contains a feature only observed in the amino-functionalized material. It shows a transition between the aromatic ring of the linker, more specifically the HOMO of the complete cluster, and a Ti 3d orbital. This transition only occurs when both an amine group and a Ti atom are present in the system. The existence of such a long-range charge transfer gives an indication as to why amine-functionalized UiO-66:Ti^{4+} shows the largest photocatalytic activity in literature.[24,25] These TDDFT findings therefore corroborate DFT calculations by Santaclara et al. for the situation where a Ti ion was grafted to a linker vacancy.[60]

Periodic Models. Further insight can be obtained by using a periodic model. We performed periodic DFT calculations of isovalently substituted UiO-66 and UiO-66(Ce). Figure 12 shows the DOS for the four considered structures, consisting of pure Zr, Hf, Ti, or Ce nodes. Pure UiO-66(Ti) has again to be considered as a theoretical limit. Note that although PBE is known to underestimate band gaps, it has been observed to reproduce trends correctly for UiO-66-type materials.[41] This is further confirmed by single-point HSE06 calculations[66,67] for UiO-66(Ti) and UiO-66(Ce) (see Supporting Information).

As shown by Figure 12, the DOS of the Zr and Hf material show almost no difference, since the electronic characteristics of the bare ions are very similar. This behavior was also found

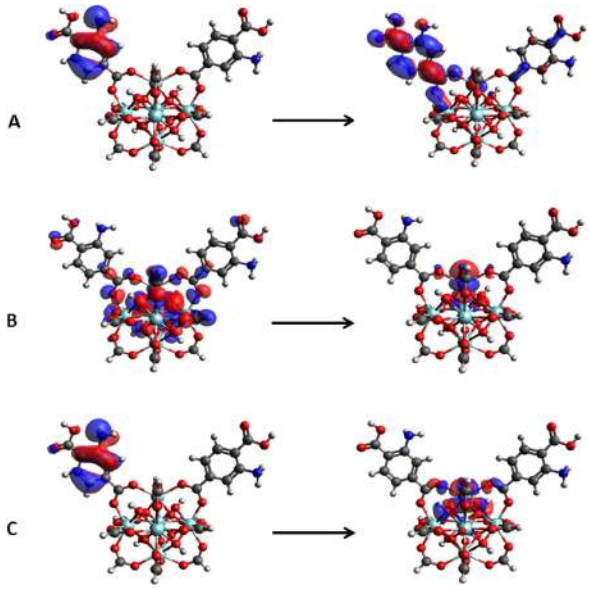

Figure 11. Orbitals contributing to the three main excitations observed in the spectrum of $Zr_5TiO_4(OH)_4(HCOO)_{10}(BDC\text{-}NH_2)_2$ (see Figure 10).

DOI: 10.1021/acs.inorgchem.8b00425
Inorg. Chem. 2018, 57, 5463−5474

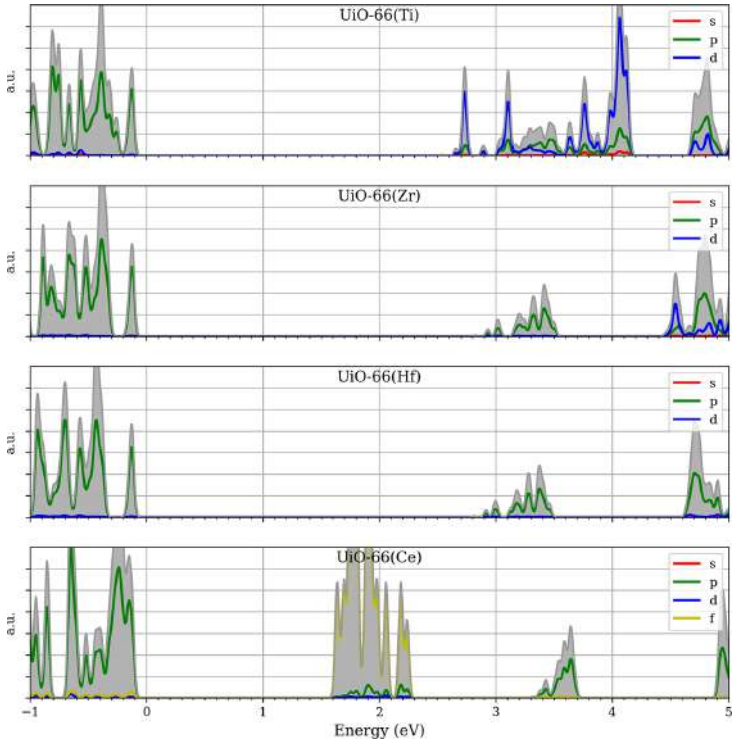

Figure 12. Total (gray) and projected (red, green, blue and yellow) density of states of (from top to bottom) UiO-66(Ti), UiO-66(Zr), UiO-66(Hf) and UiO-66(Ce). The energy is expressed with respect to the Fermi energy (E_F = 0).

experimentally by Nasalevich and co-workers[27] and using cluster calculations in the previous section. However, introducing titanium in the metal node alters the LUCO states of UiO-66. It introduces 3d states that are sufficiently low in energy to go below the linker-based band forming the LUCO of the pristine UiO-66. The overlap between the Ti 3d and the linker orbitals suggests better charge transfer possibilities and explains why an increased photocatalytic activity is observed for Ti-containing UiO-66. Note that Santaclara et al. reported that adsorbing Ti onto a linker vacancy would improve the activity even further.[60] Periodic calculations on UiO-66(Ce) show the appearance of a broad band within the original UiO HOCO-LUCO gap. This band consists of the 4f orbitals of the Ce ions. In the Ce^{4+} state, these orbitals are completely empty and hence form the new LUCO of the material. The LUCO therefore changes from ligand- to metal-based, similar to Ti-doped UiO-66, although no energetic overlap between the new and original LUCO states is now observed. Coincidentally, the Ce gap state appears at a similar energy from the HOCO as the state introduced by an amine group in UiO-66-NH_2 from the LUCO.[41] However, although the effect on the overall band gap is comparable (see Figure 4), both excitations are physically different. The amine group gives rise to a completely filled band and therefore creates a new HOCO state. This results in linker-based absorption. In contrast, cerium brings down the LUCO state and excitation occurs to a cerium level.

The observed Ce f band can be qualitatively linked to our previously obtained results. The occurrence of 4f levels in the band gap of UiO-66 indicates that Ce can take different charge states depending on the Fermi level location and that a charge transfer transition, measurable by optical spectroscopy, is to be expected. Indeed, the empty 4f band within the band gap of the pristine UiO-66 is energetically reachable for an electron that has been excited to the linker LUCO via an energy transfer process. The broad band observed in the absorption spectrum of Figure 4 was already attributed to this charge transfer channel. A charge state transition level must therefore be present in the band gap. The predicted location of the 4f band shows a good correspondence with the thermodynamic (3+/4+) charge state transition level, which was also used to construct Figure 7. The location of the Kohn–Sham single-particle levels (Figure 12) is not exactly the same as the location of the charge state transition level. This is however not to be expected given their different physical meaning.[68−71]

CONCLUSION

Lanthanide MOFs represent an interesting class of materials with specific electronic properties exploitable for luminescent and

DOI: 10.1021/acs.inorgchem.8b00425
Inorg. Chem. 2018, 57, 5463−5474

photocatalytic applications. Unfortunately, pure Ln-MOFs are notoriously unstable and difficult to synthesize. In this work, a simple microwave-assisted synthesis methodology was proposed for the fast incorporation of transition metal and lanthanide cations in the robust UiO-66 material, giving rise to an entire new set of highly stable materials with unprecedented electronic properties. Combining spectroscopic data with computational results allowed to understand the changes in electronic structure of the different materials in a synergistic way.

By using experimentally observed CT values in Ce- and Eu-doped UiO samples, the (2+/3+) and (3+/4+) charge state transition levels were predicted for the entire Ln series, displaying a zigzag curve with respect to the band structure of the host material (see Figure 7). Absolute intensity measurements confirmed this model, showing that for dopants with transition levels resonant to the HOCO−LUCO gap of UiO-66 an extra decay pathway becomes available. Further confirmation was obtained using DFT calculations. For isovalently substituted samples, only Ti shows a CT pathway. This is because Ti 3d levels overlap energetically with the linker LUMO state while Hf and Zr states only occur in a higher energy range. For Ln-doped materials, cerium insertion in the node introduces an empty 4f band within the pristine UiO-66 band gap, which also gives rise to CT. Similar charge transitions were observed for Yb and Eu. We therefore propose these Ln-based materials as prime candidates in catalytic studies. Moreover, the general applicability of our synthesis procedure combined with the stability of the proposed materials may encourage researchers to conduct further studies and open up a new chapter in Ln-MOF luminescence and photocatalytic studies.

■ ASSOCIATED CONTENT

Supporting Information

The Supporting Information is available free of charge on the ACS Publications website at DOI: 10.1021/acs.inorgchem.8b00425.

Synthesis procedures; XRD diffractograms; BF-STEM EDX measurements; XPS scan of UiO-66:Ti^{4+}; nitrogen sorption isotherms; photoluminescence and UV/vis reflectance spectra; single-point HSE06 densities of states (PDF)

■ AUTHOR INFORMATION

Corresponding Authors

*E-mail: Veronique.VanSpeybroeck@UGent.be.
*E-mail: Pascal.VanDerVoort@UGent.be.
*E-mail: Kurt.Lejaeghere@UGent.be.

ORCID

Jonas J. Joos: 0000-0002-7869-2217
Arthur De Vos: 0000-0002-4916-6066
Philippe F. Smet: 0000-0003-4789-5799
Veronique Van Speybroeck: 0000-0003-2206-178X
Pascal Van Der Voort: 0000-0002-4874-0943
Kurt Lejaeghere: 0000-0002-4462-8209

Notes

The authors declare no competing financial interest.

■ ACKNOWLEDGMENTS

The Fund for Scientific Research-Flanders (FWO) and the Research Board of Ghent University (BOF) are acknowledged for their financial support. Computational resources and services were provided by the Stevin Supercomputer Infrastructure of Ghent University and by the Flemish Supercomputer Center (VSC), funded by the Hercules Foundation and the Flemish Government - Department EWI.

■ REFERENCES

(1) Thematic Issue: Metal−Organic Frameworks. *Chem. Rev.* **2012**, *112*, 673−1268.
(2) Zhou, H.; Kitagawa, S. Metal-Organic Frameworks (MOFs). *Chem. Soc. Rev.* **2014**, *43*, 5415−5418.
(3) Maurin, G.; Serre, C.; Cooper, A.; Férey, G. The new age of MOFs and of their porous-related solids. *Chem. Soc. Rev.* **2017**, *46*, 3104−3107.
(4) Santaclara, J.; Kapteijn, F.; Gascon, J.; van der Veen, M. Understanding metal-organic frameworks for photocatalytic solar fuel production. *CrystEngComm* **2017**, *19*, 4118−4125.
(5) Allendorf, M. D.; Bauer, C. A.; Bhakta, R. K.; Houk, R. J. T. Luminescent metal-organic frameworks. *Chem. Soc. Rev.* **2009**, *38*, 1330−1352.
(6) Wang, J.; Wang, C.; Lin, W. Metal-Organic Frameworks for Light Harvesting and Photocatalysis. *ACS Catal.* **2012**, *2*, 2630−2640.
(7) Nasalevich, M. A.; van der Veen, M.; Kapteijn, F.; Gascon, J. Metal-organic frameworks as heterogeneous photocatalysts: advantages and challenges. *CrystEngComm* **2014**, *16*, 4919−4926.
(8) Lustig, W. P.; Mukherjee, S.; Rudd, N. D.; Desai, A. V.; Li, J.; Ghosh, S. K. Metal-organic frameworks: functional luminescent and photonic materials for sensing applications. *Chem. Soc. Rev.* **2017**, *46*, 3242−3285.
(9) De Vos, A.; Hendrickx, K.; Van Der Voort, P.; Van Speybroeck, V.; Lejaeghere, K. Missing linkers: an alternative pathway to UiO-66 electronic structure engineering. *Chem. Mater.* **2017**, *29*, 3006−3019.
(10) Yu, Y.; Chen, G.; Zhou, Y.; Han, Z. Recent advances in rare-earth elements modification of inorganic semiconductor-based photocatalysts for efficient solar energy conversion: A review. *J. Rare Earths* **2015**, *33*, 453−462.
(11) Kumar, G. S.; Devi, G. L. Review on Modified TiO_2 Photocatalysis under UV/Visible Light: Selected Results and Related Mechanisms on Interfacial Charge Carrier Transfer Dynamics. *J. Phys. Chem. A* **2011**, *115*, 13211−13241.
(12) Qin, X.; Liu, X.; Huang, W.; Bettinelli, M.; Liu, X. Lanthanide-Activated Phosphors Based on 4f-5d Optical Transitions: Theoretical and Experimental Aspects. *Chem. Rev.* **2017**, *117*, 4488−4527.
(13) Cheng, P. *Lanthanide Metal−Organic Frameworks*; Structure and Bonding series; Springer: Berlin, 2014.
(14) Xu, H.; Cao, C.; Kang, X.; Zhao, B. Lanthanide-based metal-organic frameworks as luminescent probes. *Dalton Trans.* **2016**, *45*, 18003−18017.
(15) Pagis, C.; Ferbinteanu, M.; Rothenberg, G.; Tanase, S. Lanthanide-Based Metal-Organic Frameworks: Synthetic Strategies and Catalytic Applications. *ACS Catal.* **2016**, *6*, 6063−6072.
(16) Liang, Y.; Yang, G.; Liu, B.; Yan, Y.; Xi, Z.; Wang, Y. Four super water-stable lanthanide-organic frameworks with active uncoordinated carboxylic and pyridyl groups for selective luminescence sensing of Fe^{3+}. *Dalton Trans.* **2015**, *44*, 13325−13330.
(17) Tu, J.; Zeng, X.; Xu, F.; Wu, X.; Tian, Y.; Hou, X.; Long, Z. Microwave-induced fast incorporation of titanium into UiO-66 metal-organic frameworks for enhanced photocatalytic properties. *Chem. Commun.* **2017**, *53*, 3361−3364.
(18) Leus, K.; Bogaerts, T.; De Decker, J.; Depauw, H.; Hendrickx, K.; Vrielinck, H.; Van Speybroeck, V.; Van Der Voort, P. Systematic study of the chemical and hydrothermal stability of selected "stable" Metal Organic Frameworks. *Microporous Mesoporous Mater.* **2016**, *226*, 110−116.
(19) Cavka, J. H.; Jakobsen, S.; Olsbye, U.; Guillou, N.; Lamberti, C.; Bordiga, S.; Lillerud, K. P. A new zirconium inorganic building brick forming metal organic frameworks with exceptional stability. *J. Am. Chem. Soc.* **2008**, *130*, 13850−13851.
(20) Valenzano, L.; Civalleri, B.; Chavan, S.; Bordiga, S.; Nilsen, M. H.; Jakobsen, S.; Lillerud, K. P.; Lamberti, C. Disclosing the Complex

DOI: 10.1021/acs.inorgchem.8b00425
Inorg. Chem. 2018, 57, 5463−5474

Structure of UiO-66 Metal Organic Framework: A Synergic Combination of Experiment and Theory. *Chem. Mater.* **2011**, *23*, 1700−1718.
(21) Marshall, R. J.; Forgan, R. S. Postsynthetic Modification of Zirconium Metal-Organic Frameworks. *Eur. J. Inorg. Chem.* **2016**, *2016*, 4310−4331.
(22) Kim, M.; Cahill, J. F.; Fei, H.; Prather, K. A.; Cohen, S. M. Postsynthetic Ligand and Cation Exchange in Robust Metal-Organic Frameworks. *J. Am. Chem. Soc.* **2012**, *134*, 18082−18088.
(23) Smith, S. J.; Ladewig, B. P.; Hill, A. J.; Lau, C.; Hill, M. R. Post-synthetic Ti Exchanged UiO-66 Metal-Organic Frameworks that Deliver Exceptional Gas Permeability in Mixed Matrix Membranes. *Sci. Rep.* **2015**, *5*, 7823.
(24) Sun, D.; Liu, W.; Qiu, M.; Zhang, Y.; Li, Z. Introduction of a mediator for enhancing photocatalytic performance via post-synthetic metal exchange in metal-organic frameworks (MOFs). *Chem. Commun.* **2015**, *51*, 2056−2059.
(25) Lee, Y.; Kim, S.; Kang, J.; Cohen, S. M. Photocatalytic CO_2 reduction by a mixed metal (Zr/Ti), mixed ligand metal-organic framework under visible light irradiation. *Chem. Commun.* **2015**, *51*, 5735−5738.
(26) Wang, A.; Zhou, Y.; Wang, Z.; Chen, M.; Sun, L.; Liu, X. Titanium incorporated with UiO-66(Zr)-type Metal-Organic Framework (MOF) for photocatalytic application. *RSC Adv.* **2016**, *6*, 3671−3679.
(27) Nasalevich, M. A.; Hendon, C. H.; Santaclara, J. G.; Svane, K.; van der Linden, B.; Veber, S. L.; Fedin, M. V.; Houtepen, A. J.; van der Veen, M. A.; Kapteijn, F.; Walsh, A.; Gascon, J. Electronic origins of photocatalytic activity in d^0 metal organic frameworks. *Sci. Rep.* **2016**, *6*, 23676.
(28) Yasin, A.; Li, J.; Wu, N.; Musho, T. Study of the inorganic substitution in a functionalized UiO-66 metal-organic framework. *Phys. Chem. Chem. Phys.* **2016**, *18*, 12748−12754.
(29) Yang, L.; Ganz, E.; Svelle, S.; Tilset, M. Computational exploration of newly synthesized zirconium metal-organic frameworks UiO-66, −67, −68 and analogues. *J. Mater. Chem. C* **2014**, *2*, 7111−7125.
(30) Santiago-Portillo, A.; Baldovi, H.; García Fernandez, M. T.; Navalon, S.; Atienzar, P.; Ferrer, B.; Alvaro, M.; Garcia, H.; Li, Z. Ti as Mediator in the Photoinduced Electron Transfer of Mixed-Metal NH_2-UiO66(Zr/Ti). Transient Absorption Spectroscopy Study and Application in Photovoltaic Cell. *J. Phys. Chem. C* **2017**, *121*, 7015−7024.
(31) Dorenbos, P. A Review on How Lanthanide Impurity Levels Change with Chemistry and Structure of Inorganic Compounds. *ECS J. Solid State Sci. Technol.* **2013**, *2*, R3001−R3011.
(32) Joos, J. J.; Poelman, D.; Smet, P. F. Energy level modeling of lanthanide materials: review and uncertainty analysis. *Phys. Chem. Chem. Phys.* **2015**, *17*, 19058−19078.
(33) Seijo, L.; Barandiarán, Z. Ab Initio Calculations on Excited States of Lanthanide Containing Materials; In *Handbook on the Physics and Chemistry of Rare Earths*; Gschneidner, K. A., Eyring, L., Eds.; Elsevier: New York, 2016.
(34) Biswas, S.; Van Der Voort, P. A General Strategy for the Synthesis of Functionalised UiO-66 Frameworks: Characterisation, Stability and CO_2 Adsorption Properties. *Eur. J. Inorg. Chem.* **2013**, *2013*, 2154−2160.
(35) Lammert, M.; Wharmby, M. T.; Smolders, S.; Bueken, B.; Lieb, A.; Lomachenko, K. A.; De Vos, D.; Stock, N. Cerium-based metal organic frameworks with UiO-66 architecture: synthesis, properties and redox catalytic activity. *Chem. Commun.* **2015**, *51*, 12578−12581.
(36) Görller-Walrand, C.; Binnemans, K. Rationalization of crystal-field parametrization. In *Handbook on the Physics and Chemistry of Rare Earths*; Gschneidner, K. A., Eyring, L., Eds.; Elsevier: New York, 1996.
(37) Rogers, E.; Dorenbos, P. Vacuum energy referred $Ti^{3+/4+}$ donor/acceptor states in insulating and semiconducting inorganic compounds. *J. Lumin.* **2014**, *153*, 40−45.
(38) Levin, J. R.; Dorfner, W. L.; Dai, A. X.; Carroll, P. J.; Schelter, E. J. Density Functional Theory as a Predictive Tool for Cerium Redox Properties in Nonaqueous Solvents. *Inorg. Chem.* **2016**, *55*, 12651−12659.
(39) Loschen, C.; Migani, A.; Bromley, S. T.; Illas, F.; Neyman, K. M. Density functional studies of model cerium oxide nanoparticles. *Phys. Chem. Chem. Phys.* **2008**, *10*, 5730−5738.
(40) Frisch, M. J.; Trucks, G. W.; Schlegel, H. B.; Scuseria, G. E.; Robb, M. A.; Cheeseman, J. R.; Scalmani, G.; Barone, V.; Mennucci, B.; Petersson, G. A.; Nakatsuji, H.; Caricato, M.; Li, X.; Hratchian, H. P.; Izmaylov, A. F.; Bloino, J.; Zheng, G.; Sonnenberg, J. L.; Hada, M.; Ehara, M.; Toyota, K.; Fukuda, R.; Hasegawa, J.; Ishida, M.; Nakajima, T.; Honda, Y.; Kitao, O.; Nakai, H.; Vreven, T.; Montgomery, J. A., Jr.; Peralta, J. E.; Ogliaro, F.; Bearpark, M.; Heyd, J. J.; Brothers, E.; Kudin, K. N.; Staroverov, V. N.; Kobayashi, R.; Normand, J.; Raghavachari, K.; Rendell, A.; Burant, J. C.; Iyengar, S. S.; Tomasi, J.; Cossi, M.; Rega, N.; Millam, J. M.; Klene, M.; Knox, J. E.; Cross, J. B.; Bakken, V.; Adamo, C.; Jaramillo, J.; Gomperts, R.; Stratmann, R. E.; Yazyev, O.; Austin, A. J.; Cammi, R.; Pomelli, C.; Ochterski, J. W.; Martin, R. L.; Morokuma, K.; Zakrzewski, V. G.; Voth, G. A.; Salvador, P.; Dannenberg, J. J.; Dapprich, S.; Daniels, A. D.; Farkas, O.; Foresman, J. B.; Ortiz, J. V.; Cioslowski, J.; Fox, D. J. *Gaussian 09*, revision D.01; Gaussian, Inc.: Wallingford, CT, 2009.
(41) Hendrickx, K.; Vanpoucke, D. E. P.; Leus, K.; Lejaeghere, K.; Van Yperen-De Deyne, A.; Van Speybroeck, V.; Van Der Voort, P.; Hemelsoet, K. Understanding Intrinsic Light Absorption Properties of UiO-66 Frameworks: A Combined Theoretical and Experimental Study. *Inorg. Chem.* **2015**, *54*, 10701−10710.
(42) Lee, C.; Yang, W.; Parr, R. G. Development of the Colle-Salvetti correlation-energy formula into a functional of the electron density. *Phys. Rev. B: Condens. Matter Mater. Phys.* **1988**, *37*, 785−789.
(43) Becke, A. D. Density-functional thermochemistry. III. The role of exact exchange. *J. Chem. Phys.* **1993**, *98*, 5648−5652.
(44) Weigend, F.; Ahlrichs, R. Balanced basis sets of split valence, triple zeta valence and quadruple zeta valence quality for H to Rn: Design and assessment of accuracy. *Phys. Chem. Chem. Phys.* **2005**, *7*, 3297−3305.
(45) Freysoldt, C.; Grabowski, B.; Hickel, T.; Neugebauer, J.; Kresse, G.; Janotti, A.; Van de Walle, C. G. First-principles calculations for point defects in solids. *Rev. Mod. Phys.* **2014**, *86*, 253−305.
(46) Runge, E.; Gross, E. K. U. Density-functional theory for time-dependent systems. *Phys. Rev. Lett.* **1984**, *52*, 997−1001.
(47) Marques, M. A. L., Ullrich, C., Nogueira, F., Rubio, A., Burke, K., Gross, E. K. U., Eds. *Time-Dependent Density Functional Theory*; Lecture Notes in Physics; Springer-Verlag: Berlin, 2006.
(48) Dreuw, A.; Head-Gordon, M. Single-Reference ab Initio Methods for the Calculation of Excited States of Large Molecules. *Chem. Rev.* **2005**, *105*, 4009−4037.
(49) Kresse, G.; Furthmüller, J. Efficiency of ab-initio total energy calculations for metals and semiconductors using a plane-wave basis set. *Comput. Mater. Sci.* **1996**, *6*, 15−50.
(50) Hafner, J. Ab-Initio Simulations of Materials Using VASP: Density-Functional Theory and Beyond. *J. Comput. Chem.* **2008**, *29*, 2044−2078.
(51) Kresse, G.; Joubert, D. From ultrasoft pseudopotentials to the projector augmented-wave method. *Phys. Rev. B: Condens. Matter Mater. Phys.* **1999**, *59*, 1758−1775.
(52) Lejaeghere, K.; et al. Reproducibility in density functional theory calculations of solids. *Science* **2016**, *351*, aad3000.
(53) Perdew, J. P.; Burke, K.; Ernzerhof, M. Generalized Gradient Approximation Made Simple. *Phys. Rev. Lett.* **1996**, *77*, 3865−3868.
(54) Vinet, P.; Ferrante, J.; Rose, J.; Smith, J. Compressibility of solids. *J. Geophys. Res.* **1987**, *92*, 9319.
(55) Brozek, C. K.; Dincă, M. Cation exchange at the secondary building units of metal-organic frameworks. *Chem. Soc. Rev.* **2014**, *43*, 5456−5467.
(56) Zhao, J.; Mi, L.; Hu, J.; Hou, H.; Fan, Y. Cation Exchange Induced Tunable Properties of a Nanoporous Octanuclear Cu(II) Wheel with Double-Helical Structure. *J. Am. Chem. Soc.* **2008**, *130*, 15222−15223.
(57) Son, D.; Hughes, S. M.; Yin, Y.; Alivisatos, P. A. Cation Exchange Reactions in Ionic Nanocrystals. *Science* **2004**, *306*, 1009−1012.

DOI: 10.1021/acs.inorgchem.8b00425
Inorg. Chem. 2018, 57, 5463−5474

(58) Fei, H.; Pham, C. H.; Oliver, S. R. J. Anion Exchange of the Cationic Layered Material $[Pb_2F_2]^{2+}$. *J. Am. Chem. Soc.* **2012**, *134*, 10729−10732.
(59) Wißmann, G.; Schaate, A.; Lilienthal, S.; Bremer, I.; Schneider, A. M.; Behrens, P. Modulated synthesis of Zr-fumarate MOF. *Microporous Mesoporous Mater.* **2012**, *152*, 64−70.
(60) Santaclara, J. G.; Olivos-Suarez, A. I.; Gonzalez-Nelson, A.; Osadchii, D.; Nasalevich, M. A.; van der Veen, M. A.; Kapteijn, F.; Sheveleva, A. M.; Veber, S. L.; Fedin, M. V.; Murray, A. T.; Hendon, C. H.; Walsh, A.; Gascon, J. Revisiting the Incorporation of Ti(IV) in UiO-type Metal-Organic Frameworks: Metal Exchange versus Grafting and Their Implications on Photocatalysis. *Chem. Mater.* **2017**, *29*, 8963−8967.
(61) Janulevicius, M.; Marmokas, P.; Misevicius, M.; Grigorjevaite, J.; Mikoliunaite, L.; Sakirzanovas, S.; Katelnikovas, A. Luminescence and luminescence quenching of highly efficient $Y_2Mo_4O_{15}:Eu^{3+}$ phosphors and ceramics. *Sci. Rep.* **2016**, *6*, 26098.
(62) Liu, Y.; Decadt, R.; Bogaerts, T.; Hemelsoet, K.; Kaczmarek, A. M.; Poelman, D.; Waroquier, M.; Van Speybroeck, V.; Van Deun, R.; Van Der Voort, P. Bipyridine-Based Nanosized Metal-Organic Framework with Tunable Luminescence by a Postmodification with Eu(III): An Experimental and Theoretical Study. *J. Phys. Chem. C* **2013**, *117*, 11302−11310.
(63) Dorenbos, P. Ce^{3+} 5d-centroid shift and vacuum referred 4f-electron binding energies of all lanthanide impurities in 150 different compounds. *J. Lumin.* **2013**, *135*, 93−104.
(64) Hoefdraad, H. Charge-transfer spectra of tetravalent lanthanide ions in oxides. *J. Inorg. Nucl. Chem.* **1975**, *37*, 1917−1921.
(65) Seijo, L.; Barandiarán, Z. Intervalence charge transfer luminescence: The anomalous luminescence of cerium-doped $Cs_2LiLuCl_6$ elpasolite. *J. Chem. Phys.* **2014**, *141*, 214706.
(66) Heyd, J.; Scuseria, G. E.; Ernzerhof, M. Hybrid functionals based on a screened Coulomb potential. *J. Chem. Phys.* **2003**, *118*, 8207−8215.
(67) Heyd, J.; Scuseria, G. E.; Ernzerhof, M. J. Erratum: Hybrid functionals based on a screened Coulomb potential [J. Chem. Phys.118, 8207 (2003)]. *J. Chem. Phys.* **2006**, *124*, 219906.
(68) Chakrabarty, A.; Patterson, C. H. Transition levels of defects in ZnO: Total energy and Janak's theorem methods. *J. Chem. Phys.* **2012**, *137*, 054709.
(69) Broqvist, P.; Alkauskas, A.; Pasquarello, A. Hybrid-functional calculations with plane-wave basis sets: Effect of singularity correction on total energies, energy eigenvalues, and defect energy levels. *Phys. Rev. B: Condens. Matter Mater. Phys.* **2009**, *80*, 085114.
(70) Gallino, F.; Pacchioni, G.; Di Valentin, C. D. Transition levels of defect centers in ZnO by hybrid functionals and localized basis set approach. *J. Chem. Phys.* **2010**, *133*, 144512.
(71) Joos, J. J.; Lejaeghere, K.; Korthout, K.; Feng, A.; Poelman, D.; Smet, P. F. Charge transfer induced energy storage in CaZnOS:Mn - insight from experimental and computational spectroscopy. *Phys. Chem. Chem. Phys.* **2017**, *19*, 9075−9085.

DOI: 10.1021/acs.inorgchem.8b00425
Inorg. Chem. 2018, 57, 5463−5474

Paper III

Electronic properties of heterogenized Ru(II) polypyridyl photoredox complexes on covalent triazine frameworks

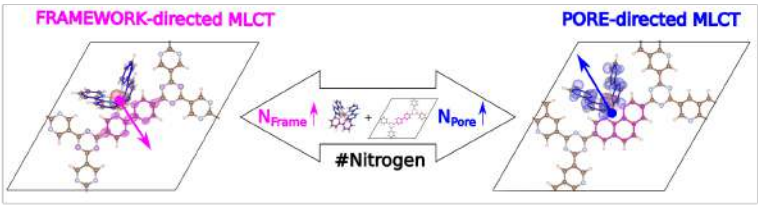

A. De Vos, K. Lejaeghere,
F. Muniz Miranda, C. V. Stevens,
P. Van Der Voort and V. Van Speybroeck

Journal of Material Chemistry A, **2019**, *7*, 8433–8442

A. De Vos performed the research and wrote the manuscript.

Journal of Materials Chemistry A

PAPER

View Article Online
View Journal | View Issue

Cite this: J. Mater. Chem. A, 2019, 7, 8433

Electronic properties of heterogenized Ru(II) polypyridyl photoredox complexes on covalent triazine frameworks†

Arthur De Vos, [a] Kurt Lejaeghere, *[a] Francesco Muniz Miranda, [a] Christian V. Stevens, [b] Pascal Van Der Voort [c] and Veronique Van Speybroeck *[a]

Received 16th January 2019
Accepted 13th March 2019

DOI: 10.1039/c9ta00573k

rsc.li/materials-a

Ru(II) polypyridyl complexes have been successful for a wide range of photoredox applications thanks to their efficient light-induced metal-to-ligand charge transfer. Using the computational framework of density-functional theory, we report how these complexes can be anchored onto covalent triazine frameworks while maintaining their favorable electronic properties. We moreover show that variation of the nitrogen content of the framework linkers or complex ligands endows the heterogenized catalyst with a unique versatility, spanning a wide range of absorption characteristics and redox potentials. By judiciously choosing the catalyst building blocks, it is even possible to selectively guide the charge transfer toward either the scaffold or the accessible pore sites. Rational design of sustainable and efficient photocatalysts thus comes within reach.

1 Introduction

To sustain a growing global population, a more efficient and environmentally friendly harvesting of energy is required. This is especially important for the chemical industry, which is one of the most energy-intensive sectors, strongly relying on fossil fuels for the production of chemical products.[1] Photocatalysis is a more sustainable approach, as it relies on naturally present sun light in combination with photocatalytic materials to transfer solar into chemical energy.[2–5] This transfer can be efficiently achieved by homogeneous photocatalysis with the aid of photocatalytic complexes.[3,6] However, as most promising photocatalysts contain precious metals, it is highly desirable to develop recyclable and reusable heterogeneous photocatalytic systems. The use of photocatalytic complexes in a homogeneous suspension necessitates an environmentally unfriendly cycle to remove the catalyst from the products. Heterogeneous catalysts in which the photocatalytic complexes are anchored on a porous framework can avoid this last step and therefore serve as an environmentally cleaner alternative.[7–10] In this work, we not only demonstrate how covalent triazine frameworks (CTFs) provide such a support for photocatalytic Ru complexes, but show that they introduce an additional possibility for tuning the electronic response—and hence efficiency—of the combined photocatalytic system.

The photocatalytic complexes of interest consist of a Ru^{2+} ion octahedrally chelated by three bidentate polypyridyl ligands L, denoted as Ru(II)L_3 (see Fig. 1). The photoactivity of these complexes is caused by their long-lived metal-to-ligand charge transfer (MLCT) state induced by light absorption.[3] This MLCT and resulting availability of the excited electron on the ligands enables its good performance as catalytic center, where it triggers oxidation or reduction reactions in surrounding systems.[3,11–17] Proven photoredox applications include carbon dioxide reduction,[18,19] solar cell development,[20] water splitting,[2,21–23] as well as Diels–Alder cycloadditions.[24]

In this paper we consider the heterogenization of these Ru(II)L_3 complexes onto covalent triazine frameworks using a computational approach. CTFs are part of a much broader family of porous frameworks suitable for anchoring photocatalytic complexes. This family includes metal–organic frameworks (MOFs)[25] and covalent-organic frameworks (COFs),[26–28] many of which have the high surface areas mandatory to function as a good support material. Moreover MOFs and COFs are highly tunable due to the variability of their building blocks, adding a second pathway to modify the material in addition to the anchored complex. Such alternative modification strategies are ideal to engineer electronic and optical behavior.[29,30] Unfortunately, most MOF structures tend

[a]Center for Molecular Modeling (CMM), Ghent University, Technologiepark 46, 9052 Zwijnaarde, Belgium. E-mail: Kurt.Lejaeghere@UGent.be; Veronique.VanSpeybroeck@UGent.be

[b]Research Group SynBioC, Department of Green Chemistry and Technology, Faculty of Bioscience Engineering, Ghent University, Campus Coupure, Coupure Links 653 bl. B, 9000 Gent, Belgium

[c]Center for Ordered Materials, Organometallics and Catalysis (COMOC), Department of Inorganic and Physical Chemistry, Ghent University, Krijgslaan 281 (S3), 9000 Gent, Belgium

† Electronic supplementary information (ESI) available. See DOI: 10.1039/c9ta00573k

View Article Online
Journal of Materials Chemistry A Paper

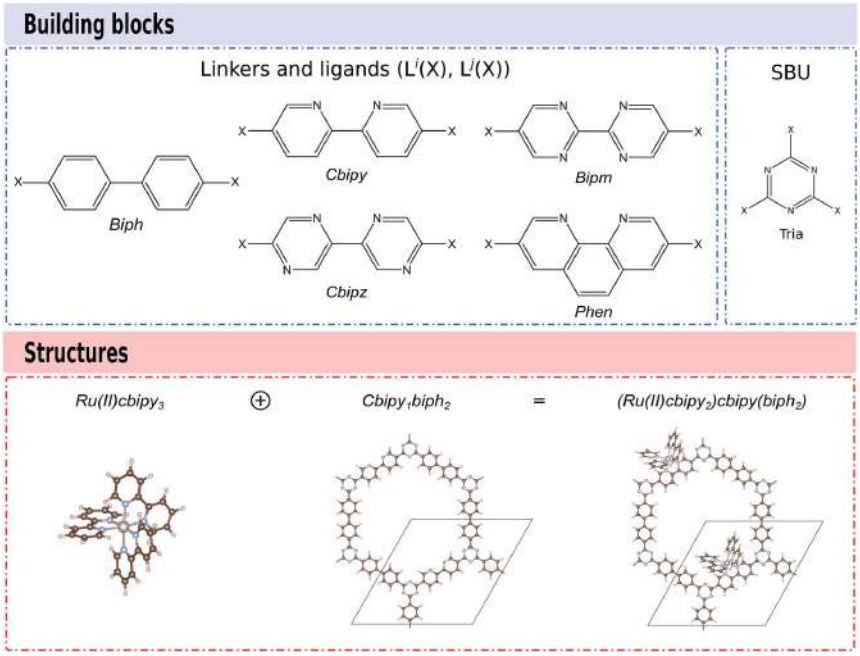

Fig. 1 Building blocks of both the CTF monolayer and the Ru(II)L$_3$ complexes (top). The heterogeneous photocatalyst of interest consists of a structure in which the Ru(II)L$_3$ complex is anchored on a CTF monolayer, for which an example is given (bottom) (blue: N, brown: C, white: H, grey: Ru).

to lack stability under reaction conditions.[13,31,32] COFs, on the other hand, are more stable, and even display some (photo) catalytic activity in their pristine form,[33–38] although they lack an inorganic catalytic center compared to MOFs. Using COFs as a support for photocatalytic complexes may lead toward more efficient and robust heterogeneous photocatalysis.

CTFs are an especially promising class of COFs known to be thermally and chemically stable.[35,39–42] They are 2D porous frameworks made upon the trimerization of aromatic nitriles. CTFs are particularly interesting to anchor photocatalytic complexes, as they are much lighter than most other porous materials and do not possess toxic or environmentally unfriendly elements. In addition, 2D heterostructures have attracted widespread attention thanks to their compelling properties, which are useful for many potential applications.[43]

In order to use CTFs as support material, bidentate nitrogen-containing linkers similar to the chelating ligands of the Ru(II)L$_3$ complex should be present in the framework. We start from a biphenyl-based CTF,[44] which we will refer to as CTF-1-2R[45] (the name CTF-2, which has also been used for this material[44] was originally proposed for a naphthalene-based structure[46]). Note that CTF-1-2R intrinsically has some photocatalytic activity.[44] We then replace a number of biphenyl linkers with polypyridyl ones suited to anchor the Ru(II)L$_3$ complex (see Fig. 1). Hug *et al.* recently synthesized such a CTF-1-2R containing a 2-2′-bipyridine (bipy) linker.[47] Similar strategies can be applied for MOFs,[48] where photocatalytic complexes were already successfully anchored to both linkers[49,50] and nodes.[51]

In the following sections, we perform a computational investigation of the combined Ru(II)L$_3$–CTF heterogeneous photocatalyst and explore in how far the favorable electronic properties of Ru(II)L$_3$ complexes are maintained upon anchoring. To investigate this point, we vary the bidentate moieties in both the Ru(II)L$_3$ complex and the CTF support and show how small synthetic modifications allow tuning the light absorption and redox properties of the catalyst. The CTF and the Ru(II)L$_3$ complex are first considered separately, after which the properties of the coupled catalyst are compared in detail. The combined Ru(II)L$_3$–CTF heterogeneous photocatalyst has a larger versatility than the isolated complex as both the framework and the Ru(II)L$_3$ complex can be varied. In addition, it makes it possible to obtain asymmetrically surrounded Ru(II)L$_3$ complexes in a rather natural way. We show that depending on the composition of the system the MLCT can be guided[52]

View Article Online
Paper Journal of Materials Chemistry A

either to the framework or to the pore of the material, producing a versatile photocatalyst for either interface- or pore-driven catalytic applications.

2 Methodology

2.1 Structures

We considered several variants of the CTF-1-2R framework to act as a scaffold for Ru(II)L_3 complexes. CTF-1-2R itself only contains biphenyl linkers (biph) and is therefore unsuited to function as a catalytic support for the photocatalytic Ru(II)L_3 complex. To introduce appropriate anchor sites, four experimentally available bidentate nitrogen-containing linkers were instead considered, *cis*-bipyridine (cbipy), phenanthroline (phen), *cis*-bipyrazine (cbipz), and bipyrimidine (bipm), as well as their monodentate *trans* configurations (tbipy, tbipz) (see Fig. 1). This set of linkers allows changing the nitrogen content of the CTF's aromatic system, with nitrogen counts ranging from two to four per linker. Moreover, experimental synthesis of these materials should be possible, as demonstrated by the successful synthesis of a bipyridine-based CTF by Hug *et al.*[47]

We modeled the nitrogen-containing CTFs by considering a single CTF-1-2R monolayer, which contains three biph linkers and two triazine (tria) secondary building blocks (SBU) per unit cell. The influence of multilayer stacking is therefore not taken into account. In each layer we replaced one, two or three of the biph linkers by a particular polypyridyl one (L^i), forming a modified CTF-1-2R. We will refer to a given CTF in terms of its constituent linkers, *e.g.* $biph_3$ for CTF-1-2R and $L_n{}^i biph_{3-n}$ for the modified systems with n the number of replaced biph linkers. The systematic and controlled inclusion of polypyridyl linkers within the CTF allows us to assess the influence of nitrogen content on the CTF properties. The work of Wang *et al.* moreover indicates that it is indeed possible to make such mixed-linker CTFs.[53]

The properties of the Ru(II)L_3 complex were varied using the same four bidentate ligands. Ru(II)L_3 complexes used for homogeneous photocatalysis consist of three bidentate nitrogen-containing ligands for which generally two or three are equal.[3,12–15] We will denote these complexes as Ru(II)$L_2{}^j L_1{}^i$, with the most prominent example being Ru(II)cbipy$_3$. When embedded into the CTF, the L^i linker is shared between the framework and the complex, while the other two chelating ligands L^j extend into the pore. Such metal-functionalized COFs may be produced either post-synthetically or by using prefunctionalized linkers during the CTF synthesis.[13,54] We denote the resulting heterogenized photocatalyst as (Ru(II)$L_2{}^j$)$L_1{}^i$($L_n{}^i biph_{2-n}$) with $n = 0$, 1, 2. The presence of mixed-ligand complexes rather than complexes with only a single type of ligand allows us to tune the photocatalytic activity in much more detail.

2.2 Computational details

All periodic calculations were performed using density-functional theory (DFT) in the projector-augmented wave (PAW) approach[55] with the VASP 5.4.4 package[56–59] and employing the PBE functional.[60] Although the semilocal PBE functional substantially underestimates band gaps, it correctly reproduces electronic-structure trends at a fraction of the cost of higher-level methods.[29,45,61] We confirmed this using selected HSE06 calculations (see Fig. S2–S5†).[62,63] Note, however, that for quantitative purposes, even more advanced theories would be required, as conjugated systems typically yield poor absolute electron affinity and band gap predictions.[64] van der Waals interactions were modeled by the DFT-D3 method of Grimme with Becke–Johnson damping.[65,66] The recommended GW-ready PAW potentials were used because of their high precision,[67,68] employing a $1s^1$, $2s^22p^2$, $2s^22p^3$ and $4s^24p^65s^24d^6$ valence electron configuration for respectively H, C, N and Ru. In addition, a plane wave basis set was employed with a kinetic energy cut-off of 800 eV for all structures.

For CTF monolayers a $2 \times 2 \times 1$ Γ-centered grid was used to sample the first Brillouin zone. We imposed an electronic energy convergence criterion of 10^{-5} eV together with an ionic relaxation threshold of 10^{-4} eV. These settings were used to uniformly rescale the CTF's in-plane lattice parameters from −4% to 4% in steps of 1% and fit a Rose–Vinet equation of state (see *e.g.* Fig. S8†).[69] Because of the intrinsic periodicity imposed by VASP, an interlayer distance of 22 Å was maintained, and the van der Waals radius in the D3 scheme was reduced to 20 Å to remove dispersion interaction between the monolayers. The equilibrium lattice parameters were extracted from the equation of state, at which the structures were relaxed using more stringent electronic and ionic convergence criteria of 10^{-7} eV and 10^{-6} eV, respectively. In this last optimization run, the interlayer vacuum region was increased to 40 Å when a Ru(II)L_3 complex was anchored onto the CTF to obtain reliable energies.

The Ru(II)L_3 complexes were calculated in a $40 \times 40 \times 40$ Å^3 unit cell using a 2+ charge, a Γ-point k-grid and an electronic and ionic convergence threshold of 10^{-7} eV and 10^{-6} eV. Similarly, the Ru^{2+} ion and nitrogen-containing linkers were calculated in a $20 \times 21 \times 23$ Å^3 and $40 \times 30 \times 22$ Å^3 box (see Fig. S6†) to obtain the formation energy (see "The photocatalytic complex" and "The heterogeneous photocatalyst"). In the case of a charged system, an energy correction was applied to remove monopolar interactions with its periodic images (see Section S2†).[68,70,71]

Density of states (DOS) calculations were performed with a $6 \times 6 \times 1$ Γ-centered grid for the CTF and a Γ-point grid for the building blocks and Ru(II)L_3 complexes. In addition, the threshold for the electronic self-consistent cycle was tightened to 10^{-8} eV. The DOS were plotted using the pymatgen package.[72] Depending on the feature of interest, different DOS plots were aligned using either a judiciously chosen energy or potential reference, or by quantitatively positioning them with respect to the vacuum potential. In the latter case, the vacuum potential was either explicitly calculated (neutral systems) or determined from the electron affinity, *i.e.* the energy change upon adding a supplementary electron (charged systems).

3 The scaffold

To understand the role of the CTF scaffold's composition in the heterogeneous photocatalyst, we first consider the CTF alone. We examine both the energetic and the electronic influence of introducing polypyridyl linkers within the $biph_3$ monolayer,

View Article Online
Journal of Materials Chemistry A Paper

which are needed to create a suitable anchor site for the Ru(II)L_3 complex (see "Structures").

3.1 Energetics

As CTFs are made upon trimerisation of aromatic nitriles (see Fig. 1, X = CN), the CTF stability can be assessed by evaluating the formation energy in terms of these constituting linkers (see Table S5†):

$$E_{\mathrm{Form}} = E_{\mathrm{CTF}} - \sum_i E_{\mathrm{L}^i(\mathrm{CN})} = \sum_i \Delta E_{\mathrm{L}^i(\mathrm{CN})} \quad (1)$$

The formation energy is depicted in Fig. 2a. We see that all frameworks are stable, but that the stability scales unfavorably with the number of polypyridyl linkers. This destabilization per linker is of the order of 1.8 eV and is approximately equal for all linkers within a 40 meV range, independent of their nitrogen content.

To investigate the role of the individual linkers in more detail, eqn (1) can be approximated to attribute the formation energy to independent contributions of the different linkers. In this case, the formation energy can be seen as the sum of stabilization energies ΔE_{L^i}(CN) per linker, independent of the framework in which they are incorporated. These stabilization energies per linker can be obtained from the formation energies of different CTFs *via* a least-squares fit (see Table S6†). The agreement between the actual and the fitted formation energies is better than 3 meV, indicating that there is no energetic interaction between individual linkers across the bridging triazine unit.

3.2 Electronic structure

The densities of states for a few considered CTFs are shown in the right panel of Fig. 3 (see Section S5.2 for a full overview and Fig. S2† for a HSE06 validation of Fig. 3). The decomposition with respect to the building blocks shows the appearance of both localized and delocalized states. The delocalized states, which include the conduction band minimum (CBM), are spread out over the entire structure and agree well with the traditional solid-state concept of an energy band. In contrast, there are also localized states, such as the top of the valence band, which are characterized by sharp peaks in the DOS. The corresponding orbitals are confined to individual components of the CTF and retain a more discrete, molecular character.[29,73,74] These localized states are therefore often referred to as crystal orbitals, and the top of the valence band is classified as highest occupied crystal orbital (HOCO). Strikingly, the energy and shape of these localized electron levels is very similar to those in the CTF constituents (see Fig. 3, left panel). This suggests that some features of the linkers are maintained when incorporating them into the aromatic system of the periodic CTF. Such electronic structure decoupling resembles that of 0D MOFs, which are made up of independent contributions of their inorganic and organic building blocks.[29,61] Hence we would like to introduce the idea of orthogonal electronic structure engineering for COFs in a similar way as for MOFs, *i.e.* the ability to tune the overall electronic structure by independently varying the different constituents.

Finally Fig. 3 illustrates that the electronic structure of CTF-1-2R can be modified by doping it with nitrogen-containing linkers. Although the position of the HOCO relative to the vacuum energy remains fairly independent of the nitrogenous character of the framework, the CBM systematically lowers if it is increased (see Fig. 3 and S9†). As a result the band gap decreases. The band gap is plotted for the various materials in terms of the nitrogen content in Fig. 4a. The behavior of the CBM is found to be inherited from the individual linkers (see Section S4†) and is in line with current literature on similar nitrogen-based organic frameworks.[34,75,76] It is caused by the inclusion of nitrogen atoms in the aromatic ring. Because their free electron pairs are not part of the aromatic system, they lead to a π-electron-deficient system. The framework (or linker) will therefore accept electrons more easily. The resulting band gap may be more suitable for photocatalysis, as experimentally observed in nonfunctionalized CTFs.[34,36,37,44,46,76] In addition, the dependence of the band gap

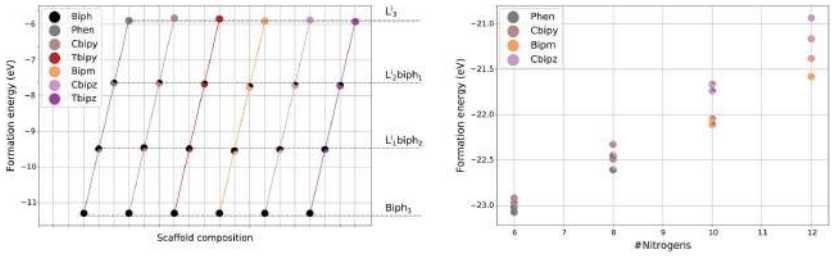

Fig. 2 Formation energy of the CTF scaffold (a) and the Ru(II)L_3 complex (b) in eV per unit cell. Each data point is colored in three parts, which represent the composition of the CTF scaffold or Ru(II)L_3 complex, respectively. In panel (a) the solid lines connect all frameworks $L^i_n biph_{3-n}$ with a fixed linker type L^i; the dashed lines correspond to different values of n.

View Article Online
Paper Journal of Materials Chemistry A

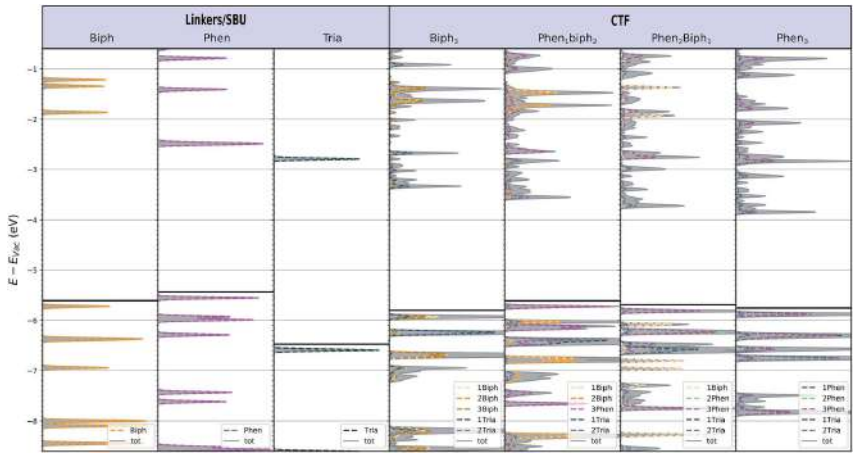

Fig. 3 Densities of states of CTF-1-2R doped with 1, 2 or 3 phenanthroline linkers (phen$_n$biph$_{3-n}$, n = 0, 1, 2, 3) compared to the electronic structure of the hydrogen-terminated constituents (biph, phen, tria). The DOS are aligned with respect to the vacuum energy.

on nitrogen content may be relevant during photocatalysis as it could favor the transport of excited electrons from the photocatalytic complex to the framework (see "The heterogeneous photocatalyst").

4 The photocatalytic complex

Essential to the photocatalytic performance of the envisioned heterogeneous photocatalyst is the activity of the Ru(II)L$_3$ complex. Similar to the CTF scaffold, several nitrogen-containing ligands can be considered to further tune the properties of this complex. Here we investigate the energetics and electronic properties of mixed-ligand Ru(II)L$_3$ complexes with up to two different polypyridyl moieties (see "Structures").

4.1 Energetics

Ru(II)L$_3$ complexes are a combination of a Ru^{2+} ion and nitrogenous bidentate ligands (see Fig. 1 with X = H). Their stability can therefore be calculated from the following formation energy (see Table S8†):

$$E_{\mathrm{Form}} = E_{\mathrm{RuL_3}^{2+}} - \sum_j E_{\mathrm{L}^j(\mathrm{H})} - E_{\mathrm{Ru}^{2+}} = \sum_j \Delta E_{\mathrm{L}^j(\mathrm{H})} \qquad (2)$$

Note that by using eqn (2) competition with other ligands is not considered. However, the latter stability is corroborated by the confirmed functionality of Ru(II) complexes in several photocatalytic reactions.[2,3,11–24]

The energy can again be successfully decomposed into contributions from the different ligands with a residual error of

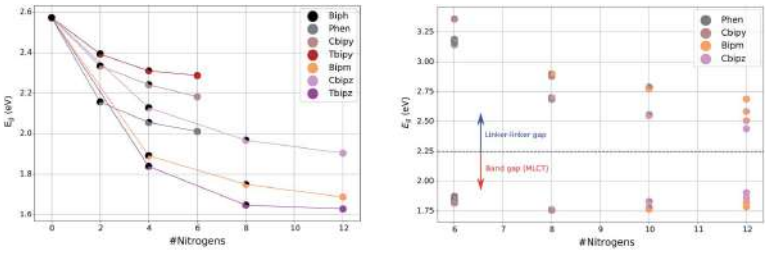

Fig. 4 Band gap of the CTF as a function of the number of linker nitrogen atoms per unit cell (a). Gap between the highest occupied and lowest unoccupied molecular orbital and analogous linker–linker gap of the Ru(II)L$_3$ complex with respect to the number of nitrogen atoms in the complex (b). Each data point is colored in three parts, which represent the composition of the CTF scaffold or Ru(II)L$_3$ complex, respectively.

View Article Online
Journal of Materials Chemistry A Paper

less than 4 meV ($\Delta E_{L/(H)}$, see Table S9†). This implies that there is little energetic coupling between the different ligands across the Ru ion, so the main differences between Ru(II)L_3 complexes can be attributed to the Ru(II)–L/ bonds.

The experimentally observed stability of Ru(II)L_3 complexes is confirmed in our calculations (see Fig. 2b). Moreover, we note that ligands with few nitrogen atoms bind more strongly into a Ru(II)L_3 complex, which is in line with their larger basicity and associated stronger electron-donating character. This simple criterion suggests that a Ru(II)L_3 complex might be post-synthetically applied to an existing CTF crystal when the complex ligands have a higher nitrogen content than the framework linkers. In this way the Ru(II)L_3 complex would anchor more strongly to the framework and exchange one of its ligands for a framework linker. We investigate this conjecture in more detail in "The heterogeneous photocatalyst".

4.2 Electronic structure

The highest occupied molecular orbital (HOMO) of Ru(II)L_3 complexes is centered on the Ru^{2+} ion and corresponds to a t_{2g} state of an octahedrally surrounded complex. The lowest unoccupied molecular orbital (LUMO), on the other hand, is located on the chelating ligands with the highest nitrogen content and thus highest electron affinity (see Fig. 5 or Section S6.2 for a full overview and Fig. S4† for a HSE06 validation of Fig. 5). The HOMO–LUMO gap therefore represents a qualitative measure of the MLCT, which is one of the key properties in the photocatalytic process of interest. The nitrogen dependence of the LUMO location moreover allows tuning the MLCT to a specific ligand, which is of interest when anchoring the complex to a CTF. This larger reduction potential of Ru(II)L_3 complexes with increasing nitrogen content was also observed experimentally.[3]

Similar to CTFs, the electronic structure of a Ru(II)L_3 complex can to a large extent be considered as a superposition of contributions of its components (see Fig. S10†). Therefore, even here the concept of orthogonal electronic structure engineering can be introduced. As the Ru(II)L_3 complex contains the same type of linkers/ligands as the CTF, its electronic structure moreover evolves in a similar way as a function of nitrogen content. Indeed, the lowest unoccupied linker state lowers as the nitrogen content increases, while the highest occupied linker state remains rather constant. This leads to an overall decrease of the ligand–ligand (LL) gap with increasing nitrogen content (see Fig. 4b and 5). On the other hand, the HOMO is now a Ru-based state and lowers as much in energy with nitrogen content as the LUMO. As shown in Fig. 4b, this gives rise to a fairly constant HOMO–LUMO gap. Hence, the absorption behavior is similar across the different mixed Ru(II)L_3 complexes, although the redox potential is changing. This feature makes our Ru(II)L_3 complexes an interesting set for photocatalysis as it allows adapting both the direction of the MLCT and the chemical activity while targeting the same range of absorption wavelengths.

5 The heterogeneous photocatalyst

Both the CTF scaffold and the homogeneous Ru(II)L_3 catalyst display interesting properties for photocatalytic purposes. They can be combined in numerous ways, which enables fine-tuning the material beyond what is possible in the individual constituents. However, it is not guaranteed that the beneficial behavior of the components is transferred to the combined Ru(II)L_3–CTF system. We consider the energetics and electronic properties of a systematic subset of heterogeneous photocatalysts below (see Table S1†). Not only does this demonstrate that the photocatalytic properties of both the complex and the framework are

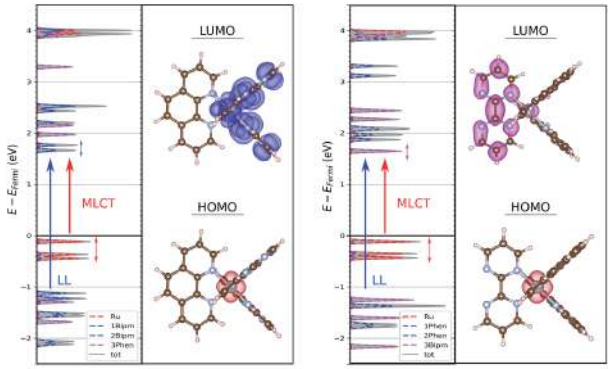

(a) Ru(II)bipm$_2$phen$_1$ (b) Ru(II)phen$_2$bipm$_1$

Fig. 5 Metal-to-ligand (MLCT) and ligand–ligand (LL) transitions in Ru(II)bipm$_2$phen$_1$ (a) and Ru(II)phen$_2$bipm$_1$ (b) together with the corresponding orbitals.

maintained, but they can even be varied with an unparalleled versatility, allowing different phototransfer directions and redox potentials.

5.1 Energetics

Similar to the treatment of the CTF scaffold or the Ru(II)L_3 complex, the formation energy of the Ru(II)L_3–CTF catalyst can be calculated with respect to the individual constituents (see Table S11†). We find the same trends in stability when we vary the components of either the Ru(II)L_3 complex or the CTF (see Fig. S12†). Incorporating nitrogenous linkers in either part not only destabilizes the material, but by approximately the same amount as in the separate building blocks (see Table S12†). The energetics of the combined Ru(II)L_3–CTF catalyst can therefore be predicted to some extent from this underlying behavior.

Of particular interest to the combined Ru(II)L_3–CTF catalyst is the energy required or released when anchoring the photocatalytic complex onto the support framework. We calculated the energy needed to anchor a Ru(II)L_3^j complex with three equal ligands onto a $L_{n+1}{}^i\text{biph}_{2-n}$ CTF to form the anchored (Ru(II)L_2^j)$L_1{}^i(L_n{}^i\text{biph}_{2-n})$ complex ($n = 0, 1, 2$). For all considered catalysts this energy was found to be negative (see Table S13†), indicating that the heterogeneous photocatalyst can indeed be formed through a spontaneous process of ligand exchange. Moreover highly nitrogen-containing Ru(II)L_3^j complexes anchor more strongly to CTFs with a lower nitrogen content, which possess a higher basicity. This is in correspondence with the energetics of the isolated Ru(II)L_3 complex.

5.2 Electronic structure

Ru(II)L_3 complexes combine a band gap in the visible wavelength range with an intrinsic charge transfer upon light absorption. The combined Ru(II)L_3–CTF catalyst will only be successfully created if these advantages remain intact. A first requirement is that the electronic structure of the complex within the catalyst should not differ too much from that of the isolated one. Fig. 6 (left) illustrates that the energy levels of the pristine Ru(II)bipm$_2$phen complex (left panel) are indeed retrieved when anchoring it onto a phenanthroline-containing framework (right panel) (see Fig. S14 and S15 for further examples and Fig. S5a† for an HSE06 validation of Fig. 6 (left)). Furthermore the redox potential of the complex remains almost unaltered, indicating that the heterogeneous photocatalyst may be applied to the same reactions as the homogeneous one. The principle of orthogonal electronic structure engineering therefore also extends to the combined Ru(II)L_3–CTF catalyst, in which not only states of the Ru(II)L_3 complex, but also from the CTF are recovered (see Fig. S13†).

A second point of attention is the electronic structure near the band gap. We showed in "The photocatalytic complex" that the Ru(II)L_3 complex has a Ru-centered HOMO and a ligand-based LUMO. When anchored, the HOCO moves toward a non-anchoring CTF linker state (see Fig. 6, left). Excitations from this level may be of interest, but it is spatially separated from the Ru^{2+} ion. Further study is therefore needed to elucidate whether transitions between such a framework linker and the Ru(II)L_3 complex are realistic. We instead focus on MLCT excitations of the anchored Ru(II)L_3 separately, which we find to display the same trends as the Ru(II)L_3 complex. Indeed the LUCO and the Ru levels again decrease as a function of the nitrogen content of the Ru ligands while the highest occupied ligand states remain more or less fixed (see Fig. S14†). As a result, the MLCT gap remains independent of the used ligands, while the LL gap decreases with nitrogen content. These findings suggest a Ru(II)L_3 complex to retain its photoredox properties when it is heterogenized in the CTF. The heterogenized photocatalyst may therefore be suited for similar reactions as the isolated complex.

Although the general electronic properties of the Ru(II)L_3 complex are conserved, heterogenizing the Ru(II)L_3 complex onto the CTF does have some interesting consequences. The most prominent effect is the introduction of a CTF-centered HOCO, as mentioned above. A second result is visible for the unoccupied states (Fig. 6, left). Not only is the electron affinity increased as a function of the CTF nitrogen content, but this affects the anchoring linker differently from the ones dangling into the pore. It may even lead to a change in energy ordering between the different unoccupied ligand orbitals (see Fig. S15b and c†). In that case, an MLCT-excited electron from the Ru(II)L_3 complex may change its charge transfer direction compared to the isolated cluster, *i.e.* toward the framework rather than the other two (pore) ligands.

Attaching the Ru(II)L_3 complex to a CTF does not appear to undermine its photoactivity nor the redox reactions to which it is applied. On the contrary, modifying the CTF linkers provides an additional degree of freedom to tune the electronic response of the photocatalyst. By varying the polypyridyl linkers in the CTF or the corresponding ligands in the Ru(II)L_3 complex, the redox potential of the catalyst can be altered by up to 1 eV. This versatility is useful to further optimize Ru(II)L_3 complexes for sustainable applications, such as water splitting[23] and carbon dioxide reduction.[19] Such design may be accomplished using the qualitative guidelines established here, as well as by means of future investigations into quantitative redox potentials, *e.g.* by including the solvent and applying a higher level of theory. In addition, carefully selecting both the complex and CTF components allows the design of a guided metal-to-ligand charge transfer (see Fig. 6, right). In a mixed Ru(II)L_3 complex the MLCT is directed toward the ligand with the highest nitrogen content. When combined with the CTF, a higher nitrogen content of the framework favors a MLCT toward the anchoring linker. If the catalytic operation requires excitation to the framework, the nitrogen content should therefore be high in the CTF and low for the ligands in the pore (*e.g.* (Ru(II)cbipy$_2$)bipm(bipm$_2$)). In contrast, MLCT toward the pore can be achieved by keeping the nitrogen content of the framework at a minimum and using highly nitrogenous moieties for the pore linkers (*e.g.* (Ru(II)bipm$_2$)phen(phen$_2$)). This is also the energetically most favored scenario (see Table S13†).

View Article Online
Journal of Materials Chemistry A Paper

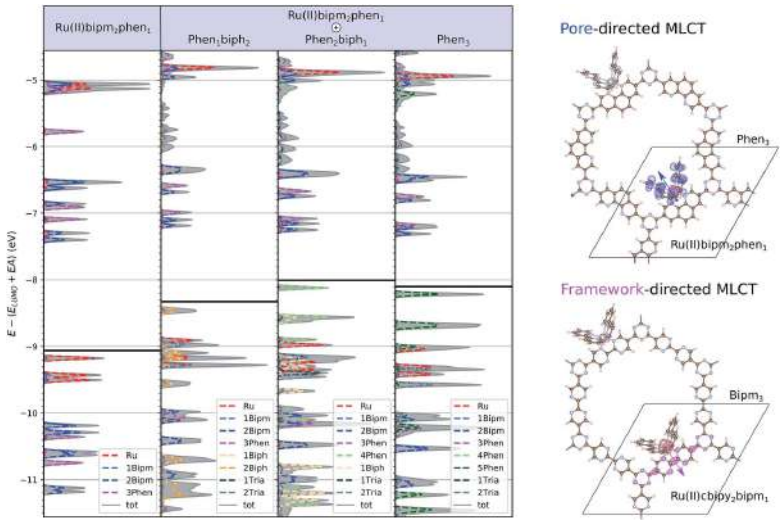

Fig. 6 Electronic states of the Ru(II)bipm$_2$phen$_1$ complex *in vacuo* and when anchored on a phen$_n$biph$_{3-n}$, n = 0, 1, 2, 3 framework (left). Depending on the Ru(II)L$_3$ complex and CTF scaffold, the charge transfer upon light absorption can be directed toward the pore or the framework (right).

6 Conclusion

Heterogenization of Ru polypyridyl complexes is an essential step in the development of more sustainable photoredox catalysts. A promising possibility in that respect is attaching the complexes to covalent triazine frameworks, which provide a robust and light-weight support. The composition of these 2D porous substrates may moreover be tuned to the redox reaction of interest. CTF-anchored complexes therefore not only offer a large accessible surface, but also a promising versatility toward functional catalyst design.

We considered a wide range of different polypyridyl-based CTF monolayers and Ru(II)L$_3$ complexes and demonstrated that it is indeed energetically favorable to anchor the Ru complexes onto the CTF. However, an essential condition for an efficient heterogeneous photocatalyst is that its photoredox properties do not deteriorate when incorporated into the CTF scaffold. We confirmed that the electronic structure of both the Ru(II)L$_3$ complex and CTF stay mostly unaltered upon combining the two systems, and that the redox potential of the photocatalytic complex remains largely the same. This behavior was shown to be even more generally valid: the energy levels of both the unfunctionalized CTF and the Ru(II)L$_3$ complex are to a large extent made up of contributions from their individual components. Also energetically, the stability of a given structure solely depends on the type of linker or ligand that is introduced into the material. This conclusion indicates that the principle of orthogonal electronic structure engineering, first demonstrated for 0D MOFs,[29] might be applicable to a wide class of crystals with molecule-like building blocks.

Although the heterogenization of photocatalytic Ru(II)L$_3$ complexes is a valuable target as such, our study additionally showed that anchoring onto a CTF scaffold provides the system with an even broader tunability than before. Band gaps, charge transfer reactions and redox potentials are all strongly adaptable by changing the nitrogen content of the different components of the catalyst. A higher nitrogen content typically lowers the energy of unoccupied polypyridyl levels and occupied Ru t_{2g} levels, while occupied linker or ligand states change only little. This behavior makes it possible to guide the light-induced charge transfer by increasing the nitrogen content of either the CTF (framework-directed MLCT) or the dangling Ru ligands (pore-directed MLCT). The versatility of CTF-anchored Ru(II)L$_3$ complexes therefore endows them with the capability to display a high photoredox activity for a wide range of target reactions and catalytic set-ups.

Conflicts of interest

The authors declare no conflict of interest.

Acknowledgements

We acknowledge financial support by the Fund for Scientific Research Flanders (FWO) and the Research Board of Ghent University through a Concerted Research Action (GOA). The

computational resources and services used in this work were provided by VSC (Flemish Supercomputer Center), funded by Ghent University, FWO, and the Flemish Government department EWI.

Notes and references

1 U.S. International Energy Agency, *International Energy Outlook*, 2016, DOE/EIA-0484(2016).
2 K. Takanabe, *ACS Catal.*, 2017, **7**, 8006–8022.
3 C. K. Prier, D. A. Rankic and D. W. C. MacMillan, *Chem. Rev.*, 2013, **113**, 5322–5363.
4 M. D. Kärkäs, J. A. Porco and C. R. J. Stephenson, *Chem. Rev.*, 2016, **116**, 9683–9747.
5 D. M. Schultz and T. P. Yoon, *Science*, 2014, **343**, 1239176.
6 J. M. R. Narayanam and C. R. J. Stephenson, *Chem. Soc. Rev.*, 2011, **40**, 102–113.
7 A. G. Slater and A. I. Cooper, *Science*, 2015, **348**, aaa8075.
8 S. M. J. Rogge, A. Bavykina, J. Hajek, H. Garcia, A. I. Olivos-Suarez, A. Sepúlveda-Escribano, A. Vimont, G. Clet, P. Bazin, F. Kapteijn, M. Daturi, E. V. Ramos-Fernandez, F. X. Llabrés i Xamena, V. Van Speybroeck and J. Gascon, *Chem. Soc. Rev.*, 2017, **46**, 3134–3184.
9 H. Takeda, M. Ohashi, Y. Goto, T. Ohsuna, T. Tani and S. Inagaki, *Adv. Funct. Mater.*, 2016, **26**, 5068–5077.
10 W. Tu, Y. Xu, S. Yin and R. Xu, *Adv. Mater.*, 2018, **30**, 1707582.
11 J. J. Concepcion, J. W. Jurss, M. K. Brennaman, P. G. Hoertz, A. O. T. Patrocinio, N. Y. Murakami Iha, J. L. Templeton and T. J. Meyer, *Acc. Chem. Res.*, 2009, **42**, 1954–1965.
12 J. M. R. Narayanam, J. W. Tucker and C. R. J. Stephenson, *J. Am. Chem. Soc.*, 2009, **131**, 8756–8757.
13 C. Wang, Z. Xie, K. E. deKrafft and W. Lin, *J. Am. Chem. Soc.*, 2011, **133**, 13445–13454.
14 S. Fukuzumi, T. Kishi, H. Kotani, Y.-M. Lee and W. Nam, *Nat. Chem.*, 2010, **3**, 38–41.
15 D. A. Nicewicz and D. W. C. MacMillan, *Science*, 2008, **322**, 77–80.
16 J.-M. Zen, S.-L. Liou, A. S. Kumar and M.-S. Hsia, *Angew. Chem., Int. Ed.*, 2003, **42**, 577–579.
17 W. Chen, F. Rein and R. Rocha, *Angew. Chem., Int. Ed.*, 2009, **48**, 9672–9675.
18 H. Takeda and O. Ishitani, *Coord. Chem. Rev.*, 2010, **254**, 346–354.
19 T. J. Meyer, *Acc. Chem. Res.*, 1989, **22**, 163–170.
20 F. Gao, Y. Wang, J. Zhang, D. Shi, M. Wang, R. Humphry-Baker, P. Wang, S. M. Zakeeruddin and M. Grätzel, *Chem. Commun.*, 2008, 2635–2637.
21 J. J. Concepcion, J. W. Jurss, J. L. Templeton and T. J. Meyer, *J. Am. Chem. Soc.*, 2008, **130**, 16462–16463.
22 N. Kaveevivitchai, R. Chitta, R. Zong, M. El Ojaimi and R. P. Thummel, *J. Am. Chem. Soc.*, 2012, **134**, 10721–10724.
23 M. Graetzel, *Acc. Chem. Res.*, 1981, **14**, 376–384.
24 S. Lin, M. A. Ischay, C. G. Fry and T. P. Yoon, *J. Am. Chem. Soc.*, 2011, **133**, 19350–19353.
25 J. R. Long and O. M. Yaghi, *Chem. Soc. Rev.*, 2012, **112**, 673–1268.
26 C. S. Diercks and O. M. Yaghi, *Science*, 2017, **355**, eaal1585.
27 A. P. Côté, A. I. Benin, N. W. Ockwig, M. O'Keeffe, A. J. Matzger and O. M. Yaghi, *Science*, 2005, **310**, 1166–1170.
28 M. S. Lohse and T. Bein, *Adv. Funct. Mater.*, 2018, **28**, 1705553.
29 A. De Vos, K. Hendrickx, P. Van Der Voort, V. Van Speybroeck and K. Lejaeghere, *Chem. Mater.*, 2017, **29**, 3006–3019.
30 D. D. Medina, M. L. Petrus, A. N. Jumabekov, J. T. Margraf, S. Weinberger, J. M. Rotter, T. Clark and T. Bein, *ACS Nano*, 2017, **11**, 2706–2713.
31 N. C. Burtch, H. Jasuja and K. S. Walton, *Chem. Rev.*, 2014, **114**, 10575–10612.
32 K. Leus, T. Bogaerts, J. De Decker, H. Depauw, K. Hendrickx, H. Vrielinck, V. Van Speybroeck and P. Van Der Voort, *Microporous Mesoporous Mater.*, 2016, **226**, 110–116.
33 J. Lan, D. Cao, W. Wang and B. Smit, *ACS Nano*, 2010, **4**, 4225–4237.
34 V. S. Vyas, F. Haase, L. Stegbauer, G. Savasci, C. Podjaski, F. Ochsenfeld and B. V. Lotsch, *Nat. Commun.*, 2015, **6**, 8508.
35 X. Jiang, P. Wang and J. Zhao, *J. Mater. Chem. A*, 2015, **3**, 7750–7758.
36 L. Stegbauer, K. Schwinghammer and B. V. Lotsch, *Chem. Sci.*, 2014, **5**, 2789–2793.
37 J. Xie, S. A. Shevlin, Q. Ruan, S. J. A. Moniz, Y. Liu, X. Liu, Y. Li, C. C. Lau, Z. X. Guo and J. Tang, *Energy Environ. Sci.*, 2018, **11**, 1617–1624.
38 T. Banerjee and B. V. Lotsch, *Nat. Chem.*, 2018, **10**, 1175–1177.
39 P. Kuhn, M. Antonietti and A. Thomas, *Angew. Chem., Int. Ed.*, 2008, **47**, 3450–3453.
40 S. Hug, M. B. Mesch, H. Oh, N. Popp, M. Hirscher, J. Senker and B. V. Lotsch, *J. Mater. Chem. A*, 2014, **2**, 5928–5936.
41 P. Kuhn, A. Forget, D. Su, A. Thomas and M. Antonietti, *J. Am. Chem. Soc.*, 2008, **130**, 13333–13337.
42 S. Ren, M. J. Bojdys, R. Dawson, A. Laybourn, Y. Z. Khimyak, D. J. Adams and A. I. Cooper, *Adv. Mater.*, 2012, **24**, 2357–2361.
43 S. Tongay, *Appl. Phys. Rev.*, 2018, **5**, 010401.
44 C. B. Meier, R. S. Sprick, A. Monti, P. Guiglion, J.-S. M. Lee, M. A. Zwijnenburg and A. I. Cooper, *Polymer*, 2017, **126**, 283–290.
45 P. Zhu and V. Meunier, *J. Chem. Phys.*, 2012, **137**, 244703.
46 M. J. Bojdys, J. Jeromenok, A. Thomas and M. Antonietti, *Adv. Mater.*, 2010, **22**, 2202–2205.
47 S. Hug, M. E. Tauchert, S. Li, U. E. Pachmayr and B. V. Lotsch, *J. Mater. Chem.*, 2012, **22**, 13956–13964.
48 C. H. Hendon, J. Bonnefoy, E. A. Quadrelli, J. Canivet, M. B. Chambers, G. Rousse, A. Walsh, M. Fontecave and C. Mellot-Draznieks, *Chem.–Eur. J.*, 2016, **22**, 3713–3718.
49 W. A. Maza and A. J. Morris, *J. Phys. Chem. C*, 2014, **118**, 8803–8817.
50 C.-C. Hou, T.-T. Li, S. Cao, Y. Chen and W.-F. Fu, *J. Mater. Chem. A*, 2015, **3**, 10386–10394.
51 D. Yang, S. O. Odoh, T. C. Wang, O. K. Farha, J. T. Hupp, C. J. Cramer, L. Gagliardi and B. C. Gates, *J. Am. Chem. Soc.*, 2015, **137**, 7391–7396.
52 M. Jäger, L. Freitag and L. González, *Coord. Chem. Rev.*, 2015, **304–305**, 146–165.

53 K. Wang, L.-M. Yang, X. Wang, L. Guo, G. Cheng, C. Zhang, S. Jin, B. Tan and A. Cooper, *Angew. Chem., Int. Ed.*, 2017, **56**, 14149–14153.
54 J.-X. Jiang, C. Wang, A. Laybourn, T. Hasell, R. Clowes, Y. Z. Khimyak, J. Xiao, S. J. Higgins, D. J. Adams and A. I. Cooper, *Angew. Chem., Int. Ed.*, 2011, **50**, 1072–1075.
55 G. Kresse and D. Joubert, *Phys. Rev. B: Condens. Matter Mater. Phys.*, 1999, **59**, 1758–1775.
56 G. Kresse and J. Hafner, *Phys. Rev. B: Condens. Matter Mater. Phys.*, 1993, **47**, 558–561.
57 G. Kresse and J. Hafner, *Phys. Rev. B: Condens. Matter Mater. Phys.*, 1994, **49**, 14251–14269.
58 G. Kresse and J. Furthmüller, *Comput. Mater. Sci.*, 1996, **6**, 15–50.
59 G. Kresse and J. Furthmüller, *Phys. Rev. B: Condens. Matter Mater. Phys.*, 1996, **54**, 11169–11186.
60 J. P. Perdew, K. Burke and M. Ernzerhof, *Phys. Rev. Lett.*, 1996, **77**, 3865–3868.
61 K. Hendrickx, D. E. P. Vanpoucke, K. Leus, K. Lejaeghere, A. Van Yperen-De Deyne, V. Van Speybroeck, P. Van Der Voort and K. Hemelsoet, *Inorg. Chem.*, 2015, **54**, 10701–10710.
62 J. Heyd, G. E. Scuseria and M. Ernzerhof, *J. Chem. Phys.*, 2003, **118**, 8207–8215.
63 J. Heyd, G. E. Scuseria and M. Ernzerhof, *J. Chem. Phys.*, 2006, **124**, 219906.
64 S.-H. Ke, *Phys. Rev. B: Condens. Matter Mater. Phys.*, 2011, **84**, 205415.
65 S. Grimme, J. Antony, S. Ehrlich and H. Krieg, *J. Chem. Phys.*, 2010, **132**, 154104.
66 S. Grimme, S. Ehrlich and L. Goerigk, *J. Comput. Chem.*, 2011, **32**, 1456–1465.
67 K. Lejaeghere, G. Bihlmayer, T. Björkman, P. Blaha, S. Blügel, V. Blum, D. Caliste, I. E. Castelli, S. J. Clark, A. Dal Corso, S. de Gironcoli, T. Deutsch, J. K. Dewhurst, I. Di Marco, C. Draxl, M. Dułak, O. Eriksson, J. A. Flores-Livas, K. F. Garrity, L. Genovese, P. Giannozzi, M. Giantomassi, S. Goedecker, X. Gonze, O. Grånäs, E. K. U. Gross, A. Gulans, F. Gygi, D. R. Hamann, P. J. Hasnip, N. A. W. Holzwarth, D. Iuşan, D. B. Jochym, F. Jollet, D. Jones, G. Kresse, K. Koepernik, E. Küçükbenli, Y. O. Kvashnin, I. L. M. Locht, S. Lubeck, M. Marsman, N. Marzari, U. Nitzsche, L. Nordström, T. Ozaki, L. Paulatto, C. J. Pickard, W. Poelmans, M. I. J. Probert, K. Refson, M. Richter, G.-M. Rignanese, S. Saha, M. Scheffler, M. Schlipf, K. Schwarz, S. Sharma, F. Tavazza, P. Thunström, A. Tkatchenko, M. Torrent, D. Vanderbilt, M. J. van Setten, V. Van Speybroeck, J. M. Wills, J. R. Yates, G.-X. Zhang and S. Cottenier, *Science*, 2016, **351**, 1415.
68 G. Kresse, M. Marsman and J. Furthmüller, *VASP the GUIDE, Computational Materials Physics*, Faculty of Physics, Universität Wien.
69 P. Vinet, J. Ferrante, J. H. Rose and J. R. Smith, *J. Geophys. Res.: Solid Earth*, 1987, **92**, 9319–9325.
70 M. Leslie and N. J. Gillan, *J. Phys. C: Solid State Phys.*, 1985, **18**, 973.
71 C. Freysoldt, B. Grabowski, T. Hickel, J. Neugebauer, G. Kresse, A. Janotti and C. G. Van de Walle, *Rev. Mod. Phys.*, 2014, **86**, 253–305.
72 S. Ping Ong, W. Davidson Richards, A. Jain, G. Hautier, M. Kocher, S. Cholia, D. Gunter, V. L. Chevrier, K. A. Persson and G. Ceder, *Comput. Mater. Sci.*, 2013, **68**, 314–319.
73 S. Ling and B. Slater, *J. Phys. Chem. C*, 2015, **119**, 16667–16677.
74 M. A. Nasalevich, M. van der Veen, F. Kapteijn and J. Gascon, *CrystEngComm*, 2014, **16**, 4919–4926.
75 A. Karmakar, A. Kumar, A. K. Chaudhari, P. Samanta, A. V. Desai, R. Krishna and S. K. Ghosh, *Chem.–Eur. J.*, 2016, **22**, 4931–4937.
76 K. Sakaushi and M. Antonietti, *Acc. Chem. Res.*, 2015, **48**, 1591–1600.

Paper IV

Optical Properties of Isolated and Covalent Organic Framework-Embedded Ruthenium Complexes

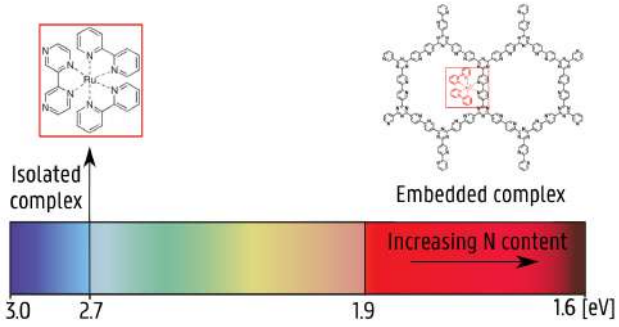

F. Muniz-Miranda, L. De Bruecker, A. De Vos,
F. Vanden Bussche, C. V. Stevens, P. Van Der Voort,
K. Lejaeghere and V. Van Speybroeck

The Journal of Physical Chemistry A, **2019**, *123*, 6854–6867

A. De Vos performed simulations on both periodic and cluster models and had a large contribution in the interpretation of the results as well as the preparation of the manuscript.

THE JOURNAL OF PHYSICAL CHEMISTRY A
Cite This: J. Phys. Chem. A XXXX, XXX, XXX–XXX
Article
pubs.acs.org/JPCA

Optical Properties of Isolated and Covalent Organic Framework-Embedded Ruthenium Complexes

Published as part of The Journal of Physical Chemistry virtual special issue "Leo Radom Festschrift".

Francesco Muniz-Miranda,[†,⊥,∥] Liesbeth De Bruecker,[†,∥] Arthur De Vos,[†] Flore Vanden Bussche,[‡,§] Christian V. Stevens,[‡] Pascal Van Der Voort,[§] Kurt Lejaeghere,*[,†] and Veronique Van Speybroeck*[,†]

[†]Center for Molecular Modeling (CMM), Ghent University, Technologiepark 46, 9052 Zwijnaarde, Belgium

[‡]Research Group SynBioC, Department of Green Chemistry and Technology, Faculty of Bioscience Engineering, Ghent University, Campus Coupure, Coupure Links 653 bl. B, 9000 Gent, Belgium

[§]Center for Ordered Materials, Organometallics and Catalysis (COMOC), Department of Inorganic and Physical Chemistry, Ghent University, Krijgslaan 281 (S3), 9000 Gent, Belgium

Supporting Information

ABSTRACT: Heterogenization of RuL_3 complexes on a support with proper anchor points provides a route toward design of green catalysts. In this paper, Ru(II) polypyridyl complexes are investigated with the aim to unravel the influence on the photocatalytic properties of varying nitrogen content in the ligands and of embedding the complex in a triazine-based covalent organic framework. To provide fundamental insight into the electronic mechanisms underlying this behavior, a computational study is performed. Both the ground and excited state properties of isolated and anchored ruthenium complexes are theoretically investigated by means of density functional theory and time-dependent density functional theory. Varying the ligands among 2,2′-bipyridine, 2,2′-bipyrimidine, and 2,2′-bipyrazine allows us to tune to a certain extent the optical gaps and the metal to ligand charge transfer excitations. Heterogenization of the complex within a CTF support has a significant effect on the nature and energy of the electronic transitions. The allowed transitions are significantly red-shifted toward the near IR region and involve transitions from states localized on the CTF toward ligands attached to the ruthenium. The study shows how variations in ligands and anchoring on proper supports allows us to increase the range of wavelengths that may be exploited for photocatalysis.

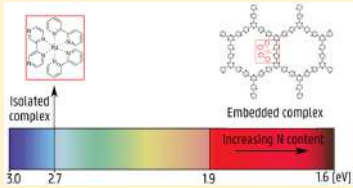

1. INTRODUCTION

Catalysis is of paramount relevance to many chemical reactions that could not occur within a reasonable time otherwise, thus disrupting either their industrial use[1] or biological functionality.[2] In the case of photocatalysis, the activation is effected by visible photons. This enables the synthesis of chemical products exploiting an easily available source of energy in mild reaction conditions, as often even the light emitted by a household bulb can be enough. Furthermore, control of the light exposure allows photocatalysis to be fine-tuned and even stopped at will, creating the ability to obtain a high degree of chemoselectivity.[3,4] However, in the attempt to design new green catalytic routes, there is a high interest in developing recyclable and reusable heterogeneous photocatalytic systems.[5−8] One way to achieve this goal is the anchoring of homogeneous complexes with photocatalytic properties on a heterogeneous stable support. This procedure is applicable in case the photocatalytic properties of the pristine complex are retained or improved in the heterogenized system. To this end, a deep knowledge is required of both electronic and excited state properties of the pristine homogeneous and anchored complex within the support. Such investigation is presented in this paper for $Ru(II)L_3$ complexes, which are commonly applied visible light photocatalysts consisting of a Ru^{2+} ion that is octahedrally chelated by three bidentate polypyridyl ligands as shown in Figure 1, parts a and b. Herein the electronic properties of such isolated and anchored ruthenium polypyridyl complexes onto a stable heterogeneous support are investigated.

Complexes of the type $Ru(2,2'\text{-bipyrdine})_3^{2+}$ are among the most interesting photoredox catalyzers. They show no catalytic properties in their ground state, but when exposed to light, their excited electronic states are able to oxidize or reduce substrate molecules through single-electron transfer (SET) processes.[10] They have proven their usefulness allowing very different reactions such as carbon dioxide reduction,[11,12] solar

Received: May 31, 2019
Revised: July 19, 2019
Published: July 19, 2019

DOI: 10.1021/acs.jpca.9b05216
J. Phys. Chem. A XXXX, XXX, XXX–XXX

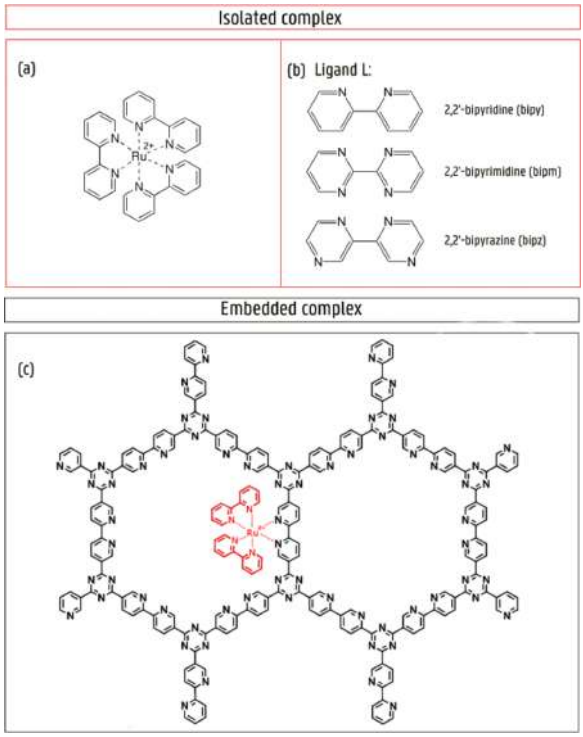

Figure 1. (a): Schematic representation of the isolated $Ru(bipy)_3^{2+}$ complex. (b): Polypyridyl ligands: *cis*-2,2′-bipyridine (bipy), 2,2′-bipyrimidine (bipm), and *cis*-2,2′-bipyrazine (bipz) considered in this study. (c) Part of the CTF synthesized in ref 9 and used as computational model here, in black. The anchored RuL_2^{2+} fragment inside one pore is shown in red.

cells development,[13,14] water splitting,[15−17] as well as Diels−Alder cycloadditions,[18,19] and can be used as a photosensitizer,[20] thus spanning both inorganic and organic reactions and acting as either reducing or oxidizing agents.[3,21−25]

The two possible relaxation mechanisms of the excited states of the Ru(II) cation are schematically shown in Scheme 1, which sketches the orbital occupancy of the frontier electron states of the ruthenium complex. The t_{2g} and e_g states originate from the octahedrally surrounded Ru(II) cation, while orbitals from the ligands are situated in between. In the ground state, depicted on the left, only the t_{2g} states are filled and ruthenium is in the Ru(II) state. By absorption of a photon in the visible region a singlet → singlet metal-to-ligand charge transfer (MLCT) excitation occurs, leaving an electron hole in the metal states. As such, the oxidation number of ruthenium increases by one. The singlet excited state can quickly convert to a lower-energy triplet excited state via nonradiative means. This mechanism is called intersystem crossing (ISC). In a recent theoretical study the decay from the singlet to triplet states was shown to occur with a time constant of 26 ± 3 fs, which was in very good agreement with experimental data. To this end a newly implemented combination of linear response time-dependent density functional theory (TD-DFT) with surface-hopping including arbitrary couplings (SHARC) was employed for the first time to model the relaxation dynamics of $Ru(bipyridine)_3^{2+}$ after light irradiation with explicit nonadiabatic and spin−orbit couplings.[26] The resulting excited state, shown in the red box in Scheme 1, is long-lived, as the decay to the singlet ground state is spin-forbidden.

The photoexcited state can then relax either by reduction of an organic substrate, maintaining an oxidized Ru(III) cation (upper arrow in Scheme 1), or by reduction of the complex via transfer of an electron from the substrate to the now vacant t_{2g} orbital of the Ru(III) cation, which then reverts to Ru(II) (lower arrow in Scheme 1).

The triplet excited state of $Ru(2,2'\text{-bipyridine})_3^{2+}$ may thus be engaged in an electron transfer process, but it may also be involved in a process called triplet−triplet energy transfer (TTET), in which the decay from the excited $Ru(2,2'\text{-bipyridine})_3^{2+}$ from its triplet to ground state involves the excitation of another molecule from its ground singlet state to its lowest triplet state. This mechanism requires the excitation of both the catalyst and substrate to a spin-triplet state and has been the subject of both theoretical[27] and application-oriented investigations.[28] The $Ru(2,2'\text{-bipyridine})_3^{2+}$ has been exploited in a number of C−C making and breaking transformations, such as trans/cis stilbene isomerization,[29] anthracene dimeri-

DOI: 10.1021/acs.jpca.9b05216
J. Phys. Chem. A XXXX, XXX, XXX−XXX

The Journal of Physical Chemistry A Article

Scheme 1. Photoactivation of an Octahedral Ruthenium Complex from the Ground State (Left Black Box) to an Excited State (Red Box) under the Influence of Visible Light, Exciting an Electron toward a State Localized on the Ligands, followed by ISC[a]

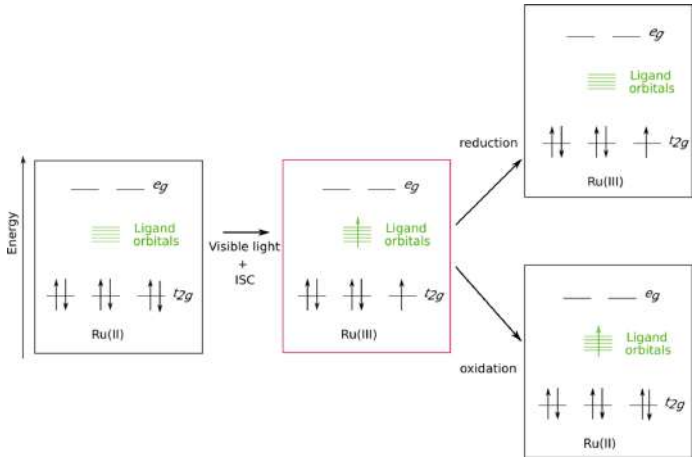

[a]The excited state relaxes by reduction (upper arrow) or oxidation (lower arrow) of the substrate. Schematic adapted from ref 3. Copyright 2013 American Chemical Society.

zation,[30] cycloadditions,[31] and trifluoromethylations of styrene substrates[32] via the TTET mechanism.

Herein we investigate the photocatalytic properties of $Ru(II)L_3$ type complexes, where the ligands may either be *cis*-2,2′-bipyridine (bipy), 2,2′-bipyrimidine (bipm), or *cis*-2,2′-bipyrazine (bipz) as schematically shown in Figure 1b. Complexes with a varying number of nitrogen containing aromatic rings have been synthesized both in the literature[33−35] and in this work. In the first instance, we investigate to what extent the nitrogen content affects the photocatalytic properties. Second, the impact of heterogenizing the $Ru(II)L_3$ complexes on covalent triazine frameworks (CTFs) (see Figure 1c), which are a subclass of the broader family of covalent organic frameworks (COFs), are assessed.[36] Unfunctionalized COFs have been explored within catalysis to some extent,[6,37−39] but additional functionalization of the materials with metal complexes may open additional perspectives for their usage within catalysis by merging some of the most important features of both the organic, i.e., stability, and the inorganic, i.e., catalytic properties, worlds.

CTFs are potentially interesting supports since they are chemically and thermally stable.[40−46] Furthermore, they are much lighter than most other porous supports and contain no toxic or environmentally unfriendly elements. These porous 2D materials are made by ionothermal trimerization of aromatic nitriles and when fabricated with bidentate nitrogen containing ligands—similar to the chelating ligands in the ruthenium homogeneous complex—they may serve as ideal anchoring materials for the latter complexes.[47] The first reports on COFs containing (bi)pyridine have appeared recently, showing great promise for applications in catalysis and gas sorption.[9,48−54] In a similar way, this has already been applied for metal organic frameworks (MOFs),[55] where photocatalytic complexes were successfully anchored to both linkers[56,57] and nodes.[58] However, MOFs are in general less stable, making it interesting to explore other heterogeneous supports.[59−61]

To optimize the photocatalytic system, a thorough understanding of the ground- and excited-state properties of the tethered RuL_3^{2+} complexes is mandatory.[62] Ground state properties of the heterogeneous system have been studied in detail in our previous work,[63] whereas in this work, we focus on the calculation of excited states. The investigation of the distribution of most singlet states can be performed experimentally by UV−vis absorption spectroscopy. Contrarily, triplet states are more difficult to characterize without a computational investigation due to electronic selection rules preventing singlet → triplet excitations to achieve a significant oscillator strength, i.e., probability of occurrence. In order to understand how the CTF support impacts the photocatalytic properties of the ruthenium complexes, a stepwise computational analysis is adopted. The ground- and excited-state electronic properties of both the isolated ruthenium complexes and the anchored systems are investigated by means of density functional theory (DFT) and time-dependent density functional theory (TD-DFT).

To this end, we embed RuL_2^{2+} (represented in red in Figure 1c) into an extensive CTF structure model (represented in black in Figure 1c).[9] This CTF organic scaffold contains bipyridine groups belonging to the CTF exposed inside the pores, which are suitable to act as linkers for the ruthenium complex, thus giving rise to a RuL_2^{2+}@CTF compound. The results are analyzed to obtain insight into the electronic charge rearrangement and optical gap tuning induced by the ligands. For the isolated ruthenium complexes, we are able to compare and validate the calculated optical properties with experimentally measured UV−vis absorption data. However, specifically investigating the excitations of COFs by means of UV−vis absorption spectroscopy is cumbersome as these

DOI: 10.1021/acs.jpca.9b05216
J. Phys. Chem. A XXXX, XXX, XXX−XXX

compounds often absorb light in a wide wavelength region, in part due their high flexibility. In addition, photoemission spectroscopy may yield results difficult to interpret without some theoretical understanding. In this light the current computational approach gives new insights into the excited state properties of the RuL_2^{2+}@CTF system, which in turn affect its photocatalytic properties. While TD-DFT calculations have been performed on COFs before,[64] to our knowledge this is one of the first applications on a COF model to which a photoactive complex has been anchored.

2. COMPUTATIONAL DETAILS

All calculations were performed with the Gaussian 16 software.[65] Ground state information was extracted at the DFT level. Excited states were investigated adopting the TD-DFT scheme,[66] within the linear-response approach due to Casida.[67]

2.1. Assessment of the Level of Theory for the Ground States. Four different exchange-correlation functionals coming from different rungs on Jacob's ladder[68] were tested on isolated RuL_3^{2+} complexes to compare their relaxed structures: the generalized gradient approximation PBE,[69] hybrid B3LYP,[70,71] long-range corrected CAM-B3LYP,[72] and metahybrid M06.[73] All computed internal normal modes of the relaxed structures show positive frequencies, ensuring that the optimized geometries represent minima of the ground state potential energy surface.

The average differences in bond lengths calculated with the various functionals and basis sets are below the 0.05 Å threshold. The optimized structures for $Ru(bipy)_3^{2+}$ are included in section S4 of the Supporting Information. All levels of theory employed here predict a positive partial Hirshfeld charge on the Ru(II) cations, with differences between the same complexes of about 0.02 $|e|$, with e the electron charge (see Table S1 of the Supporting Information).

2.2. Assessment of the Level of Theory for the Excited States. The vertical excitation spectra from the ground state geometry of $Ru(bipy)_3^{2+}$, obtained by TD-DFT,[67,74] are shown in Figure 2. Theoretical calculations were carried out both in the gas phase, i.e., without solvent, and with water and acetonitrile solvents modeled with the polarizable continuum method (PCM) to take into account the effect of the environment on the excitation energies.[75] The simulated UV−vis absorption spectra at the TD-DFT level of theory are compared with the experimental optical profiles for $Ru(bipy)_3^{2+}$ complexes in water[76] and acetonitrile solvents. The latter experimental data were generated within the framework of this work (vide infra for details on the experimental part). A side note is warranted on how to compare the theoretical and experimental data. The TD-DFT energy of the first allowed transition is an approximation of the optical gap, which is defined by a neutral excitation and as the difference between the energies of the lowest dipole-allowed excited state and the ground state.[77] As it accounts for the electron−hole recombination energy or exciton binding energy, the optical gap is systematically lower than the fundamental gap,[78] defined by a charged excitation and as the difference between the first ionization potential and the first electron affinity.[77] From UV−vis absorption measurements, optical gaps can be extrapolated as the energy of the first divergence of the spectrum from its baseline.

The spectrum calculated with the M06 functional yields the best agreement with experimental data with respect to those

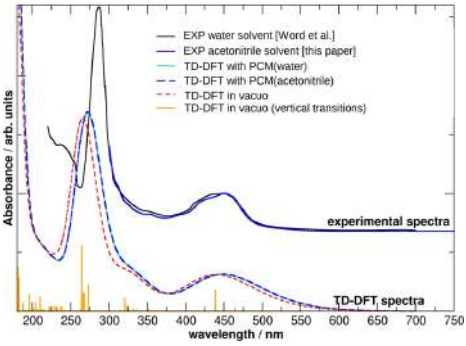

Figure 2. Experimental UV−vis absorption (top, Word et al.[76] and this paper) and TD M06 spectra (bottom) of $Ru(bipy)_3^{2+}$. Vertical excitations for the in vacuo TD M06 spectrum are reported as orange spikes. Computed spectra have been smoothed using Gaussian functions of half-width at half-height of 0.333 eV (default value of Gaussview). The computed spectra have not been rescaled nor shifted.

computed with PBE, B3LYP, and CAM-B3LYP (see Figure S1 of the Supporting Information) in terms of both shapes and positions of the bands, and no further rescaling of energies nor of wavelengths—as often employed for similar comparisons when pseudopotentials are used to simulate core electrons in metal atoms—were necessary.[79] As expected,[80,81] TD PBE spectra obtained by using a semilocal functional without Hartree−Fock exchange necessitated significant blueshifts to match the experimental data. Contrarily, TD CAM-B3LYP spectra required a significant redshift, in agreement with earlier studies on compounds ranging from metal−organic frameworks (MOFs)[82] to noble metal nanoclusters.[80] TD B3LYP spectra are rather similar to TD M06 spectra in frequencies, but the agreement regarding the shape of the absorption bands is better when using the M06 functional. As the M06/LanL2DZ level of theory correctly reproduces the optical features of the studied complexes, we have consistently used this level of theory unless otherwise stated. Errors between the various tested functionals are always smaller than 20 nm (see Figure S1 of the Supporting Information). We used the LanL2DZ[83] basis as it has been shown that the choice of basis set has a minimal influence on excitation energies, oscillator strengths, and assignments for transition metal complexes.[84] Tests with the Def2TZVPP basis set reveal a difference for the energy of the strongest transition of only 11 nm. Overall, M06 performs particularly well in systematic reviews of both organic and inorganic molecules,[85,86] yielding accurate transition energies.

Our conclusions are in agreement with ref[87] in which several functionals were tested for a few ruthenium complexes, including $Ru(bipy)_3^{2+}$. Besides the excitation energies, for which hybrid functionals and their range-separated and meta counterparts are the most accurate, Atkins et al. focused on the energy gaps between excited states, which tend to be best described by the pure generalized gradient approximation exchange-correlation functionals.[87] Since we are in this work interested in excitation energies, this confirms our choice for the M06 functional.

DOI: 10.1021/acs.jpca.9b05216
J. Phys. Chem. A XXXX, XXX, XXX−XXX

The Journal of Physical Chemistry A Article

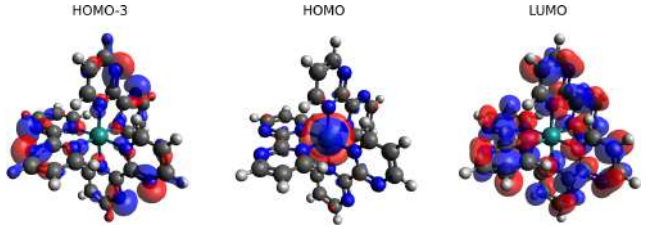

Figure 3. Isosurfaces of the HOMO−3, HOMO, and LUMO of the $Ru(bipm)_3^{2+}$ compound (complex g in Figure 4). Calculation carried out at the M06/LanL2DZ level of theory.

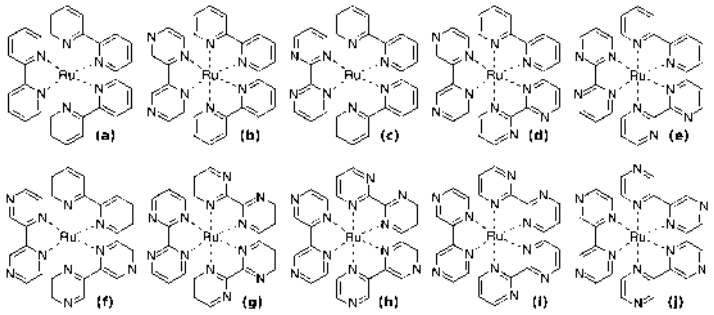

Figure 4. Ten RuL_3^{2+} complexes investigated here. (a) L = bipy × 3; (b) L = bipy × 2, bipz × 1; (c) L = bipy × 2, bipm × 1; (d) L = bipy × 1, bipz × 1, bipm × 1; (e) L = bipy × 1, bipm × 2; (f) L = bipy × 1, bipz × 2; (g) L = bipm × 3; (h) L = bipz × 2, bipm × 1; (i) L = bipz × 1, bipm × 2; (j) L = bipz × 3.

The overall shape of the spectrum is due to the many transitions from the singlet ground state to singlet excited states ($S_0 \rightarrow S_n$; n = 1, ...), which are spin-allowed. The effect of the solvent seems very modest, both from an experimental and a computational point of view. In addition, the effect of PCM with respect to the calculation in vacuo (dashed red line in Figure 2) is negligible for the first strong absorption band centered at about ∼450 nm (∼2.75 eV) and is rather small for the second peak located between 300 and 200 nm, i.e., in the UV region, with discrepancies smaller than 10 nm.

2.3. Optimization of the Ru(II)@CTF Models. To investigate the influence of embedding the ruthenium complexes within a CTF support, a Ru(II)@CTF model was constructed as schematically shown in Figure 1c. A CTF composed of triazine nodes interlinked with bipy linkers was considered. The bipy residues embedded into the CTF can naturally act as ligands for the ruthenium complexes, together with two other ligands that remain exposed inside the pore of the CTF.

The investigated model consists of two full CTF pores to minimize "edge effects" due to the sudden truncation of our cluster model (see Figure 1c). The cluster was terminated by completing the coordination of carbon atoms with hydrogen atoms. During the geometry optimization, the structures were allowed to relax freely and they converged to approximately planar structures, with small differences due to the different types of ligands.

Because the models including the COFs are very large (10 triazine and 34 pyridine rings, see Figure 1c), geometry optimizations of the models including the COFs were carried out with a step-by-step approach. First, the COFs were optimized using a small basis set (e.g., LanL1DZ). Second, the system was reoptimized with the addition of the Ru(II) cation and the two other ligands at the same level of theory. Finally, the total system was reoptimized at the M06/LanL2DZ level of theory within Gaussian 16 standard convergence criteria.

3. EXPERIMENTAL DETAILS

The UV−Vis absorption spectrum was collected using a Shimadzu UV1800 UV−vis spectrometer. The sample was prepared by dissolving 1 mg of $Ru(bipy)_3(PF_6)_2$ (Sigma-Aldrich) in 1.5 mL acetonitrile (Sigma-Aldrich, used without further purification). The solution was filtered through a 0.45 μm Whatman syringe filter and placed in a 1 cm × 1 cm cuvette. Further dilution of the sample was performed to obtain the desired absorbance range.

4. RESULTS AND DISCUSSION

4.1. Ground State Properties of Isolated Complexes. The three ligands investigated here all maintain a largely planar geometry when coordinating with a Ru(II) cation; the dihedral angles linking the two aromatic subunits are less than 1.5°. However, they contain a different number of nitrogen atoms (2 in bipy and 4 in bipm and bipz as shown in Figure 1b). Frontier orbitals of the ruthenium complexes may be sensitive to the nitrogen content of the ligands and their different aromaticity. In Figure 3, the HOMO and LUMO of $Ru(bipm)_3^{2+}$ are displayed, showing a general trend for this class of complexes. The HOMO, which is a nonbonding (n)

DOI: 10.1021/acs.jpca.9b05216
J. Phys. Chem. A XXXX, XXX, XXX−XXX

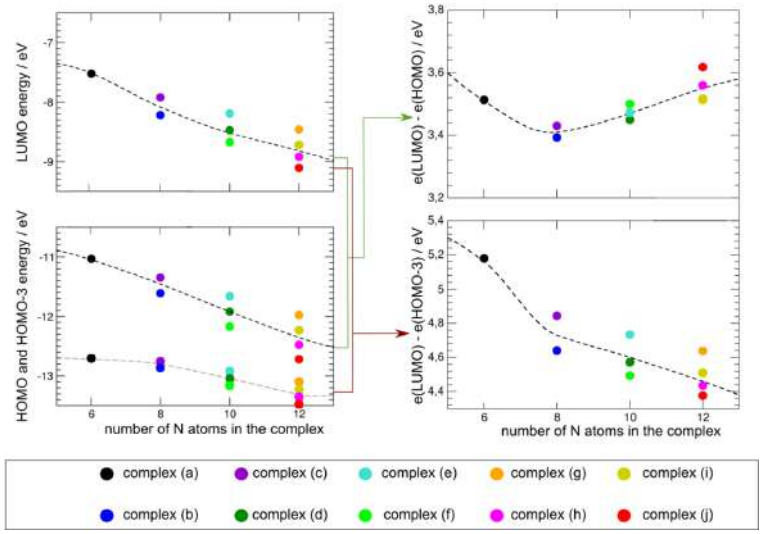

Figure 5. Energies of LUMOs (top left panel), HOMOs and HOMOs-3 (bottom left panel). Energy differences between HOMOs and LUMOs (top right panel) and HOMOs-3 and LUMOs (bottom right panel). The ten RuL_3^{2+} complexes are (a) L = bipy × 3; (b) L = bipy × 2, bipz × 1; (c) L = bipy × 2, bipm × 1; (d) L = bipy × 1, bipz × 1, bipm × 1; (e) L = bipy × 1, bipm × 2; (f) L = bipy × 1, bipz × 2; (g) L = bipm × 3; (h) L = bipz × 2, bipm × 1; (i) L = bipz × 1, bipm × 2; and (j) L = bipz × 3. Calculation carried out at the M06/LanL2DZ level of theory.

orbital, is mainly localized on the central Ru(II) cation, thus largely coinciding with a t_{2g} orbital, whereas the LUMO, which is a π^* orbital, is localized on the ligands. In addition, also the HOMO−3 orbital is visualized as it is the first occupied orbital below the HOMO, which is mainly localized on the ligands. In contrast, the HOMO−1 and HOMO−2 orbitals are mainly of the t_{2g} type (see Figure S2 of the Supporting Information).

It is now interesting to investigate to what extent the nitrogen content in the ligands affects their orbital energies. Various complexes were considered as schematically shown in Figure 4. For each of these complexes the energies of the HOMO, LUMO, and HOMO−3 in terms of the number of nitrogen atoms are plotted in Figure 5. The energies of both frontier orbitals decrease by ∼1 eV by going from the $Ru(bipy)_3^{2+}$ complex, containing only 6 nitrogen atoms (black circles), to complexes with only bipz and bipm ligands (red, pink, yellow, and orange circles), which contain 12 nitrogen atoms instead. The simultaneous decrease in energy for both types of orbitals results in a rather flat profile by about 0.2 eV for the HOMO−LUMO gaps. Nevertheless, a small minimum at $N = 8$ atoms can be discerned, a recurring feature in many energy gap profiles of these complexes as will be shown later.

While the HOMO−LUMO gap seems largely unaffected by the ligands, the energy gap between orbitals mainly localized on the ligands shows a different behavior. The contribution of the nitrogen atoms is small in the HOMO−3 orbital, as can be seen in the expansion in atomic contributions of the wave function (Table S2 in Supporting Information). As a result, the energy of the HOMO−3 is only slightly affected by the increase in number of nitrogen atoms from 6 to 12 (Figure 5 bottom left panel). Then, as expected, the energy gap between the LUMO and HOMO−3, which is indicative for ligand−ligand transitions, decreases with the number of nitrogen atoms in the complexes, as shown in the bottom right panel of Figure 4. These conclusions are in agreement with our previous work on the ground state properties of RuL_3^{2+}.[62] Thus, the energy difference between the HOMO−3 and LUMO can be considered as a sort of effective "ligand gap", i.e., an energy gap between states mainly localized on the organic rings. Even if this gap shows significant internal variations for a fixed number of nitrogen atoms in the complex, it seems to be more clearly dependent on the nitrogen content than the HOMO−LUMO gap, as it spans a full 1 eV range (see Figure 5, right panels).

Further clarification for the previous findings can be found by inspecting the electronic density of states (eDoS) for $Ru(bipy)_3^{2+}$ (see Figure 6). It confirms that the major contributions of ruthenium around the band gap are found on the HOMO, HOMO−1, and HOMO−2.

Such an analysis was also performed for the different complexes having a varying degree of nitrogen content. The eDoSs are superimposed in the left pane of Figure 7, showing that the nitrogen content actually affects all the eigenvalues of the systems. With an increasing number of nitrogen atoms in the ligands we observe decreasing energies; i.e., the distribution is shifted to the left side of the plot, as indicated by the colored arrow. The contributions of the eDoS originating from ruthenium, while mainly localized on the HOMOs and on virtual states which are about 5 eV higher in energy than the LUMOs (see Figure 6), are still affected by the number of nitrogen atoms in the complexes, as shown in the right pane of Figure 7.

The organic ligands investigated here are all heteroaromatic compounds and the degree of aromaticity might play a role to

DOI: 10.1021/acs.jpca.9b05216
J. Phys. Chem. A XXXX, XXX, XXX−XXX

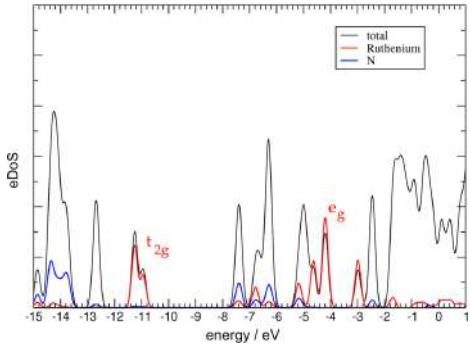

Figure 6. eDoS of $Ru(bipy)_3^{2+}$ complex, with contributions due to the Ru(II) cation and the N atoms colored in red and blue, respectively. Calculation carried out at the M06/LanL2DZ level of theory. The zero is set at the calculated ionization energy.

elucidate the observed trends for the energy levels in terms of the nitrogen content. Aromaticity is usually considered as a particular stabilization of the occupied states localized on aromatic rings with respect to the virtual states. This property can be quantified using a number of different scales and indexes. Herein we used the aromaticity index of Bird,[88,89] which is based on the resonance stabilization energy. The latter property is smaller for pyrimidine (40.6 kcal/mol) and pyrazine (40.9 kcal/mol) than for pyridine (43.3 kcal/mol).[88] This fact can be qualitatively understood in terms of electron content because adding more nitrogen atoms, with additional electron pairs that do not participate in delocalized π orbitals, decreases the overall stabilization. We notice that the energy difference between the HOMO−3 and LUMO has some correlation with Bird's aromatic stabilization energy, as shown in Figure S3 of the Supporting Information. However, we have not found any clear correlation between the HOMO−LUMO gap and the aromaticity index of Bird.[88,89] This is reasonable since this gap is strongly affected by ruthenium, which is not taken into account by this aromaticity descriptor. We also investigated the correlation with some other aromaticity indices. More information can be found in section S2.1 and Figure S4 of the Supporting Information.

In order to effectively catalyze redox reactions, ruthenium has to possess a net charge. The partial charges obtained with both the Hirshfeld and Mulliken partition schemes of the ten complexes are reported in Table S3 of the Supporting Information. As can be seen, the Ru(II) cation is consistently positive, but a correlation with the number of nitrogen atoms or aromatic descriptors is not evident, because the differences are rather small, being of the order of 0.02 |e|. As expected, the Hirshfeld charges are in absolute values smaller than the Mulliken charges.[90]

In conclusion from the ground state properties of the isolated $Ru(L)_3^{2+}$, it is observed that the HOMO−LUMO gap—approximately describing the MLCT—remains nearly unaffected by the number of nitrogen atoms, whereas the HOMO−3-LUMO gap—approximately describing the ligand−ligand gap—is reduced for a higher number of nitrogen atoms.

4.2. Excited States Properties of Isolated Complexes. The photoredox and charge-transfer properties are strongly affected by the optical properties of the complexes, in particular by their absorption and emission of UV−vis radiation. First, we discuss the singlet and triplet excitations in the visible-light range which are mainly of the MLCT type, as stated before. Afterward, we focus on the triplet metal-centered states. The triplet excitations are spin-forbidden but play an important role in TTET. The energy of the first spin-allowed transition, i.e., the energy of the first singlet state (S_1), approximates the optical gap, as discussed previously. From our TD-DFT calculations we determine how it changes with the nitrogen content of the complexes. The results are shown in the upper panel of Figure 8.

The complex showing the lowest S_1 energy contains eight nitrogen atoms and is composed of two bipy ligands and one bipz (blue dot, complex b), whereas the complex with the highest energy is $Ru(bipz)_3^{2+}$ (red dot, complex j), with a difference of about 0.4 eV. A similar distribution of values,

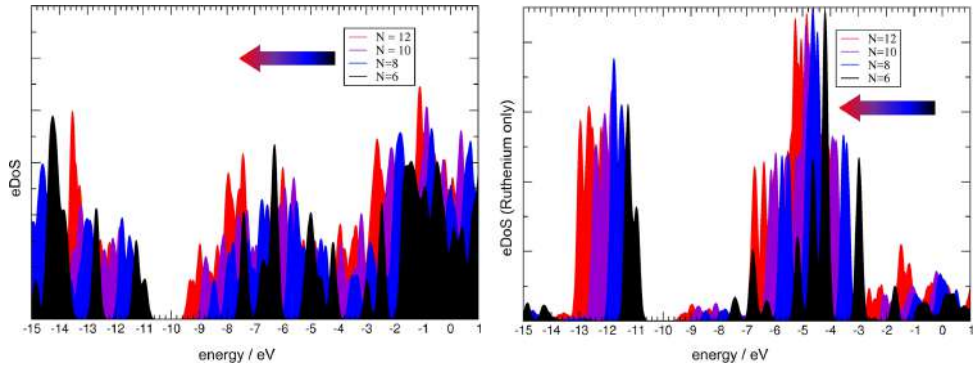

Figure 7. Total eDoS (left) and contribution localized on ruthenium (right) of the ten complexes investigated here, sorted by color according to the number of N atoms in the ligands (N = 6, 8, 10, and 12). The eDoS are superimposed. Calculations have been carried out at the M06/LanL2DZ level of theory.

DOI: 10.1021/acs.jpca.9b05216
J. Phys. Chem. A XXXX, XXX, XXX−XXX

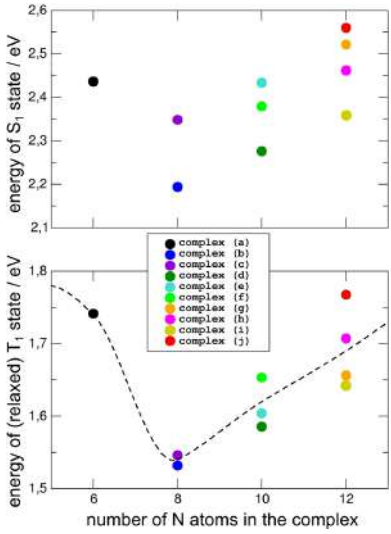

Figure 8. Vertical TD-M06 energies of the S_1 states (upper panel) and of the optimized T_1 states (lower panel). The ten RuL_3^{2+} complexes are (a) L = bipy × 3; (b) L = bipy × 2, bipz × 1; (c) L = bipy × 2, bipm × 1; (d) L = bipy × 1, bipz × 1, bipm × 1; (e) L = bipy × 1, bipm × 2; (f) L = bipy × 1, bipz × 2; (g) L = bipm × 3; (h) L = bipz × 2, bipm × 1; (i) L = bipz × 1, bipm × 2; and (j) L = bipz × 3 according to the nomclature introduced in Figure 4. Calculation carried out at the M06/LanL2DZ level of theory.

albeit with different magnitudes, can be observed for the most intense transitions of the visible spectra, occurring between 3 and 2.7 eV, at ∼430 nm as can be seen in Figure S5 of the Supporting Information. All excitation energies and their corresponding oscillator strengths are given in Table S4 of the Supporting Information.

Although the experimental absorption spectrum is mainly due to vertical excitations, adhering to the Franck−Condon principle, we also examined to which extent the geometries of the excited MLCT S_1 and S_2 states change when we optimize them. These states correspond to adiabatic, i.e., nonvertical, excitations and may be observed in fluorescence measurements. We find that their relaxed excited-state geometries are very similar to those of their respective ground states (see Figure S6 (left pane) Supporting Information). Moreover, the overall effect of geometry optimization on the excitation energies is a shift toward lower values, which is rather constant, i.e., between 0.43 and 0.66 eV for the ten RuL_3^{2+} complexes (Table S4 and S5 of the Supporting Information). For $Ru(bipy)_3^{2+}$ the S_1 energy for the relaxed geometry becomes 2.00 eV (compared with 2.45 eV when the geometry of the excited state is not optimized), corresponding to a wavelength of 618.7 nm. This is in good agreement with a fluorescence emission occurring at 615 nm.[91,92]

Nested between the $S_0 \rightarrow S_n$ transitions, there are spin-forbidden MLCT transitions to triplet states (T_n), whose contributions to the absorption spectra are negligible. However, these T_n states play a role in TTET and can still be encountered during nonradiative processes and decays which require a relaxation of the geometry. They therefore have to be taken into account to describe the electronic structures of complexes with emerging catalytic properties.[93,94] The adiabatic transition energies of the first triplet states closely follow the trend of the S_1 ones (Figure 8, bottom panel), albeit with a smaller overall variation (∼0.3 eV instead of 0.4 eV) and at lower energies. However, they still pinpoint $Ru(bipy)_2(bipz)^{2+}$ as the complex with the smallest transition energy (N = 8). As expected, the distributions of T_1 and S_1 excitation energies versus the number of nitrogen atoms also follow a pattern very similar to that of the HOMO−LUMO gaps (see Figure 5).

Transitions toward T_1, T_2, and T_3 states are all of the MLCT type. In the case of the $Ru(bipy)_3^{2+}$, $Ru(bipz)_3^{2+}$, and $Ru(bipm)_3^{2+}$ complexes, i.e., those with three equal ligands, the corresponding vertical transitions are basically degenerate as the energy difference is below the 0.02 eV threshold. This degeneracy is removed when a ligand is substituted with one of a different type, as shown in Figure S7 of the Supporting Information for the case of $Ru(bipy)_3^{2+}$. By a subsequent exchange of ligands, the T_1−T_2−T_3 energy separation increases from less than 0.02 eV to more than 0.2 eV. In addition, the triplet transitions whose degeneracy is broken by passing from RuL_3^{2+} to a $Ru(L)_2L'^{2+}$ complex (with L and L′ two different ligands), do not involve charge transfer to both L′ and L, but to only one ligand, either L′ or L.[63]

At energies higher than the triplet MLCT states, triplet states centered on ruthenium can be found, which are called metal-centered states (^{3}MC).[95] These states are found at ∼3.3 eV in the vertical excitations, which qualitatively agrees with what has been observed for the ground state eDoS (see Figure 7), showing contributions due to Ru(II) cations at energies higher than 3 eV above the LUMO.

While singlet and triplet MLCT states have a relaxed geometry close to that of the ground state, relaxed ^{3}MC states show more significant distortions: there is a loss of coplanarity between the two rings of the ligands, with dihedral angles between the two aromatic subunits of more than 7° (see Figure S6 (right pane) of the Supporting Information). This suggests that intersections with nearby excited states may occur, potentially leading to ISC phenomena.

Even if these triplet states are centered on the metal, they involve an increase in the positive Hirshfeld partial charge on the Ru(II) ion with respect to the ground state, as shown in Figure S8 of the Supporting Information. This can be explained as ^{3}MC states are thought to be predissociation states,[91,96−98] thus leaving a higher excess positive charge on the Ru(II) cation. While this latter increment is small in absolute value, in cases with a high content of nitrogen atoms, it represents an increase of about 40% in the overall positive charge on the cation, potentially changing the energetics of intermediate and transition states during catalytic processes going via the TTET mechanism.

4.3. Ground State Properties of Complexes Embedded into a COF. In second instance we investigate how the electronic properties of the ruthenium complexes are affected by embedding them into a CTF support. The CTF is composed of triazine nodes interlinked with bipy linkers and the bipy residues embedded into the CTF can naturally act as ligands for the ruthenium complexes. The fact that the ligand embedded into the CTF is bipy has also the effect of reducing the number of possible ligand combinations in the RuL_2^{2+}@

DOI: 10.1021/acs.jpca.9b05216
J. Phys. Chem. A XXXX, XXX, XXX−XXX

The Journal of Physical Chemistry A Article

Scheme 2. Schematic Representation of Orbital Energies for the Ground State of $Ru(bipy)_2^{2+}$@CTF (Left Pane) and $Ru(L)_2^{2+}$@CTF with 10 Nitrogen Atoms (Right Pane), Indicating the Proposed Change of Orbital Energies Due to an Increase of Nitrogen Content from 6 to 10 Atoms in the Ligands[a]

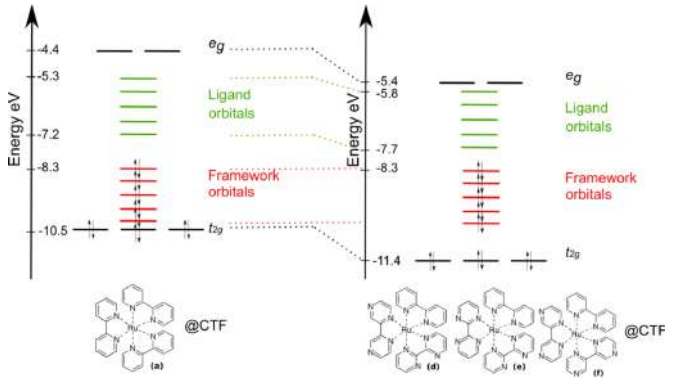

[a]The energy levels in the right pane correspond to $Ru(bipz)_2^{2+}$@CTF and $Ru(bipzbipm)^{2+}$@CTF. Calculations are at the M06 level of theory.

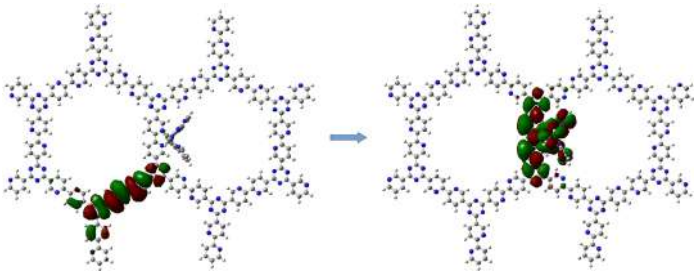

Figure 9. Orbitals involved in the first allowed transition in $Ru(bipy)_2^{2+}$@CTF complex. Calculation carried out at the M06/LanL2DZ level of theory.

CTF complex with respect to the isolated complexes from 10 to 6, i.e., complexes a–f in Figure 4.

We observe some significant electronic changes with respect to the isolated ruthenium complexes discussed before. In particular, occupied framework states are found between the states localized on the metal and on the ligands, as schematically shown in Scheme 2. This conclusion is in agreement with previous ground state calculations of RuL_2^{2+}@CTF.[63] According to the molecular orbital composition, the occupied t_{2g} and virtual e_g d orbitals of the Ru(II) cation remain separated in energy by ~6 eV for the $Ru(bipy)_2^{2+}$@CTF, which is close to the energy separation observed in the eDOS of the isolated complex (see Figure 6). However, in the Ru@CTF system, there are occupied framework states between the occupied orbitals of ruthenium and the virtual orbitals on the ligands, lowering the HOMO–LUMO gaps substantially by about 2.5–2.8 eV compared to the isolated complexes.

Furthermore, we also investigate the influence of the nitrogen content on the electronic states of the system. The nitrogen content has a clear influence on the electronic states of the system, as schematically shown in the right pane of Scheme 2. An increased nitrogen content from 6 to 10 atoms reduces the energy of t_{2g} and e_g orbitals by about 1 eV with respect to $Ru(bipy)_2^{2+}$@CTF, the shift for $Ru(bipm)_2^{2+}$@CTF is somewhat smaller, i.e. 0.6 eV. Instead the energy of the framework orbitals (~8.3 eV) is rather unaffected. The virtual orbitals of the ligands are decreasing with about 0.5 eV, thus bringing the energy gap between HOMO and LUMO to values of the order of 0.6–0.8 eV for nitrogen rich compounds such as $Ru(bipz)_2^{2+}$@CTF, $Ru(bipm)_2^{2+}$@CTF, and $Ru(bipzbipm)^{2+}$@CTF. The exact numerical values for the HOMO–LUMO gaps of the CTF-embedded complexes are reported in Table S6 of the Supporting Information.

4.4. Excited States Properties of Complexes Embedded into a COF. In CTF-embedded complexes, we notice that the orbital character of the first allowed TD M06 excitation, i.e., the first excitation with nonvanishing oscillator strength, is no longer mainly of the MLCT type as was the case for isolated complexes. Instead, we observe a charge transfer from states localized on the organic framework toward states localized on the complex, as shown in Figure 9. The target orbital is mainly localized on the bipyridine ligand of the CTF and only marginally on the ligands exposed inside the pore.

DOI: 10.1021/acs.jpca.9b05216
J. Phys. Chem. A XXXX, XXX, XXX–XXX

These orbitals are the LUMOs in case of $Ru(bipy)_2^{2+}$@CTF. It may be possible that if the pore ligands should have a higher nitrogen content, the target orbital would be situated on them instead, as ground state calculations on similar periodic systems suggest.[63]

The first allowed transition in RuL_2^{2+}@CTF is thus of the crystal to crystal charge transfer (CCCT) or crystal to ligand charge transfer (CLCT) type. In the work of De Vos et al., where periodic ground state electronic structures were performed on the ruthenium complexes in CTF frameworks, it was indeed suggested that excitations of the highest occupied crystal orbital to the linkers or ligands attached to the ruthenium ion might be interesting, but it could not be deduced whether those states would be realistic as they are spatially relatively far separated. Here we find based on excited state calculations that these transitions are indeed realistic as they have a nonvanishing oscillator strength. A list of all excitation energies and their corresponding oscillator strengths is given in Table S7 in the Supporting Information.

Changing the nitrogen content of the ligands connected to ruthenium and pointing into the pores of the material, induces a significant drop in the vertical excitation energy of the most intense transition, with values as low as 1.6 eV for an increasing number of nitrogen atoms in the ligands around ruthenium (see Figure 10). So, while in isolated complexes the excitation energy of the strongest transition is in the UV/blue visible region, the gap falls into the orange-near-infrared (NIR) region when the complex is included into the CTF (see Figure 11). Furthermore, it has to be emphasized that this effect is specific to this metal complex@CTF adduct, as the optical gap of the CTF model alone (i.e., without any anchored ruthenium complex) is ∼3.32 eV, which is close to the near-UV range of energies instead.

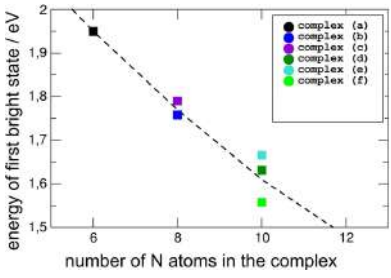

Figure 10. Change of the strongest excitation energy with the number of N atoms in the ligands around the Ru(II) cation in RuL_2^{2+}@CTF. The six RuL_2^{2+}@CTF complexes are (a) L = bipy × 2; (b) L = bipy × 1, bipz × 1; (c) L = bipy × 1, bipm × 1; (d) L = bipz × 1, bipm × 1; (e) L = bipm × 2; (f) L = bipz × 2. Calculation carried out at the M06/LanL2DZ level of theory.

While in isolated complexes the change of the excitation energy of the strongest transition with the number of nitrogen atoms of the ligands was small and nonmonotonous, a clear decrease of the excitation energy with the nitrogen content is observed in the embedded complexes (see Figure 10). This is due to the fact that the HOMO is no longer localized on the ruthenium but on the CTF, whereas the target virtual orbital is mainly localized on the ligands of the ruthenium complex.

These results show that the hybrid RuL_2^{2+}@CTF system offers an extra degree of versatility in tuning the electronic response of the photocatalyst. By tuning the nitrogen content of the anchoring linkers pointing into the pore of the RuL_2^{2+}@CTF system, the optical gap can be reduced by about 0.5 eV and the direction of the charge transfer can be designed. A schematic representation of the excitation energies corresponding to the strongest transition in both isolated, embedded ruthenium complex and isolated CTF is shown in Figure 11 together with an indication on how these excitations would be influenced by the nitrogen content.

As it is known that TD-DFT might fail to correctly reproduce charge-transfer excitations,[99] it is important to corroborate the above interpretation with ground state considerations. We notice here that the predicted TD M06 optical gaps shown in Figure 10 are in qualitative agreement with those of the occupied framework orbitals/virtual ligand orbitals described in Scheme 2 calculated with ground state M06 calculations. Furthermore, the trend with the nitrogen content is similar. Moreover, to further assess the reliability of the previous M06 ground state considerations, we have employed the range-separated CAM-B3LYP exchange correlation functional (which is often considered better suited to describe charge-transfer phenomena[100]) to compute Kohn–Sham gaps in the isolated and CTF-embedded complexes. In this case, the gap between the occupied framework orbitals and virtual ligand orbitals calculated at the CAM-B3LYP level of theory is about 1.9–1.7 eV smaller than the HOMO–LUMO gap in isolated complexes, which is in qualitative agreement with the aforementioned M06 results. With CAM-B3LYP, however, all the absolute energies are significantly blueshifted. This seems reasonable, as range-separated hybrid functionals are outperformed by global hybrid functionals for n → π* transitions.[64] To further investigate the nature of this transition, we have used the Mulliken averaged configuration (M_{AC}) index of Ciofini and co-workers that is able to spot ghost states which appear by significantly underestimating the energy.[101] This diagnostic index, which discerns unrealistic charge transfer produced by the limitations of the level of theory, is a generalization of the Mulliken estimation of

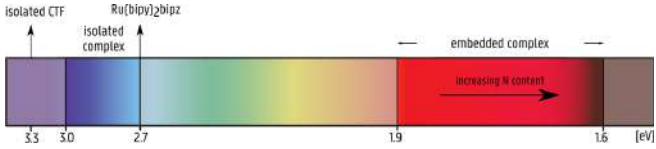

Figure 11. Schematic representation of the strongest singlet excitation energies of the isolated and embedded complexes. The lowest excitation energy for the isolated complex is found for $Ru(bipy)_2bipz$ at ∼2.7 eV. For the embedded complexes the excitation energy decreases for an increasing number of nitrogen atoms. The energy of the first transition with nonzero oscillator strength of the empty CTF is also indicated.

DOI: 10.1021/acs.jpca.9b05216
J. Phys. Chem. A XXXX, XXX, XXX–XXX

transition energy for charge transfer excitations. With it we were able to confirm the charge transfer character of the transition; it is not a ghost state as the transition energy is larger than the M_{AC} index. From this, we are ensured that our TD-DFT results are reliable.

5. CONCLUSIONS

In this work, we have investigated how polypyridyl ligands, characterized by a varying nitrogen content and aromaticity, can affect the photocatalytic properties of ruthenium-based complexes of the type RuL_3^{2+} in both the ground and the excited states. As those complexes can be exploited either as oxidant or reductant agents in photochemical reactions, this overall insight into their energetics allows a choice for the most appropriate compound for the specific task at hand. Studying triplet states with computational approaches is necessary to optimize catalytic conditions for reactions going through triplet−triplet energy transfer (TTET), since investigating nonsinglet states by means of UV−vis absorption is often unpractical.

In second instance, we studied how the heterogenization of the ruthenium complexes on a CTF support consisting of bipyridine ligands affects the electronic ground and excited state properties of the RuL_2^{2+}@CFT system.

For the isolated RuL_3^{2+}, an increase in the number of nitrogen atoms in the ligands redshifts the overall energetics of the compound, albeit without significantly altering the HOMO−LUMO gap. The energy gaps between linker−linker states, on the other hand, are significantly affected by both aromaticity and nitrogen content of the ligands. Singlet metal-to-ligand charge transfer (MLCT) excitations are found between 2.2 and 2.6 eV for complexes within varying nitrogen content. They are only slightly affected by changing the ligands. Triplet metal-to-ligand charge transfer (MLCT) excitations are situated in the 1.5−1.8 eV range and can to a certain extent be tuned for a range of applications that require specific activation energies. One particular complex, $Ru(bipy)_2(bipz)^{2+}$, shows a redshift of both singlet and ^{3}MLCT triplet excited states, making it an interesting candidate for processes induced by visible light. Changes induced in higher-energy triplet metal-centered (MC) states moreover deplete the electronic density around the Ru(II) cation, increasing its positive charge and, thus, its oxidant power.

For the complex embedded into a bipyridine-composed CTF, we observe a significant redshift of the allowed excitations to energies bordering the near IR region of the spectrum. This allows harvesting these lower energies to promote charge-transfer excitations. For example, near-infrared photocatalysis[102,103] could greatly benefit from the nanoporous environment and thus make better use of the near-infrared solar irradiation (making up 44% of solar irradiation spectrum) to reduce the ruthenium active site. Furthermore, the first allowed transition occurs from orbitals localized on the framework toward orbitals mainly localized on the ruthenium complex.

Overall, this investigation indicates how optoelectronic properties of ruthenium complexes can be changed and, possibly, tuned by the ligands and heterogenization within a CTF environment. Furthermore, this means that, potentially, a larger spectrum of radiation can be harvested to activate the complex. In the future, this kind of investigation could also be extended to other nitrogen containing aromatic ligands and transition metals, e.g., iridium, to further develop these promising platforms for heterogeneous photocatalysis.

■ ASSOCIATED CONTENT

Supporting Information

The Supporting Information is available free of charge on the ACS Publications website at DOI: 10.1021/acs.jpca.9b05216.

Charges, spectra and optimized structures of $Ru(bipy)_3^{2+}$ across different functionals; ground state orbital isosurfaces of $Ru(bipm)_3^{2+}$; atomic contributions and energies of $Ru(bipy)_3^{2+}$; influence of polypyridyl aromaticity on the electronic levels; comparison of charge schemes; excitation energies and oscillator strengths of isolated and embedded Ru(II) polypyridyl complexes; influence of excited-state optimization; removal of triplet state degeneracy; and Ru charge in metal-centered states (PDF)

■ AUTHOR INFORMATION

Corresponding Authors

*(K.L.) E-mail: kurt.lejaeghere@ugent.be.

*(V.V.S.) E-mail: Veronique.VanSpeybroeck@UGent.be.

ORCID

Arthur De Vos: 0000-0002-4916-6066

Christian V. Stevens: 0000-0003-4393-5327

Pascal Van Der Voort: 0000-0002-4874-0943

Kurt Lejaeghere: 0000-0002-4462-8209

Veronique Van Speybroeck: 0000-0003-2206-178X

Present Address

[⊥]Chimie ParisTech, PSL Research University, CNRS, Institute of Chemistry for Life and Health Sciences (i-CLeHS), FRE 2027, F-75005 Paris, France

Author Contributions

[‖]These authors contributed equally

Notes

The authors declare no competing financial interest.

■ ACKNOWLEDGMENTS

The authors acknowledge the Fund for Scientific Research Flanders (FWO) and the Research Board of Ghent University (BOF) through a Concerted Research Action (GOA) for funding. V.V.S. and L.D.B. acknowledge funding from the European Union's Horizon 2020 research and innovation program (consolidator ERC Grant Agreement No. 647755 − DYNPOR (2015-2020)). The computational resources and services used in this work were provided by VSC (Flemish Supercomputer Center), funded by Ghent University, FWO, and the Flemish Government Department EWI.

■ REFERENCES

(1) Armor, J. N. A History of Industrial Catalysis. *Catal. Today* **2011**, *163*, 3−9.

(2) Editorial. Closing in on Catalysis. *Nat. Chem. Biol.* **2009**, *5*, 515−515.

(3) Prier, C. K.; Rankic, D. A.; MacMillan, D. W. C. Visible Light Photoredox Catalysis with Transition Metal Complexes: Applications in Organic Synthesis. *Chem. Rev.* **2013**, *113*, 5322−5363.

(4) Kärkäs, M. D.; Porco, J. A.; Stephenson, C. R. J. Photochemical Approaches to Complex Chemotypes: Applications in Natural Product Synthesis. *Chem. Rev.* **2016**, *116*, 9683−9747.

(5) Slater, A. G.; Cooper, A. I. Porous Materials. Function-Led Design of New Porous Materials. *Science* **2015**, *348*, aaa8075.

DOI: 10.1021/acs.jpca.9b05216
J. Phys. Chem. A XXXX, XXX, XXX−XXX

(6) Rogge, S. M. J.; Bavykina, A.; Hajek, J.; Garcia, H.; Olivos-Suarez, A. I.; Sepúlveda-Escribano, A.; Vimont, A.; Clet, G.; Bazin, P.; Kapteijn, F.; et al. Metal−Organic and Covalent Organic Frameworks as Single-Site Catalysts. *Chem. Soc. Rev.* **2017**, *46*, 3134−3184.
(7) Takeda, H.; Ohashi, M.; Goto, Y.; Ohsuna, T.; Tani, T.; Inagaki, S. A Versatile Solid Photosensitizer: Periodic Mesoporous Organosilicas with Ruthenium Tris(Bipyridine) Complexes Embedded in the Pore Walls. *Adv. Funct. Mater.* **2016**, *26*, 5068−5077.
(8) Tu, W.; Xu, Y.; Yin, S.; Xu, R. Rational Design of Catalytic Centers in Crystalline Frameworks. *Adv. Mater.* **2018**, *30*, 1707582.
(9) Hug, S.; Tauchert, M. E.; Li, S.; Pachmayr, U. E.; Lotsch, B. V. A Functional Triazine Framework Based on N-Heterocyclic Building Blocks. *J. Mater. Chem.* **2012**, *22*, 13956−13964.
(10) Hedstrand, D.; Kruizinga, W.; Kellogg, R. Light-Induced and Dye Accelerated Reductions of Phenacyl Onium Salts by 1,4-Dihydropyridines. *Tetrahedron Lett.* **1978**, *19*, 1255−1258.
(11) Takeda, H.; Ishitani, O. Development of Efficient Photocatalytic Systems for CO_2 Reduction Using Mononuclear and Multinuclear Metal Complexes Based on Mechanistic Studies. *Coord. Chem. Rev.* **2010**, *254*, 346−354.
(12) Sekizawa, K.; Sato, S.; Arai, T.; Morikawa, T. Solar-Driven Photocatalytic CO_2 Reduction in Water Utilizing a Ruthenium Complex Catalyst on p-Type Fe_2O_3 with a Multiheterojunction. *ACS Catal.* **2018**, *8*, 1405−1416.
(13) Gao, F.; Wang, Y.; Zhang, J.; Shi, D.; Wang, M.; Humphry-Baker, R.; Wang, P.; Zakeeruddin, S. M.; Grätzel, M. A New Heteroleptic Ruthenium Sensitizer Enhances the Absorptivity of Mesoporous Titania Film for a High Efficiency Dye-Sensitized Solar Cell. *Chem. Commun.* **2008**, 2635−2637.
(14) Kamata, R.; Kumagai, H.; Yamazaki, Y.; Sahara, G.; Ishitani, O. Photoelectrochemical CO_2 Reduction Using a Ru(II)-Re(I) Supramolecular Photocatalyst Connected to a Vinyl Polymer on a NiO Electrode. *ACS Appl. Mater. Interfaces* **2019**, *11*, 5632−5641.
(15) Concepcion, J. J.; Jurss, J. W.; Templeton, J. L.; Meyer, T. J. One Site Is Enough. Catalytic Water Oxidation by $[Ru(Tpy)(Bpm)(OH_2)]^{2+}$ and $[Ru(Tpy)(Bpz)(OH_2)]^{2+}$. *J. Am. Chem. Soc.* **2008**, *130*, 16462−16463.
(16) Kaveevivitchai, N.; Chitta, R.; Zong, R.; El Ojaimi, M.; Thummel, R. P. A Molecular Light-Driven Water Oxidation Catalyst. *J. Am. Chem. Soc.* **2012**, *134*, 10721−10724.
(17) Gil-Sepulcre, M.; Böhler, M.; Schilling, M.; Bozoglian, F.; Bachmann, C.; Scherrer, D.; Fox, T.; Spingler, B.; Gimbert-Suriñach, C.; Alberto, R.; et al. Ruthenium Water Oxidation Catalysts Based on Pentapyridyl Ligands. *ChemSusChem* **2017**, *10*, 4517−4525.
(18) Lin, S.; Ischay, M. A.; Fry, C. G.; Yoon, T. P. Radical Cation Diels−Alder Cycloadditions by Visible Light Photocatalysis. *J. Am. Chem. Soc.* **2011**, *133*, 19350−19353.
(19) Matsui, K.; Shibuya, M.; Yamamoto, Y. Synthesis of Pyrroles via Ruthenium-Catalyzed Nitrogen-Transfer [2 + 2 + 1] Cycloaddition of α,ω-Diynes Using Sulfoximines as Nitrene Surrogates. *Commun. Chem.* **2018**, *1*, 21.
(20) Karges, J.; Heinemann, F.; Maschietto, F.; Patra, M.; Blacque, O.; Ciofini, I.; Spingler, B.; Gasser, G. A Ru(II) Polypyridyl Complex Bearing Aldehyde Functions as a Versatile Synthetic Precursor for Long-Wavelength Absorbing Photodynamic Therapy Photosensitizers. *Bioorg. Med. Chem.* **2019**, *27*, 2666−2675.
(21) Ghizdavu, L.; Pierard, F.; Rickling, S.; Aury, S.; Surin, M.; Beljonne, D.; Lazzaroni, R.; Murat, P.; Defrancq, E.; Moucheron, C.; et al. Oxidizing Ru(II) Complexes as Irreversible and Specific Photo-Cross-Linking Agents of Oligonucleotide Duplexes. *Inorg. Chem.* **2009**, *48*, 10988−10994.
(22) Kalyanasundaram, K. Photophysics, Photochemistry and Solar Energy Conversion with Tris(Bipyridyl)Ruthenium(II) and Its Analogues. *Coord. Chem. Rev.* **1982**, *46*, 159−244.
(23) Estalayo-Adrián, S.; Garnir, K.; Moucheron, C. Perspectives of Ruthenium(Ii) Polyazaaromatic Photo-Oxidizing Complexes Photoreactive towards Tryptophan-Containing Peptides and Derivatives. *Chem. Commun.* **2018**, *54*, 322−337.
(24) Kulkarni, M. S.; Kumbhar, A. S.; Mohan, H.; Rao, B. S. M. Synthesis, Characterization and Redox Chemistry of Ru(II) Complexes of N-Methyl Pyridyl Quinoxaline. *Dalton Trans.* **2009**, 6185−6191.
(25) Nakada, A.; Koike, K.; Nakashima, T.; Morimoto, T.; Ishitani, O. Photocatalytic CO_2 Reduction to Formic Acid Using a Ru(II)−Re(I) Supramolecular Complex in an Aqueous Solution. *Inorg. Chem.* **2015**, *54*, 1800−1807.
(26) Atkins, A. J.; González, L. Trajectory Surface-Hopping Dynamics Including Intersystem Crossing in $[Ru(Bpy)_3]^{2+}$. *J. Phys. Chem. Lett.* **2017**, *8*, 3840−3845.
(27) Olivares-Amaya, R.; Hu, W.; Nakatani, N.; Sharma, S.; Yang, J.; Chan, G. K.-L. The Ab-Initio Density Matrix Renormalization Group in Practice. *J. Chem. Phys.* **2015**, *142*, 034102.
(28) Ho, J.; Kish, E.; Méndez-Hernández, D. D.; WongCarter, K.; Pillai, S.; Kodis, G.; Niklas, J.; Poluektov, O. G.; Gust, D.; Moore, T. A.; et al. Triplet-Triplet Energy Transfer in Artificial and Natural Photosynthetic Antennas. *Proc. Natl. Acad. Sci. U. S. A.* **2017**, *114*, E5513−E5521.
(29) Wrighton, M.; Markham, J. Quenching of the Luminescent State of Tris(2,2′-Bipyridine)Ruthenium(II) by Electronic Energy Transfer. *J. Phys. Chem.* **1973**, *77*, 3042−3044.
(30) Islangulov, R. R.; Castellano, F. N. Photochemical Upconversion: Anthracene Dimerization Sensitized to Visible Light by a Ru^{II} Chromophore. *Angew. Chem., Int. Ed.* **2006**, *45*, 5957−5959.
(31) Lu, Z.; Yoon, T. P. Visible Light Photocatalysis of [2 + 2] Styrene Cycloadditions via Energy Transfer. *Angew. Chem., Int. Ed.* **2012**, *51*, 10329−10332.
(32) Lin, Q.-Y.; Xu, X.-H.; Qing, F.-L. Chemo-, Regio-, and Stereoselective Trifluoromethylation of Styrenes via Visible Light-Driven Single-Electron Transfer (SET) and Triplet-Triplet Energy Transfer (TTET) Processes. *J. Org. Chem.* **2014**, *79*, 10434−10446.
(33) Strouse, G. F.; Anderson, P. A.; Schoonover, J. R.; Meyer, T. J.; Keene, F. R. Synthesis of Polypyridyl Complexes of Ruthenium(II) Containing Three Different Bidentate Ligands. *Inorg. Chem.* **1992**, *31*, 3004−3006.
(34) Kubeil, M.; Vernooij, R. R.; Kubeil, C.; Wood, B. R.; Graham, B.; Stephan, H.; Spiccia, L. Studies of Carbon Monoxide Release from Ruthenium(II) Bipyridine Carbonyl Complexes upon UV-Light Exposure. *Inorg. Chem.* **2017**, *56*, 5941−5952.
(35) Myahkostupov, M.; Castellano, F. N. Synthesis and Characterization of Tris(Heteroleptic) Ru(II) Complexes Bearing Styryl Subunits. *Inorg. Chem.* **2011**, *50*, 9714−9727.
(36) Gonçalves, R. S. B.; de Oliveira, A. B. V.; Sindra, H. C.; Archanjo, B. S.; Mendoza, M. E.; Carneiro, L. S. A.; Buarque, C. D.; Esteves, P. M. Heterogeneous Catalysis by Covalent Organic Frameworks (COF): Pd(OAc)2@COF-300 in Cross-Coupling Reactions. *ChemCatChem* **2016**, *8*, 743−750.
(37) Vyas, V. S.; Haase, F.; Stegbauer, L.; Savasci, G.; Podjaski, F.; Ochsenfeld, C.; Lotsch, B. V. A Tunable Azine Covalent Organic Framework Platform for Visible Light-Induced Hydrogen Generation. *Nat. Commun.* **2015**, *6*, 8508.
(38) Stegbauer, L.; Schwinghammer, K.; Lotsch, B. V. A Hydrazone-Based Covalent Organic Framework for Photocatalytic Hydrogen Production. *Chem. Sci.* **2014**, *5*, 2789−2793.
(39) Banerjee, T.; Lotsch, B. V. The Wetter the Better. *Nat. Chem.* **2018**, *10*, 1175−1177.
(40) Ding, S.-Y.; Wang, W. Covalent Organic Frameworks (COFs): From Design to Applications. *Chem. Soc. Rev.* **2013**, *42*, 548−568.
(41) Kuhn, P.; Antonietti, M.; Thomas, A. Porous, Covalent Triazine-Based Frameworks Prepared by Ionothermal Synthesis. *Angew. Chem., Int. Ed.* **2008**, *47*, 3450−3453.
(42) Feng, X.; Ding, X.; Jiang, D. Covalent Organic Frameworks. *Chem. Soc. Rev.* **2012**, *41*, 6010−6022.
(43) Stewart, D.; Antypov, D.; Dyer, M. S.; Pitcher, M. J.; Katsoulidis, A. P.; Chater, P. A.; Blanc, F.; Rosseinsky, M. J. Stable and Ordered Amide Frameworks Synthesised under Reversible Conditions Which Facilitate Error Checking. *Nat. Commun.* **2017**, *8*, 1102.

DOI: 10.1021/acs.jpca.9b05216
J. Phys. Chem. A XXXX, XXX, XXX−XXX

(44) Halder, A.; Karak, S.; Addicoat, M.; Bera, S.; Chakraborty, A.; Kunjattu, S. H.; Pachfule, P.; Heine, T.; Banerjee, R. Ultrastable Imine-Based Covalent Organic Frameworks for Sulfuric Acid Recovery: An Effect of Interlayer Hydrogen Bonding. *Angew. Chem., Int. Ed.* **2018**, *57*, 5797−5802.
(45) Ding, S.-Y.; Gao, J.; Wang, Q.; Zhang, Y.; Song, W.-G.; Su, C.-Y.; Wang, W. Construction of Covalent Organic Framework for Catalysis: Pd/COF-LZU1 in Suzuki-Miyaura Coupling Reaction. *J. Am. Chem. Soc.* **2011**, *133*, 19816−19822.
(46) Waller, P. J.; Gándara, F.; Yaghi, O. M. Chemistry of Covalent Organic Frameworks. *Acc. Chem. Res.* **2015**, *48*, 3053−3063.
(47) Liu, M.; Guo, L.; Jin, S.; Tan, B. Covalent Triazine Frameworks: Synthesis and Applications. *J. Mater. Chem. A* **2019**, *7*, 5153−5172.
(48) Hug, S.; Stegbauer, L.; Oh, H.; Hirscher, M.; Lotsch, B. V. Nitrogen-Rich Covalent Triazine Frameworks as High-Performance Platforms for Selective Carbon Capture and Storage. *Chem. Mater.* **2015**, *27*, 8001−8010.
(49) Park, K.; Gunasekar, G. H.; Prakash, N.; Jung, K.-D.; Yoon, S. A Highly Efficient Heterogenized Iridium Complex for the Catalytic Hydrogenation of Carbon Dioxide to Formate. *ChemSusChem* **2015**, *8*, 3410−3413.
(50) Tahir, N.; Muniz-Miranda, F.; Everaert, J.; Tack, P.; Heugebaert, T.; Leus, K.; Vincze, L.; Stevens, C.; Van Speybroeck, V.; Van Der Voort, P. Immobilization of Ir(I) Complex on Covalent Triazine Frameworks for CAH Borylation Reactions: A Combined Experimental and Computational Study. *J. Catal.* **2019**, *371*, 135−143.
(51) Johnson, E. M.; Haiges, R.; Marinescu, S. C. Covalent-Organic Frameworks Composed of Rhenium Bipyridine and Metal Porphyrins: Designing Heterobimetallic Frameworks with Two Distinct Metal Sites. *ACS Appl. Mater. Interfaces* **2018**, *10*, 37919−37927.
(52) Aiyappa, H. B.; Thote, J.; Shinde, D. B.; Banerjee, R.; Kurungot, S. Cobalt-Modified Covalent Organic Framework as a Robust Water Oxidation Electrocatalyst. *Chem. Mater.* **2016**, *28*, 4375−4379.
(53) Popov, D. A.; Luna, J. M.; Orchanian, N. M.; Haiges, R.; Downes, C. A.; Marinescu, S. C. A 2,2′-Bipyridine-Containing Covalent Organic Framework Bearing Rhenium(i) Tricarbonyl Moieties for CO_2 Reduction. *Dalton Trans. Camb. Engl. 2003* **2018**, *47*, 17450−17460.
(54) Gunasekar, G. H.; Park, K.; Jeong, H.; Jung, K.-D.; Park, K.; Yoon, S. Molecular Rh(III) and Ir(III) Catalysts Immobilized on Bipyridine-Based Covalent Triazine Frameworks for the Hydrogenation of CO_2 to Formate. *Catalysts* **2018**, *8*, 295.
(55) Hendon, C. H.; Bonnefoy, J.; Quadrelli, E. A.; Canivet, J.; Chambers, M. B.; Rousse, G.; Walsh, A.; Fontecave, M.; Mellot-Draznieks, C. A Simple and Non-Destructive Method for Assessing the Incorporation of Bipyridine Dicarboxylates as Linkers within Metal-Organic Frameworks. *Chem. - Eur. J.* **2016**, *22*, 3713−3718.
(56) Maza, W. A.; Morris, A. J. Photophysical Characterization of a Ruthenium(II) Tris(2,2′-Bipyridine)-Doped Zirconium UiO-67 Metal−Organic Framework. *J. Phys. Chem. C* **2014**, *118*, 8803−8817.
(57) Hou, C.-C.; Li, T.-T.; Cao, S.; Chen, Y.; Fu, W.-F. Incorporation of a $[Ru(Dcbpy)(Bpy)_2]^{2+}$ Photosensitizer and a $Pt(Dcbpy)Cl_2$ Catalyst into Metal−Organic Frameworks for Photocatalytic Hydrogen Evolution from Aqueous Solution. *J. Mater. Chem. A* **2015**, *3*, 10386−10394.
(58) Yang, D.; Odoh, S. O.; Wang, T. C.; Farha, O. K.; Hupp, J. T.; Cramer, C. J.; Gagliardi, L.; Gates, B. C. Metal-Organic Framework Nodes as Nearly Ideal Supports for Molecular Catalysts: NU-1000- and UiO-66-Supported Iridium Complexes. *J. Am. Chem. Soc.* **2015**, *137*, 7391−7396.
(59) Wang, C.; Xie, Z.; deKrafft, K. E.; Lin, W. Doping Metal−Organic Frameworks for Water Oxidation, Carbon Dioxide Reduction, and Organic Photocatalysis. *J. Am. Chem. Soc.* **2011**, *133*, 13445−13454.
(60) Burtch, N. C.; Jasuja, H.; Walton, K. S. Water Stability and Adsorption in Metal-Organic Frameworks. *Chem. Rev.* **2014**, *114*, 10575−10612.
(61) Leus, K.; Bogaerts, T.; De Decker, J.; Depauw, H.; Hendrickx, K.; Vrielinck, H.; Van Speybroeck, V.; Van Der Voort, P. Systematic Study of the Chemical and Hydrothermal Stability of Selected "Stable" Metal Organic Frameworks. *Microporous Mesoporous Mater.* **2016**, *226*, 110−116.
(62) Daniel, C. Photochemistry and Photophysics of Transition Metal Complexes: Quantum Chemistry. *Coord. Chem. Rev.* **2015**, *282*−*283*, 19−32.
(63) De Vos, A.; Lejaeghere, K.; Muniz-Miranda, F.; Stevens, C. V.; Van der Voort, P.; Van Speybroeck, V. Electronic Properties of Heterogenized Ru(II) Polypyridyl Photoredox Complexes on Covalent Triazine Frameworks. *J. Mater. Chem. A* **2019**, *7*, 8433−8442.
(64) Jacquemin, D.; Perpète, E. A.; Vydrov, O. A.; Scuseria, G. E.; Adamo, C. Assessment of Long-Range Corrected Functionals Performance for n→pi* Transitions in Organic Dyes. *J. Chem. Phys.* **2007**, *127*, 094102.
(65) Frisch, M. J.; Trucks, G. W.; Schlegel, H. B.; Scuseria, G. E.; Robb, M. A.; Cheeseman, J. R.; Scalmani, G.; Barone, V.; Petersson, G. A.; Nakatsuj, H.; et al. *Gaussian 16*, Revision B.01; Gaussian, Inc.: Wallingford, CT, 2016.
(66) Runge, E.; Gross, E. K. U. Density-Functional Theory for Time-Dependent Systems. *Phys. Rev. Lett.* **1984**, *52*, 997−1000.
(67) Casida, M. E.; Jamorski, C.; Casida, K. C.; Salahub, D. R. Molecular Excitation Energies to High-Lying Bound States from Time-Dependent Density-Functional Response Theory: Characterization and Correction of the Time-Dependent Local Density Approximation Ionization Threshold. *J. Chem. Phys.* **1998**, *108*, 4439−4449.
(68) Perdew, J. P.; Ruzsinszky, A.; Tao, J.; Staroverov, V. N.; Scuseria, G. E.; Csonka, G. I. Prescription for the Design and Selection of Density Functional Approximations: More Constraint Satisfaction with Fewer Fits. *J. Chem. Phys.* **2005**, *123*, 062201.
(69) Perdew, J. P.; Burke, K.; Ernzerhof, M. Generalized Gradient Approximation Made Simple. *Phys. Rev. Lett.* **1996**, *77*, 3865−3868.
(70) Lee, C.; Yang, W.; Parr, R. G. Development of the Colle-Salvetti Correlation-Energy Formula into a Functional of the Electron Density. *Phys. Rev. B: Condens. Matter Mater. Phys.* **1988**, *37*, 785−789.
(71) Becke, A. D. Density-functional Thermochemistry. III. The Role of Exact Exchange. *J. Chem. Phys.* **1993**, *98*, 5648−5652.
(72) Yanai, T.; Tew, D. P.; Handy, N. C. A New Hybrid Exchange−Correlation Functional Using the Coulomb-Attenuating Method (CAM-B3LYP). *Chem. Phys. Lett.* **2004**, *393*, 51−57.
(73) Zhao, Y.; Truhlar, D. G. The M06 Suite of Density Functionals for Main Group Thermochemistry, Thermochemical Kinetics, Noncovalent Interactions, Excited States, and Transition Elements: Two New Functionals and Systematic Testing of Four M06-Class Functionals and 12 Other Functionals. *Theor. Chem. Acc.* **2008**, *120*, 215−241.
(74) Adamo, C.; Jacquemin, D. The Calculations of Excited-State Properties with Time-Dependent Density Functional Theory. *Chem. Soc. Rev.* **2013**, *42*, 845−856.
(75) Tomasi, J.; Mennucci, B.; Cammi, R. Quantum Mechanical Continuum Solvation Models. *Chem. Rev.* **2005**, *105*, 2999−3094.
(76) Word, T. A.; Whittington, C. L.; Karolak, A.; Kemp, M. T.; Woodcock, H. L.; van der Vaart, A.; Larsen, R. W. Photoacoustic Calorimetry Study of Ligand Photorelease from the Ru(II)Bis(2,2′-Bipyridine)(6,6′-Dimethyl-2,2′-Bipyridine) Complex in Aqueous Solution. *Chem. Phys. Lett.* **2015**, *619*, 214−218.
(77) Baerends, E. J.; Gritsenko, O. V.; van Meer, R. The Kohn−Sham Gap, the Fundamental Gap and the Optical Gap: The Physical Meaning of Occupied and Virtual Kohn−Sham Orbital Energies. *Phys. Chem. Chem. Phys.* **2013**, *15*, 16408−16425.
(78) Kronik, L.; Stein, T.; Refaely-Abramson, S.; Baer, R. Excitation Gaps of Finite-Sized Systems from Optimally Tuned Range-Separated Hybrid Functionals. *J. Chem. Theory Comput.* **2012**, *8*, 1515−1531.
(79) Muniz-Miranda, F.; Menziani, M. C.; Pedone, A. DFT and TD-DFT Assessment of the Structural and Optoelectronic Properties of

DOI: 10.1021/acs.jpca.9b05216
J. Phys. Chem. A XXXX, XXX, XXX−XXX

an Organic−Ag_{14} Nanocluster. *J. Phys. Chem. A* **2015**, *119*, 5088−5098.
(80) Muniz-Miranda, F.; Menziani, M. C.; Pedone, A. Assessment of Exchange-Correlation Functionals in Reproducing the Structure and Optical Gap of Organic-Protected Gold Nanoclusters. *J. Phys. Chem. C* **2014**, *118*, 7532−7544.
(81) De Meyer, T.; Steyaert, I.; Hemelsoet, K.; Hoogenboom, R.; Van Speybroeck, V.; De Clerck, K. Halochromic Properties of Sulfonphthaleine Dyes in a Textile Environment: The Influence of Substituents. *Dyes Pigm.* **2016**, *124*, 249−257.
(82) Hendrickx, K.; Vanpoucke, D. E. P.; Leus, K.; Lejaeghere, K.; Van Yperen-De Deyne, A.; Van Speybroeck, V.; Van Der Voort, P.; Hemelsoet, K. Understanding Intrinsic Light Absorption Properties of UiO-66 Frameworks: A Combined Theoretical and Experimental Study. *Inorg. Chem.* **2015**, *54*, 10701−10710.
(83) Hay, P. J.; Wadt, W. R. *Ab Initio* Effective Core Potentials for Molecular Calculations. Potentials for the Transition Metal Atoms Sc to Hg. *J. Chem. Phys.* **1985**, *82*, 270−283.
(84) Petit, L.; Maldivi, P.; Adamo, C. Predictions of Optical Excitations in Transition-Metal Complexes with Time Dependent-Density Functional Theory: Influence of Basis Sets. *J. Chem. Theory Comput.* **2005**, *1*, 953−962.
(85) Laurent, A. D.; Jacquemin, D. TD-DFT Benchmarks: A Review. *Int. J. Quantum Chem.* **2013**, *113*, 2019−2039.
(86) Jacquemin, D.; Perpète, E. A.; Ciofini, I.; Adamo, C.; Valero, R.; Zhao, Y.; Truhlar, D. G. On the Performances of the M06 Family of Density Functionals for Electronic Excitation Energies. *J. Chem. Theory Comput.* **2010**, *6*, 2071−2085.
(87) Atkins, A. J.; Talotta, F.; Freitag, L.; Boggio-Pasqua, M.; González, L. Assessing Excited State Energy Gaps with Time-Dependent Density Functional Theory on Ru(II) Complexes. *J. Chem. Theory Comput.* **2017**, *13*, 4123−4145.
(88) Bird, C. W. Heteroaromaticity, *S*, a Unified Aromaticity Index. *Tetrahedron* **1992**, *48*, 335−340.
(89) Bird, C. W. The Relationship of Classical and Magnetic Criteria of Aromaticity. *Tetrahedron* **1996**, *52*, 9945−9952.
(90) Wiberg, K. B.; Rablen, P. R. Comparison of Atomic Charges Derived via Different Procedures. *J. Comput. Chem.* **1993**, *14*, 1504−1518.
(91) Innocenzi, P.; Kozuka, H.; Yoko, T. Fluorescence Properties of the $Ru(Bpy)_3^{2+}$ Complex Incorporated in Sol−Gel-Derived Silica Coating Films. *J. Phys. Chem. B* **1997**, *101*, 2285−2291.
(92) Juris, A.; Balzani, V.; Belser, P.; von Zelewsky, A. Characterization of the Excited State Properties of Some New Photosensitizers of the Ruthenium (Polypyridine) Family. *Helv. Chim. Acta* **1981**, *64*, 2175−2182.
(93) Alary, F.; Boggio-Pasqua, M.; Heully, J. L.; Marsden, C. J.; Vicendo, P. Theoretical Characterization of the Lowest Triplet Excited States of the Tris-(1,4,5,8-Tetraazaphenanthrene) Ruthenium Dication Complex. *Inorg. Chem.* **2008**, *47*, 5259−5266.
(94) Alary, F.; Heully, J.-L.; Bijeire, L.; Vicendo, P. Is the ^{3}MLCT the Only Photoreactive State of Polypyridyl Complexes? *Inorg. Chem.* **2007**, *46*, 3154−3165.
(95) Mukuta, T.; Tanaka, S.; Inagaki, A.; Koshihara, S. Y.; Onda, K. Direct Observation of the Triplet Metal-Centered State in $[Ru(bpy)_3]^{2+}$ Using Time-Resolved Infrared Spectroscopy. *ChemistrySelect* **2016**, *1*, 2802−2807.
(96) Alcover-Fortuny, G.; Wu, J.; Caballol, R.; de Graaf, C. Quantum Chemical Study of the Interligand Electron Transfer in Ru Polypyridyl Complexes. *J. Phys. Chem. A* **2018**, *122*, 1114−1123.
(97) Lord, R. L.; Allard, M. M.; Thomas, R. A.; Odongo, O. S.; Schlegel, H. B.; Chen, Y.-J.; Endicott, J. F. Computational Modeling of the Triplet Metal-to-Ligand Charge-Transfer Excited-State Structures of Mono-Bipyridine−Ruthenium(II) Complexes and Comparisons to Their 77 K Emission Band Shapes. *Inorg. Chem.* **2013**, *52*, 1185−1198.
(98) Österman, T.; Abrahamsson, M.; Becker, H.-C.; Hammarström, L.; Persson, P. Influence of Triplet State Multidimensionality on Excited State Lifetimes of Bis-Tridentate RuII Complexes: A Computational Study. *J. Phys. Chem. A* **2012**, *116*, 1041−1050.
(99) Dreuw, A.; Head-Gordon, M. Failure of Time-Dependent Density Functional Theory for Long-Range Charge-Transfer Excited States: The Zincbacteriochlorin−Bacteriochlorin and Bacteriochlorophyll−Spheroidene Complexes. *J. Am. Chem. Soc.* **2004**, *126*, 4007−4016.
(100) Kobayashi, R.; Amos, R. Erratum to 'The Application of CAM-B3LYP to the Charge-Transfer Band Problem of the Zincbacteriochlorin−Bacteriochlorin Complex' [Chem. Phys. Lett. 420 (2006) 106−109]. *Chem. Phys. Lett.* **2006**, *424*, 225.
(101) Campetella, M.; Maschietto, F.; Frisch, M. J.; Scalmani, G.; Ciofini, I.; Adamo, C. Charge Transfer Excitations in TDDFT: A Ghost-Hunter Index. *J. Comput. Chem.* **2017**, *38*, 2151−2156.
(102) Zhang, L.; Wang, W.; Sun, S.; Jiang, D. Near-Infrared Light Photocatalysis with Metallic/Semiconducting H_xWO_3/WO_3 Nanoheterostructure in Situ Formed in Mesoporous Template. *Appl. Catal., B* **2015**, *168*, 9−13.
(103) Liu, W.-X.; Zhu, X.-L.; Liu, S.-Q.; Gu, Q.-Q.; Meng, Z.-D. Near-Infrared-Driven Selective Photocatalytic Removal of Ammonia Based on Valence Band Recognition of an α-MnO_2 /N-Doped Graphene Hybrid Catalyst. *ACS Omega* **2018**, *3*, 5537−5546.

DOI: 10.1021/acs.jpca.9b05216
J. Phys. Chem. A XXXX, XXX, XXX−XXX

B

List of Publications

Publications in International Peer–Reviewed Journals

1. **Optical Properties of Isolated and Covalent Organic Framework-Embedded Ruthenium Complexes**
   Francesco Muniz-Miranda, Liesbeth De Bruecker, Arthur De Vos, Flore Vanden Bussche, Christian V. Stevens, Pascal Van Der Voort, Kurt Lejaeghere, Veronique Van Speybroeck
   J. Phys. Chem. A, **2019**, *123*, 6854-6867
   IF: 2.836, Number of citations: 0

2. **Electronic Properties of Heterogenized Ru (II) Polypyridyl Photoredox Complexes on Covalent Triazine Frameworks**
   Arthur De Vos, Kurt Lejaeghere, Francesco Muniz-Miranda, C. Stevens, Pascal Van der Voort and Veronique Van Speybroeck
   J. Mater. Chem. A, **2019**, *7*, 8433–8442
   IF: 10.733, Number of citations: 1

3. **Exploring Lanthanide Doping in UiO-66: A Combined Experimental and Computational Study of the Electronic Structure**
   Kevin Hendrickx, Jonas J. Joos, Arthur De Vos, Dirk Poelman, Phillipe F. Smet, Veronique Van Speybroeck, Pascal Van Der Voort and Kurt Lejaeghere

Inorg. Chem., **2018**, *57*, 5463–5474,
IF: 4.850, Number of citations: 11

4. **Missing Linkers: An Alternative Pathway to UiO-66 Electronic Structure Engineering**
   Arthur De Vos, Kevin Hendrickx, Pascal Van Der Voort, Veronique Van Speybroeck and Kurt Lejaeghere
   Chem. Mater., **2017**, *29*, 3006–3019
   IF: 10.159, Number of citations: 47

5. **Water Coordination and Dehydration Processes in Defective UiO-66 Type Metal Organic Frameworks**
   Matthias Vandichel, Julianna Hajek, An Ghysels, Arthur De Vos, Michiel Waroquier and Veronique Van Speybroeck
   CrystEngComm, **2016**, *18*, 7056–7069
   IF: 3.382, Number of citations: 28

6. **First-Principles Study of Antisite Defect Configurations in $ZnGa_2O_4$:Cr Persistent Phosphors**
   Arthur De Vos, Kurt Lejaeghere, Danny E. P. Vanpoucke, Jonas J. Joos, Phillipe F Smet and Karen Hemelsoet
   Inorg. Chem., **2016**, *55*, 2402–2412
   IF: 4.850, Number of citations: 47

Conference Contributions

Oral Presentations

1. **First-Principles Insight Into Heterogeneous Photocatalysis at Photoactive Ru Complexes on Covalent Triazine Frameworks**
   Arthur De Vos, Kurt Lejaeghere, Francesco Muniz-Miranda, Pascal Van Der Voort and Veronique Van Speybroeck
   6th International Conference on Metal-Organic Frameworks, Auckland, New Zealand, December 9–13, 2018

2. **Towards Modeling Long-Range Disorder in MOFs: Development of a Computational Toolbox to Extend the Length Scale in Molecular Simulations**
   Sven M.J. Rogge, Ruben Demuynck, Arthur De Vos, Kevin Hendrickx, Kurt Lejaeghere, Guillaume Maurin, Steven Vandenbrande, Sander Vandenhaute, Pascal Van Der Voort, Louis Vanduyfhuys, Toon Verstraelen, Michel Waroquier, Jelle Wieme, and Veronique Van Speybroeck
   CECAM workshop: Multi-Scale Modelling of Flexible and Disordered Porous Materials, Paris, France, June 11–13, 2018

3. **Towards a Molecular Level Understanding of Chemical and Physical Phenomena in Metal-Organic Frameworks**
   Jelle Wieme, Chiara Caratelli, Ruben Demuynck, Arthur De Vos, Julianna Hajek, Alexander E.J. Hoffman, Aran Lamaire, Kurt Lejaeghere, Sven M.J. Rogge, Steven Vandenbrande, Louis Vanduyfhuys, and Veronique Van Speybroeck
   Premier Congrès Français des MOFs, COFS et Polymères Poreux, Paris, France, May 16–17, 2018

4. **Missing linkers: An Alternative Pathway to UiO-66 Electronic Structure Engineering**
   Arthur De Vos, Kevin Hendrickx, Pascal Van Der Voort, Veronique Van Speybroeck and Kurt Lejaeghere
   European Congress and Exhibition on Advanced Materials and Processes, Thessaloniki, Greece, September 17–22, 2017

5. **Orthogonal Band Gap Engineering of UiO-66 Frameworks Through Active Control of Defects**
   Kurt Lejaeghere, Arthur De Vos, Kevin Hendrickx, Sven M. J. Rogge, Pascal Van Der Voort and Veronique Van Speybroeck

EMN Meeting 2016 on Active Matter, Las Vegas, NV, USA October 10–14, 2016

6. **Generation of Active Sites for Catalysis in UiO-66 Studied by a Complementary Set of Static and Dynamic Simulations**
   Julianna Hajek, Kurt De Wispelaere, Arthur De Vos, Michiel Waroquier, Dirk De Vos and Veronique Van Speybroeck
   Annual IAP Meeting IAP-PAI P7/05, Liège, Belgium , September 12, 2016

7. **Understanding Light-Absorption in MOFs: Combined Experimental and Theoretical Study of UiO-66 Type Frameworks**
   Kevin Hendrickx, Arthur De Vos, Kevin Hemelsoet, Pascal Van Der Voort and Veronique Van Speybroeck
   5th International Conference on Metal-Organic Frameworks & Open Framework Compounds, Long Beach, CA, USA, September 11–15, 2016

8. **Orthogonal Band Gap Engineering in Zr Based MOFs**
   Arthur De Vos, Kevin Hendrickx, Sven M. J. Rogge, Kurt Lejaeghere and Veronique Van Speybroeck
   IAP-WP2, Zwijnaarde, Belgium , June 17, 2016

Poster Presentations

1. **Insight in Heterogeneous Photocatalysis by Anchoring a Photoactive Ru Complex on a Covalent Triazine Framework**
   Arthur De Vos, Kurt Lejaeghere, Francesco Muniz-Miranda, Pascal Van Der Voort and Veronique Van Speybroeck
   MOFSIM2019, Ghent, Belgium, April 10–12, 2019

2. **Insight in Heterogeneous Photo Catalysis by Anchoring a Photo Active Ru Complex on a Covalent Triazine Framework**
   Arthur De Vos, Kurt Lejaeghere, Francesco Muniz-Miranda, Pascal Van Der Voort and Veronique Van Speybroeck
   Computational spectroscopy: bridging theory and experiment, Como, Greece, September 9–14, 2018

3. **Understanding Light-Absorption in MOFs: Combined Experimental and Theoretical Study of UiO-66 Type Frameworks**
   Kevin Hendrickx, Arthur De Vos, Karen Hemelsoet, Pascal Van Der Voort and Veronique Van Speybroeck

Chemical Research in Flanders (CRF-1), Blankenberge, Belgium, October 24–26, 2016

4. **Understanding Intrinsic Light Absorption Properties of UiO-66 Frameworks: A Combined Theoretical and Experimental Study**
   Kevin Hendrickx, Arthur De Vos, Pascal Van Der Voort and Veronique Van Speybroeck
   Annual IAP meeting, Liège, Belgium, September 12, 2016

5. **Combined Theoretical-Experimental Study of Chromium Doped Zinc Gallate Phosphor**
   Arthur De Vos, Kurt Lejaeghere, Danny E. P. Vanpoucke, Jonas J. Joos, Phillipe F. Smet and Karen Hemelsoet
   MolSim 2016: Understanding Molecular Simulations, Amsterdam, The Netherlands, January 6–15, 2016

6. **Combined Theoretical-Experimental Study of Chromium Doped Zinc Gallate Phosphor**
   Arthur De Vos, Danny E. P. Vanpoucke, Kurt Lejaeghere, Jonas J. Joos, Phillipe F. Smet, Karen Hemelsoet,
   IAP Annual meeting, Hasselt, Belgium, September 11, 2015

7. **Combined Theoretical-Experimental Study of Chromium Doped Zinc Gallate Phosphor**
   Arthur De Vos, Kurt Lejaeghere, Danny E. P. Vanpoucke, Jonas J. Joos, Phillipe F. Smet, Karen Hemelsoet
   XVIITH INTERNATIONAL KRUTYN SUMMER SCHOOL 2015, Krutyń, Poland, June 14–20, 2015

Master's Thesis

Combined Theoretical-Experimental Study of Luminescent Materials

Arthur De Vos
Master's thesis performed at the Center for Molecular Modeling (CMM), Ghent University, 2014–2015
Supervisors: Veronique Van Speybroeck and Philippe Smet

C

High-Performance Computing Infrastructure

The computational resources and services used in this Ph.D. dissertation were provided by Flemish Supercomputer Center (VSC), funded by Ghent University, the Fund for Scientific Research Flanders (FWO) and the Flemish Government Department of Economy, Science and Innovation (EWI). A list of granted computational projects on Tier-1 and a table with used infrastructure details (Tier-1/2) are provided (see below). Figure C.1 displays the computational time that was used on Tier-2, which amounts to more than 800 core years.

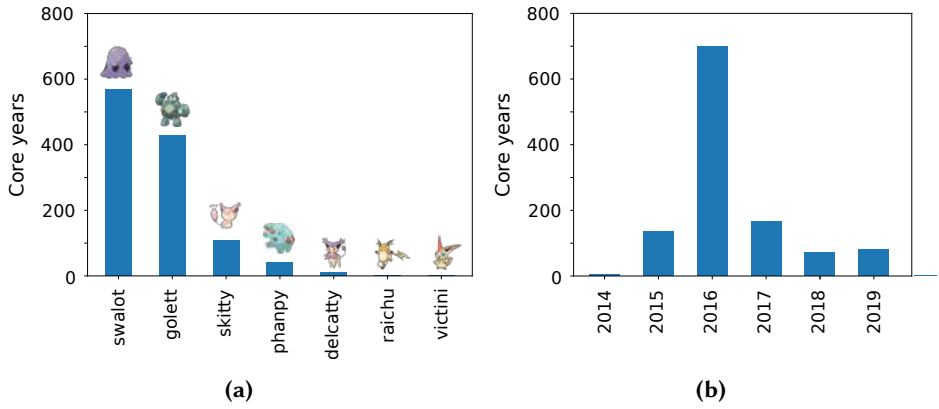

Figure C.1: (a) Computational time used on the Tier-2 clusters. (b) Computational time used per year.

BrENIAC

1. *Stacking silver differently for improved surface properties*
   Jul 2019 - Mar 2018
   4776 node days

2. *First-principles insight into heterogeneous photocatalysis at photoactive complexes on a Covalent Organic Framework*
   Jul 2018 - Mar 2018
   2304 node days

3. *Discovering the temperature dependence of charged defect concentrations in Ge using HSE06*
   Nov 2017 - Apr 2017
   3887 node days

4. *Electronic properties of 2D nitrogen-containing Covalent organic Frameworks from First-Principles Simulations*
   Jul 2017 - Dec 2017
   2128 node days

5. *Electronic properties of 3D nitrogen-containing Covalent organic Frameworks from First-Principles Simulations*
   Apr 2017 - Sep 2017
   3789 node days

Muk

1. *Defect engineering in UiO-66: How linker defects affect the electronic structure.*
   Jul 2016 - Dec 2016
   4116 node days

Cluster name	Processor architecture	Memory/node	Interconnect	Tier level
skitty	2×18-core Intel Xeon Gold 6140 (Skylake @ 2.3GHz)	192 GB	EDR Infiniband	Tier-2
victini	2×18-core Intel Xeon Gold 6140 (Skylake @ 2.3GHz)	96 GB	10 GbE	Tier-2
BrENIAC	2×14-core Intel Xeon E5-2680v4 (Broadwell-EP @ 2.4GHz)	128/256 GB	EDR Infiniband	Tier-1
swalot	2×10-core Intel Xeon E5-2660v3 (Haswell-EP @ 2.6 GHz)	128 GB	FDR Infiniband	Tier-2
golett	2×12-core Intel Xeon E5-2660v3 (Haswell-EP @ 2.5 GHz)	64 GB	FDR-10 Infiniband	Tier-2
phanpy	2×12-core Intel Xeon E5-2660v3 (Haswell-EP @ 2.5 GHz)	512 GB	FDR Infiniband	Tier-2
delcatty	2×8-core Intel Xeon E5-2670 (Sandy Bridge @ 2.6 GHz)	64 GB	FDR Infiniband	Tier-2
muk	2×8-core Intel Xeon E5-2670 (Sandy Bridge @ 2.6 GHz)	64 GB	FDR Infiniband	Tier-1
raichu	2×8-core Intel Xeon E5-2670 (Sandy Bridge @ 2.6 GHz)	32 GB	1 GbE	Tier-2

Acknowledgements

This research was supported by the Research Foundation Flanders (FWO) through a personal mandate.

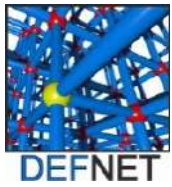

Funding was also received from the European Union's Horizon 2020 research and innovation programme under the European Research Council consolidator grant agreement no. 647755 (project acronym: DYNPOR), the European Union's Horizon 2020 research and innovation programme under the Marie Skłodowska–Curie grant agreement no. 641887 (project acronym: DEFNET), and BELSPO in the frame of IAP/7/05.

The computational resources (Stevin Supercomputer Infrastructure) and services used in this work were provided by the VSC (Flemish Supercomputer Center), funded by Ghent University, FWO, and the Flemish Government – department EWI.